

# Mechanics of Growth and Coalescence of Pre-existing Voids in a Ductile Matrix

THÈSE N° 5034 (2011)

PRÉSENTÉE LE 10 JUIN 2011

À LA FACULTÉ SCIENCES ET TECHNIQUES DE L'INGÉNIEUR  
LABORATOIRE DE CONCEPTION DE SYSTÈMES MÉCANIQUES  
PROGRAMME DOCTORAL EN SYSTÈMES DE PRODUCTION ET ROBOTIQUE

ÉCOLE POLYTECHNIQUE FÉDÉRALE DE LAUSANNE

POUR L'OBTENTION DU GRADE DE DOCTEUR ÈS SCIENCES

PAR

**Tomasz JODŁOWSKI**

acceptée sur proposition du jury:

Prof. M.-O. Hongler, président du jury  
Prof. J. Giovanola, directeur de thèse  
Prof. L. Delannay, rapporteur  
Prof. A. Mortensen, rapporteur  
Prof. T. Pardoen, rapporteur



ÉCOLE POLYTECHNIQUE  
FÉDÉRALE DE LAUSANNE

Suisse  
2011



# Preface

Pursuing this work to a happy end would not have been possible without the involvement of many individuals and institutions, and it is my pleasure to thank all those who participated in this research project. I would particularly like to thank:

- Professor Jacques Giovanola, supervisor of this thesis, who hosted me in the LCSM laboratory and supported me in a number of ways over the last several years, gave me the opportunity to work on this project, provided kind support, was available for discussion despite his tight schedule and for the critical assessment of my work.
- Members of the LCSM laboratory for a warm welcome and a pleasant atmosphere, particularly Claire Chabanel for coping with all administrative work, and my officemates and friends: Daniele Cannizzaro, Grégory Piot, Elia Deschenaux, David Hoover, Yves Rothenbühler and Quentin Theurillat, for many enriching professional and private discussions.
- Doctor Andreas Rossoll, an expert in fracture mechanics, materials, simulations, fortran, cycling, swimming, tango and in many others fields, for help with numerical and experimental issues. Here, I would also like to show my appreciation for the help received from Doctor Joël Cugnoni, Abaqus guru, for solving technical problems related to this software.
- Members of the AMB workshop, Marc Jeanneret, Nicolas Favre, Stéphane Haldner, who were handling my numerous orders for samples and tooling preparation.
- The CIME team who made the SEM analysis possible: Fabienne Bobard and Marco Cantoni for the introduction to the SEM technique, Danièle Laub for help with SEM sample preparation technique development, Emmanuelle Boehm Courjault for help with the EBSD material characterization.

This work was also graciously supported by many individuals and institutions outside of the EPFL and amongst them I would like to thank:

- Professor Andrzej Zieliński from Cracow University of Technology (CUT), my former teacher and supervisor, who inspired me with the idea and motivated me to do a PhD.
- Professor Laurent Delannay and Doctor Sylvain Dancette from the Université Catholique de Louvain, Applied Mechanics and Mathematics (SST/IMMC/MEMA), for making available and customizing their polycrystal plasticity model used in the computational part of this project and for a fruitful collaboration.
- Professor Thomas Pardoen, Doctor Cihan Tekoğlu and their colleagues from Université Catholique de Louvain, Materials and Process Engineering unit (SST/IMMC/IMAP), for their time and knowledge shared during my stay at UCL.
- Swissmetal, particularly Doctors Claudio Penna and Natanael Dewobroto, for help with the selection of materials used in the experimental part of the thesis and for providing them free of charge.
- Doctors Iwan Jerjen and Philipp Schuetz from the Swiss Federal Laboratory for Materials Science and Technology (EMPA), Electronics/Metrology unit, for performing computed tomography (CT) and generating 3D images of tested samples. I am also grateful to Doctor Eric Maire from INSA, Lyon, for CT in situ scans of tensile samples, which unfortunately we were not able to use in this report.
- The Swiss National Science Foundation (SNSF) for financial support (Project FNS 200020 – 107473).

I owe my deepest gratitude to many people who, even if not directly involved in this research project, contributed by their personal support: Valérie Renaudin, Meta Djojosebroto, Ursula Held, Piotr Krawczyk, Riccardo Puragliesi and Rafal Obrzud.

I would like to thank to my mom, Irena Jodłowska... for being a great mom. (Dziękuję mojej mamie ... za bycie wspaniałą mamą).

I am grateful to my wife, Joanna Malik-Jodłowska, for love, patience, tolerance and support at all times and in every endeavor.

*Thank you, Merci, Grazie, Danke, Dziękuję ...*

# Contents

<b>Contents</b>	<b>v</b>
<b>Abstract</b>	<b>ix</b>
<b>Résumé</b>	<b>xi</b>
<b>List of Figures</b>	<b>xiii</b>
<b>List of Tables</b>	<b>xix</b>
<b>1 Introduction</b>	<b>1</b>
1.1 General background and motivation . . . . .	1
1.2 General topic of dissertation . . . . .	2
1.3 Outline of dissertation . . . . .	2
<b>2 State of the art</b>	<b>5</b>
2.1 General outline of the state of the art . . . . .	5
2.2 Void nucleation, growth and coalescence . . . . .	6
2.2.1 Void nucleation . . . . .	6
2.2.2 Void growth . . . . .	7
2.2.3 Void coalescence . . . . .	15
2.2.4 Sequential nature of the VNGC process . . . . .	17
2.2.5 Effect of loading conditions . . . . .	18
2.2.6 Example of a complete VNGC model . . . . .	18
2.3 Crystal plasticity . . . . .	20
2.3.1 Poynting and Swift effect . . . . .	22
2.4 Model materials . . . . .	23
2.5 Gaps in our knowledge . . . . .	24
2.6 Postulate . . . . .	25
<b>3 Materials and experimental procedures</b>	<b>27</b>
3.1 Outline of the approach . . . . .	27
3.2 Model material selection and validation . . . . .	28
3.2.1 Concept of model material . . . . .	28
3.2.2 Requirements . . . . .	28
3.2.3 Selection . . . . .	29

3.2.4	Characterization . . . . .	31
3.2.5	Validation . . . . .	36
3.2.6	Summary . . . . .	40
3.3	Experimental techniques . . . . .	42
3.3.1	Mechanical testing . . . . .	42
3.3.2	Metallographic techniques . . . . .	45
3.3.3	Image analysis technique and resolution . . . . .	48
3.3.4	Void orientation and size analysis . . . . .	50
3.3.5	Densitometry . . . . .	61
3.3.6	EBSD and texture measurement . . . . .	65
3.3.7	X-ray computed tomography . . . . .	66
3.4	Numerical simulations . . . . .	66
3.4.1	Constitutive behavior . . . . .	66
3.4.2	Continuum calculations . . . . .	68
3.4.3	Single cell calculations . . . . .	69
3.4.4	Crystal plasticity . . . . .	75
<b>4</b>	<b>Results</b>	<b>77</b>
4.1	General outline of the results . . . . .	77
4.2	Global behavior . . . . .	79
4.2.1	Sample response . . . . .	79
4.2.2	Texture evolution . . . . .	82
4.2.3	Numerical simulations . . . . .	86
4.3	Fracture behavior . . . . .	97
4.3.1	Void nucleation . . . . .	97
4.3.2	Void evolution . . . . .	101
4.3.3	Fracture initiation . . . . .	104
4.3.4	Fracture mechanism . . . . .	108
4.4	Void size analysis . . . . .	116
4.4.1	Void orientation . . . . .	116
4.4.2	Void size distributions . . . . .	121
4.4.3	Void elongation . . . . .	134
4.4.4	Void growth . . . . .	145
4.4.5	Void coalescence . . . . .	150
4.5	Void size computations . . . . .	154
4.5.1	Macroscopic simulations . . . . .	154
4.5.2	Void evolution under tensile dominated loadings . . . . .	155
4.5.3	Void evolution under shear dominated loadings . . . . .	163
4.6	Key experimental and numerical results . . . . .	176
4.6.1	Material behavior under loading . . . . .	176
4.6.2	Fracture mechanisms . . . . .	176
4.6.3	Size dependence . . . . .	178

<b>5</b>	<b>Discussion</b>	<b>179</b>
5.1	General outline of the discussion . . . . .	179
5.2	Global behavior . . . . .	179
5.2.1	Texture induced anisotropy . . . . .	180
5.2.2	Shape changes in PT samples . . . . .	182
5.2.3	Effect of pre-existing voids on coalescence and ductility . . . . .	183
5.3	Fracture behavior . . . . .	185
5.3.1	Fracture mechanism . . . . .	186
5.3.2	Void nucleation . . . . .	187
5.3.3	Void growth . . . . .	188
5.3.4	Void coalescence . . . . .	196
5.4	Size effects . . . . .	201
5.4.1	Initial shape . . . . .	202
5.4.2	Void evolution . . . . .	202
<b>6</b>	<b>Conclusions and perspectives</b>	<b>205</b>
6.1	Summary of results . . . . .	205
6.2	Conclusions . . . . .	206
6.3	Perspectives . . . . .	208
<b>A</b>	<b>Abandoned materials</b>	<b>211</b>
A.1	GGG40 . . . . .	211
A.2	AISI 303, 303 SE and 304 . . . . .	211
A.3	Copper alloys . . . . .	212
A.3.1	$\alpha$ - $\beta$ - CuZn39Pb3 . . . . .	212
A.3.2	62A and E63 . . . . .	213
A.3.3	C97 and B98 . . . . .	213
<b>B</b>	<b>Sample design</b>	<b>217</b>
<b>C</b>	<b>Void size analysis</b>	<b>219</b>
<b>D</b>	<b>Kinematic boundary conditions</b>	<b>221</b>
	<b>Nomenclature</b>	<b>222</b>
	<b>Bibliography</b>	<b>229</b>
	<b>Curriculum Vitae</b>	<b>245</b>





# Abstract

This research project experimentally and numerically investigates the growth and coalescence of pre-existing voids for a wide range of stress states in a ductile matrix with a special focus on shear dominated loading conditions and presents quantitative kinetics data for these processes. The results obtained contribute to further development of current fracture models by generating reliable experimental data for void growth and coalescence, which can be used to evaluate the existing fracture models.

A lead-containing copper alloy has been selected as model material, in which lead inclusions act as pre-existing voids – as demonstrated by unit cell numerical simulations for a wide range of stress states. A second copper alloy of similar composition, but without lead allows us to obtain mechanical properties of the matrix. By comparing the behavior of the two alloys it is possible to evaluate the effect of the voids on the macroscopic mechanical behavior. The model materials are deformed and fractured in combined torsion / tension tests and notched tensile tests to subject them to the desired wide range of stress triaxialities. Quantitative fractography and metallography provide the desired kinetics data on void shape, size and orientation, that can be correlated with numerical simulations, as well as existing void growth and coalescence models. The influence of stress-state and micro-structural characteristics on void growth and void coalescence – particularly for zero nominal stress triaxiality conditions – is illustrated at the hand of the results of the investigation.

Contrary to the predictions of current micromechanical models, significant growth of small voids resulting in moderate increases in the total void volume is observed in torsion specimens. This growth may be triggered by the developing texture of the matrix material and particularly by twinning. By means of FEM computations with 3D single cell simulations comprising initially ellipsoidal voids, the effect of the initial texture and texture evolution is emphasized. The numerical results showed that the experimentally observed texture of the material accelerates void growth under relatively high stress triaxialities, and possibly allows growth of small voids under low and zero stress triaxialities. The initial shape of the lead inclusions and possibly their growth, was found to be dependent on their initial size. These results emphasize the need for a complete and rather detailed modeling of microstructural and de-

formation features in order to model damage process correctly.

The presented work contributes to a better understanding of void growth and coalescence fracture processes, particularly under shear dominated loading conditions.

**Keywords:** ductile fracture, void growth, void coalescence, low stress triaxiality, polycrystalline plasticity, anisotropy, texture evolution, brass, lead, pre-existing voids, soft inclusions.

# Résumé

Ce projet de recherche étudie expérimentalement et numériquement la croissance et la coalescence de cavités préexistantes dans une matrice ductile soumise à un large éventail d'état de contrainte, avec une attention particulière donnée aux chargements dominés par le cisaillement. Il développe des données quantitatives sur la cinétique de ces processus. Les résultats obtenus contribuent au développement de modèles de rupture améliorés en mettant à disposition des données expérimentales fiables pour la croissance et la coalescence de cavités, qui peuvent être utilisées pour l'évaluation des modèles de rupture existants.

Un alliage cuivreux contenant du plomb a été choisi comme matériau modèle, dans lequel les inclusions de plomb jouent le rôle de cavités préexistantes – comme le démontrent des simulations avec des cellules élémentaires – pour une large fourchette d'états de contrainte. Un second alliage cuivreux de même composition, mais sans plomb permet d'obtenir les propriétés de la matrice et par comparaison avec le comportement de l'alliage contenant du plomb d'évaluer l'effet des cavités sur le comportement mécanique macroscopique. Les matériaux modèles sont déformés et fracturés dans des essais de torsion / traction combinées et des essais de traction avec des éprouvettes lisses et entaillées pour atteindre les valeurs de triaxialité désirées. La fractographie et la métallographie quantitatives fournissent les données cinétiques sur la forme, la taille et l'orientation de cavités, qui peuvent ensuite être corrélées avec les résultats de simulations numériques et les prédictions de modèles existants de croissance et de coalescence des cavités. L'influence des caractéristiques microstructurales et de l'état de contrainte – en particulier pour une triaxialité nominale nulle – sur la croissance et la coalescence de cavités est illustrée sur la base des résultats expérimentaux.

Contrairement aux prédictions des modèles micromécaniques actuels, on observe dans les éprouvettes de torsion une croissance importante des petites cavités, qui résulte en une augmentation modérée de la fraction volumique des cavités. Cette croissance peut être causée par le développement de la texture de la matrice et particulièrement par le maillage de celle-ci. L'effet de la texture initial et de son évolution est mis en évidence au moyen de simulations éléments finis basées sur un modèle de plasticité polycristalline de cellules unitaires tridimensionnelles contenant des cavités ellipsoïdales. Les résultats

numériques montrent que la texture du matériau observée expérimentalement accélère la croissance des cavités soumises à des triaxialités relativement hautes mais permet aussi celle de petites cavités pour des triaxialités faibles ou nulles. On trouve que la forme initiale des inclusions de plomb et possiblement leur croissance dépendent de leur taille d'origine. Ces résultats mettent en exergue la nécessité d'une modélisation complète et détaillée de tous les aspects microstructuraux et de déformation pour modéliser correctement les processus d'endommagement.

Ce travail contribue à une meilleure compréhension des processus de rupture gouvernés par la croissance et la coalescence de cavités spécialement pour des cas de charge dominés par le cisaillement.

**Mots-clés:** rupture ductile, croissance de cavités, coalescence de cavités, triaxialité faible, plasticité polycristalline, anisotropie, évolution de la texture, laiton, plomb, cavités préexistantes, inclusions molles.

# List of Figures

3.1	Microstructure of A1 and A2 alloy revealed by etching . . . . .	30
3.2	Typical lead inclusion-void system in an ion milled A1 . . . . .	31
3.3	A lead inclusion in tested <i>NT3</i> sample . . . . .	32
3.4	Microstructure of A1 lead-containing brass . . . . .	34
3.5	Typical inclusion-void system in an undeformed A2 . . . . .	35
3.6	Axisymmetric single cell shape and boundary conditions . . . . .	37
3.7	2D axisymmetric single cell response. . . . .	39
3.8	Effect of lead presence on material hardening. . . . .	41
3.9	Geometry of tested samples . . . . .	42
3.10	Position of the tensile and torsional specimens in the initial round bar. . . . .	43
3.11	Typical representation of the results of 3 torsion tests and of the calculated mean curve . . . . .	46
3.12	Steps in the specimen preparation for SEM investigation. . . . .	46
3.13	Definition of sectioning planes of the tested samples. . . . .	47
3.14	BSE profile for the Cu-Zn matrix and Pb inclusion interface simulated using Casino - a Monte-Carlo simulation software. . . . .	49
3.15	Distribution of orientations of major axes in <i>AT</i> and <i>AR</i> planes	52
3.16	Interpretation of cumulative number graphs. . . . .	52
3.17	Size distribution of major axis ( <i>M</i> ) measured in <i>AR</i> plane 3 times in different regions of the same nondeformed sample. . . . .	54
3.18	Size distribution of major ( <i>M</i> ) and minor ( <i>m</i> ) axis in unde- formed material . . . . .	55
3.19	Measurement of inclusion characteristic parameters <i>M</i> , <i>m</i> <sub>1</sub> and <i>m</i> <sub>2</sub> in torsional sample. . . . .	57
3.20	Calculation of void axis elongation factor. . . . .	58
3.21	Torsional sample sectioning for densitometry measurements. . . . .	62
3.22	Schematic representation of the alloy components . . . . .	63
3.23	A1 and A2 constitutive law. . . . .	67
3.24	Sample axisymmetric models with boundary conditions applied	68
3.25	3D single cell for tensile dominated loadings. . . . .	70
3.26	3D single cell for shear dominated loadings. . . . .	71
3.27	3D single cell containing lead inclusions for shear dominated loadings. . . . .	74
3.28	3D periodic macroscopic model with a finite void. . . . .	75

4.1	A1 and A2 smooth round tensile ( <i>ST</i> ) tests results. . . . .	80
4.2	A1 notched round tensile test ( <i>NTx</i> ) results. . . . .	81
4.3	A2 notched round tensile ( <i>NTx</i> ) test results. . . . .	81
4.4	A1 pure torsional ( <i>PT</i> ) and tensile-torsional ( <i>TTx</i> ) test results.	83
4.5	A2 pure torsional ( <i>PT</i> ) and tensile-torsional ( <i>TTx</i> ) test results.	83
4.6	Comparison of A1 and A2 pure torsional ( <i>PT</i> ) test results. . .	84
4.7	Rate of torque increase vs sample rotation angle in the <i>PT</i> sample	84
4.8	A2 constitutive law obtained from <i>ST</i> and <i>PT</i> tests. . . . .	85
4.9	A2 pole figures for undeformed material ( <i>UD</i> ), smooth round tensile ( <i>ST</i> ) and notched round tensile ( <i>NT3</i> ) tests . . . . .	87
4.10	A2 pole figures for undeformed material ( <i>UD</i> ) and two pure torsional ( <i>PT</i> ) tests . . . . .	88
4.11	<i>ST</i> experimental and simulation results. . . . .	90
4.12	<i>NT1</i> experimental and simulation results. . . . .	91
4.13	<i>NT2</i> experimental and simulation results. . . . .	91
4.14	<i>NT3</i> experimental and simulation results. . . . .	92
4.15	<i>PT</i> experimental and simulation results. . . . .	92
4.16	<i>TT1</i> experimental and simulation results. . . . .	93
4.17	<i>TT2</i> experimental and simulation results. . . . .	93
4.18	Samples deformed up to fracture under <i>PT</i> loading . . . . .	94
4.19	Evolution of <i>D</i> , external diameter in the <i>PT</i> sample . . . . .	95
4.20	Evolution of <i>d</i> , internal diameter in the <i>PT</i> sample . . . . .	95
4.21	Evolution of <i>t</i> wall thickness in the <i>PT</i> sample . . . . .	96
4.22	A1 round notched tensile <i>NT3</i> fracture surface . . . . .	98
4.23	A1 fracture surfaces resulting from <i>NT3</i> and <i>PT</i> loading con- ditions. . . . .	99
4.24	A2 hard inclusions in electro-polished samples . . . . .	99
4.25	A2 fracture surfaces resulting from <i>ST</i> and <i>PT</i> loading . . . .	100
4.26	A1 <i>PT</i> experimental results - interrupted tests. . . . .	102
4.27	Shape and orientation of inclusions in A1 at various extents of <i>PT</i> loading . . . . .	102
4.28	A2 <i>PT</i> experimental results - interrupted tests. . . . .	103
4.29	Shape and orientation of A2 inclusions at various extents of <i>PT</i> loading . . . . .	104
4.30	A1 round notched tensile <i>NT1</i> interrupted test. . . . .	106
4.31	A1 <i>NT1</i> interrupted test samples . . . . .	106
4.32	A2 round notched tensile <i>NT1</i> interrupted test. . . . .	107
4.33	A2 <i>NT1</i> interrupted test samples . . . . .	107
4.34	A1 and A2 alloy <i>ST</i> sample cross sections close to the fracture surface. . . . .	108
4.35	A1 tensile fracture surfaces. . . . .	110
4.36	A2 tensile fracture surfaces. . . . .	111
4.37	A1 torsion fracture surfaces. . . . .	112
4.38	A2 torsion fracture surfaces. . . . .	113
4.39	A1 torsion cross sections, <i>AT</i> plane. . . . .	114
4.40	A2 torsion cross section, <i>AT</i> plane. . . . .	115

4.41	Inclusion orientation in tensile and notched tensile samples. . .	117
4.42	Inclusion orientation in $AT$ plane for torsional loadings. . . . .	117
4.43	Inclusion orientation in $AR$ plane for torsional loadings. . . . .	118
4.44	Behavior of inclusions at grain boundaries. . . . .	118
4.45	Inclusion deformation in torsional loading. . . . .	119
4.46	Void orientation angle as a function of loading conditions, observed in $AT$ and $AR$ planes in fractured samples. . . . .	120
4.47	Cumulative size distribution of the major axis $M$ measured in the $AR$ plane at three locations in the same undeformed original round bar. . . . .	122
4.48	Cumulative size distribution of major ( $M$ ) and minor ( $m$ ) axis in undeformed material. . . . .	123
4.49	Cumulative size distribution of the major axis ( $M$ ) in tensile and notched tensile tests. . . . .	124
4.50	Cumulative size distribution of the minor axis ( $m$ ) in tensile and notched tensile tests. . . . .	125
4.51	Cumulative size distribution of the major axis ( $M$ ) in torsion and tensile torsion tests. . . . .	127
4.52	Cumulative size distribution of the first minor axis ( $m_1$ ) in torsion and tensile torsion tests. . . . .	128
4.53	Cumulative size distribution of the second minor axis ( $m_2$ ) in torsion and tensile torsion tests. . . . .	129
4.54	Cumulative size distribution of the major axis ( $M$ ) in interrupted torsion tests. . . . .	130
4.55	Cumulative size distribution of the first minor axis ( $m_1$ ) in interrupted torsion tests. . . . .	131
4.56	Cumulative size distribution of the second minor axis ( $m_2$ ) in interrupted torsion tests. . . . .	132
4.57	Cumulative size distribution of the second minor axis ( $m_2$ ) in pure torsion tests obtained with computed tomography. . . . .	133
4.58	Estimate of the $f$ error. . . . .	135
4.59	Initial void aspect ratio $W_0$ as a function of major axis initial length. . . . .	137
4.60	Major void axis elongation factor $f_M$ at fracture under tensile loading as a function of the initial major axis length. . . . .	138
4.61	Minor void axis elongation factor $f_m$ at fracture under tensile loading as a function of the initial minor axis length. . . . .	139
4.62	Major void axis elongation factor $f_M$ at fracture under torsional loading as a function of major axis initial length. . . . .	140
4.63	Minor void axis elongation factor $f_m$ at fracture under torsional loading as a function of minor axis initial length. . . . .	141
4.64	Major void axis elongation factor $f_M$ at various angles of torsional deformation as a function of major axis initial length. . .	142
4.65	Minor void axis elongation factor $f_m$ at various angles or torsional deformation as a function of minor axis initial length. . .	143

4.66	Second minor void axis elongation factor $f_{m2}$ in pure torsion tests as a function of the initial length of the second minor axis. Results obtained using computed tomography (CT) present the whole data set. . . . .	144
4.67	Void aspect ratios $W_1$ and $W_2$ at the onset of coalescence as a function of loading conditions. . . . .	146
4.68	Void volume fraction at the onset of coalescence as a function of loading conditions. . . . .	146
4.69	Void aspect ratios $W_1$ and $W_2$ in interrupted <i>PT</i> experiments as a function of the sample twist angle. . . . .	148
4.70	Void volume fraction in interrupted <i>PT</i> experiments as a function of the sample twist angle. . . . .	148
4.71	Void volume fraction under <i>PT</i> loading as a function of the sample twist angle - densitometry measurement. . . . .	149
4.72	3D images of the inside of the <i>A1</i> alloy . . . . .	150
4.73	Schematic explanation of the void growth . . . . .	152
4.74	Minor void axis elongation factor at the end of coalescence ( $f_m^c$ ) in the <i>NT3</i> sample of the <i>A1</i> alloy as a function of minor axis length at the onset of coalescence. . . . .	153
4.75	Stress triaxiality $T$ as a function of equivalent plastic strain $\varepsilon_{eq}^{pl}$ and average stress triaxiality $T_{avg}$ for different loading conditions, calculated with the <i>A2</i> constitutive law and $J_2$ material model. . . . .	156
4.76	Response of the 3D single cell for tensile loadings . . . . .	158
4.77	Single cell simulation results for the <i>ST</i> loading. . . . .	159
4.78	Single cell simulation results for the <i>NT1</i> loading. . . . .	160
4.79	Single cell simulation results for the <i>NT2</i> loading. . . . .	161
4.80	Single cell simulation results for the <i>NT3</i> loading. . . . .	162
4.81	Shape of the single cell for tensile dominated loadings . . . . .	163
4.82	Response of the 3D single cell for shear loadings . . . . .	166
4.83	Single cell simulation results for the <i>PT</i> loading. . . . .	168
4.84	Single cell simulation results for the <i>TT1</i> loading. . . . .	169
4.85	Single cell simulation results for the <i>TT2</i> loading. . . . .	170
4.86	Shape of the single cell for shear dominated loadings . . . . .	171
4.87	Evolution of the void axis elongation factors $f_M$ , $f_{m1}$ in single cell simulations for the <i>PT</i> loading, for a model containing a void and a lead inclusion. . . . .	174
4.88	$W_1$ and $W_2$ single cell simulation results for the <i>PT</i> loading, for a model containing a void and lead inclusion . . . . .	175
4.89	<i>VVF</i> single cell simulation results for the <i>PT</i> loading, for a model containing a void and lead inclusion . . . . .	175
5.1	Microstructure of <i>A1</i> alloy after <i>PT</i> deformation . . . . .	183
5.2	Rate of torque increase vs sample rotation angle in the <i>PT</i> sample	184
5.3	. . . . .	185
5.4	Fracture surfaces of the <i>A1</i> and <i>A2</i> in <i>PT</i> samples. . . . .	187



---

A.1	CuZn39Pb3 $\alpha$ - $\beta$ double phase microstructure . . . . .	213
A.2	62A, E63, C97 and B98 tensile test results. . . . .	214
A.3	B98 fracture surface (SE). . . . .	215
B.1	Geometry of tested samples . . . . .	217
C.1	Distribution of orientation of major axes in tensile and notch tensile samples. . . . .	219
C.2	Distribution of orientation of major axes in torsional and tensile torsional samples - AT plane. . . . .	220
C.3	Distribution of orientation of major axes in torsional and tensile torsional samples - AR plane. . . . .	220
D.1	Single cell simulation results for the <i>PT</i> loading using kinematic boundary conditions. . . . .	223



# List of Tables

3.1	Chemical composition of selected model materials in % by weight	29
3.2	Microhardness test results for alloys <i>A1</i> and <i>A2</i> . . . . .	31
3.3	Thermal properties of <i>A1</i> matrix (=A2) and technical lead. . .	32
3.4	Axial loads in T experiments. . . . .	44
3.5	Displacement/rotational rates. . . . .	45
3.6	Ludwik-type power law fit parameters for alloys <i>A1</i> and <i>A2</i> . . .	67
3.7	Lead plastic behavior. . . . .	68
4.1	Average values of the axis elongation factors $f_M$ , $f_{m1}$ and $f_{m2}$ , the void growth factor $f_V$ , and the resulting VVF in the repre- sentative data range . . . . .	144
4.2	Equivalent plastic strain $\varepsilon_{eq}^{pl}$ and average stress triaxiality $T_{avg}$ at the onset of coalescence in tested samples for different loading conditions. . . . .	155
4.3	Summary of the results of single cell simulations for tensile dom- inated loadings . . . . .	163
4.4	Change in size of the 3D macroscopic sample in tangential ( $\Delta T$ ) and radial ( $\Delta R$ ) directions, calculated in the 1-3 (R-T) planes, under various loading conditions [%]. . . . .	164
4.5	Summary of results of single cell simulations for shear domi- nated loadings . . . . .	172
A.1	Chemical composition of abandoned materials in % by weight.	212



# Chapter 1

## Introduction

### 1.1 General background and motivation

Many industrial materials are metallic ductile alloys that exhibit extensive plastic deformation before fracture. Ductile fracture is the preferred fracture mode in structural materials because high fracture strains allow dissipation of significant energy. Fracture of a vast number of ductile metallic materials is controlled by the void nucleation, growth and coalescence (VNGC) process.

The VNGC process has been extensively investigated and modeled since the late sixties. In micromechanical models, evolution of damage in a representative volume element (RVE) is described in terms of continuum mechanics. The VNGC models allow failure of materials under general geometrical and loading situations to be considered, and they have the potential of predicting effects such as: the degradation of the load carrying capacity induced by the presence of porosity, material anisotropy due to non uniform elongation of voids in different directions, onset of fracture and crack propagation and scale effects.

The evolution of damage in materials was rapidly found to be strongly dependent on stress triaxiality, and high stress triaxiality loading conditions were identified to be the most severe. For this reason, in most investigations, authors concentrated mainly on high triaxiality loading conditions assuming spherical or axisymmetric ellipsoid voids. Such models predict either void collapse or no porosity change under low stress triaxiality. However, low stress triaxiality loadings play a significant role in several important problems for industry such as machining and shear dominated forming operations, which have received little attention in terms of modeling of the VNGC processes. In low or zero stress triaxiality, effects such as the change of void orientation and shape during deformation, play a significant role. It is only recently that these effects under shear dominated loadings started to generate more interest.

Although knowledge in the field of fracture mechanics has been growing

rapidly, and experimental programs have led to an increased understanding of the basic fracture processes, there is still a significant amount of work to be done in order to use VNGC models to predict ductile fracture behavior of technologically useful materials subjected to complex load paths in complex structures.

## 1.2 General topic of dissertation

The goal of the present research is to gain additional understanding of the physical mechanisms accompanying ductile fracture development in industrial ductile alloys of high technological importance for engineering structures.

The scientific objective is aimed at elucidating and modeling the micro-fracture mechanisms and mechanical aspects controlling ductile fracture evolution for various loading conditions in materials experiencing very large strains before fracture and which contain pre-existing voids, particularly under low stress triaxiality conditions.

The research concentrates on generating well characterized and reliable experimental data for void growth and coalescence. We aim to increase the knowledge in ductile fracture by performing and analyzing results of fracture tests for different geometries of samples and under various loading conditions to obtain a desired range of stress triaxiality. In our experiments, we use copper alloys, which are industrially important materials. In these alloys, small additions of lead, on the order of 1 wt. % are frequently used to improve the machinability. From the point of view of our research, the presence of lead inclusions, which act as pre-existing voids and adapt their shape to the surrounding matrix, gives us the opportunity to track their shape evolution even under low and zero stress triaxiality loading conditions.

The experimental and numerical results obtained elucidate the role of other microstructural effects such as texture development (including twinning), on the fracture process in materials undergoing high strains and particularly on the void growth and void coalescence at the high strains reached under low stress triaxiality conditions.

## 1.3 Outline of dissertation

The thesis is composed of five chapters and several appendices and is organized as follows:

**Chapter 2** provides a review of the literature, which describes and analyzes the most frequently used constitutive damage models for ductile frac-

ture and the materials used in fracture experiments. In terms of modeling, we review the literature treating the effect of void shape, the influence of a hard inclusion embedded in the void, void rotation and the anisotropy of the surrounding matrix material, including crystal plasticity. At the end of the chapter we list existing gaps in the knowledge in order to formulate our research proposal.

**Chapter 3** describes the research approach followed in the investigation. The approach combines experimental observations of appropriately selected materials and numerical simulations. We describe the two selected materials, validate the assumption underlying the selection and provide details of the experimental and numerical techniques developed to characterize and quantify fracture processes.

**Chapter 4** presents the results of the fracture experiments, microscopic observations of the micro-structure of tested samples and various numerical simulations performed to explain the observed phenomena. The results shed light on the mechanisms and kinetics of void growth and coalescence in a ductile matrix subjected to arbitrary loading and deformation by providing an experimental database of void shapes and volumes at the onset of coalescence.

**Chapter 5** analyzes and discusses the experimental and numerical results presented previously in Chapter 4, and compare them with data published in the literature. It concentrates particularly on the influence of the texture evolution and twinning on void growth under shear loading conditions.

**Chapter 6** summarizes the key findings of the research and explains how they contribute to a better understanding of void nucleation growth and coalescence fracture processes, particularly under shear dominated loading conditions. In this chapter we also propose possible ways to continue the project and future directions for the research.

The appendices contain some complementary information; **Appendix A** provides a brief description of other materials examined during the research to select an appropriate test material and reasons for which they were abandoned. **Appendix B** contains details of sample design. **Appendix C** presents distributions of orientations of inclusions in tested samples pertaining to information already presented in the text in a different form. **Appendix D** presents results of the single cell simulation under pure torsional loading with kinematic boundary conditions.





## Chapter 2

# State of the art

### 2.1 General outline of the state of the art

This literature review describes and analyzes the most frequently used constitutive damage models of ductile fracture. In the description presented in Section 2.2, we follow the three sequential stages of ductile fracture, that is nucleation, growth and coalescence of voids. Later in this study, we concentrate on void growth and coalescence and therefore in this chapter we provide only a brief description of void nucleation, since it is outside the scope of our research. As far as void growth is concerned, we review the effect of the void shape, the influence of a hard inclusion embedded in the void, void rotation, the effect of anisotropy of the surrounding matrix material and crystal plasticity models to represent such anisotropy. We also discuss the competition and cooperation mechanisms, the sequential nature of the VNGC process, the effect of the loading conditions and present an example of a complete VNGC model. In the description of void coalescence we include both one and two void population models.

In polycrystalline metals, the major cause of the anisotropic plastic response is the crystallographic texture resulting from reorientation of the crystal lattices of grains during deformation. In Section 2.3, we present the history of the development of crystal plasticity models not related directly to VNGC. In the review, we concentrate on the use of crystal plasticity models to simulate behavior of copper alloys.

As our approach is both experimental and numerical, it is crucial to select an appropriate model material allowing for easy observation and quantification of the desired fracture effects. Before making our choice in the next chapter, in this Section 2.4, we also review model materials used in the literature.

In Section 2.5 we elucidate existing gaps in our knowledge in order to formulate our research postulate in Section 2.6.

## 2.2 Void nucleation, growth and coalescence

Fracture, as generally defined in mechanical or structural engineering, happens when a material or a part of it is subjected to loads or deformations and loses its load carrying capacity breaking into two or several pieces. Ductile materials frequently used in engineering can undergo extensive plastic deformation before fracture takes place. The strains at which fracture occurs depend strongly on the purity of the material and very pure materials, e.g. pure Cu, can exhibit a perfect necking under tensile loading, that is a reduction of the cross-section down to a sharp point. In commercially pure alloys however, the fracture is usually initiated at local heterogeneities such as inclusions or second phase particles where small cavities or voids are formed. The process of nucleation of voids followed by their stable expansion leading to unstable joining of adjacent voids, is known as void nucleation, growth and coalescence (VNGC). A modeling methodology, the local approach to fracture (LAF), has been developed to simulate the VNGC processes in order to calculate the macroscopic fracture properties of materials. Comprehensive descriptions of local approaches to static and dynamic fracture mechanics can be found for instance in Garrison and Moody (1987), Anderson (1991), Antoun et al (2003), Besson (2004), Pineau and Pardoen (2007) and Benzerga and Leblond (2010). In Sections 2.2.1, 2.2.2 and 2.2.3 we describe briefly the sequential stages of the VNGC type of fracture.

### 2.2.1 Void nucleation

Void nucleation is the formation of small cavities in the initially dense bulk material. This event occurs usually at local heterogeneities of the microstructure, such as impurities, non-metallic inclusions or second phase particles by their cleavage or separation i.e. decohesion.

In the case of the fracture of inclusions, a cavity forms if the maximum stress in a particle reaches the particles' strength. In the case of void nucleation by particle-matrix interface de-bonding, two physical conditions, a critical stress criterion and an energy criterion, have been proposed (Tanaka and Mori, 1970). The energy criterion says that the elastic strain energy released by de-bonding of the particle must be on the order of the newly created surface energy. In their study, Tanaka and Mori (1970) have shown that this criterion principally applies to relatively small particles because it is always satisfied when inclusions are above a certain size limit. Tanaka and Mori (1970) have indicated the size limit to be 25 nm, while Argon et al (1975) have proposed 10 nm. For inclusions above this size limit, the separation is controlled by the stress criterion which states that the cavities are nucleated as soon as the local normal stress at the particle-matrix interface equals or exceeds the particle interfacial strength (Argon et al, 1975). Curran et al (1987) provide a description of early attempts to construct micro-statistical

void nucleation models.

Some materials are nucleation-controlled, meaning that the nucleation phase may already lead to unstable fracture. A VAR steel studied by Cannizzaro (2006) is an example of such a material. It will be presented in more detail in Section 2.2.4. Occasionally, cavities can also exist within the material before deformation and in such cases, the nucleation phase of fracture is absent and the material fractures due to void growth and coalescence only.

### 2.2.2 Void growth

The void growth stage of ductile fracture is a stable total void volume increase in a material being plastically deformed, without reduction in the number of voids, sometimes also associated to change in void shape.

The fracture process of many ductile metallic materials is controlled by void growth and therefore this mechanism has been extensively investigated and modeled since the late sixties. Researchers have identified many parameters which strongly influence void growth, including; the geometry of the loaded structure and resulting stress-strain conditions, the size and type of the nucleating inclusion, the initial void shape, the relative distribution of voids, the properties of the matrix material, the environmental or aging effects, the rate of loading or deformation, and possibly others.

Various models have been developed in the scope of the local approach to fracture to account for these effects. Below we present a brief description of the development and features of the best known void growth models.

#### Uncoupled models

Uncoupled void growth models were derived from analysis of the expansion of isolated cavities in an infinite matrix i.e. a remote uniform field. The first models were developed by McClintock (1968) and Rice and Tracey (1969) who examined a cylindrical and spherical void, respectively. Voids, which kept their shape all the time, were under a triaxial stress system whose principal components did not rotate with respect to the material. In the McClintock (1968) analysis it was also assumed that the axial deformation of the cavity was one of generalized plane strain. The Rice and Tracey (RT) formula describing the growth rate of a spheroidal void was used for example by Huang (1991) in the following form:

$$\ln \frac{R}{R_0} = 0.427 \int_0^{\varepsilon_{eq}} \exp \left( \frac{3}{2} \frac{\sigma_m}{\sigma_0} \right) d\varepsilon_{eq} \quad (2.1)$$

where  $R$  is the current void radius,  $R_0$  the initial void or inclusion radius,  $\varepsilon_{eq}$  the equivalent macroscopic plastic strain,  $\sigma_m$  the hydrostatic mean stress, and  $\sigma_0$  the current flow stress of the matrix material. The presented model and expression is valid only for rather high stress triaxiality values,  $\frac{\sigma_m}{\sigma_0} > 1$ .

The McClintock (1968) and Rice and Tracey (1969) models predict higher void growth rate and therefore lower fracture strains at high stress triaxiality. This observation corresponds well to the experimental results, which document higher porosity and resulting macroscopic crack initiation in the middle of the neck than at the outside of tensile samples, thus in the regions of the highest stress triaxiality. These observations were made in smooth round tensile samples (Puttick, 1959; Garrison and Moody, 1987; Tvergaard and Needleman, 1984), or in notched round tensile samples (Hancock and Mackenzie, 1976). In pre-cracked compact tension specimens, just ahead of the crack-tip where the stress triaxiality is the highest it causes the crack to propagate by growth of voids and link up with the blunting crack (McMeeking, 1977).

The RT model models plastic yield according to the von Mises theory. As a result, the model does not provide a condition for the ultimate failure, and consequently a separate failure criterion had to be introduced. Nevertheless, it gives a fairly simple and realistic description of the ductile fracture process in a number of applications (Marini et al, 1985), and forms the basis for other uncoupled ductile fracture criteria (for example: Mudry, 1985; Hancock and Mackenzie, 1976). Budiansky et al (1982) extended the RT model for viscoplastic materials.

## Coupled models

Coupled models include dilatational constitutive functions and more adequately simulate the full ductile fracture process. The dilatational constitutive laws incorporate the void volume fraction, the evolution of which depends on the hydrostatic stress and consequently take into account the softening effects, i.e. degradation of the load carrying capacity induced by the presence of porosity.

Some of the earliest coupled models were developed by Berg (1970) and Gurson (1977), who analyzed growth of a spherical cavity in a perfectly plastic spherical body. Berg (1970) obtained an elliptical yield criterion, linking the damage and stress triaxiality linearly, while Gurson (1977) derived a non-elliptical model which sets a non-linear relationship between the two parameters. Therefore, the Gurson model better matches the analytical and numerical evidence (Hancock and Mackenzie, 1976) of the exponential damage-stress triaxiality relationship expressed in the RT model. Gurson has established the following yield function for porous materials which depends on the void

volume fraction  $f$ :

$$\Phi(\sigma_h, f, \sigma_y) \equiv \frac{\sigma_e^2}{\sigma_y^2} + 2q_1 f \cosh\left(\frac{3}{2} \frac{q_2 \sigma_h}{\sigma_y}\right) - 1 - (q_1 f)^2 \quad (2.2)$$

where  $\sigma_e$  is the von Mises equivalent stress, and the  $q_1$  and  $q_2$  parameters introduced by Tvergaard (1981) were equal to 1 in Gurson's original work. This constitutive relationship reduces to the von Mises condition if  $f = 0$ . The model, initially developed for a perfectly plastic material, was extended to strain hardening materials by regarding  $\sigma_y$  as a measure of the effective flow stress, and by defining a law for the evolution of the mean yield stress of the matrix material. The model in question, even if the plastically-deforming matrix material continues to harden, may predict softening of the global material response due to porosity increase.

The strongly detrimental effect of the initial porosity (or volume fraction of inclusions and second-phase particles) on the strains to fracture was known from experiments (Edelson and Baldwin, 1977; Bourcier et al, 1986), so the critical void volume fraction became naturally a simple fracture criterion. Many fracture tests aimed at correlating void growth rates and critical porosities with plastic strain and stress triaxiality, usually under tensile loadings (Marini et al, 1985; Mudry, 1985; Garrison and Moody, 1987; Curran et al, 1987; Benzerga, 2000).

The non-coupled and coupled models discussed above assume no void shape change and therefore their applicability is limited to relatively high stress triaxialities where voids expand self-similarly, maintaining their initial shape. On the other hand, the shape changes need to be taken into account under low or zero stress triaxiality where voids are subjected to compression in one or several directions and may tend to close. In the following section we describe attempts to take into account void shape changes.

### **Void shape**

The influence of the void shape on void growth was extensively studied (Sovik and Thaulow, 1997; Pardo and Hutchinson, 2000; Benzerga, 2000; Lassance et al, 2007; Scheyvaerts, 2008) and was found to have an important impact on the growth of porosity. Oblate voids were found to grow faster than prolate voids, and under low triaxiality the void shape was found to change significantly as shown by Budiansky et al (1982); Becker et al (1989a); Sovik and Thaulow (1997); Gologanu et al (1997); Lee and Mear (1992, 1999). As an example, Mir et al (2005) demonstrated the influence of the stress triaxiality on void shape in smooth round tensile samples. As the distance from the center of the sample increases, the mean void aspect ratio increases, meaning that voids are more elongated away from the center of the sample where the stress triaxiality is lower.

Tvergaard (1981, 1982) introduced the  $q_1$  and  $q_2$  constants in the Gurson yield function, presented in Equation 2.2 with the aim of compensating for the neglected void shape changes. The predictions of this modified model, called the Gurson-Tvergaard-Needleman (GTN) model, were found to be in better agreement with the results of a numerical analysis of a periodic array of voids. The GTN model was later adjusted (Faleskog and Shih, 1997; Koplik and Needleman, 1988; Perrin and Leblond, 1990) by providing supplementary values of the  $q$  parameters for other ranges of material flow properties. Also, other models similar to the Gurson or GTN, were proposed e.g. by Rousselier (1986) or Curran et al (1987), but none of these models provide an explicit description of the void shape change.

Void shape has been introduced explicitly by Gologanu et al (1993, 1994, 1997). The Gologanu-Leblond-Devaux model (GLD) is based on the solution for the expansion of an initially spheroidal prolate or oblate void, embedded in a confocal, spheroid, elasto-plastic material subjected to axisymmetric loading conditions. This formulation of the problem leads to the axisymmetric shape of the void and transversely isotropic symmetry of the void-matrix system. The form of the GLD model, which is a revised Gurson model, maintains the original Gurson structure and introduces an additional parameter describing the void shape and an evolution law for this parameter. The GLD model, with a heuristic extension to account for strain hardening, was validated by Pardoen and Hutchinson (2000, 2003a); Benzerga (2000); Benzerga et al (2004a,b); Klocker and Tvergaard (2003); Flandi and Leblond (2005a,b); Pardoen (2006); Lassance et al (2007); Monchiet et al (2008). Scheyvaerts (2008) developed a model for plane strain conditions in which voids were still assumed to stay axisymmetric, but a correction was introduced to account for the different evolution of the shape in directions perpendicular to the principal axis of the void, defined as the direction 1. The void radii  $R_2$  and  $R_3$  were used to detect the onset of localization as accurately as possible, but this correction does not enter the void growth model. During plastic deformation, the behavior of the material surrounding the void is isotropic-linear-elastic and  $J_2$  elastoplastic.

Another group of models for dilute and nondilute porosity were developed using homogenization techniques. They are capable of handling general ellipsoidal microstructures and therefore have the potential to perform better under general three-dimensional loading conditions, including nonaligned loadings. For example Talbot and Willis (1985), building on the work of Willis (1977, 1978), used a "linear homogeneous comparison" material to provide a generalization of the Hashin-Shtrikman bounds (Hashin and Shtrikman, 1963) in the framework of nonlinear composites. A more general nonlinear homogenization method has been introduced by Ponte-Castaneda (1991, 1992) who used it to obtain "variational bounds" and estimates of the effective mechanical properties of nonlinear composites. Michel and Suquet (1992) and Suquet (1993) derived an equivalent bound for two-phase power law media using Hölder-type inequalities.

The Ponte-Castaneda and Zaidman (1994) model (PC) of void growth was developed in the scope of the nonlinear homogenization technique, to account for the evolution of the material microstructure under large quasi-static deformations. The model uses the void volume fraction and the void aspect ratios of a typical void as the state variables characterizing the evolution of the size and shape of the pores. The model is appropriate for low stress triaxiality conditions, and predicts well the onset of the localization of strain in the intervoid ligament, although for high triaxiality loading conditions, the GTN model gives better results. Kailasam and Ponte-Castaneda (1998) proposed a general constitutive theory for the effective behavior and microstructure evolution in heterogeneous materials consisting of randomly oriented and distributed ellipsoidal inclusions, that undergo general, three-dimensional finite strain loading conditions. The special case of porous metals was further considered by Kailasam et al (1997); Kailasam and Ponte-Castaneda (1998); Kailasam et al (2000); Aravas and Ponte-Castaneda (2004); Danas and Ponte-Castaneda (2009a,b). For instance, Aravas and Ponte-Castaneda (2004) presented a constitutive model for porous metals subjected to general three-dimensional finite deformations. The model takes into account the evolution of porosity and models anisotropy induced by changes in the shape and orientation of voids during deformation. The authors introduced two aspect ratios of the local representative ellipsoid. Nevertheless, the anisotropy of the material results from the changing microstructure (shape of voids) and not from the developing texture of the matrix material.

### **Influence of a hard inclusion**

Under high stress triaxiality conditions, voids expand in all directions hence the nucleating inclusion has no influence on void growth and its presence can be neglected. In contrast, under low or zero stress triaxiality, cavities tend to close along one axis, and the internal hard inclusion may prevent this closure. The above-mentioned models do not consider the described locking effect of the inclusion and predict either no porosity change (Gurson, GTN) or void collapse (GLD, PC) under zero stress triaxiality. Fleck et al (1989) tackled the problem of the contact of the void with the inner inclusion under shear and confirmed it to be important under shear and axisymmetric straining when the stress triaxiality is low. (See also Pardoen et al (1998) and Bonfoh et al (2004)). Siruguet and Leblond (2004a,b) developed a model to account for the void shape change and the locking effect of hard inclusions present in voids.

### **Void rotation**

The orientation of ellipsoid voids results in different micro-structural properties of the material in different straining directions and therefore causes general plastic anisotropy. Void orientation is particularly important for shear-

dominated loadings, under which voids are known to rotate. Consequently, void rotation plays a significant role in problems such as shear dominated forming operations, mixed mode ductile fracture cracking or void growth on inclined soft grain boundaries. Void rotation affects void growth and coalescence.

Void rotation did not receive much attention at the beginning of research on ductile fracture, but the situation has changed and more results are now available in the literature. Analysis of the growth of initially spherical or elliptical voids in material undergoing simple shear combined with superimposed hydrostatic tensions was investigated by Fleck and Hutchinson (1986). Later void growth under shear was investigated by Pardoen and Hutchinson (2000); Benzerga (2000); Bordreuil et al (2003); Lassance et al (2007); Tvergaard (2008), including the finite element cell calculations for voids growing under shear. Leblond and Mottet (2008) worked on a coalescence model combining shear and tensile localization. Scheyvaerts (2008) developed the model for plane strain conditions. The voids are usually assumed to rotate in a plane and only one variable describes its orientation. General results of the studies indicate that prolate voids follow the material rotation, while oblate voids rotate much faster than the surrounding material and in counter rotation. If the void aspect ratio is smaller, the void rotates faster.

Gologanu et al (1997); Ponte-Castaneda and Zaidman (1994); Kailasam and Ponte-Castaneda (1998) introduced void rotation laws in their models. For instance, Gologanu et al (1997) have proposed how to account for void rotation by imposing that the void follows the rotation of the surrounding material, which is correct for prolate voids but not for oblate voids.

In the case of spherical voids, their orientation is only defined once void elongation starts. The relatively simple void growth models, e.g. GTN, assume an invariably spherical shape of voids and their rotation is neglected. Nahshon and Hutchinson (2008) extended heuristically the Gurson model in order to account for the shear effect by using the third invariant of stress. (See also Xue (2007)). The model was implemented by Nielsen and Tvergaard (2009).

## Anisotropy

For some analyses, materials can be regarded as initially isotropic. In reality however, their microstructure evolves leading to a general anisotropic response, particularly when they are subjected to large deformations. Part of the material anisotropy which is present from the start, may be due to processing and fabrication methods. The other part is induced by the evolution of the microstructure under large plastic deformations. The changes induced in the microstructure include effects such as material texture, grain elongation,



## **2.2. VOID NUCLEATION, GROWTH AND COALESCENCE 13**

deformability of second-phase particles and eventually their shape and spatial distribution (Keralavarma and Benzerga, 2010).

The Gurson model, initially developed for an ideally isotropic material, was extended for void shape effects (Gologanu et al, 1993, 1994, 1997) and for plastic anisotropy of the matrix material (Benzerga and Besson, 2001). The anisotropy due to void shape and the anisotropy of the matrix material were both found to affect void growth at the first order. Void shape effects were also accounted for by means of alternative variational principle using the concept of a linear comparison material (Ponte-Castaneda, 1991; Ponte-Castaneda and Zaidman, 1994; Kailasam and Ponte-Castaneda, 1998).

Benzerga (2002); Benzerga et al (2004a,b) proposed a heuristic model combining void shape and plastic anisotropy effects. More recently Monchiet et al (2008) and Keralavarma and Benzerga (2008) have tackled a Gurson-like homogenization problem to obtain a new yield function that couples plastic anisotropy and void shape effects.

Gan et al (2006) considered the influence of micro-structural conditions such as crystallographic slip within face centered cubic (f.c.c) single crystals, on the simulation results of cylindrical voids under plane strain conditions. The influence of plastic anisotropy on creep damage evolution in f.c.c single crystals was investigated by Qi and Bertram (1999), who noticed major differences in the creep strain and the accumulated damage depending on crystal orientation with respect to the tensile axis. Shu (1998) used an elasto-viscoplastic strain gradient crystal plasticity theory to study void growth under uniaxial and biaxial strain fields under plane strain conditions. Using a double slip orientation model developed by Rashid and Nemat-Nasser (1992), Shu observed a size scale effect for voids smaller than a certain size with respect to the size of the single cell. His observations led him to the conclusion that small voids have the tendency to grow more slowly than big voids, also noted by Horstemeyer and Ramaswamy (2000). A similar result was obtained by Tvergaard and Niordson (2004), who applied a non-local elastic-plastic model to study the growth of voids small enough to be comparable with a characteristic material length. Wen et al (2005) extended the Gurson model to account for void size effects. They found that void size has practically no effect on the stress-strain curve at small initial void volume fractions, and that the void size becomes significant only at large void volume fractions.

Orsini and Zikry (2001) studied the behavior of rate-dependent porous f.c.c crystalline materials subjected to finite inelastic deformations. In this study, single cell models with periodic or random void distribution were used to investigate effects of void distribution and geometry, strain hardening, geometrical softening, localized plastic strains and slip-rates, hydrostatic stresses on failure paths and ligament damage. The results illustrated that the rotation of the crystalline lattice and plastic activity on slip systems are concentrated

mainly in the ligament region between the voids. The hydrostatic stress also increased in this region to approximately twice the yield stress. O'Regan et al (1997) employed a constitutive model with a triple slip model to perform finite element calculations of void growth in hexagonal close packed (h.c.p.) single crystals. They found the relative angles between the slip systems to play a greater role in determining the void growth rate than the orientation of the lattice with respect to the tensile axis. Kysar et al (2005) analyzed the case of cylindrical voids embedded in a single crystal in plane strain conditions and using slip-line theory. They found that the stress and deformation state around the void are heterogeneous and that they are in the form of angular sectors. In each sector only one effective slip system is active. Potirniche et al (2006) studied the effect of crystalline lattice orientations on void growth and coalescence in f.c.c. single crystals under uniaxial and biaxial loadings. The lattice orientations were found to have a significant effect on void growth rates and shapes. In certain orientations, voids grew twice as fast compared to other orientations under uniaxial loading. Under biaxial loading the influence of lattice orientation on the increase in void volume fraction vanishes. Under high triaxiality conditions, plastic anisotropy due to the initial lattice orientation was reported to have only a minor role in influencing the void growth rate, which was controlled mainly by the stress triaxiality, the magnitude of accumulated strain and the spatial localization of the plastic strains.

While the presented crystal plasticity studies (O'Regan et al, 1997; Shu, 1998; Orsini and Zikry, 2001; Gan et al, 2006; Potirniche et al, 2006) were carried out under 2D plane strain loading conditions and thus assuming cylindrical void shape, Schacht et al (2003), Liu et al (2007) and Yerra et al (2010) addressed void growth under 3D loading conditions. Schacht et al (2003) investigated void growth in f.c.c. single crystals using single cells with a pair of micro-voids. Void growth and deformation behavior was found to be strongly dependent on the initial crystallographic orientation. A similar observation was reported by Yerra et al (2010) who dealt with void growth and coalescence in single crystals using a single cell with fully periodic boundary conditions. They stated that plastic anisotropy related to single crystal behavior and damage evolution are strongly coupled. This coupling results in significant differences in strain at the onset of void coalescence, depending on the initial lattice orientation.

Anisotropy of the material affects void growth and also the void coalescence stage of ductile fracture as shown e.g. by Steglich et al (2008), who tried to reproduce anisotropic fracture of 2024-T351 aluminum alloy in notched tensile experiments, using the model developed by Pardoen and Hutchinson (Pardoen and Hutchinson, 2000, 2003a; Pardoen, 2006).

Crystal plasticity will be discussed independently of void growth in Section 2.3.

### 2.2.3 Void coalescence

Void coalescence is a direct result of the stable void growth process and can be regarded as unstable void growth. At the end of the coalescence process, two or more voids join into one larger void or form a crack.

In a material undergoing plastic deformation, voids increase their volume, which leads to a decrease in the size of the inter-void ligaments. When the ligament size becomes too small, neighboring voids start to interact; the plastic deformation localizes in the inter-void ligament, whereas outside of the ligament, material unloads elastically (Pardoen and Hutchinson, 2000). Void interaction may accelerate void growth within clusters of closely spaced voids and make the process unstable. The coalescence process leads to formation of macroscopic cracks and can result in an abrupt slope change of the load-displacement curve (Tvergaard and Needleman, 1984; Benzerga, 2000).

Factors influencing the coalescence of voids, include their shape and relative spacing, the stress state and eventually the presence of a second population of inclusions nucleating a second population of voids in the inter-void ligament. In the temperature transition region of steels coalescence can occur by cleavage of the ligament between voids. Also, the void-particle interaction was shown to have a significant influence on coalescence, particularly at low triaxialities (Kuna and Sun, 1996; Hutchinson and Tvergaard, 1987; Staub and Boyer, 1998; Fleck et al, 1989; Siruguet and Leblond, 2004a,b). Below we describe coalescence models which take into account some of the listed effects and group them into two categories: models for one or two populations of voids.

#### One population of voids

Neither the RT nor the Gurson model accounts for void interactions and thus they must be supplemented with a void coalescence criterion, which usually assumes that coalescence occurs when a critical void volume fraction is achieved. In the GTN model, Tvergaard and Needleman (1984) introduced a critical void density parameter  $f_c$  to account for the void coalescence effects, and since then researchers tried to determine the  $f_c$  value as a material constant.

Later, it was demonstrated that a constant critical void volume fraction is not an appropriate coalescence criterion because it can be affected by the void shape, the void distribution or the level of the stress triaxiality and void rotation (Koplik and Needleman, 1988; Thomason, 1985a; Sovik and Thaulow, 1997; Pardoen and Hutchinson, 2000). Tvergaard (1981); Tvergaard and Needleman (1984) extended the original Gurson model to include the effect of neighboring voids by introducing the parameters  $q_1$ ,  $q_2$  and  $q_3$ . ( $q_3$  is equal to  $q_2^2$  in Equation 2.2). However, Koplik and Needleman (1988) demonstrated

that the introduction of  $q$  factors into the Gurson model is not sufficient to describe the accelerated void growth during coalescence and proposed the use of an effective porosity  $f^*$  to represent this phenomenon.

Thomason (1985a,b) developed a coalescence criterion which, in addition to porosity, takes into account the shape of the ellipsoid void, the distance between voids, stress concentration due to void shape and stress triaxiality. The model derivation for an isotropic, perfectly plastic material is based on the assumption that coalescence occurs when the inter-void ligament reaches its limit load. The microstructural parameters in the Thomason model (void relative distance  $X$ , porosity  $f$ , the void aspect ratio  $W$  and the aspect ratio of the cell) can be evaluated using a coupled criterion such as Gurson's or GLD (Gologanu et al, 2001a,b).

In recent years, new attempts have been made to improve the Thomason coalescence criterion and bring its predictions closer to the behavior of real materials. Zhang et al (2000) used the Thomason approach to account for void coalescence effects while Benzerga et al (1999) and Gologanu et al (2001a,b) introduced a two layer approach. Pardoën and Hutchinson (2000, 2003a) proposed a model for the final unloading process. The model, based on the GTN and Thomason models, accounts for void shape and distribution influences on void coalescence. Benzerga (2002); Benzerga et al (2004b) combined localization-based and limit-load based coalescence models with the GLD model. They used the resulting model to predict the fracture anisotropy of rolled plates. Yerra et al (2010) combined two different versions of the Thomason coalescence criterion with a crystal plasticity description of the material.

The improvements made to the Thomason conditions for the onset of void coalescence have already been validated in single cell simulations or using experimental data (Pardoën et al, 1998; Benzerga, 2000; Besson and Guillemer-Neel, 2003; Benzerga et al, 2004a,b; Ragab, 2004; Huber et al, 2005; Pardoën and Hutchinson, 2003a; Pardoën et al, 2004; Pardoën, 2006; Lassance et al, 2007; Weck et al, 2008)). On the other hand, the prediction of softening of the material during coalescence by these models still requires additional evaluation.

## Two populations of voids

In materials containing two populations of nucleating inclusions, the localization of plastic deformation in the inter-void ligament and its failure can be controlled by the complete VNGC process of a second population of voids (Cox and Low, 1973; Thompson and Weirauch, 1976).

## **2.2. VOID NUCLEATION, GROWTH AND COALESCENCE 17**

Faleskog and Shih (1997) studied void growth and coalescence of a material containing two populations of voids under high stress triaxiality. In their study, the growth of large voids caused the increase in strains and stress around small micro-voids that activated an unstable deformation mode, causing their accelerated growth and coalescence. For high-strength metals, this evolution of the microstructure can result in a brittle-like (low additional plastic strain) ductile fracture mode.

The effect of a second population of voids was also studied by e.g. Zhang et al (2000); Perrin and Leblond (2000); Enakoutsa et al (2005); Leblond and Mottet (2008); Fabrègue and Pardoën (2008). Zhang et al (2000) merged the modified Gurson model with a Thomason coalescence criterion (Thomason, 1985a) to obtain a complete failure model. Leblond and Mottet (2008) worked on a coalescence model combining shear and tensile localization. Fabrègue and Pardoën (2008) developed a constitutive model for elastoplastic solids containing two populations of voids. They found that the development of the secondary population of voids accelerated the void coalescence process, but has little influence on the preceding growth of the first population of large voids. The drop in ductility caused by the presence of secondary voids was found to be larger if one or more of the following happened: the nucleation strain decreased, the volume fraction increased or the primary voids were flat.

### **2.2.4 Sequential nature of the VNGC process**

In general, fracture development in ductile alloys is assumed to proceed sequentially through the subsequent stages of void nucleation, growth and coalescence. However, in the complex microstructure of real alloys, two or more competing mechanisms may exist in parallel. The resulting superposition of interacting mechanisms is sometimes called the "competition and cooperation" mechanism (Scheyvaerts et al, 2010), and it may affect the sequential nature of the VNGC process.

For example, in materials in which the nucleating particles are firmly bound to the matrix, the nucleation phase may already lead to fracture as pointed out by Thomason (1990, 1998). A VAR steel studied by Cannizzaro (2006) is an example of such a material, in which the tempered carbides debond from the matrix at very high interfacial stress. The high stress in the matrix material and the loss of the consolidation effect of the carbide are the reasons for which at the onset of void nucleation the void coalescence condition is already met. As a result, very little additional plastic deformation is needed to fully coalesce voids.

The competition and cooperation nature of the VNGC process may also be obvious, for example, in alloys containing two populations of voids. In this case, nucleation of the second population of microvoids may compete with the

growth and coalescence of the primary, large voids Zhang et al (2000); Perin and Leblond (2000); Enakoutsa et al (2005); Leblond and Mottet (2008); Fabrègue and Pardoën (2008). Due to void distribution effects, stable void growth may be interrupted earlier in the deformation history by unstable void coalescence (Devillers-Guerville et al, 1997; Besson et al, 2000).

### 2.2.5 Effect of loading conditions

A very interesting phenomenon was observed by Bao and Wierzbicki (2004) and later investigated in more detail in their further papers (Bao and Wierzbicki, 2005; Wierzbicki et al, 2005). They performed a series of fracture tests in order to determine the critical equivalent strain at the onset of fracture (ductility). Two types of fracture test were performed for the same 2024-T351 aluminum alloy. The tests were shear (upsetting) and tensile (notched tensile) dominated, and were in the range of low ( $-1/3$ ) to high (0.9) stress triaxiality. Bao and Wierzbicki (2004) observed that during the transition from tensile to shear dominated loadings there is a sharp change in the slope of the ductility plot, followed by a significant reduction in ductility under shear-dominated loadings. As a result, it is impossible to use hypothetical fracture loci obtained from existing fracture models using critical equivalent fracture strain as the only failure criterion because they may lead to significant errors. Neither is it permissible to extrapolate results obtained from tensile specimens to the ranges of low or negative stress triaxialities. They distinguished two fracture modes: VNGC - for high triaxiality (above 0.4 for Al), and "shear fracture" for zero and negative triaxiality. In a later paper (Wierzbicki et al, 2005) they investigated the Lode parameter related to the third invariant of the stress tensor to model this phenomenon.

A similar investigation was performed by Barsoum and Faleskog (2007a,b) in a mid-strength and high-strength steel using double notched tube specimens loaded in combined tension and torsion. They confirmed the previous observations of two distinctively different ductile rupture mechanisms depending on the stress state observed by Bao and Wierzbicki (2004), and named them "internal necking" and "internal shearing" for high and low stress triaxiality regimes respectively. In terms of modeling, they developed a model based on the Rice theoretical framework which characterizes the stress state in terms of the stress triaxiality and the Lode parameter. The model uses a different failure criterion depending on the failure mode detected, and is capable of capturing the transition between two fracture mechanisms.

### 2.2.6 Example of a complete VNGC model

Here we describe an extended Gurson model presented by Pardoën (2006) as an example of an integrated VNGC model. The model incorporates contributions of the GLD and Thomason models described previously in the text. It

## 2.2. VOID NUCLEATION, GROWTH AND COALESCENCE 19

assumes the presence of one population of pre-existing spheroidal voids which can change their shape and orientation upon loading. The shape of voids along with the porosity, affects the onset of coalescence.

The model considers competition between two possible modes of plasticity, that is, between solutions to two plasticity problems. One solution refers to diffuse plasticity and is called "void growth" and the second refers to localized plasticity in the inter-void ligament and is called "void coalescence". The two solutions take the form of two plastic yield surfaces defined by the equations 2.3 - 2.4:

$$\Phi_{growth} \equiv \frac{C}{\sigma_y^2} \|\sigma' + \eta \sigma_h^g \mathbf{X}\| + 2q(g+1)(g+f) \cosh\left(\kappa \frac{\sigma_h^g}{\sigma_y}\right) - (g+1)^2 - q^2(g+f)^2 = 0 \quad (2.3)$$

$$\Phi_{coalescence} \equiv \frac{\|\sigma'\|}{\sigma_y} + \frac{3}{2} \frac{|\sigma_h|}{\sigma_y} - F(W, \chi) = 0 \quad (2.4)$$

$$\text{with } F(W, \chi) = \frac{3}{2}(1 - \chi^2) \left[ \alpha \left( \frac{1 - \chi}{\chi W} \right)^2 + \beta \sqrt{\frac{1}{\chi}} \right] \quad (2.5)$$

where  $f$ ,  $W$ ,  $\chi$  and  $\sigma_y$  are internal variables: porosity  $f$ , void aspect ratio  $W$  (or  $S \equiv \ln W$ ), relative void spacing  $\chi$ , and mean yield stress of the matrix material  $\sigma_y$ ; the symbol  $\|\cdot\|$  represents the von Mises norm;  $\sigma$  is the Cauchy stress tensor;  $\sigma'$  is its deviatoric part,  $\sigma_h^g$  is a generalized hydrostatic stress;  $\mathbf{X}$  is a tensor associated with the void axis; and  $C$ ,  $\eta$ ,  $g$ ,  $\kappa$  are parameters.

The two equations of the plastic yield surfaces need to be supplemented by the evolution laws for the internal variables:

*Evolution law for  $f$*

$$\text{Growth and coalescence: } \dot{f} = (1 - f) \dot{\varepsilon}_{kk}^p \quad (2.6)$$

*Evolution law for  $W$  (or  $S = \ln W$ )*

$$\text{Growth: } \dot{S} = \frac{3}{2}(1 + h_1) \left( \dot{\varepsilon}^p - \frac{\dot{\varepsilon}_{kk}^p}{3} \delta \right) : \mathbf{P} + h_2 \dot{\varepsilon}_{kk}^p \quad (2.7)$$

$$\text{Coalescence: } \dot{W} = \frac{W(2\chi^2 - 1)}{2f} \left[ \frac{3}{2} \dot{\varepsilon}^p : \mathbf{P} - \frac{1}{2} \dot{\varepsilon}_{kk}^p \right] \quad (2.8)$$

*Evolution laws for  $\sigma_y$*

$$\text{Growth: } \sigma_y \dot{\varepsilon}_y^p (1 - f) = \sigma : \dot{\varepsilon}^p \quad (2.9)$$

$$\text{Coalescence: } \dot{\sigma}_y = \frac{\partial \sigma_y}{\partial \varepsilon_y^p} \frac{\chi^2}{f} \dot{\varepsilon}_e^p \quad (2.10)$$

*Evolution for  $\chi$*

$$\text{Coalescence: } \dot{\chi} = \frac{\chi(3 - 2\chi^2)}{6f} \left[ \frac{3}{2} \dot{\varepsilon}^p : \mathbf{P} - \frac{1}{2} \dot{\varepsilon}_{kk}^p \right] \quad (2.11)$$

where  $h_1$  and  $h_2$  are parameters,  $\mathbf{P}$  is a projector tensor and  $\delta$  is the Kronecker tensor. Further definitions of the symbols and other details of the model are presented by Pardoen and Hutchinson (2000, 2003a); Pardoen (2006). Parameters  $C$ ,  $\eta$ ,  $g$ ,  $\kappa$ ,  $h_1$ ,  $h_2$  and  $\alpha$  in Equations 2.3-2.11 can be expressed in terms of the state variables,  $W$  and  $f$  as presented by Gologanu et al (1993, 1994).

Properties of the matrix material obey the  $J_2$  constitutive law. Under normal deformation conditions,  $\Phi_{growth}$  will increase due to strain hardening and then decrease due to damage softening. The damage softening resulting from void growth and reduction of the inter-void ligament  $\chi$ , will also cause contraction of  $\Phi_{coalescence}$ . At a certain deformation, the two yield surfaces intersect and a transition to coalescence occurs. Subsequent deformation will cause  $\Phi_{coalescence}$  to contract towards the zero stress state. The parameter  $\chi$  is calculated during the void growth phase only to detect the condition of coalescence and it does not influence the void growth response.

The shape of the voids is defined by one state variable  $W$  and therefore voids are assumed to stay axisymmetric under all loading conditions. Following the proposition of Gologanu et al (1997), in the presented model, voids are assumed to rotate with the material.

The model can be enhanced by introduction of nucleation models (Lasance et al, 2006; Huber et al, 2005; Besson, 2004), new rotation law based on results of single cell simulations (Scheyvaerts, 2008), or by introducing anisotropy following the framework proposed by Benzerga et al (2004b).

## 2.3 Crystal plasticity

In polycrystalline metals and alloys undergoing plastic deformation the crystal lattices of grains re-orientate and form a texture. The resulting texture is an important cause of anisotropy of the plastic response and other physical properties (Truszkowski, 2001). Models of polycrystalline plasticity provide better predictions of the mechanical properties of the sample compared to other constitutive laws (Kalidindi et al, 1992; Delannay et al, 2005). Sachs (1928) and Taylor (1938) initiated the development of poly-crystal plasticity



models. The Sachs model, which is known as the lower bound model, assumes that each grain deforms independently of the neighboring grains. Each grain is under a uniform stress field, equal to the macroscopic stress. The Taylor model, known as the upper bound model, assumes that each grain undergoes the same shape changes i.e. strains. The strain of each grain is equal to the strain of the macroscopic specimen. These models neglect possible heterogeneities that may occur during deformation of polycrystalline structures and grain interactions.

The main mechanisms of plastic deformation at room temperature, among other parameters, depend on the stacking fault energy of the strained material. In the case of face-centered cubic (FCC) metals with medium and high stacking fault energies (e.g. Al, Cu), deformation happens mainly because of crystallographic slip. In materials with low stacking fault energies (e.g. brass, MP45 alloy or Hadfield steel), twinning additionally plays an important role (Asgari et al, 1997; El-Danaf et al, 2001; Karaman et al, 2000). The different deformation mechanisms result in a different crystallographic texture. This effect was of interest to many authors e.g. Wasserman (1963); Dillamore and Roberts (1964); Smallman and Green (1964); Goodman and Hu (1968). Staroselsky and Anand (1997) provide a comparison between experimentally measured textures of commercially pure copper and 70 – 30 brass as examples of materials with low and high SFE, respectively.

The different plastic deformation mechanisms of brass and copper also manifests itself at the macroscopic scale by the change in the strain hardening rate as a function of strain. The strain hardening rate decreases continuously in copper, while it has an area of stability at intermediate strain levels in brass (Truszkowski, 2001). Asgari et al (1997) found in their experimental study that the area of stability (or plateau) of the strain hardening rate can be related to the onset of twinning, and that it is caused by the twin-twin and twin-slip interactions.

In terms of analytical and computational modeling, twinning is a more complicated deformation mechanism compared to dislocation slip and raises new issues. In addition to the twinning shear, it creates new twinned regions, which have a different orientation than the surrounding matrix (Staroselsky and Anand, 1997). These regions need to be considered and modeled as new grains with an evolving volume fraction (Rangaswamy et al, 2002), which affects the deformation texture as discussed above. Another issue is that twinning decreases the macroscopic stress and increases ductility, which results in different strain-stress behavior under different deformation paths (English and Chin, 1965; Heye and Wasserman, 1968; Chin, 1975; Asgari et al, 1997; Staroselsky and Anand, 1997; El-Danaf et al, 2000, 2001). Van-Houtte (1978) adapted the Taylor model to take into account grain reorientation due to twinning. Later, Tomé et al (1991) and Lebensohn and Tomé (1994) underlined some limitations of Van Houtte’s scheme and proposed their own, valid in the

framework of the Taylor-type (Taylor, 1938; Asaro and Needleman, 1985) and self-consistent poly-crystal models.

Kalidindi (2001) derived a model based on the assumption that the differences between the brass and copper textures are mainly due to micro-scale shear banding and less to deformation twinning. The assumptions were justified by the results of experimental observations of Asgari et al (1997), in which formation of thin deformation twins results in decreases of slip-length which causes stress concentration at the twin-matrix interface. The elevated stress causes dislocations to pass through the twins and trigger micro-scale shear banding. Kalidindi's model is capable of describing qualitatively the differences in the texture of low and high SFE metals and therefore the differences between brass and copper texture.

Leffers and Juul-Jensen (1991) used a similar approach in which they assumed that the formation of the brass-type texture is not the direct effect of the created volume of twins and therefore new orientations. It results rather from the planar flow provoked by the developed micro-bands forming a lamellar microstructure. This reasoning is supported by experimental observations which show that the development of the brass-type texture cannot be fully explained by the impact of the volume fraction of twins on the texture image only (Leffers and Van-Houtte, 1989; Leffers and Ray, 2009).

A recent extensive review on the issue of transition from the copper-type texture to the brass-type texture is provided by Leffers and Ray (2009).

### 2.3.1 Poynting and Swift effect

In some alloys, pure torsion (also called free end torsion) experiments result in an elongation of the specimen in the direction of the twist axis. The elongation of samples of geometry similar to those used in this study was already reported for high strength steels (Cannizzaro et al, 2005; Cannizzaro, 2006; Giovanola et al, 2006), in which fracture is controlled by void nucleation and not by growth and coalescence.

The effect of the elongation of an axisymmetric specimen along the symmetry axis about which it is being twisted is known as the Poynting or Swift effect. Poynting (1909, 1912) analyzed the behavior of isotropic materials. He attributed the origin of lengthening to the difference between axial components of the stress on the internal and external ligaments respectively. In order to equilibrate the stress components, the wire as a whole must lengthen. The effect observed by Poynting in elastic wires was also observed by Swift (1947) in tubular specimens during plastic deformation. The permanent lengthening of a tubular specimen was also reported by Billington (1976) in aluminum, copper and iron or Miller and McDowell (1996a,b) in 304L stainless steel.

More recently, Weber et al (2000) observed the opposite effect of shortening in highly anisotropic alumina fiber reinforced aluminum wires.

The observed changes in length are attributed to anisotropy, for example, due to the preferential orientation of grains, or more recently to the evolution of crystallographic texture within the material (Montheillet et al, 1984, 1985; Tóth et al, 1988, 1990; Weber et al, 2000).

## 2.4 Model materials

By model material we mean a material that exhibits predominantly the desired effects that we want to investigate. Model materials are frequently used to enable observation of a given fundamental phenomenon and they have proven to be useful for studying a wide range of effects. In the field of fracture mechanics (ductile fracture), several materials have been proposed as model materials.

Two model materials were presented in Weck et al (2006). Both materials contain high purity copper sheets with an array of 10 micron sized holes all the way through the sheet. In the case of the second material, a hole containing sheet is bonded on both sides by hole-free sheets. The materials were developed and used for 2D SEM and 3D X-ray computed tomography observations of hole growth and in particular, coalescence events (see also Weck et al, 2008). Earlier Magnusen et al (1988) and Jia et al (2002) also used perforated tensile specimens containing random and regular arrays of holes.

A very ductile and commercially pure aluminum (Al) metal matrix which was reinforced by spherical ceramic particles of  $ZrO_2/SiO_2$  was used to successfully observe and quantify nucleation and growth of voids with SEM and XRCT (Babout et al, 2001). This model material failed in a VNGC mechanism, and ceramic particles did not break. The growth phase measured locally (on isolated particles), and globally (in the entire block), was compared with the Rice and Tracey predictions which were shown to overestimate the global deformation and to give a reasonable agreement of the local void growth rate.

Gammage et al (2004) used aluminum AA2618 reinforced with different volume fractions of SiC to develop the SCEMA damage model (a model for deformation of two-phase materials with heterogeneous second phase distributions). Damage coalescence is treated using a micro-crack linkage model that is sensitive to both the local volume fraction of damaged second phase particles and local stress acting between damaged particles. Damage starts at inclusions that crack and then propagates through the matrix to link with other cracked inclusions.

The model materials described above were specifically created for the purpose of research and have no obvious industrial application. In the course of this investigation, when selecting our model material we sought an industrial material of significant importance so that the research findings might have direct industrial implications.

## 2.5 Gaps in our knowledge

Fracture of a vast number of ductile metallic materials is controlled by void nucleation growth and coalescence processes. It has been extensively investigated and modeled since the late sixties. In the investigations, authors concentrated mainly on high triaxiality loading conditions, assuming spherical or axisymmetric ellipsoidal voids.

The influence of parameters such as the initial void shape (aspect ratio), the nature and size of the inclusions that initiate the void, the distribution of neighboring voids and interactions with these voids, or the geometry of the structure and global loading were extensively tested under high stress triaxiality.

It is only recently that more analytical studies were carried out to investigate the fracture behavior of materials under low stress triaxiality, taking into account additional effects which play a role in large deformations under shear loading: general ellipsoidal (not axisymmetric) shape of voids, their rotation, influence of the anisotropy of the matrix material (both initial and developing texture anisotropy) and behavior under general three-dimensional loading conditions.

As far as the shape of voids is concerned, in many cases it is assumed to be axisymmetric ellipsoidal even under shear loading conditions, and the void rotation is described using only one parameter (orientation angle). This approach limits applications of the models to simple geometries and loading conditions. In fact, such models can be used to calculate cases of complicated geometries or loading conditions, but the models were neither designed for these applications nor validated against experimental data for such conditions.

Even though, in several cases, materials can be regarded as initially isotropic, it is by now, well understood that when they are subjected to large deformations their microstructure evolves leading to an overall anisotropic response. Available analysis of the VNGC in anisotropic material usually describes the anisotropy due to void geometry changes (different void elongation in different directions) and not due to evolving microstructure and texture of the matrix material. Only a few authors addressed this problem by developing VNGC models or by performing single cell simulations using crystal plasticity descrip-

tions of the matrix material. Influence of anisotropy and in particular texture induced anisotropy, on void growth and coalescence cannot thus be considered as extensively studied.

From the literature review we found that authors, during their research, focused usually either on moderate to high triaxiality or on low triaxiality loading conditions. Not enough experimental results exist for void nucleation, growth and coalescence modeling covering a wide range of loading conditions and stress triaxialities. Existing experimental studies analyzing the VNGC in real materials describe voids in terms of void area fraction (or void volume fraction), and there are not enough studies analyzing voids in terms of shape and orientation changes of 3D ellipsoids which could be used to validate void shape predictions of the VNGC models.

Finally few, if any, completely integrated VNGC models applicable to given ductile microstructures have been assembled and validated for practical applications using industrial materials. The practitioner still does not have a reliable tool validated for low and high stress triaxialities with which to evaluate fracture behavior of real structures under generalized loading.

## 2.6 Postulate

Although the knowledge in the field of ductile fracture mechanics has been growing rapidly, there is still a significant amount of work to be done in order to employ VNGC models for ductile fracture predictions for technologically useful materials subjected to complex load paths in complex structures. The acknowledged deficiencies of existing micromechanical models mentioned above, lead us to formulate the following postulate for our research:

- The mechanisms and kinetics of void growth and coalescence in a ductile matrix subjected to arbitrary loading and deformation conditions can be elucidated, and
- Models can be validated, augmented or developed
- By performing a coupled experimental, fractographic and numerical analytical investigation of a model material with specimens evoking a range of stress states, quantifying the ductile damage and simulating the results with existing or improved models.

The research therefore concentrates on generating well characterized and reliable experimental data for void growth and coalescence that could be used to evaluate existing void growth and coalescence models in order to provide more reliable tools for fracture predictions.



## Chapter 3

# Materials and experimental procedures

### 3.1 Outline of the approach

The object of the research was to study the void growth and coalescence process in ductile alloys. The research approach combines experimental techniques, careful metallographic and fractographic observations, numerical simulations (single microscopic cell and complete specimens) and analytical modeling of the observed micromechanisms of fracture.

First, appropriate materials were selected, so called model materials that allow the study of various stages of void growth and coalescence mechanisms uncoupled from the nucleation stage. We selected lead-containing brass as the principal model material and considered very soft, compared to matrix, lead inclusions, to act as pre-existing voids. The lead-free counterpart of the first alloy is our second model material. The two alloys are almost identical except for the lead content. The lead alloy will be used to observe and measure void growth while the lead-free alloy will be used to determine properties of the non-voided material (matrix of lead alloy). We describe the selected model materials and validate the assumption of lead inclusions acting as pre-existing voids using 2D single cell calculations in Section 3.2.

Second, experimental techniques were developed to characterize the model materials in order to observe and measure changes in void orientation, void axes elongation and void volume growth in the lead-containing alloy. Described mechanical testing techniques were applied to both lead and lead-free alloys. Results of smooth round tensile tests of the lead-free alloy are used to estimate the response in terms of stress-strain curve of non-voided material (matrix of the leaded alloy), as the lead-free alloy behaves as if it contained no voids over a large range of strain. This work is reported in Section 3.3.

Third, results of experiments were investigated in more detail using nu-

merical computations. Mechanical tests are simulated using lead-free alloy stress-strain curve to calibrate and to validate our constitutive model, and to obtain suitable boundary and loading conditions for single cell calculations. Then we performed 3D single cell simulations for various loading cases corresponding to loading conditions in the mechanical tests to analyze the experimentally observed void growth. Measured material constitutive behavior, model geometries together with boundary conditions and plasticity models used for computations are described in Section 3.4.

## 3.2 Model material selection and validation

### 3.2.1 Concept of model material

A model is a material that exhibits desired effects in an easily observable, and if possible, in an independent way, not coupled to other effects. Our objective for the model material was to select an alloy, that would allow quantification of void growth under different stress conditions, as well as investigation of the coalescence mechanisms, without the nucleation process.

### 3.2.2 Requirements

Requirements for the model material to be used for the research are based on its fracture mechanism and microstructure. The model material should behave as follows:

- The material should exhibit only void growth and void coalescence stages of ductile fracture.
- The void growth may be observed and quantified at different levels of deformation under various loading conditions.
- The material should be a commercially available alloy.

The model material should isolate the void growth and coalescence phases from the nucleation phase of the fracture process. This may be achieved by selecting an alloy containing one of the following: pre-existing voids or soft or weakly bonded or easily fracturing inclusions. In the case of an alloy with weakly bonded or easily fracturing inclusions, it is necessary to reach nucleation conditions as early as possible in the loading history. Pre-existing voids or a single population of voids nucleating inclusions, would ensure that the alloy's fracture is driven by a single mechanism. Fractured surface containing ligaments necked down to a sharp edge between dimples containing the same type of inclusions would indicate that there is not a second void population in the alloy which is activated at a later stage and influences the growth and coalescence process.



For this work the model material ideally should contain an homogeneous distribution of spherical or elliptical relatively large voids or inclusions. The required shape of void/inclusions will allow the description of their size in terms of the characteristic parameters (lengths of the major and minor axes). We require the homogeneous distribution of voids or inclusions, as a significant amount of work is done using symmetrical arrays of voids. To avoid ambiguity while interpreting quantitative void growth results, the material should not nucleate a second population of void (thus it should not contain a second population of inclusions) nor should it nucleate voids spontaneously at grain boundaries or at triple points. A relatively large size of voids/inclusions would facilitate microscopic observation and measurements.

We searched for a model material amongst commercially available alloys in order to examine the applicability of known mathematical models of local fracture to existing industrial materials. The use of a commercial material has two major advantages: the material is easily available and importantly makes the results of the research directly applicable to industry.

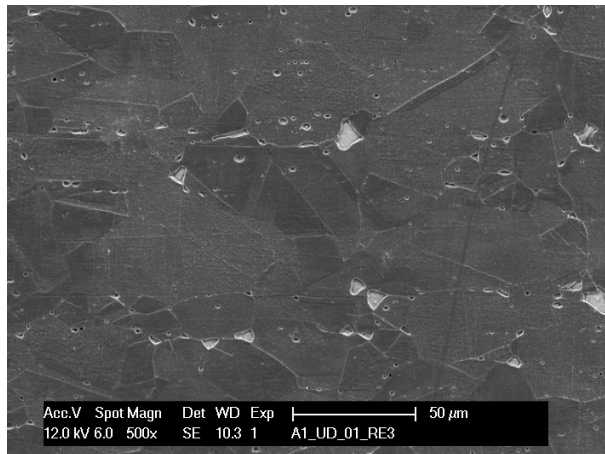
### 3.2.3 Selection

We selected a 9% Zn brass containing on average 1.85% lead as the principal model material *A1*. The *A1* alloy was used to observe and measure void growth. A second alloy termed *A2*, is the lead-free counterpart, and was used to determine properties of the matrix of the lead-containing alloy. Both alloys were manufactured and provided by Swissmetal as 32 mm diameter round bars manufactured from one batch for each material. Table 3.1 shows their chemical composition, trade names and ASTM standards. Figure 3.1 compares microstructures of *A1* and *A2* alloys observed using scanning electron microscope (SEM) and secondary electron detector (SE). The two alloys are briefly described in the next sections. The thermomechanical processing is proprietary and is unknown to us.

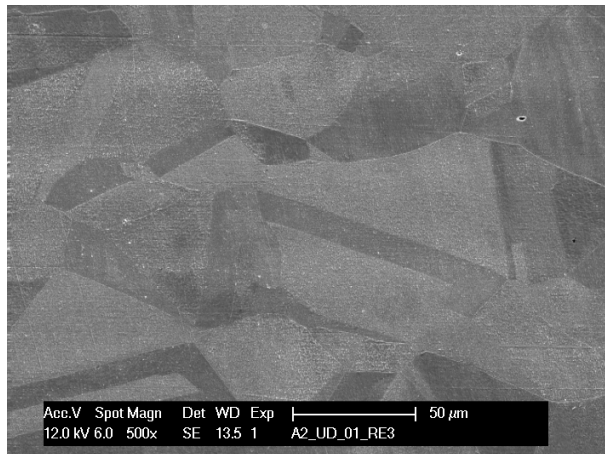
*Table 3.1: Chemical composition of selected model materials in % by weight. 90A and E90 are Swissmetal trade names of A1 and A2 alloys respectively.*

Code	ASTM	Cu	Ni	Zn	Sn	Pb	Other el.
<i>A1</i>	C31400	88.0-90.0	≤ 0.4	Rem.	≤ 0.1	1.5-2.2	Fe ≤ 0.1
<i>A2</i>	C22000	89.0-91.0	—	Rem.	—	≤ 0.05	Fe ≤ 0.03

However results of the microhardness test presented in Table 3.2 indicate that matrix of the *A1* alloy has similar mechanical behavior as the matrix of *A2*, as the obtained values for the *A1* and *A2* alloy are very similar and differ at most by 1.33% in the case of the HV 0.05 test. Values presented in Table 3.2 provide an average of three experiments for each load and material, performed on polished and electro-etched surfaces. In the *A1* alloy tests were



(a) A1 alloy.



(b) A2 alloy.

Figure 3.1: Microstructure of A1 and A2 alloy revealed by etching (SE).

conducted in grains containing no lead inclusions.

Table 3.2: Microhardness test results for alloys A1 and A2.

Material	HV 0.3	HV 0.1	HV 0.05
A1	109.0	110.9	113.1
A2	108.4	109.6	111.6

### 3.2.4 Characterization

#### Pre-existing voids

It was observed in polished and ion milled A1 samples that there is a small void associated with each lead inclusion. The void appears in the lead inclusion or at the lead-matrix interface. As observed in Figure 3.2, lead (seen as bright spots) does not occupy all the cavity volume in the brass matrix. As voids are already present in the alloy it can be assumed that there is no nucleation stress and voids start to deform and grow as soon as load is applied.

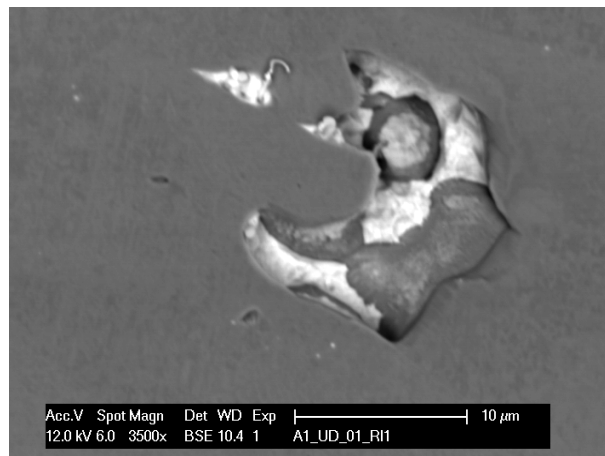


Figure 3.2: Typical lead inclusion-void system in an ion milled, non-deformed A1 (BSE).

The cause of the void associated with the lead inclusion is the solidification shrinkage of lead and the difference between the coefficients of thermal expansion and solidus temperatures of the inclusion and matrix. On cooling, the matrix solidifies first as the lead cools down and as lead has a larger coefficient of thermal extension it shrinks more than the solidified surrounding matrix and leaves a void. Values of these coefficients for technical lead and for the A2 alloy, which has composition similar to the A1 alloy matrix are given by ASM (1979) and are provided in Table 3.3.

If we assume that a very soft lead inclusion with an internal void, acts as a pre-existing void of a size corresponding to that of the lead inclusion, the

Table 3.3: Thermal properties of A1 matrix (=A2) and technical lead.

Material	Thermal exp. coef. [ $\mu\text{m} / \text{m} \cdot \text{K}$ ]	Solidus temp. [ $^{\circ}\text{C}$ ]
Matrix	18.4	1020
Lead	29.3	327.4

chosen model material allows us to uncouple the void growth process from void nucleation effects. To validate this assumption we performed numerical simulations of single axisymmetric cells in three configurations subjected to various loading paths as described in detail in Section 3.2.5. The calculations show that in most of the loading cases (the exception being under pure hydrostatic pressure), the presence of a voided lead inclusion does not significantly affect the mechanical response of the cell in terms of mesoscopic stress and strain. Thus we can indiscriminately assimilate a lead inclusion containing a void, or a lead inclusion to a void.

### Preliminary observation

The high chemical contrast between lead and matrix is one of the major advantages of the A1 alloy. Figures 3.3(a) and 3.3(b) present the same inclusion observed with either a secondary electron detector (SE) or back scatter electron detector (BSE) respectively. Lead is much heavier than the surrounding Cu-Zn matrix and appears as a bright spot in micrographs taken with the BSE detector, while the matrix is gray. By boosting the contrast, one can make it relatively easy to detect and measure lead inclusions, making lead-containing brass suitable for analysis using an automated image recognition software.

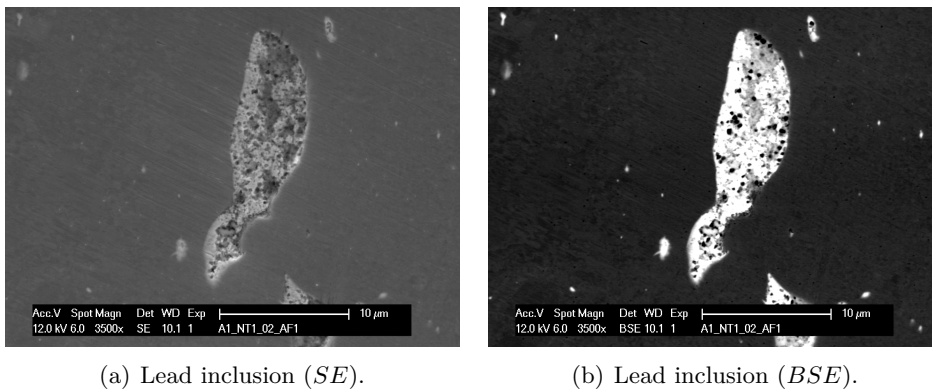


Figure 3.3: A lead inclusion in tested NT3 sample observed with SE and BSE detectors.

Very soft lead deforms extensively during the polishing stage of prepara-

tion for SEM observation and it is displaced within the void. As a result of this extensive deformation, in most cases, the whole void is covered with a spongy lead structure, which also covers the pre-existing additional void responsible for zero nucleation stress. This explains why grown voids are usually not visible in deformed samples (see Figure 3.3). Evidence of the pre-existing voids can be thus found only in ion milled samples (Figure 3.2) or samples fractured at high triaxiality.

The spongy lead structure presented in Figure 3.3(b) is only observable at high magnification. At lower magnifications it appears as a solid bright spot (see Figure 3.4(a)) and is considered as a single element by image analysis software. The BSE micrographs are thus suitable for void size analysis.

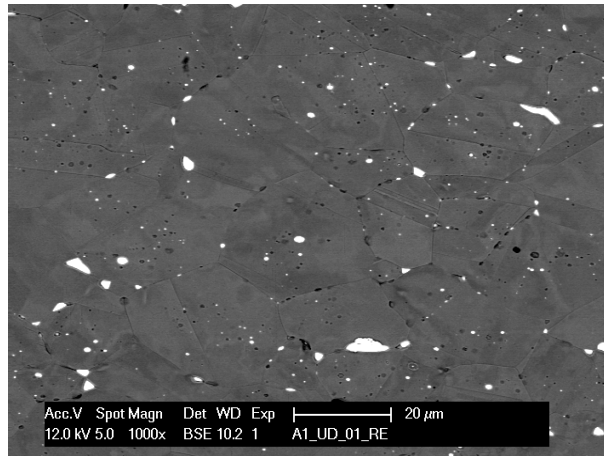
### Shape and distribution of inclusions

Depending on the alloy composition and on the manufacturing process, the distribution of lead inclusions may be different. In general, in lead-containing brasses, lead appears at grain boundaries and at triple points (ASM, 1979). If a material is deformed up to a certain strain value, its matrix can recrystallize which may cause some of the lead inclusions to appear in grains. In the A1 alloy, inclusions appear both in grains and at grain boundaries. Figure 3.4(a) shows a typical microstructure of the A1 alloy. It can be observed that in the A1 recrystallized alloy, lead forms more or less ellipsoidal inclusions which are distributed relatively homogeneously although they have a tendency to align in the direction of the axis of the round bar (horizontal direction in Figures 3.4(a) and 3.4(b)). Visible dark spots are voids occupied by lead before it was etched out.

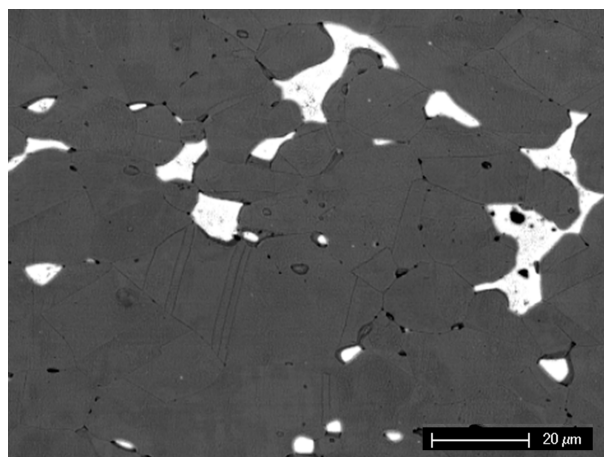
For the rest of our investigation, when quantifying void size and orientation, we will assume 1) that the void contour is given by the contour of the lead inclusion and 2) that all the lead inclusions contain a small shrinkage void. We will then assign to each void an ellipsoidal shape with major axis  $M$  and minor axes  $m_1$  and  $m_2$ , as discussed in more detail below. Furthermore, we will assume that the cross-sections always cut the voids in planes parallel to the major or minor axes. Justification of this assumption is provided in Section 3.3.4.

It was observed in the material received, that inclusions at grain boundaries or at triple points are bigger than those within the grains and that their shape adapts to the shape of surrounding grain boundaries. The size of inclusions is also influenced by the extent of recrystallization. Although the typical microstructure of the alloy contains a relatively homogeneous distribution of ellipsoidal inclusions, very close to the axis of the round bar, the material was found to occasionally contain very big inclusions of irregular shape as illustrated in Figure 3.4(b). These inclusion shapes are due to limited recryst-

tallization in this region of the round bar.



(a) Typical.



(b) Close to the axis of the round bar.

Figure 3.4: Microstructure of A1 lead-containing brass revealed by etching (BSE).

### Response to different loading conditions

With the exception of pure hydrostatic pressure, lead-containing alloys are very convenient for studying the evolution of inclusion shape under various loading conditions. Under low or negative triaxiality soft lead inclusions adapt their shape to the imposed deformation field, whereas the shape of voids nucleated at hard brittle inclusions is influenced by the wedging action of the inclusions. Also at high strain, when hard inclusions would break into small pieces making it impossible to track and measure them (see Appendix A), lead inclusions elongate with the matrix and allow tracking of changes in the

inclusion shape.

### Lead-free counterpart

The *A2* alloy is the lead-free counterpart of the *A1* alloy, which means it has a very similar chemical composition but does not contain lead. As lead does not dissolve in the Cu-Zn solution it can be assumed that the two alloys have almost the same matrix composition and microstructure. The only considerable difference concerns the average grain diameter which is 26 and 79  $\mu\text{m}$  for the *A1* and *A2* alloy, respectively.

The *A2* alloy was also found to contain inclusions. Figure 3.5 presents a typical hard inclusion-void system in an electro-polished sample of a nondeformed material. The inclusion-matrix decohesion appears always at the poles of inclusions aligned with the direction of the axis of the round bar (vertical direction in Figure 3.5). This fact indicates that the pre-existing voids associated with hard inclusions, originate during the manufacturing process of the round bars.

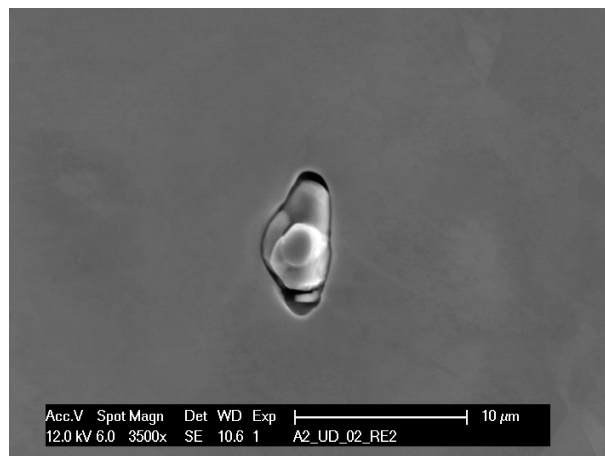


Figure 3.5: Typical inclusion-void system in an electro-polished undeformed *A2* (SE).

The inclusion volume fraction in the *A2* material was estimated using the average distance and the average size of the inclusions in the fracture surface of tensile bars and was found to be approximately 0.02%<sup>1</sup>. The hard type inclusions observed in the *A2* alloy were also observed in the *A1* alloy. They always appear within big lead inclusions and do not act as nucleation sites for a second population of voids. In addition, being trapped in soft lead, they will not be able to wedge open the voids significantly as they deform. Thus we conclude that the presence of a second family of hard inclusions in the *A1*

<sup>1</sup>Correction for the transversal strain in the tensile bar was taken into account in this estimation.

alloy does not affect the growth of lead-containing voids.

The very low volume fraction of inclusions in the *A2* material compared to the lead volume fraction in the *A1* alloy makes it possible, for certain analyzes, to assume that *A2* behaves over a large range of strains as if it contained no voids. Hence its stress-strain curve will provide a good estimate of the matrix response in material *A1*. Furthermore, by performing experiments on both materials, we can also directly investigate the influence of pre-existing voids on the fracture behavior of the material.

As far as the numerical code simulations of experiments are concerned, the use of the two, lead and lead-free alloys, provides a good opportunity to test the existing local approach to fracture models (LAF). Assuming that the LAF models are able to predict behavior of porous materials correctly, it should be possible to reproduce the behavior of the leaded alloy using the constitutive law obtained from the lead-free counterpart combined with lead inclusion distribution information. The distribution information would be obtained from the leaded alloy.

### **Availability**

The model materials we selected are commercially available alloys. This is important for two major reasons: the material is readily available, and the results we obtain will be directly applicable to industry.

### **3.2.5 Validation**

For this research we assume that in the *A1* model material the lead inclusions act as pre-existing voids and uncouple void growth and coalescence from the nucleation stage of ductile fracture. We validate this assumption by comparing results of single cell calculations for models a) with a full lead inclusion, b) with a lead inclusion containing a void in the middle, c) and with a full void.

We also compare results of numerical simulations of the smooth round tensile test using the Gurson-Tvergaard-Needleman model and von Mises plasticity, to provide evidence that the differences in apparent hardening of the two model materials can be reasonably assigned to void growth in the *A1* alloy.

### **Lead influence on material**

A numerical study was performed to investigate the influence of lead inclusions on the strengthening and softening of the *A1* material. Axisymmetric single cell calculations were performed for models approximating the actual situation in the *A1* alloy under various loadings: full lead inclusion (Case A), lead inclusion containing a void in the middle (Case B), and full void (Case C)



as presented in Figure 3.6. On the basis of the microstructural analysis, case B best represents the situation of the A1 alloy with its lead inclusion containing a void. Calculations were performed under constant stress triaxialities, and up to a mesoscopic equivalent strain  $E_{eq}$  corresponding to equivalent plastic strains  $\varepsilon_{eq}^{pl}$  at fracture initiation in different tested samples. The average stress triaxialities  $T_{avg}$  and equivalent plastic strains  $\varepsilon_{eq}^{pl}$  were obtained from continuum macroscopic sample simulations described in Section 3.4.2. Single cell response in terms of mesoscopic stress  $\Sigma_2$  and mesoscopic strain  $E_2$  in direction 2 were recorded. Mesoscopic stress  $\Sigma_2$  is defined as a sum of nodal forces over the actual surface, and mesoscopic strain  $E_2$  measures the difference of actual height and initial height (zero deformation) of the single cell divided by its initial height.

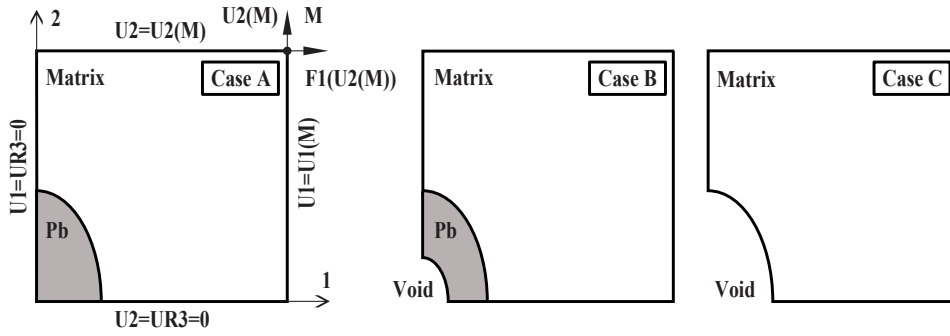


Figure 3.6: Axisymmetric single cell shape and boundary conditions:  $U$  - displacements;  $UR$  - rotations,  $F$  - force.

### Boundary conditions

The single cell axisymmetric models used for the calculations are presented in Figure 3.6. The initial dimensions of the voids and inclusions in the single cell models were calculated to replicate the volume fraction and the mean aspect ratio of the lead-void system in real material (see Sections 3.3.5 and 3.3.4 for details). Assuming a cubic<sup>2</sup> shape of the single cell and an edge length equal to 2, the major and minor radii are as follows:

- $M_0^{Pb}/2 = M_0^{Void}/2 = 0.442$
- $m_0^{Pb}/2 = m_0^{Void}/2 = 0.258$

The small void in the lead inclusion (Case B only) was assumed to be of the same aspect ratio as the lead inclusion and the major and minor radii were set as follows:

<sup>2</sup>The shape of the single cell was assumed to be cubic instead of cylindrical for the purpose of matching sizes of this and other 3D cubic single cells presented in Section 3.4.3.

- $M_0^{AV}/2 = 0.175$
- $m_0^{AV}/2 = 0.102$

Symmetric boundary conditions were applied as presented in Figure 3.6. Outside edges were constrained to follow the displacement of the master node M (a reference node shared by the two edges). Deformation of the single cell was controlled by displacement of the master node M in direction 2. During simulation, constant triaxiality was maintained by applying an appropriate force in direction 1. The constant stress triaxiality loading conditions were imposed using a user-defined element (UEL), providing an active control mechanism on the displacements of the master node in order to maintain constancy of stress triaxiality at each increment. The UEL was programmed by Andreas Rossoll (EPFL/STI/IMX/LMM) on the basis of the Eberle and Klingbeil (1996) report.

Using an axisymmetric model to evaluate void growth is appropriate for tensile and notched tensile loading conditions because inclusions at the specimen center remain axisymmetric. On the other hand, torsional boundary conditions and thus deformation of the void, cannot be correctly simulated by axisymmetric boundary conditions even if a relevant level of triaxiality is maintained. In the axisymmetric single cell, we impose zero stress triaxiality by imposing that the axial stress  $\sigma_2$  be twice the radial stress  $\sigma_1$  and of a negative value. Of course, this loading is far from that encountered in the torsional tests (no radial loads) and the associated void kinematics (void rotation) are also completely different. Results attempting to simulate torsional loadings are thus approximate. The evolution of void shape carried out with 3D single cells and taking into account different levels of deformation in directions 1 and 3 will be described in Chapter 4.

### Effect of lead content

Figure 3.7 presents the response of the different cases of single cells in terms of mesoscopic stress  $\Sigma_2$  and mesoscopic strain  $E_2$  in direction 2. Symbols *PT*, *TT1*, *TT2*, *ST*, *NT1*, *NT2* and *NT3* correspond to names of various samples described in Section 3.3.1. They also refer to various levels of imposed stress triaxiality and are arranged in an ascending order, where  $T = 0$  in *PT* and  $T = 1.465$  in *NT3*. Further values are provided in Table 4.2.

For most of the loading conditions, the response of the single cell does not vary with configuration. Only for conditions simulating the notched tensile loading conditions does the response depend on the model configuration. This is because the lead inclusion is perfectly bonded with the matrix and the inclusion cannot increase in volume. Cases B and C, under all loading conditions, behave similarly and thus we conclude that the presence of lead in the voids is not significantly strengthening the alloy. Moreover, for the voided cases of single cells (B and C), voids were observed to close under triaxiality lower than

1/3. This effect will be discussed in more detail in Chapter 4. The results of Figure 3.7 demonstrate that a lead inclusion containing a void behaves like a void and validate our assumption in choosing the model material A1.

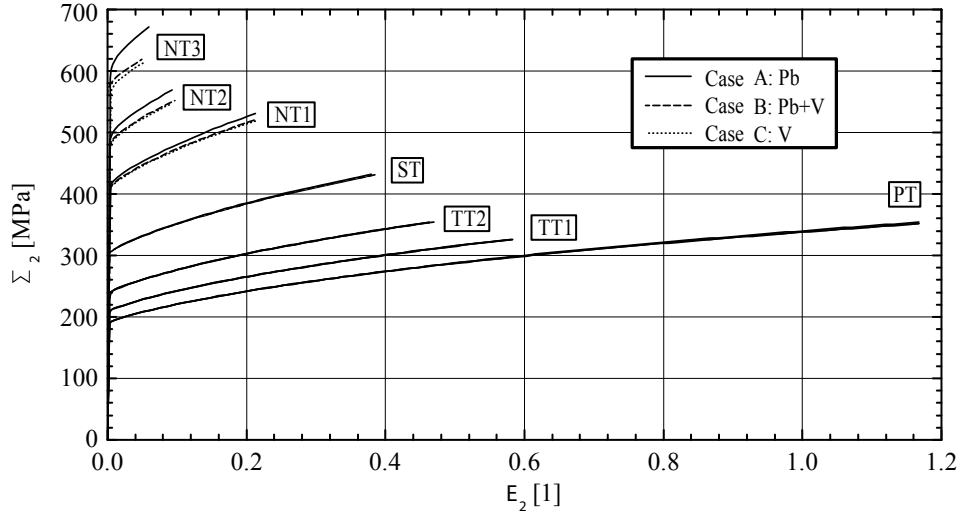


Figure 3.7: 2D axisymmetric single cell response.

### Strain hardening

Figure 3.8(a) presents the smooth round tensile test results for both model materials in terms of axial load versus axial displacement. The alloys have similar yield loads. As the deformation progresses, we observe relatively small differences in strain hardening of the two alloys.

Figure 3.8(b) presents results of numerical simulations of the same smooth round tensile test (*ST*) using an axisymmetric boundary condition. Line  $J_2$  represents the A2 alloy simulation result using the A2 tensile constitutive law, while the line GTN represents results of A1 alloy simulation, using the A2 constitutive law with void evolution described by the Gurson-Tvergaard-Needleman model (GTN,  $q_1 = 1.5$ ,  $q_2 = 1$ ,  $q_3 = 2.25$  and void volume fraction  $VVF = 1.54\%$ ). In the case of the GTN simulation, the constitutive law was adapted to exactly match the yield stress of the  $J_2$  simulation, while the strain hardening was the same as for the  $J_2$  simulation of the A2 alloy. Further details on the round tensile test simulation are provided in Section 3.4.2.

The simulation results presented in Figure 3.8(b) show a relatively small difference in the hardening behavior of the two materials similar to the difference observed in Figure 3.8(a) for the *ST* tests. The voided material exhibits smaller strain hardening compared to non-voided material, although the difference in strain hardening in the simulations is not as pronounced as in the

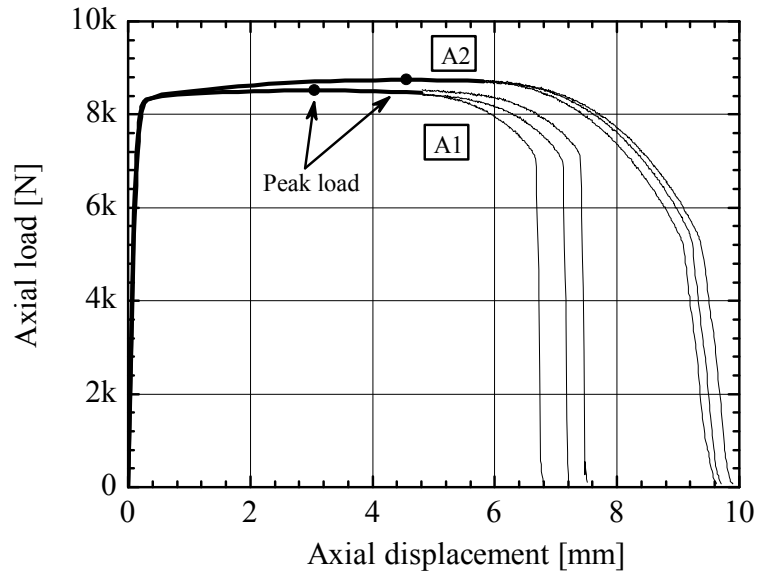
experimental results. This smaller difference may be due to the fact that the GTN model is not completely appropriate for use under low stress triaxialities, but may also result from small differences in the chemical composition of the two matrices and the difference in grain size (see Table 3.1).

The simulation with the GTN model suggests that the differences in hardening of the two materials can be reasonably assigned to void growth in the *A1* material. It also suggests that matrix properties of the *A1* alloy are well represented by the *A2* alloy.

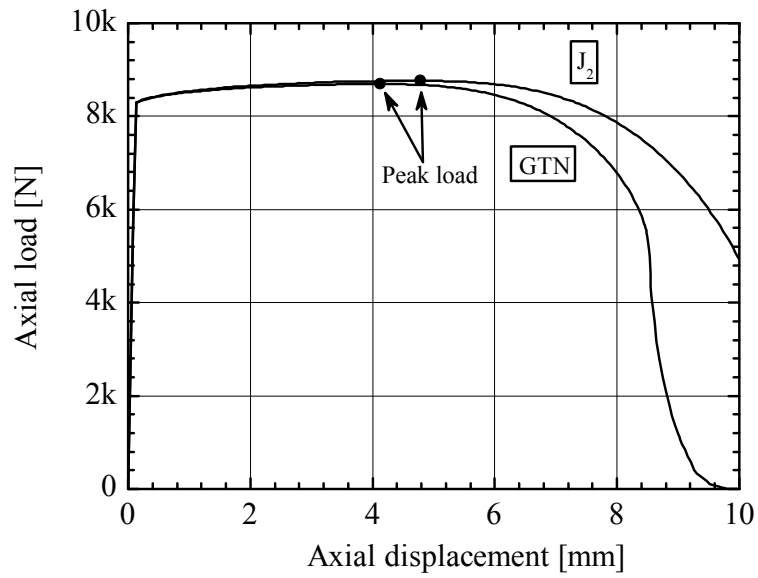
### 3.2.6 Summary

The search for a model material led to the selection of two alloys: *A2* and *A1*. The first is 10% Zn brass, while the second is an alloy of similar composition with the addition of lead. Both alloys have almost the same composition and a similar matrix microstructure, as lead does not dissolve in Cu-Zn phase. The stress-strain curves are very similar with the exception of a small difference in the hardening rate, which possibly results from microstructural differences (resulting from small compositional differences or differences in thermodynamical processing), but mainly from the effect of material porosity in the *A1* alloy. The lead-free *A2* alloy can be assumed to be void free, while in *A1*, lead inclusions behave like pre-existing voids. The major advantages of the selected materials are as follows:

- Dual voided and nonvoided microstructure, allowing observation and quantification of the influence of pre-existing voids on the material behavior.
- Relatively homogeneous distribution of quasi-ellipsoidal voided lead inclusions that can be considered to behave as voids.
- Good observability of voids (lead inclusions) due to the very high chemical contrast between lead and matrix. Suitable for analysis using automated image recognition software.
- Possibility of observation of void evolution for low and negative triaxialities, as lead adapts to the shape of voids.
- Zero nucleation stress, as each lead inclusion contains a void, and starts growing or deforming as soon as a load is applied.
- No second phase inclusions able to nucleate another void population in the lead-containing alloy because impurities concentrate in lead.
- Easily available commercial ductile alloys allowing observation of void growth and coalescence at high strains.



(a) A1 and A2 smooth round tesile test (*ST*) results (3 tests for each alloy).



(b) A2  $J_2$  and GTN calculation results.

Figure 3.8: Effect of lead presence on material hardening.

### 3.3 Experimental techniques

#### 3.3.1 Mechanical testing

##### Samples

Smooth round tensile specimens ( $ST$ ), notched round tensile specimens ( $NTx$ ) and thin-walled tubular specimens ( $T$ ) for torsional tests, illustrated in Figure 3.9 were fabricated with an N5 surface finish, from 32 mm diameter round bars. All the tensile specimens had a diameter of 6 mm in the gauge section. Sizes of the notches were as follows:  $NT1$  - 6 mm,  $NT2$  - 2.4 mm,  $NT3$  - 1.2 mm. The outer diameter of the cylindrical gauge section in the  $T$  samples was 20 mm, the wall thickness was 2 mm and the gauge length was 6 mm. The exact dimensions of the samples are provided in Appendix B.

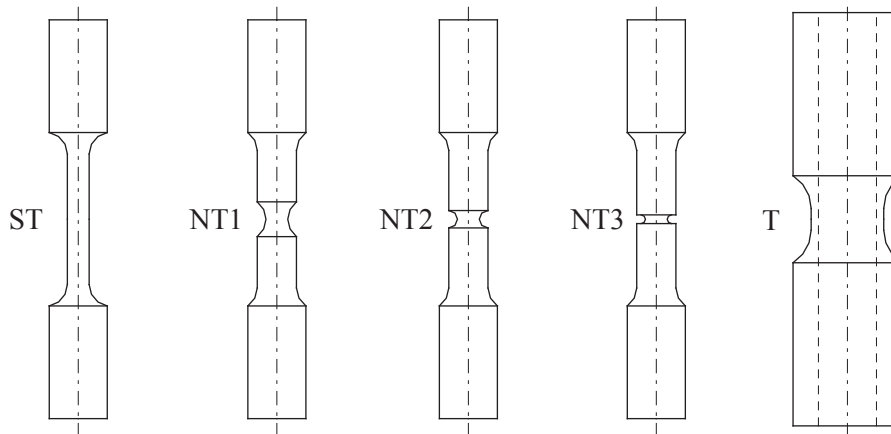


Figure 3.9: Geometry of tested samples:  $ST$  - smooth round tensile;  $NT1$ ,  $NT2$  and  $NT3$  - notched round tensile;  $T$  - thin-walled tubular.

Due to the production process and the large diameter of the ordered bars of materials, their microstructure, (in terms of grain size and lead distribution) changes with the distance from the bar axis (see Figure 3.4). To minimize this effect and to ensure that materials with similar microstructures were used in all the tests, we decided to shift the axes of the  $ST$  and  $NTx$  samples with respect to the axis of the bars of raw material. The tensile samples were offset by 7.5 mm as presented in Figure 3.10(a), while the axes of the thin-walled torsion samples coincided with the axis of the round bar as presented in Figure 3.10(b). The resulting relative position of the tensile and torsional samples ensured that we tested material from the same zone in the raw material bar for all specimen geometries. The relative position of the specimens is presented in an isometric view in Figure 3.10(c), and in cross section in Figure 3.10(d).

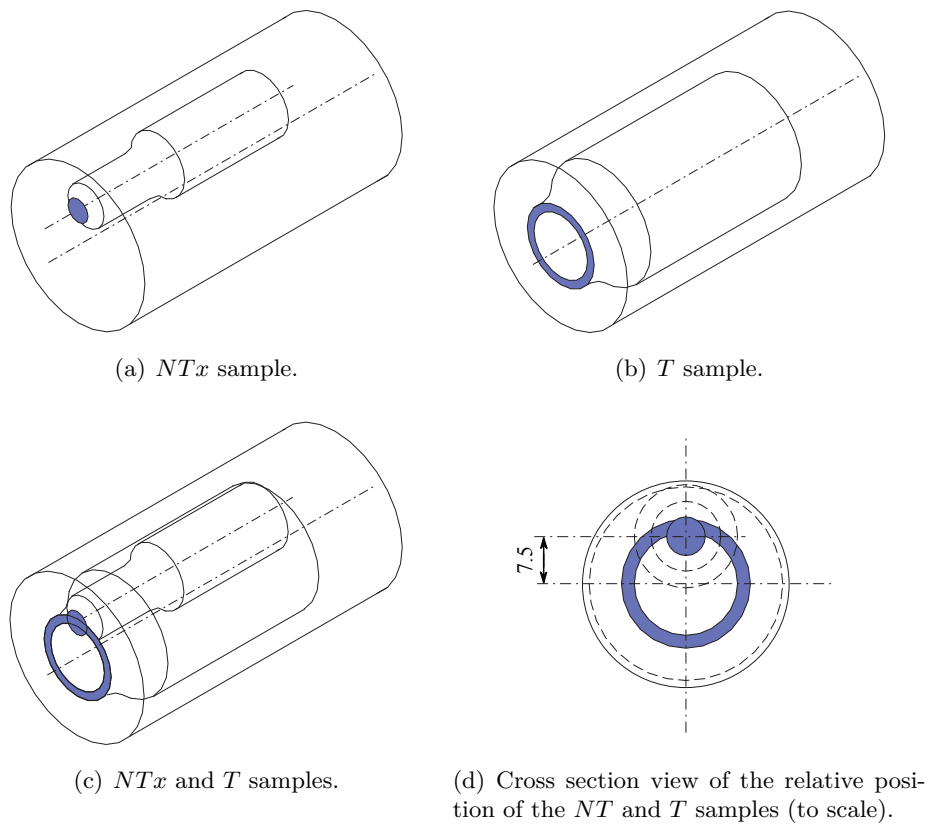


Figure 3.10: Position of the tensile and torsional specimens in the initial round bar.

### Experimental arrangement

All the mechanical tests were performed using a 100kN / 1100Nm tension-torsion MTS servo-hydraulic testing machine. The axial force, axial displacement, rotation angle and torque were measured using built-in transducers and load cells. The change in diameter of the notch of the round notched samples was measured using a diametral extensometer (MTS 632-19F-20) equipped with custom made knife edges. To ensure that the diametral extensometer stays in the same position with respect to the notch during the experiment, it was attached with a special support directly to the sample. Deformation of the smooth round tensile samples was measured using an axial extensometer (MTS 634-31F-24).

### Experiments

All the experiments were performed under control of the main tensile or torsional displacement (rotation). Smooth, round tensile samples (*ST*) were stretched until fracture at constant grip speed. The speed of the grips in the notched round tensile tests (*NTx*) (deformation in the axial direction) was controlled by measurement of the diametral extensometer, so that the rate of change of the diameter at the notch stayed constant (deformation in direction perpendicular to the axis). Torsional samples (*T*) were tested in pure torsional (*PT*) and tensile-torsional (*TTx*) loadings. The axial loads of the *TTx* experiments are presented for the various materials in Table 3.4. For the *TTx* tests, they were applied to the samples before starting torsional loading and maintained constant during the tests.

*Table 3.4: Axial loads in T experiments.*

Sample	Materials A1 & A2
<i>PT</i>	0 N
<i>TT1</i>	10180 N
<i>TT2</i>	20360 N

For certain materials and torsional loading configurations it was impossible to break the samples before the rotational range of the testing machine was exceeded. In these cases, the samples were unloaded until torque 0 Nm was reached. The specimens were released and the machine grip displaced to their original positions. The grips were clamped again and tests were continued until complete failure or until a new reclamping operation was required. Table 3.5 provides displacement or angular deformations rates for all experiments.

During the tests, samples were clamped using hydraulic grips of 16 and 30 mm diameter for tensile and thin-walled torsional samples respectively. Steel cylinders of 16 mm diameter were inserted into the thin-walled torsional samples at both ends to prevent radial deformation of the samples and slipping in



Table 3.5: Displacement/rotational rates.

Sample	Axial	Diametral	Torsional
ST	0.01 mm/s	—	—
NTx	—	0.0081 mm/s	—
PT	—	—	0.18 deg/s
TTx	0.0167 mm/s*	—	0.18 deg/s

(\*during axial force application)

the grips.

### Data reduction method

Three samples of each material, geometry and loading conditions were tested to obtain a rough estimate of the scatter in the behavior of the materials under various stress triaxialities. In later sections, one single mean curve, representative of the three tests will be presented. Only the failure stages of each of the three tests will be plotted to illustrate the scatter of the main load and strain to fracture. The mean curve was obtained by averaging the three experimental results and fitting a polynomial to the averaged data. Loading history, also recorded during the unloading steps if the sample did not brake, allowed us to match plots of subsequent parts of the experiments.

Figure 3.11 presents typical results of a set of three pure torsion experiments. Line 1 shows the result of a pure torsion test including unloading, lines 2 present the final stages of the three experiments, line 3 is the mean curve of the three tests. Figure 3.11 shows that the torque rotation curves are very reproducible and that the relatively small scatter affects only the deformation to fracture.

### 3.3.2 Metallographic techniques

Several metallographic techniques have been developed in order to allow observation and characterization of the microstructures, as well as to observe and measure void growth in deformed samples. Standard preparation procedures consisting of sample cutting, grinding and polishing were used for void growth observation. Some samples were etched to reveal grain boundaries. Other samples were ion milled to investigate details of the microstructures. Figure 3.12 presents the steps of sample preparation for Scanning Electron Microscopy (SEM) observations.

Tested samples were usually broken into two (except for several torsion samples). The thin-walled torsional samples were sectioned in the two planes defined in Figure 3.13(a). The axial-radial (*AR*) plane is any plane containing

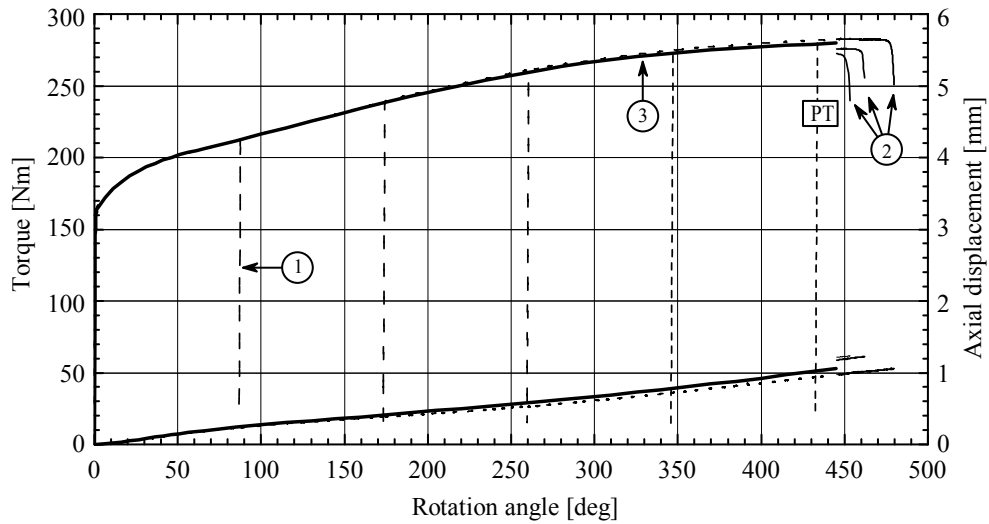


Figure 3.11: Typical representation of the results of 3 torsion tests and of the calculated mean curve (torque-rotation and axial displacement-rotation curves).

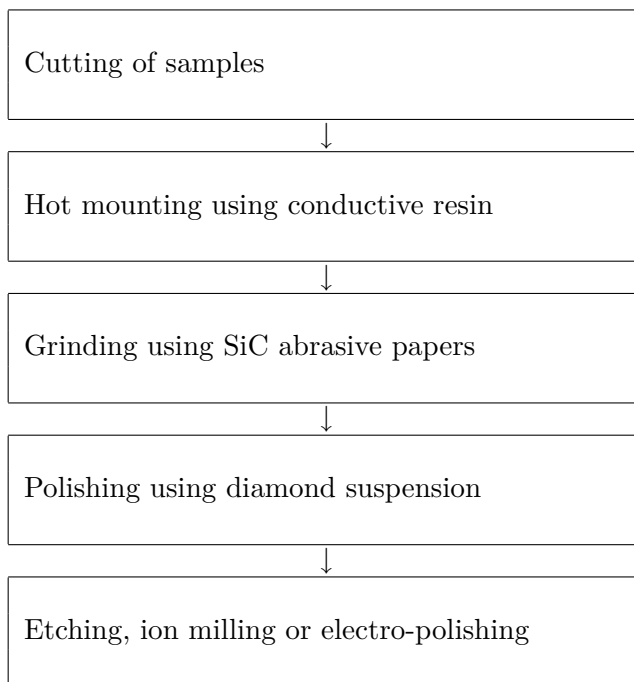
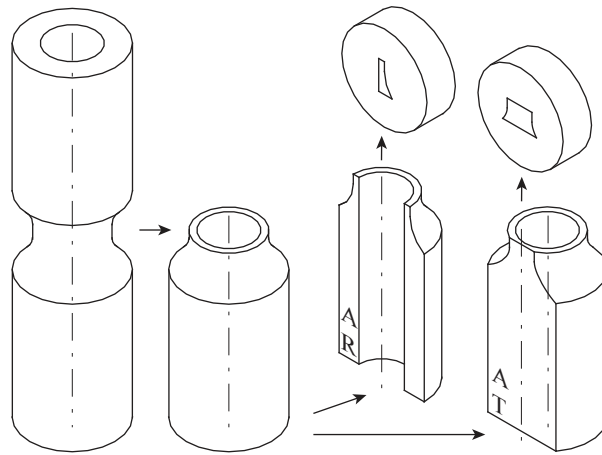
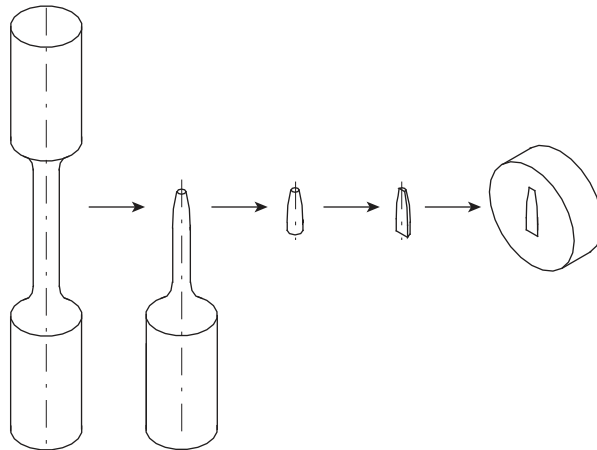


Figure 3.12: Steps in the specimen preparation for SEM investigation.

the axis of the sample. The axial-tangential plane ( $AT$ ) is any plane parallel to the axis of the sample and 9 mm distant from it. This distance places the cutting plane in the middle of the thickness of the gauge ring. Both the smooth and notched round tensile specimens were cut in  $AR$  planes as shown in Figure 3.13(b).



(a) Thin-walled samples sectioned in axial-radial ( $AR$ ) and axial-tangential ( $AT$ ) planes.



(b) Tensile samples sectioning.

Figure 3.13: Definition of sectioning planes of the tested samples.

Sectioned samples were hot mounted using phenolitic hot mounting resin with carbon filler using a hot mounting press. Samples were heated to  $180^{\circ}\text{C}$ , held at that temperature for 8 min under a load of 20 kN, and cooled to ambient temperature for 8 min. Grinding was performed using SiC waterproof paper with the following grit sizes: #320, #500, #800.

Samples were water-cooled only during grinding and then had no contact

with tap water in further preparation steps. This precaution was necessary because lead in contact with tap water, may form hydrocerussite crystals as observed also by Sun et al (2007). This crystallization would affect void observation and measurements.

Samples were polished using a diamond suspension. Polishing cloth MD-Nap was used for diamond sizes of 9  $\mu\text{m}$ , 3  $\mu\text{m}$  and 1  $\mu\text{m}$ , while cloth MD-Mol was used for 1/4  $\mu\text{m}$ . Polishing cloths were moistened with DP-Lubricant Blue.

Two etches were used. The first was the general purpose etch (20 ml  $\text{NH}_4\text{OH}$  + 20 ml  $\text{H}_2\text{O}$  + 15 ml 3%  $\text{H}_2\text{O}_2$ ), while the second was the etch #34 according to ASTM norm E407 ASTM (1994) (etch: 2 g  $\text{FeCl}_3$  + 20 ml  $\text{HCl}$  + 100 ml  $\text{H}_2\text{O}$ , wash: 5 ml  $\text{HCl}$  + 45 ml  $\text{H}_2\text{O}$ ). All samples were etched from a few seconds up to one minute.

### 3.3.3 Image analysis technique and resolution

Scanning electron microscopy (SEM) was employed for observing samples using a secondary electron detector (SE) to show the topography of the sample, as well as a back scatter electron detector (BSE or chemical contrast), to give an idea of the chemical composition of the material and in particular to highlight the lead inclusions.

#### Microscope settings

Void size analysis was performed on micrographs taken using the BSE detector. Lead inclusions and voids were considered as the same objects. For each sample 20 pictures were taken and analyzed. Results of the analysis were normalized to a surface of 1  $\text{mm}^2$ . The usual settings of the XLF-30 electron microscope for void analysis were as follows: acceleration 12  $kV$ , spot size electronic setting "6", working distance 10 mm, magnification 1500 $\times$ , contrast 95%, brightness 48%, high resolution digital imaging (1424  $\times$  1064 pixels), slow scan (0.42 ms, 968 lines). For each micrograph, 4 frames were averaged in order to obtain high quality images and the contrast was boosted to facilitate the automated image analysis. No ultrasound cleaning was employed for polished samples as lead was observed to form small particles and leave its initial position, affecting the size and number of measured inclusions.

#### Microscope resolution

To investigate the resolution of the microscope, we calculated the BSE profile for the Cu-Zn matrix and lead (Pb) inclusion interface using a Monte-Carlo simulation software - Casino (see Drouin et al, 2007) with parameters used to take micrographs for void size analysis: acceleration voltage 12  $kV$ ,

beam radius 10 nm. The resulting BSE profile is presented in Figure 3.14. The back scattered electron (BE) coefficient is a ratio of back scattered electrons and the total number of electrons sent to a sample position "0" which is the position of the matrix and lead inclusion interface. We can observe that the response of the sample becomes constant for position  $-6$  nm and lower for Cu-Zn matrix, or position  $+6$  nm for lead inclusion. Thus we can conclude that the theoretical best resolution of the microscope (the smallest inclusion that can be observed) is approximately 12 nm, and the boundary is defined with a tolerance of  $\pm 6$  nm.

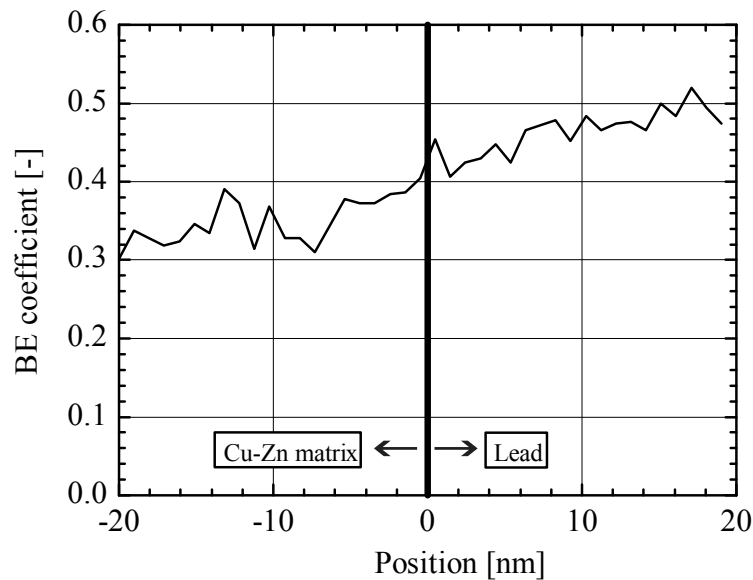


Figure 3.14: BSE profile for the Cu-Zn matrix and Pb inclusion interface simulated using *Casino* - a Monte-Carlo simulation software.

### Micrograph resolution

Micrographs used for void size analysis were  $1424 \times 1064$  pixels in size. At the magnification used for void size analysis  $20 \mu\text{m}$  is equal to 345 pixels, so in these micrographs, one pixel is  $\cong 60$  nm.

### Overall resolution

The micrograph resolution of 60 nm is the inferior one of the two calculated, and is the "real" resolution of the micrograph. Every inclusion smaller than 60 nm is either observed as one pixel or is not observable.

### Representative data range

We decided to improve the quality of the experimental data for void volume fraction calculations by selecting a narrower representative range of data than that measured in the study. To do this we set up lower and upper size limits for inclusions to be analyzed.

Below a certain size, inclusions are detectable but not appropriate for size analysis because the image resolution becomes significant with respect to dimensions of the inclusion, i.e. the resolution is inferior to the inclusion size. We also do not consider very big inclusions which tend to follow the shape of grain boundaries and are not necessarily ellipsoidal.

To make the upper and lower size limits universal for all the analyzed samples, we decided to designate them in terms of the minimal and maximal inclusion cumulative number  $N$ :  $1 \cdot 10^3 \leq N \leq 5.5 \cdot 10^3$  (see also Section 3.3.4). In nondeformed samples these limits correspond to the lengths of the major  $M$  and minor  $m$  axes:

- $0.98 \mu\text{m} \leq M \leq 3.1 \mu\text{m}$
- $0.65 \mu\text{m} \leq m \leq 1.6 \mu\text{m}$

In evaluating void growth in the deformed samples, we monitor the cumulative number of voids with sizes within these limits. By filtering the very small and very big inclusions, we obtain a set of relatively homogeneously (equidistantly) distributed inclusions of spherical or elliptical shape. Such sets of inclusions can be well approximated (described) in terms of characteristic parameters such as major or minor inclusion axes.

This procedure means that we will focus the investigation of void growth in the model materials in a specific size range, while still recording information for all the observed sizes ranges.

### 3.3.4 Void orientation and size analysis

#### Initial assumptions

In the void orientation and size analysis, we assume that inclusions have an ellipsoidal shape and that their volume can be calculated using the lengths of three perpendicular axes. In the analyzed SEM micrographs, the major axis is defined as the distance between the two most distant points of the cross-section of the inclusion while the minor axis is calculated so that the equivalent ellipse has the same area as the analyzed inclusion. By doing so, we assume also that the cut through the sample (surface of the SEM analyzed sample) always passes through the center of an inclusion. This analysis method is consistent with quantitative metallographic practices and justifiable

by statistical considerations (Curran et al, 1987)

This easily accessible method of analyzing polished fractured samples was chosen because it allows the analysis of large surfaces (limited only by the sample's size) and thus analyses of a large number of observed inclusions. Other imaging techniques such as X-ray computed tomography (Babout et al, 2001; Weck et al, 2006) or focused ion beam (FIB) have become more popular in fracture mechanics as they allow one to obtain exact shapes of the inclusions and estimate the void volume fraction ( $VVF$ ) more precisely and even perform in situ observations. On the other hand, they are only able to operate on relatively small samples and are prone to errors due to non-homogeneous distribution of inclusions in the real structure.

### Void orientation

Figure 3.15 presents the distribution of orientation of the major axis in nondeformed<sup>3</sup> material, observed in two perpendicular planes  $AT$  and  $AR$  (lines  $UD - AT$  and  $UD - AR$  respectively). The angle,  $0\ deg$ , refers to the direction of the sample axis (which is also the longitudinal direction of the original extruded bar) and the drawn lines show the number of observed inclusions within the orientation interval of  $5\ deg$  ( $\pm 2.5\ deg$  starting at  $0\ deg$ ). Lines were obtained by linking results for each angle that is a natural multiple of  $5\ deg$  (positive and negative angles of  $0, 5, \dots, 90$ ). For example, for all the lines there are approximately  $4 \cdot 10^3$  inclusions/ $\text{mm}^2$  with orientation  $0 \pm 2.5\ deg$ , and approximately  $3 \cdot 10^3$  inclusions/ $\text{mm}^2$  with orientation  $5 \pm 2.5\ deg$  for  $UD - AR$ .

We notice that inclusions observed in both  $AR$  and  $AT$  planes have an initial orientation in the direction of the axis of the sample which results from the manufacturing process of the bar. Assuming that the shape of initial voids is axisymmetric, this observation allows us to calculate the average distribution of orientation for nondeformed material (line  $UD - avg$ ) that will be used for comparison to the distributions for deformed materials.

### Void cumulative number plots

To calculate void elongation and void growth, we use graphs of the cumulative number of voids, on which we plot the cumulative number of voids with a characteristic parameter greater than a certain value. Figure 3.16(a) presents a scheme of a cumulative number plot for parameter  $M$  (length of the major axis) for the nondeformed material ( $UD$ ). It can be seen that the line does not touch the vertical axis as the minimal detectable value of the

<sup>3</sup>Here we designate as undeformed or nondeformed material the as-received extruded material, before testing.

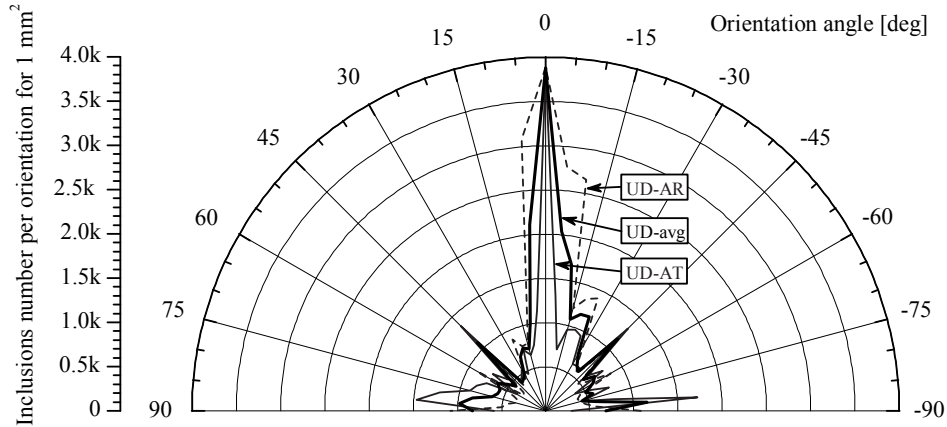
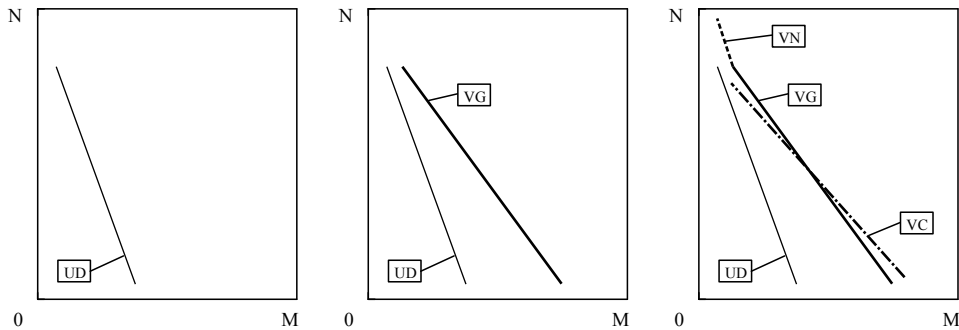


Figure 3.15: Distribution of orientations of major axes in AT and AR planes, nondeformed material, all inclusion sizes.

$M$  parameter is greater than 0 and neither does it touch the horizontal axis as the cumulative number of observed inclusions ( $N$ ) cannot be smaller than 1.



(a) Cumulative number graph for nondeformed material. (b) Cumulative number graph for void growth. (c) Cumulative number graph for void nucleation, growth and coalescence.

Figure 3.16: Interpretation of cumulative number graphs.

If we deform the material observing the same voids and the only mechanism acting on the material is void growth, the cumulative number plot will change and take the form of the void growth line  $VG$  presented in Figure 3.16(b). The total cumulative number of voids does not change as no new inclusions appear in the material.

If there are other mechanisms than void growth in the material, the  $VG$  line will take a different form. In the case of nucleation, the shape of the main part of the curve will not change and it will remain as for the case of void



growth ( $VG$ ) however, a new portion of the line will appear, presented as a dotted line ( $VN$ ) in Figure 3.16(c). If there is coalescence taking place while loading the material, it would affect the  $VG$  line which would change shape. The total cumulative number of voids would drop and depending on the size of inclusions that coalesce, the resulting plot can take different forms.

In real experiments using this technique, we cannot measure the same set of inclusions before and after the experiment, therefore for analyzing and calculating the void growth we use statistical distributions assuming that the material is homogeneous. This assumption becomes a better estimate if the number of analyzed inclusions increases.

In this analysis approach, we should be able to quantify both nucleation and coalescence of voids (Curran et al, 1987). However, the experimental evidence shows, as can be expected, that there is no nucleation in analyzed micrographs of material A1. Almost all of the observed dimples in analyzed fracture surfaces contain lead, and thus we can conclude that there is no secondary void population nucleating in components other than lead inclusions (Section 4.3.1).

Let us consider a theoretical situation, in which a population of very small lead inclusions exists in nondeformed material but which cannot be detected by our system due to its limited resolution. For these voids, if they grow enough, they could be detected in deformed samples and increase the total number of observed inclusions. Even in this case, the grown voids will not affect our size measurements as they will still be outside the representative range of data. Such small lead inclusions would need to grow from their initial size of 60 nm or less (resolution of the measurement system) to 0.98  $\mu\text{m}$  (the smallest major axis length in the representative data range), which is approximately 15 $\times$ . We know that none of the void characteristic parameters grow more than 4.5 $\times$  (see void elongation factor plots in Section 4.4.3), therefore we consider that nucleation will not be observed in our size analysis, nor will it affect it.

The coalescence we observe is concentrated for the most part on what becomes the fracture surface and below this plane in an isolated manner where there was usually high concentration of lead particles. Further details are presented in Section 4.3.3.

### Measurement of scatter

To verify measurement scatter of the cumulative number of inclusions presented in the following section as well as their accuracy, we compare the void major axis size distribution in the  $AR$  plane and measured 3 times in the same, nondeformed sample. 10 pictures were taken randomly over regions of

the sample at radial distances of 4 mm (*LOW*), 7 mm (*MID*) and 10 mm (*HIG*) from the round bar axis. Results of this analysis are presented in Figure 3.17. We observe that for large inclusions there is a non negligible scatter of the three different measurements in three regions of one sample, while for small inclusions, the results are reproducible in all three regions. This observation justifies the choice of the size range on which to focus the study.

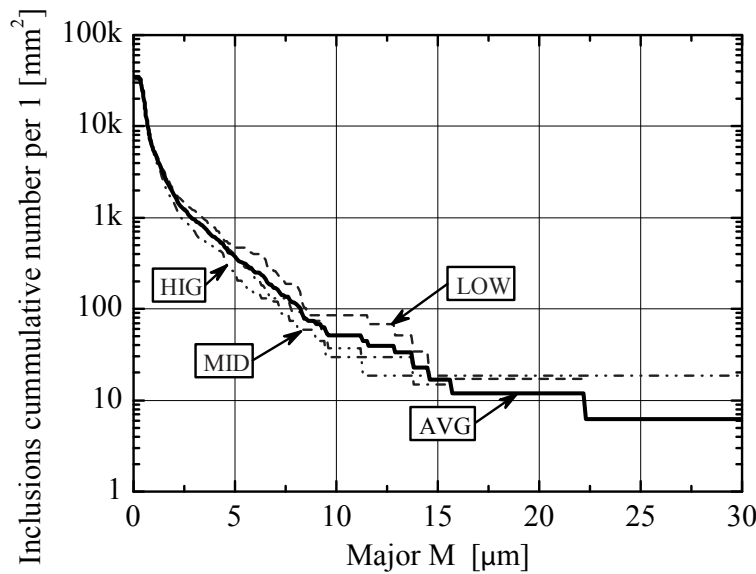


Figure 3.17: Size distribution of major axis ( $M$ ) measured in  $AR$  plane 3 times in different regions of the same nondeformed sample.

### Initial axisymmetric void

Figure 3.18 shows cumulative number plots of major and minor axes measured in  $AT$  and  $AR$  planes in nondeformed material. The solid lines represent results for the  $AT$  plane ( $M^{AT}$ ,  $m^{AT}$ ), and dotted lines represent results for the  $AR$  plane ( $M^{AR}$ ,  $m^{AR}$ ). As explained in detail earlier in Section 3.3.4, the orientation of both  $M^{AT}$  and  $M^{AR}$  major axes is the same in the global reference system. For this reason, the plots presented in Figure 3.18 are two independent measurements of the same parameter and we can therefore calculate an average distribution of  $M$  - major axis of the 3D ellipsoid. Additionally,  $M^{AT}$  and  $M^{AR}$  distributions provide an estimate of the measurement uncertainty.

The minor axes  $m^{AT}$  and  $m^{AR}$  of which we present cumulative number plots, were measured in perpendicular directions and represent different parameters. On the other hand, the cumulative plots are very similar and the

difference between them is of the order of magnitude of data scatter within one sample provided in Figure 3.17. Based on this result, we can assume that the two distributions of minor axes are similar, and that measured 3D inclusions are axisymmetric in the undeformed material. In further calculations, for the undeformed material the minor axis  $m$  distribution will be used which is calculated as the average distribution of  $m^{AT}$  and  $m^{AR}$ .

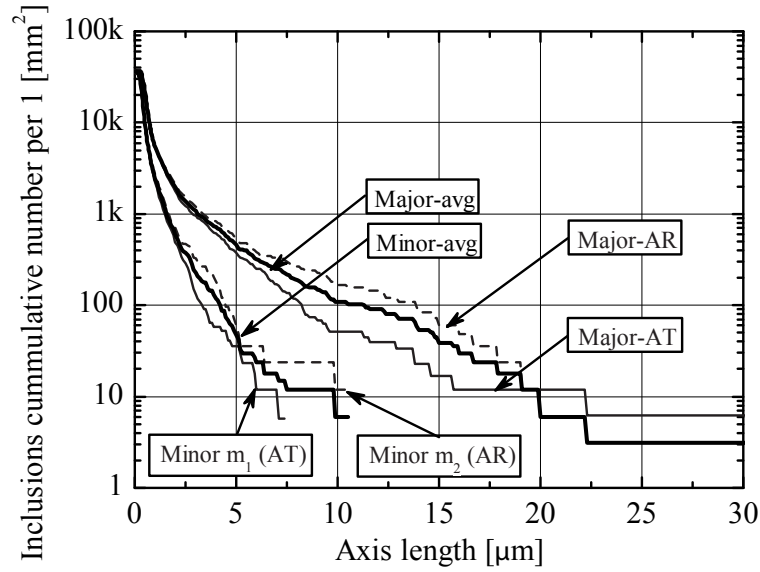


Figure 3.18: Size distribution of major ( $M$ ) and minor ( $m$ ) axis in undeformed material

### Orientation of axisymmetric void - implications

The usual orientation of the axisymmetric voids in the direction of the bar axis allows us to measure void characteristic parameters in one cut only, in tensile or notched tensile samples. If the sample is cut in any plane containing its symmetry axis (which we assume is always the case), then major and minor axes measured in this cut  $M^{cut}$  and  $m^{cut}$  are major and minor axes of the 3D ellipsoid  $M$  and  $m_1 = m_2$ :

- $M^{cut} \rightarrow M$
- $m^{cut} \rightarrow m = m_1 = m_2$

The assumption of axisymmetry of voids is not valid in material after torsional and tensile torsional loadings, and an independent measurement of two minor axes and the major axis is necessary to fully characterize voids. Figure 3.19 indicates how to perform measurements of the inclusion characteristic parameters in torsional samples.

Figure 3.19(a) and Figure 3.19(b) present nondeformed and tested samples, respectively. The ellipsoid in the middle represents the 3D shape of a void. Drawings of samples on both sides show how they were cut by  $AT$  and  $AR$  planes. The projections onto the  $AT$  and  $AR$  planes can be observed above the 3D void. Representative micrographs of polished samples are presented on both sides of the void projections.

In the undeformed sample (Figure 3.19(a)) the void is axisymmetric and thus:

- $M^{AT} = M^{AR} \rightarrow M$
- $m^{AT} = m^{AR} \rightarrow m = m_1 = m_2$

In tested samples (Figure 3.19(b)) the void is not axisymmetric and thus:

- $M^{AT} \rightarrow M$
- $m^{AT} \rightarrow m_1$
- $M^{AR} \rightarrow m_2$

The major axis of the 3D void is measured as the major axis in the  $AT$  plane. First, the minor axis is measured as the minor axis in the  $AT$  plane. Second, the minor axis is measured as the major axis in the  $AR$  plane. Note that because of void rotation, the first minor axis and the major axis cannot be measured in the  $AR$  plane. Further evidence and explanations will be provided in Chapter 4.

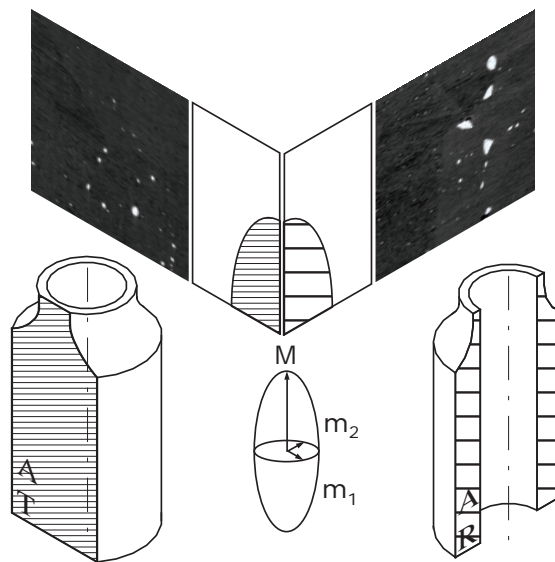
### **Void elongation calculations**

It is possible to calculate void elongation by comparing cumulative number plots for deformed samples and nondeformed material. We describe this elongation by defining the void elongation factors. In this section we will explain the calculation of void elongation factors using as example the void major axis elongation factor  $f_M$ . The elongation factors for the two minor axes,  $f_{m1}$  and  $f_{m2}$ , are calculated in a similar way.

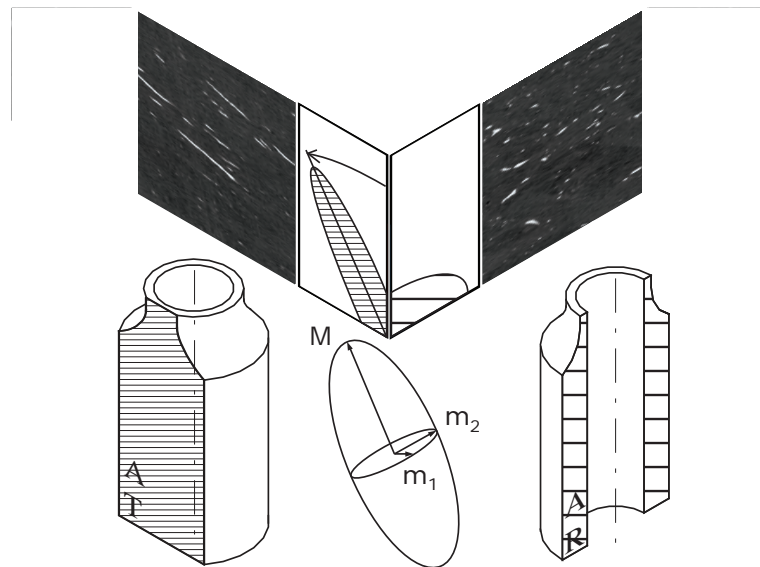
Figure 3.20(a) presents a scheme of the cumulative distribution of the length of the major axis for nondeformed ( $UD$ ) and deformed ( $DEF$ ) material. For each cumulative number  $N_i$  (or value of major axis length of nondeformed material  $M_{UDi}(N_i)$ ), we can calculate the void elongation factor  $f_{Mi}$  as:

$$f_{Mi} = f_{Mi}(M_{UDi}(N_i)) = \frac{M_{DEFi}(N_i)}{M_{UDi}(N_i)} \quad (3.1)$$

We can plot the axis length elongation factor  $f_{Mi}$  as a function of the initial axis length  $M_{UD}$ , to obtain the graph shown in Figure 3.20(b). The average

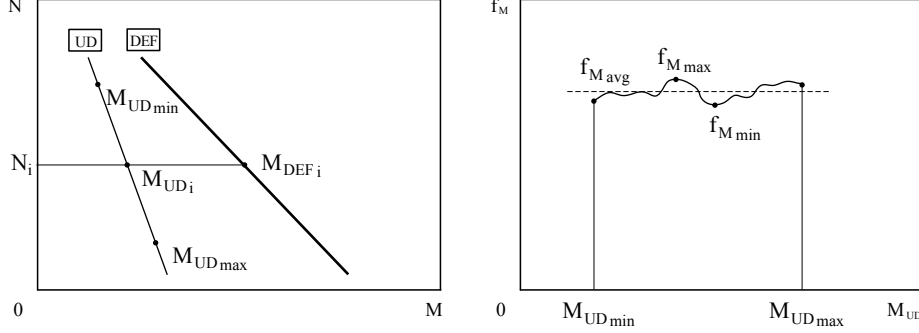


(a) Nondeformed sample.



(b) Tested sample.

Figure 3.19: Measurement of inclusion characteristic parameters  $M$ ,  $m_1$  and  $m_2$  in torsional sample.



(a) Void axis elongation factor at a point. (b) Average value of void axis elongation factor.

Figure 3.20: Calculation of void axis elongation factor.

value of the axis elongation factor used for void volume growth calculations is calculated as an average of its maximal and minimal values:

$$f_M = f_{M_{avg}} = \frac{\max(f_{Mi}) + \min(f_{Mi})}{2} \quad (3.2)$$

Points  $M_{UDmin}$  and  $M_{UDmax}$  presented in Figure 3.20(a) are defined by the lower and upper limit of the representative data set respectively as described in Section 3.3.3.

### Void aspect ratio calculations

The procedure described in the preceding section can be applied to calculate the initial aspect ratio  $W_0$  of nondeformed material. In this case, for the calculations, we use distributions of the major and first minor axis:

$$W_{0i} = W_{0i}(M_{UDi}(N_i)) = \frac{M_{UDi}(N_i)}{m_{1UDi}(N_i)} \quad (3.3)$$

The average value of the void aspect ratio is calculated as an average of its maximal and minimal values:

$$W_0 = W_{0avg} = \frac{\max(W_{0i}) + \min(W_{0i})}{2} \quad (3.4)$$

For calculating the void aspect ratio after deformation, another procedure was used. It is possible to calculate the void aspect ratio after deformation  $W_{1i}$  using the initial void aspect ratio  $W_{0i}$  and axis length elongation factors  $f_{Mi}$  and  $f_{m1i}$ :

$$W_{1i} = \frac{M_{DEFi}(N_i)}{m_{1DEFi}(N_i)} = \frac{f_{Mi}(N_i) \cdot M_{UDi}(N_i)}{f_{m1i}(N_i) \cdot m_{1UDi}(N_i)} = \frac{f_{Mi}(N_i)}{f_{m1i}(N_i)} W_{0i}(N_i) \quad (3.5)$$

The average value of the void aspect ratio after deformation  $W_1$  is calculated as before, i.e. an average of its maximal and minimal values over the representative data set:

$$W_1 = W_{1avg} = \frac{\max(W_{1i}) + \min(W_{1i})}{2} \quad (3.6)$$

Similarly, we calculate the second void aspect ratio after deformation  $W_2$ :

$$W_2 = W_{2avg} = \frac{\max(W_{2i}) + \min(W_{2i})}{2} \quad (3.7)$$

In nondeformed material, values of  $W_{20}$  are assumed to be equal to  $W_{10}$  and thus both are denoted  $W_0$ .

### Void volume fraction calculations

Void volume fraction close to the fracture surface ( $VVF_f$ ) is calculated using values of the ellipsoid axes elongation factors obtained from SEM observations (see Section 3.3.4). Micrographs of fractured samples were taken very close to the fracture surface, therefore *the results obtained refer to the void size and shape just before coalescence fracture initiation*. In interrupted samples, micrographs were taken at the places where fracture was expected to initiate (i.e. the center of the gauge cylinder). In this section, we explain the calculation of the  $VVF$  and provide necessary derivations.

The volume of an ellipsoid void with  $M$ ,  $m_1$  and  $m_2$  as major, first minor and second minor axes respectively, can be expressed in the three following forms:

$$V_V = \frac{\pi}{6} M m_1 m_2 \quad (3.8)$$

$$V_{V_0} = \frac{\pi}{6} M_0 m_{1_0} m_{2_0} \quad (3.9)$$

$$V_{V_f} = \frac{\pi}{6} M_f m_{1_f} m_{2_f} \quad (3.10)$$

where  $V_V$ ,  $V_{V_0}$  and  $V_{V_f}$  are respectively the actual, initial (undeformed material) and final (just before fracture) volumes of the same ellipsoidal void during deformation.

Volume growth of an ellipsoid due to deformation can be calculated as the difference of the final and initial volumes. Using Equations 3.8 and 3.9 we can write:

$$\Delta V_{Vi} = V_{Vi} - V_{V0i} = \frac{\pi}{6} (M_i \cdot m_{1i} \cdot m_{2i} - M_{0i} \cdot m_{10i} \cdot m_{20i}) \quad (3.11)$$

By normalizing Equation 3.11 with initial volume  $V_{V0i}$  (Equation 3.9) we obtain:

$$\frac{\Delta V_{Vi}}{V_{V0i}} = \frac{M_i \cdot m_{1i} \cdot m_{2i}}{M_{0i} \cdot m_{10i} \cdot m_{20i}} - 1 \quad (3.12)$$

Ratios of the final and initial axis lengths are the axis elongation factors defined previously in Equations 3.1 and 3.2, so Equation 3.12 can be expressed as:

$$\frac{\Delta V_{Vi}}{V_{V0i}} = f_{Mi} \cdot f_{m1i} \cdot f_{m2i} - 1 \quad (3.13)$$

By combining Equations 3.11 and 3.13 and solving  $V_{Vi}$  we obtain:

$$V_{Vi} = f_{Mi} \cdot f_{m1i} \cdot f_{m2i} \cdot V_{V0i} \quad (3.14)$$

We can define a void growth factor  $f_{Vi}$  as the product of the three axis elongation factors:

$$f_{Vi} = f_{Mi} \cdot f_{m1i} \cdot f_{m2i} \quad (3.15)$$

Equation 3.14 can thus be rewritten in the form:

$$V_{Vi} = f_{Vi} \cdot V_{V0i} \quad (3.16)$$

Using Equation 3.16, we calculate the volume of a void after deformation knowing the initial void volume and axis elongation factors. To calculate the volume of all voids in a sample we need to sum them over all observed inclusions:

$$\sum V_{Vi} = \sum f_{Vi} \cdot V_{V0i} \quad (3.17)$$

Assuming that the initial voids are all geometrically similar, and that the relative elongation of the ellipsoid axes is independent of the absolute void size, the void growth factor  $f_{Vi}$  becomes constant and can be removed from the summation and denoted  $f_V$ . This assumption will be discussed in more detail in Chapter 4. Finally we obtain:

$$V_V = f_V \cdot V_{V0} \quad (3.18)$$

We will operate on non dimensional values, thus we will calculate the void volume fraction  $VVF$ . We start from the  $VVF$  definition:

$$VVF = \frac{V_L + V_A}{V_M + V_L + V_A} = \frac{V_V}{V_M + V_V} \quad (3.19)$$

where  $V_L$  is the lead volume,  $V_A$  is the additional volume of the voids within the lead inclusions,  $V_M$  is the matrix volume.

Similarly the initial void volume fraction  $VVF_0$  can be defined as:

$$VVF_0 = \frac{V_L + V_{A0}}{V_M + V_L + V_{A0}} = \frac{V_{V0}}{V_M + V_{V0}} \quad (3.20)$$



We notice that Equations 3.19 and 3.20 differ only by the volume of additional voids in the lead inclusions which changes during deformation, while the matrix and lead volumes do not change. We solve both equations for  $V_M$ :

$$V_M = \frac{V_{V_0}}{VVF_0} - V_{V_0} \quad (3.21)$$

$$V_M = \frac{V_{V_f}}{VVF_f} - V_{V_f} \quad (3.22)$$

By comparing Equations 3.21 and 3.22, and applying Equation 3.18 we can calculate the void volume fraction after deformation,  $VVF$ :

$$VVF = \frac{f_V \cdot VVF_0}{1 + VVF_0 \cdot (f_V - 1)} \quad (3.23)$$

The above equation allows us to calculate void volume fractions of deformed material  $VVF$  using the initial void volume fraction  $VVF_0$  and volume growth factor  $f_V$ . The latter can be calculated using information obtained from SEM observations of tested samples, using Equations 3.1, 3.2 and 3.15 and the average value of the void growth factor  $f_V$ . The void volume fraction for fractured material is obtained by using the void growth factor derived for fractured material:

$$VVF_f = \frac{f_{V_f} \cdot VVF_0}{1 + VVF_0 \cdot (f_{V_f} - 1)} \quad (3.24)$$

### 3.3.5 Densitometry

Densitometry measurements using a hydrostatic weighing technique were performed on nondeformed material to estimate the initial void volume fraction taking into account voids in lead inclusions. Additional densitometry experiments were also performed on some torsional samples to validate estimates based on microstructural observations (Equations 3.23 and 3.24).

#### Experimental arrangement

A Sartorius MC 210P microbalance was used with a sensitivity of  $\pm 10 \mu\text{g}$ , and a Sartorius Gravity Determination Kit YDK 0.1 (IG Instrumenten-Gesellschaft, Zurich, Switzerland) which was slightly modified for the purpose of the experiments. (Kouzeli (2001) provides further details on the experimental set-up). Distilled water was chosen as an immersion fluid since it is one of the few liquids for which the temperature dependence of density is well known.

### Experiments

The preparation for measurement consisted of cutting the torsion samples as described in Figure 3.21. The 6 mm long slice of gauge cylinder of the nondeformed sample was used as a reference, while another slice of the same length of deformed sample was used for densitometry measurement of the damaged material. Before measurement, all specimens, tweezers and suspension wires were cleaned and degreased to avoid contamination of the liquid and to ensure good wetting. After weighing in air, the samples were pre-wetted in an ultrasonic bath of distilled water for about a minute.

The specimens were weighed 5 times in air. After taring the balance, specimens were weighed 5 times in fluid. In between weighings, the samples were held in a distilled water bath. The temperature of air and fluid was measured to an accuracy of  $0.2^{\circ}\text{C}$  to allow densities to be determined reliably.

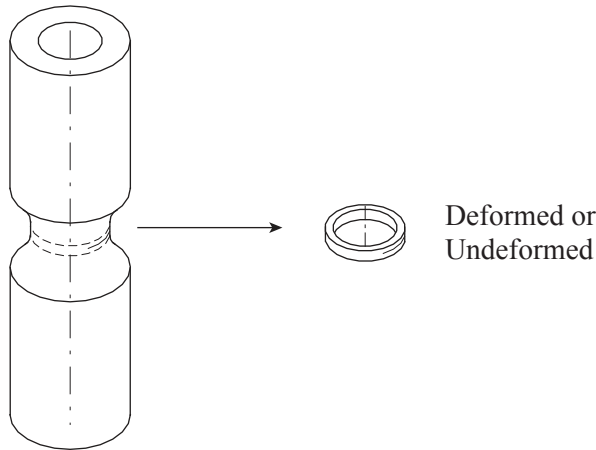


*Figure 3.21: Torsional sample sectioning for densitometry measurements.*

### Void volume fraction calculations

In the *A1* alloy there is a small void associated with each lead inclusion which originates from the difference between the coefficients of thermal expansion and solidus temperatures of the lead and matrix.

From the materials chemical composition presented in Table 3.1 we can calculate the average lead volume fraction (*LVF*), but not the volume fraction of the small voids associated with lead inclusions, called the additional volume fraction (*AVF<sub>0</sub>*). We have to combine theoretical calculations with experimental measurements to obtain this value.

We calculate the lead volume fraction and use it to calculate the density of the theoretical alloy containing no voids  $\rho_t$ . This theoretical density is then

compared to real (experimental) values for the nondeformed material  $\rho_r$ . We assume that voids are responsible for any density difference.

Lead volume fractions of the theoretically dense alloy and lead and void volume fractions of the real alloy are represented schematically in Figure 3.22. The left part of Figure 3.22 represents the theoretical alloy, while the right part represents the real alloy with additional void volumes (pores) created by the lead inclusions.

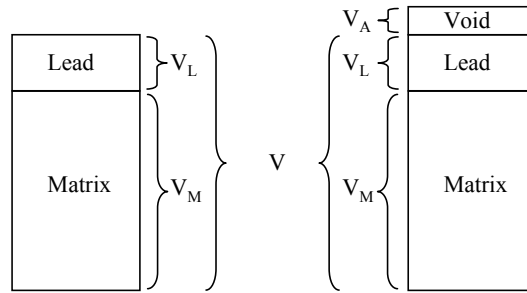


Figure 3.22: Schematic representation of the alloy components: left - theoretically fully dense alloy, right - real alloy.

Observing Figure 3.22, we note that the total volume of the theoretical alloy is the sum of the lead volume  $V_L$  and matrix volume  $V_M$ , and the total mass of the alloy is equal to sum of the masses of lead  $M_L$  and matrix  $M_M$ :

$$V_M + V_L = V \quad (3.25)$$

$$M_M + M_L = M \quad (3.26)$$

We can rewrite the above equations using matrix and lead volume fractions ( $MVF$  and  $LVF$ ), as well as matrix and lead weight fractions ( $MWF$  and  $LWF$  respectively):

$$MVF + LVF = 1 \quad (3.27)$$

$$MWF + LWF = 1 \quad (3.28)$$

Starting with the definition of density for the matrix  $\rho_M$  and for lead  $\rho_L$ :

$$\rho_M = \frac{M_M}{V_M} \quad (3.29)$$

$$\rho_L = \frac{M_L}{V_L} \quad (3.30)$$

and using proportion calculations, we can derive the following expression for  $LVF$ :

$$LVF = \frac{M_L \cdot \rho_M}{M_M \cdot \rho_L + M_L \cdot \rho_M} \quad (3.31)$$

$MWF$  and  $LWF$  are known from the chemical composition of the alloy (mean lead content of the alloy  $A1$  in Table 3.1):  $LWF = 0.0185$  and  $MWF = 1 - LWF$ . The density of lead  $\rho_L = 11.340 \text{ Mg/m}^3$  is provided in ASM (1979), and the density of the matrix  $\rho_M = 8.79 \text{ Mg/m}^3$  is a value experimentally measured for lead-free alloy  $A2$ .

Here, we assume that alloy  $A2$  has a similar chemical composition to the matrix of alloy  $A1$ . In reality the  $A1$  alloy is contains  $Ni \leq 0.4\%$ , and also the Cu-Zn composition may vary by  $\pm 1\%$  by weight between  $A1$  and  $A2$ . Composition differences are not corrected for in this analysis. The calculated value of  $LVF$  is:

$$LVF = 0.0144 \quad (3.32)$$

Observing the left side of Figure 3.22, and using Equations 3.25, 3.29 and 3.30 we can calculate the density of the theoretical alloy:

$$\rho_t = \frac{M_M + M_L}{V_M + V_L} \quad (3.33)$$

$$\rho_t = \frac{1}{\frac{LVF}{\rho_L} + \frac{1-LVF}{\rho_M}} \quad (3.34)$$

The calculated value of the theoretical density is then:

$$\rho_t = 8.837 \text{ Mg/m}^3 \quad (3.35)$$

We observe a small difference between the theoretical density value and the experimental value  $\rho_r = 8.828 \text{ Mg/m}^3$ , which we attribute to the presence of the additional void volume (porosity). Thus we use this difference to calculate the volume of the voids within the lead inclusion. Observing the right side of the Figure 3.22, we see that for the nondeformed real alloy, Equation 3.27 takes the form:

$$MVF + LVF + AVF_0 = 1 \quad (3.36)$$

Assuming that the additional, initial internal voids are empty and therefore that they have a density of 0, we can start from the definition of density to calculate the additional void volume (referred to a volume  $V = V_M + V_L$ )  $AVF_0$ :

$$\rho_r = \frac{M_L + M_M}{V_L + V_M + V_{A0}} \quad (3.37)$$

After solving for  $V_{A0}$  and dividing by the theoretical alloy volume  $V = V_M + V_L$  we obtain the voids volume relative to the theoretical volume of our alloy:

$$AVF_0 = \frac{\rho_t}{\rho_r} - 1 \quad (3.38)$$

The calculated value of the additional void volume fraction:

$$AVF_0 = 0.9561 \cdot 10^{-3} \quad (3.39)$$

Knowing all the information necessary, we can calculate the initial void volume fraction ( $VVF_0$ ). Before doing so we need to recall that we consider lead to behave as a void, thus we treat both lead inclusions and pores associated with them (additional void volume) indiscriminately as voids. From the illustration on the right side of Figure 3.22 we can write:

$$VVF_0 = \frac{V_L + V_{A0}}{V + V_{A0}} = \frac{\frac{V_L}{V} + \frac{V_{A0}}{V}}{1 + \frac{V_{A0}}{V}} \quad (3.40)$$

$$VVF_0 = \frac{LVF + AVF_0}{1 + AVF_0} \quad (3.41)$$

The resulting value of the initial void volume fraction:

$$VVF_0 = 0.0154 \quad (3.42)$$

To conclude, the initial additional void volume constitutes 7% of the lead volume and notably increases the initial void volume fraction ( $VVF_0$ ) of the lead alloy.

### 3.3.6 EBSD and texture measurement

We performed scanning electron backscattered diffraction measurements (EBSD) on several samples to measure texture evolution upon deformation and to visualize it using pole figure plots. For each sample, three squares of  $375 \times 375 \mu\text{m}$  were scanned with a resolution of  $2 \mu\text{m}$ . Samples were electro-polished using Struers Electrolyte D2 (15 V, 10 sec.) prior to the EBSD scanning.

### 3.3.7 X-ray computed tomography

Computed tomography was used to generate a three-dimensional image of the inside of the *A1* alloy. Samples of  $0.7 \times 0.7$  mm in section were cut from the center of the gauge cylinders of macroscopic samples; nondeformed and the deformed *PT* sample. Scanning was performed using an approximate resolution of  $1.22 \mu\text{m}$  per pixel, so that every inclusion smaller than  $1.22 \mu\text{m}$  is either observed as one voxel (volumetric picture element) or not observable. Slices close to the surface (fracture surface in the case of the *PT* sample), were not analyzed due to poor sampling in the measurement. The total analyzed volume was  $0.587 \text{ mm}^3$  in nondeformed and  $0.635 \text{ mm}^3$  in tested samples. Size distribution results, performed using the VG Studio Max software were normalized to a volume of  $1 \text{ mm}^3$ . The threshold for selecting inclusions was chosen manually. Samples were scanned by Mr. Iwan Jerjen and part of the analysis was performed by Mr. Philipp Schuetz from EMPA, Electronics/Metrology unit, in Dübendorf, Switzerland.

## 3.4 Numerical simulations

We performed numerical simulations to analyze the experimental results in greater detail. We reproduced tensile and torsion experiments to calibrate and validate the plasticity models we used. The stress and strain states in samples obtained from these calculations served to create appropriate boundary conditions for 3D single cell models. In this section we describe constitutive behavior, model geometries and boundary conditions used for the simulations.

### 3.4.1 Constitutive behavior

#### Tensile constitutive behavior

The true stress-strain relationship for the materials was obtained from the averaged ST test results (see Section 3.3.1), and calculated directly from the force and elongation data. Figure 3.23 shows the true stress-true strain curve obtained for the two materials up to the onset of necking.

The area of the stress-strain curve after yielding ( $\varepsilon_{eq}^{pl} \geq 0.005$ ), was used to extrapolate the constitutive behavior to high strains. The extrapolated constitutive law obeys the Ludwik-type (Ludwik, 1909) power equation - Equation 3.43:

$$\sigma = \sigma_0 + k\varepsilon^n \tag{3.43}$$

Obtained power fit parameters are presented in Table 3.6. The extrapolation was validated against the smooth round tensile experimental data and a good agreement was found. (Compare the *A2* line in Figure 3.8(a) and the  $J_2$  line

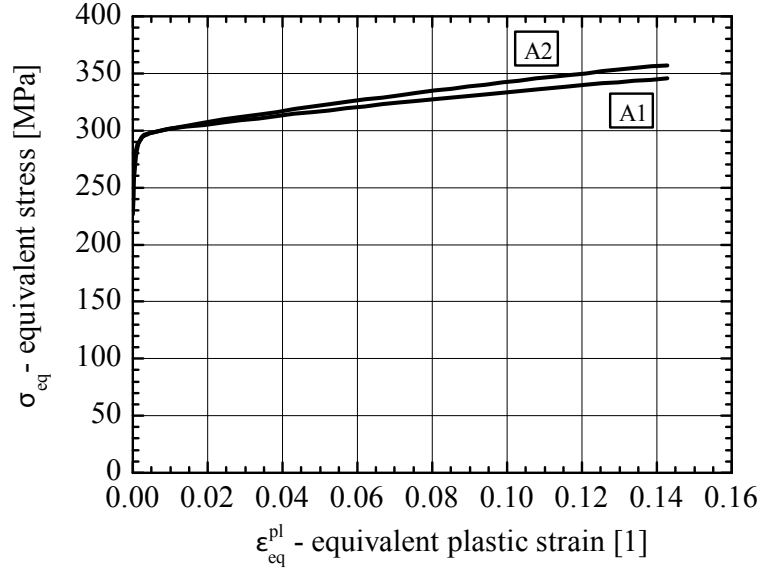


Figure 3.23: A1 and A2 constitutive law.

in Figure 3.8(b)), or the A2 and  $J_2$  lines in Figure 4.11.

The two alloys exhibit very similar yielding behaviors but the hardening behavior is different, most probably due to non-zero initial void volume fractions in the case of the lead-containing alloy, as discussed earlier. As the chemical composition of the two alloys is very similar this should not affect the hardening rate. The elastic properties were found to be the same for both of alloys:  $E = 106$  GPa - obtained in smooth round tensile tests,  $\nu = 0.3$  - provided by ASM (1979). In our continuum calculations, we will always use the A2 constitutive data for defining the matrix and global behaviors of both materials. A1 constitutive data incorporates void evolution and would change with loading conditions. The A2 void volume fraction is very small compared to A1 and before the onset of necking (when accelerated growth of voids is known to occur), it can be considered as void free. The use of the A2 constitutive law will allow us to calculate stress triaxialities and strains in samples without damage. In the case of single cell calculations, the A2 constitutive behavior will serve to represent the behavior of the matrix material.

Table 3.6: Ludwik-type power law fit parameters for alloys A1 and A2.

	$\sigma_0$	$k$	$n$
A1	294.44	241.94	0.791
A2	293.52	300.24	0.789

### Lead constitutive behavior

Mechanical properties of the technical lead provided by ASM (1979), were used to define lead constitutive behavior for single cell numerical calculations:  $E = 14$  GPa,  $\nu = 0.3$ . Piecewise, linear plastic constitutive behavior was defined as presented in Table 3.7:

*Table 3.7: Lead plastic behavior.*

Equivalent plastic strain $\varepsilon_{eq}^{pl}$	Equivalent stress $\sigma_{eq}$
0	8
0.9	27

### 3.4.2 Continuum calculations

Code calculations of the smooth round tensile bar (*ST*), notched round tensile bars (*NTx*), and thin-walled tubular specimens with different levels of axial load (*TTx*) were conducted for axisymmetric boundary conditions. The calculations were performed using the ABAQUS commercial code, and models were meshed with *CGAX8* elements, a 8-node biquadratic axisymmetric quadrilateral with full integration and twist.

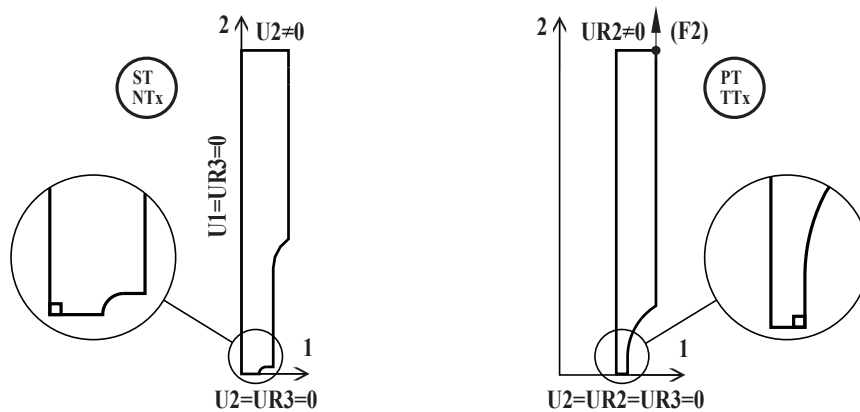


*Figure 3.24: Sample axisymmetric models with boundary conditions applied:  $U$  - displacements;  $UR$  - rotations,  $F$  - force.*

Figure 3.24 presents two models for continuum calculations with boundary conditions applied. The model on the left shows the *NT3* sample, while the model on the right, the torsional sample (*TTx*). Samples were modeled using both axial and planar symmetry. A small geometric perturbation was introduced in the *ST* and *TTx* models to control the location of necking. Other tensile and torsional samples were modeled and had similar boundary conditions to the presented samples.



In each calculation, the deformation of the sample was displacement controlled to reproduce the experimental conditions. Deformation in tensile samples was controlled by imposing the displacement  $U_2$  of the upper edge in direction 2. In torsional samples, deformation was controlled by the upper edge rotation about axis 2. For *TT1* and *TT2* samples an axial force was applied on the upper edge in direction 2.

The stress triaxiality and strain history were recorded in different elements of the tensile and notched tensile sample as presented in Figure 3.24. In the case of the tensile and notched tensile samples, it was the element at the center of the sample, which is the element with the highest stress triaxiality. In the torsional and tensile torsional samples, it was the element on the symmetry plane at the outer cylindrical face, which is the element with the highest equivalent strain.

### 3.4.3 Single cell calculations

3D single cell simulations were performed to analyze void growth under different loading conditions, modeling the conditions in different samples. Several geometries were used to adequately reproduce tensile and torsional experimental loading conditions.

The initial dimensions of the void are the same in each configuration and were calculated to maintain the volume fraction of the lead-void system in the real material ( $VVF_0 = 1.54\%$ ) and the experimental initial mean aspect ratio ( $W_0 = 1.71$ ). Figure 3.25 and 3.26 present geometries of the single cell for tensile and torsion loading respectively. The single cell geometry for torsion loading was created by mirroring single cells for tensile loading, although they differ with respect to boundary conditions. Assuming a cubic shape of the single cell and edge length equal to 2, the major and minor radii are as follows:

- $M_0/2 = 0.442$
- $m_0/2 = 0.258$

The calculations were performed using the ABAQUS commercial code and models were meshed with *C3D8* elements, a 8-node linear brick, with full integration and hourglass control.

#### 3D single cell for tensile loading

Figure 3.25 shows the shape of and boundary conditions applied to the 1/8 3D single cell for tensile dominated loading. The visible faces are marked with full circles while the invisible faces are marked with empty circles.

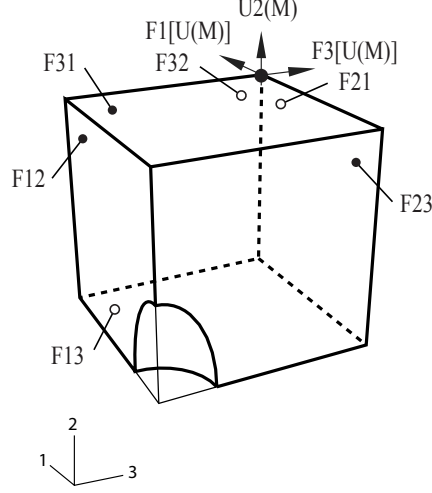


Figure 3.25: 3D single cell for tensile dominated loadings.

Symmetrical boundary conditions were applied to the internal faces  $F23$ ,  $F12$  and  $F13$  as listed below:

- $F12 \longrightarrow U_3^{F12} = 0$
- $F13 \longrightarrow U_2^{F13} = 0$
- $F23 \longrightarrow U_1^{F23} = 0$

The external faces  $F21$ ,  $F31$  and  $F32$  were constrained to follow the displacements of the master node  $M$  (a reference node shared by the three faces), and to remain parallel to the corresponding opposite faces  $F12$ ,  $F12$  and  $F23$ , by imposing the following equations:

- $F21 \longrightarrow U_3^{F21} - U_3^M = 0$
- $F31 \longrightarrow U_2^{F31} - U_2^M = 0$
- $F32 \longrightarrow U_1^{F32} - U_1^M = 0$

Deformation of the single cell was controlled by the displacement of the master node  $M$  at the corner of the single cell in direction 2. Displacement and rate of displacement of the master node,  $M$ , correspond roughly to the displacement and rate of displacement of two upper nodes of the element at the center of tensile and notched tensile samples described in Section 3.4.2. Constant triaxiality was maintained during simulation by applying appropriate force, using an user-defined element (UEL), providing an active control mechanism on the displacements of the master node in order to maintain constancy of stress triaxiality at each increment. Average stress triaxiality for each loading condition and stretch of the single cell in 2-directions was known from the  $J_2$  continuum calculations of the whole macroscopic sample. The same

level of force was applied in directions 1 and 3. The UEL was programmed by Andreas Rossoll (EPFL/STI/IMX/LMM) on the basis of a derivation by Eberle and Klingbeil (1996).

### 3D single cell for torsional loading

Figure 3.26 presents the shape and boundary conditions applied to the 1/4 3D single cell for shear dominated loading. The single cell was designed to account for non uniform void growth observed in experiments in directions 1 and 3. The visible faces are marked with full circles while the invisible faces are marked with empty circles.

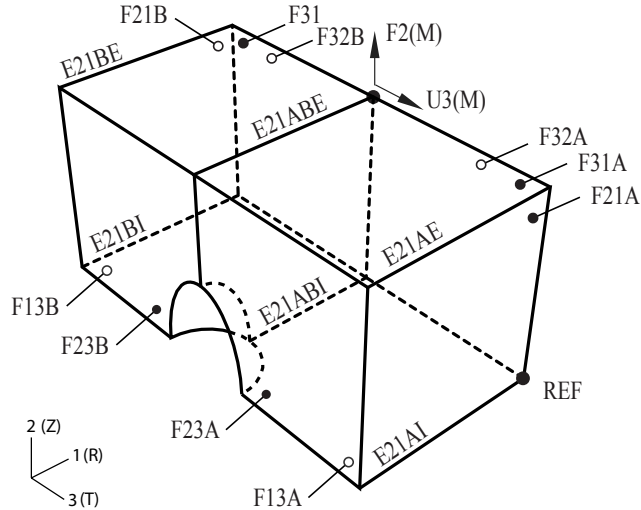


Figure 3.26: 3D single cell for shear dominated loadings.

Deformation of the single cell was controlled by the displacement of the master node  $M$  in direction 3. Displacement and rate of displacement of the master node  $M$  correspond roughly to displacement (at the perimeter) and rate of displacement of two upper nodes of the element at the outer cylindrical surface of the torsion model described in Section 3.4.2. The correct level of the stress triaxiality was achieved by applying a constant load to the master node in direction 2. The load was calculated to produce a mesoscopic stress  $\sum_2$  corresponding to the stress  $\sigma_2$  in real tensile-torsion samples (see Section 3.2.5 for definition of mesoscopic stress).

Symmetrical boundary conditions were applied to the internal faces  $F23A$  and  $F23B$ :

- $U_1^{F23A} = 0$
- $U_1^{F23B} = 0$

The external faces  $F32A$  and  $F32B$  were constrained to follow the displacements of the master node  $M$  in direction 1, and to remain parallel to the corresponding opposite faces,  $F23A$  and  $F23B$  by imposing the following equations:

- $U_1^{F32A} - U_1^M = 0$
- $U_1^{F32B} - U_1^M = 0$

Fully periodic boundary conditions were achieved by imposing the following equations on the edges and faces:

### Edges

*Top middle edge - E12ABE:*

- $U_2^{E12ABE} - U_2^M = 0$
- $U_3^{E12ABE} - U_3^M = 0$

*Top right edge - E21AE:*

- $U_2^{E21AE} - U_2^M = 0$
- $U_3^{E21AE} - U_3^{REF} - U_3^M = 0$

*Top left edge - E21BE:*

- $U_2^{E21BE} - U_2^M = 0$
- $U_3^{E21BE} + U_3^{REF} - U_3^M = 0$

*Top left and right edges - E21AE and E21BE:*

- $U_1^{E21AE} - U_1^{E21BE} = 0$

*Bottom middle edge - E12ABI:*

- $U_2^{E12ABI} = 0$
- $U_3^{E12ABI} = 0$

*Bottom right edge - E21AI:*

- $U_2^{E21AI} = 0$
- $U_3^{E21AI} + U_3^{REF} = 0$

*Bottom left edge - E21BI:*

- $U_2^{E21BI} = 0$
- $U_3^{E21BI} - U_3^{REF} = 0$

*Bottom left and right edges - E21AI and E21BI:*

- $U_1^{E21AI} - U_1^{E21BI} = 0$

### Surfaces

*Top surfaces - F31A and F31B:*

- $U_1^{F31A} - U_1^{F31B} = 0$
- $U_2^{F31A} + U_2^{F31B} - 2 \cdot U_2^M = 0$
- $U_3^{F31A} + U_3^{F31B} - 2 \cdot U_3^M = 0$

*Bottom surfaces - F13A and F13B:*

- $U_1^{F13A} - U_1^{F13B} = 0$
- $U_2^{F13A} + U_2^{F13B} = 0$
- $U_3^{F13A} + U_3^{F13B} = 0$

*Left and right surfaces - F21A and F21B:*

- $U_1^{F21A} - U_1^{F21B} = 0$
- $U_2^{F21A} - U_2^{F21B} = 0$
- $U_3^{F21A} - U_3^{F21B} - 2 \cdot U_3^{REF} = 0$

### 3D single cell containing lead inclusion for torsional loading

Figure 3.27 presents the shape of the 1/2 3D single cell for shear dominated loading. It was created by mirroring the 1/4 single cell described in detail in previous section in plane 1 – 3. The size of the single cell and the void is the same as previously. The size of the lead inclusion was calculated to maintain nominal lead content in the alloy  $LVF = 1.44\%$ . The final dimensions of the lead inclusion are as follows:

- $M_0^L/2 = 0.411$
- $m_0^L/2 = 0.240$

The lead inclusion was placed in the middle of the void so that the additional void volume observed in the lead inclusions is distributed between the wall of the void and the lead inclusion. Frictionless contact was established between the void and the lead inclusions.

Boundary conditions were imposed on the single cell using the same equations as in the case of a 1/4 single cell for shear dominated loadings presented above. Equations describing boundary conditions of the bottom part of the single cell were updated to account for antisymmetry of the deformation. Faces  $F31A$ ,  $F31B$ ,  $F21A$ ,  $F21B$  presented in Figure 3.26 were not constrained.

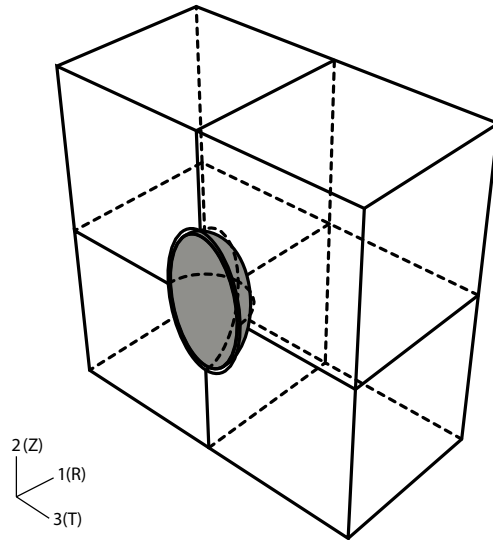


Figure 3.27: 3D single cell containing lead inclusions for shear dominated loadings.

### 3D periodic macroscopic sample with a finite void

Figure 3.28 shows a 3D periodic macroscopic model with a finite void. This model was used to decide which boundary conditions imposed on the 3D single cell for torsional loadings reproduces best the behavior of the macroscopic sample and takes into account the development of the porosity. Due to the periodicity of the sample, only a circular section of the cylindrical sample can be modeled. The image on the left indicates the shape of the periodic model, while the image on the right presents a magnified view of its bottom part containing a void.

Dimensions of the model correspond to dimensions of the real sample. Dimensions of the finite void were selected so that the  $VVF$  of the bottom fragment of the model shown in Figure 3.28 corresponds roughly to the experimental  $VVF$  of the A1 alloy (1.54%). The bottom fragment is 1 mm high, and 12 deg wide. Dimensions of the void are as follows:

- $M_0/2 = 0.442$  mm
- $m_0/2 = 0.258$  mm

Boundary conditions and relations imposed on nodes to introduce periodicity, were defined in a cylindrical coordinate system. Twisting of the sample was controlled by rotation of nodes at the  $STO$  surface around the axis of the sample - direction  $Z$ .

Periodicity over the circumference was achieved by correlating displacements of matching nodes of the  $STL$  and the  $STR$  surfaces using the Abaqus multi point constraint option (MPC). MPC, type CYCLSYM imposes the

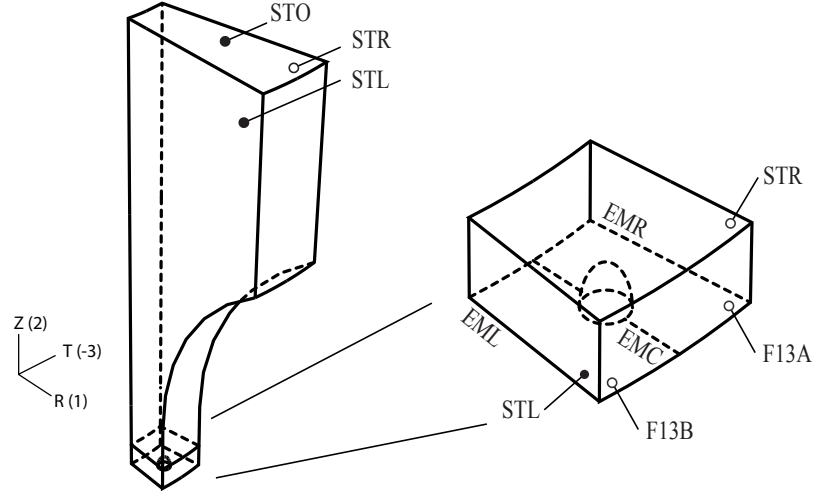


Figure 3.28: 3D periodic macroscopic model with a finite void.

cyclic symmetry by equating radial, circumferential, and axial displacement components (and rotations, if active) at two nodes.

Periodicity in an axial direction was achieved by correlating displacements of the matching nodes of the  $F13A$  and  $F13B$  surfaces. Appropriate equations provided previously in Section 3.4.3 for Cartesian coordinate systems, take the following form in the cylindrical coordinate system:

- $U_R^{F13A} - U_R^{F13B} = 0$
- $U_T^{F13A} + U_T^{F13B} = 0$
- $U_Z^{F13A} + U_Z^{F13B} = 0$

Displacements  $U_T$  and  $U_Z$  were set to 0 at edges  $EML$ ,  $EMC$  and  $EMR$ .

### 3.4.4 Crystal plasticity

Plastic anisotropy was observed in experimental results. It is modeled by means of an advanced crystal plasticity code, termed UMAT. The UMAT model developed was used to account for texture induced anisotropy. It is a statistical (or Monte Carlo) model which takes into consideration deformation interactions between neighboring crystalline grains, and is fast enough for implementation in every Gauss point of a FE simulation. The model simulates only dislocation mechanisms of plasticity (Taylor plasticity) and the version we used does not take into account twinning effects. The model was used by courtesy of Professor Laurent Delannay from Université Catholique de Louvain (UCL) - Department of Mechanical Engineering (CESAME-MEMA). Details

of the model can be found in Dancette et al (2010) (Taylor, no twin model) or in Van-Houtte et al (2005).

The crystal plasticity model was calibrated using *A2 ST* experimental data. The texture evolution was obtained by EBSD (see Section 3.3.6).

The crystal plasticity model incorporates the strain rate dependence. This behavior was not characterized in experiments using our materials and for the tested ranges of strain rates. We decided to perform the UMAT calculations for all samples at strain rates of the same order of magnitude. Both material models,  $J_2$  and UMAT, were calibrated using the *ST* experimental data. The *ST* computations were performed at experimental grip displacement rates. In the case of all other simulations, the grip displacement rates were decreased 10 times (see Table 3.5 for the experimental loading rates).



# Chapter 4

## Results

### 4.1 General outline of the results

Chapter 4 presents results of the fracture experiments, microscopic observations of the microstructure of tested samples and several numerical simulations performed to explain the observed phenomena. It is composed of four main sections:

Section 4.2 - Global behavior, which compares the behavior of the *A1* and *A2* alloys in terms of the global sample response. We present force-displacement or torque-twist angle plots for all tested sample shapes and loading cases in order to observe the influence of the pre-existing voids on strains to fracture. In the case of the *PT* samples, we characterize the evolution of texture and the resulting Swift effect. At the end of this section, we present axisymmetric simulations of the global sample behavior using von Mises plasticity ( $J_2$ ) and a crystal plasticity model. Numerically calculated dimensions of the *PT* sample (external and internal wall diameter thickness), are compared to the values measured in tested samples.

Section 4.3 - Fracture behavior, which qualitatively describes the subsequent stages of ductile fracture (nucleation, growth and coalescence of voids) in both brass alloys. We identify pre-existing voids in order to prove that the nucleation stage does not exist in tensile dominated loadings. We track void evolution in *PT* samples to observe reorientation of voids and changes of void axis lengths under torsion dominated loadings. Finally, we present interrupted notched tensile tests to correlate the onset of coalescence with macroscopic behavior of samples, and to evaluate fracture mechanisms. At the end of the section, a complete set of micrographs of fracture surfaces as well as cross sections for all tested materials, sample shapes and loading conditions is provided.

Section 4.4 - Void size analysis, which quantitatively characterizes void evolution and growth in the *A1* alloy. First, the orientation of voids in non-deformed material and tested samples is explained, together with implications

for our measurements and calculations of void growth. We present cumulative size distributions of the characteristic void shape parameters (lengths of the major and two minor axes). Cumulative size distributions are transformed into void elongation plots, demonstrating how the axis lengths evolve with respect to their initial length. Averaged void elongation parameters over representative data ranges, allows us to characterize porosity in the non-deformed material and in test samples in terms of representative 3D ellipsoids, and to calculate void volume fractions ( $VVF$ ) from microscopic observation of inclusions. Densitometry measurements and computer tomography scanings are performed to confirm the observed  $VVF$  growth under  $PT$  loading conditions.

Section 4.5 - Void size computations, which describe the results of the numerical investigation of void growth. The principal goal of this investigation is to find explanations for the observed void growth under  $PT$  loading conditions. 3D single cell simulations using voided models and models containing a lead inclusion are performed using both the  $J_2$  plasticity and the constitutive crystal plasticity behavior of the matrix material. We also perform 3D macroscopic simulations of torsion tests to define the correct boundary conditions for single cells.

Key observations of Chapter 4 are summarized in Section 4.6.

## 4.2 Global behavior

The macroscopic behavior of the *A1* and *A2* alloys is described in this section. We present experimental results for all test configurations to verify the influence of pre-existing voids on the strain to fracture. We measure the evolution of texture anisotropy and investigate its influence on sample response by performing macroscopic sample simulations, using both the  $J_2$  plasticity and crystal plasticity models (UMAT).

### 4.2.1 Sample response

#### Smooth round tensile test

Figure 4.1 shows smooth round tensile test results for the *A1* and *A2* model materials, in terms of axial load versus axial displacement.

The two alloys exhibit very similar yield loads, even if the initial void volume fraction ( $VVF$ ) is different, due to lead inclusions considered as voids in the *A1* alloy. The  $VVF$  in the *A1* alloy is approximately 1.54%, while the volume fraction of inclusions in the *A2* alloy is close to 0%.

As the deformation progresses, we observe relatively small differences in strain hardening of the two alloys. This difference could result from the initial void volume fraction in the *A1* brass, but it may also result from small differences in the chemical composition of the two matrices (see Section 3.2.5) and from the difference in grain size.

Both alloys exhibit a significant stage of stable geometric and void softening, which is much more pronounced in the *A2* alloy. In the lead-free alloy, there is a very small (compared to *A1*) initial volume of unbonded small hard inclusions. The small volume fraction of inclusions in the *A2* alloy accounts for the higher strain to fracture initiation.

In both alloys at the end of the stable softening stage, we observe a rapid loss of load carrying capacity. After this point the *A1* alloy becomes unstable (fast load drop not measurable with "static" instrumentation), while the *A2* alloy has a change in the rate of softening but deformation is still stable and measurable. The onset of the rapid loss of load carrying capacity is related to void coalescence and formation of a crack in the middle of the sample (see Section 4.3). In *A1*, lead tends to appear at grain boundaries and thus once coalescence has started, it progresses rapidly following big voids at grain boundaries. *A2* also exhibits grain boundary fracture, but voids nucleated at small and hard inclusions need to have grown more to start coalescing and allow crack propagation.

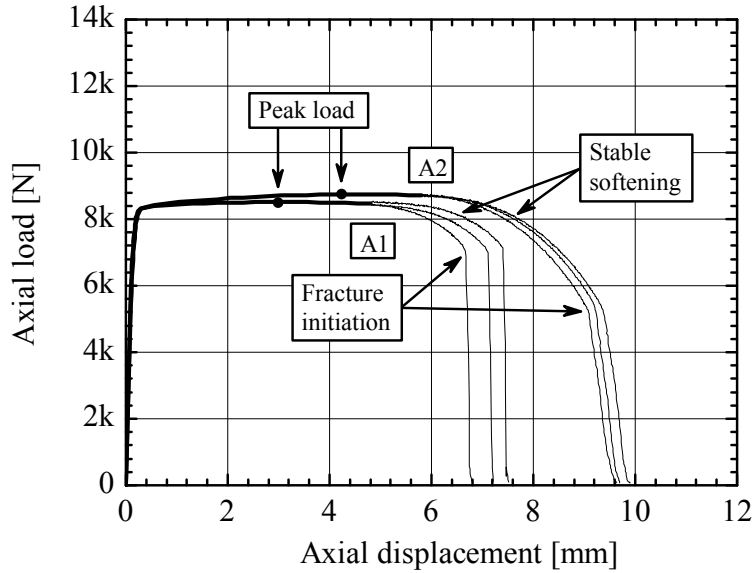


Figure 4.1: A1 and A2 smooth round tensile (ST) tests results.

### Notched round tensile test

Figures 4.2 and 4.3 present results of notched round tensile tests, for A1 and A2 alloys respectively. Scales of the axes are set to facilitate the comparison of the two plots, and thus Figure 4.3 shows only a part of the *NT1* plot. The *NT1* plot for the whole range of grips travel will be presented and discussed in detail in Section 4.3.3.

Comparing the two figures, we note the very large influence of the presence of initial voids on the deformation to fracture. The onset of coalescence occurs much earlier in the loading history in the lead-containing A1 alloy than in the lead-free A2 alloy and the loss of load carrying capacity is also clearly more pronounced. Notched A1 samples are capable of undergoing much less deformation compared to A2. The notch does not appreciably change the stiffness of the sample and the elastic response of all samples is about the same.

### Thin-walled tubular torsion test

The very large effect of pre-existing voids on the behavior of the materials presented in the previous section for notched round tensile bars, is also extremely clear in torsional and tensile-torsional experiments. Figure 4.4 and 4.5 present results for the A1 and A2 alloys respectively. The procedure used to create these Figures is described in Section 3.3.1, Data Reduction Method.

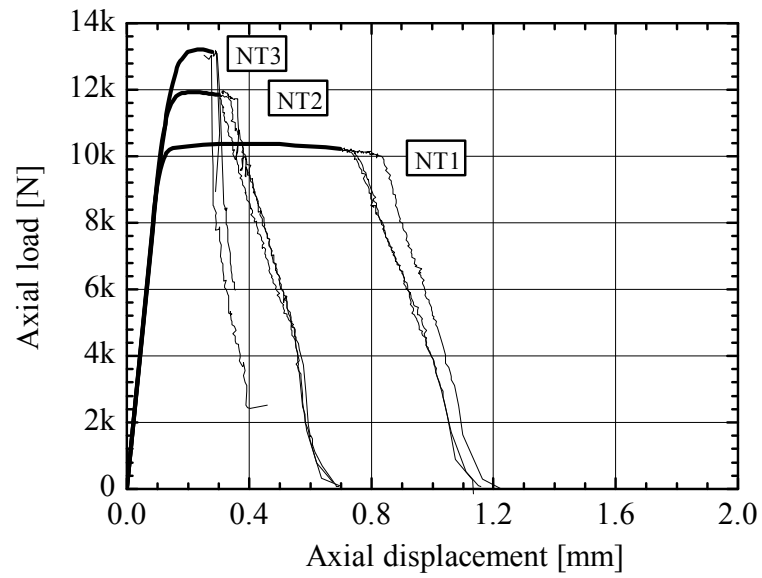


Figure 4.2: A1 notched round tensile test ( $NTx$ ) results.

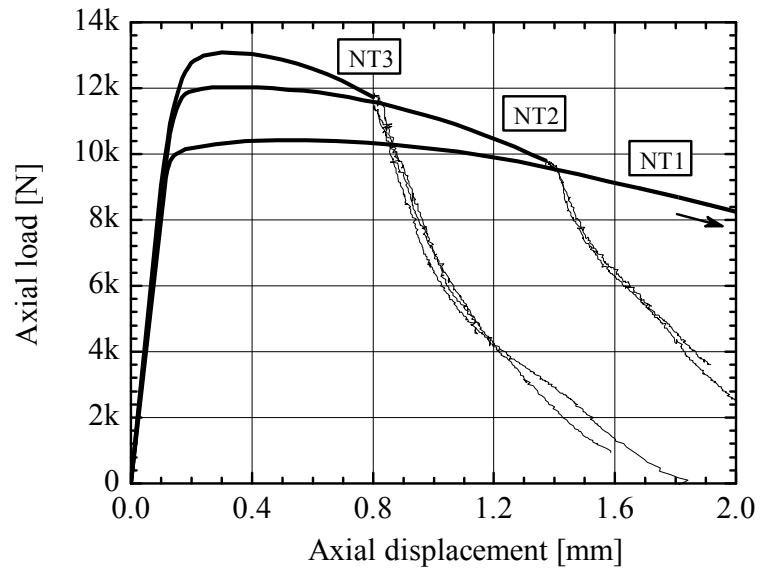


Figure 4.3: A2 notched round tensile ( $NTx$ ) test results.

We observe that the sample twist angle (or rotation of the grips) to fracture is lower in the lead-containing alloy and the difference between the two alloys decreases as the axial load increases. For *PT* loading, the twist angle to fracture is three times higher for the *A2* alloy than the *A1*, while for *TT2* it is only 1/3 higher.

In the *PT* experiments we observe significant elongation in the axial direction. The elongation of twisted samples under zero axial load is called the Swift effect and it is claimed to originate in anisotropy associated with developing deformation texture.

## 4.2.2 Texture evolution

### Elongation of PT samples

Figure 4.6 presents *PT* results for the *A1* and *A2* alloys in a single plot. The scale of the axial elongation axis was adapted to facilitate the comparison of the elongation results for the two materials.

We observe that the rate of elongation of the samples depends on the twist angle and is not linear. For example, in the *A2* alloy we observe that at a twist angle of 90 deg, there is a visible change in the elongation rate, and at this same twist angle, the strain hardening becomes roughly linear. This correlation suggests that the elongation of the sample has a microstructural origin and is not an effect of sample geometry. A similar change in elongation rate appears in the *A1* alloy at 50-60 deg but is not as pronounced.

The changes in strain hardening and rate of elongation of the *PT* samples can be correlated with other effects observed in the *A1* and *A2* brasses. Figure 4.7 presents the torque increase rate versus the sample twist angle plot (corresponding roughly to strain hardening rate versus strain plots used in the literature). The rate of strain hardening for brass exhibits a plateau at intermediate strain levels. Microscopic observations by Asgari et al (1997) show that the plateau in the strain hardening rate can be correlated with the onset of twinning, and it is the twin-twin and twin-slip hardening interactions which prevent the decrease in the strain hardening rate in brass at these intermediate strain levels. In view of these observations, we suggest that the changes in strain hardening and elongation rate are correlated with twinning. This will be discussed in Chapter 5.2.2.

### Initial texture and texture evolution

Both materials, *A1* and *A2*, exhibit texture anisotropy. The initial anisotropy results from the manufacturing of the bar. We investigated it in detail using as example the *A2* alloy to avoid additional anisotropy and other effects resulting

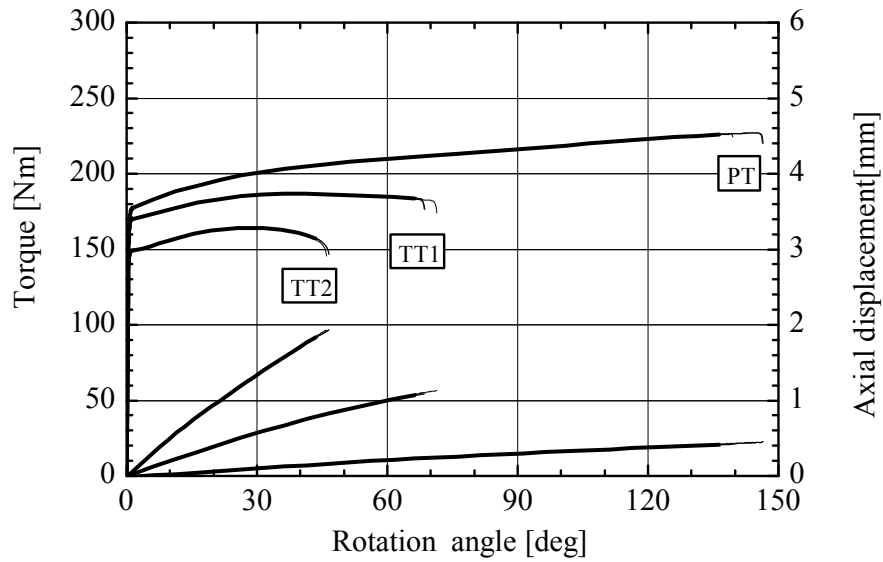


Figure 4.4: A1 pure torsional (PT) and tensile-torsional (TTx) test results.

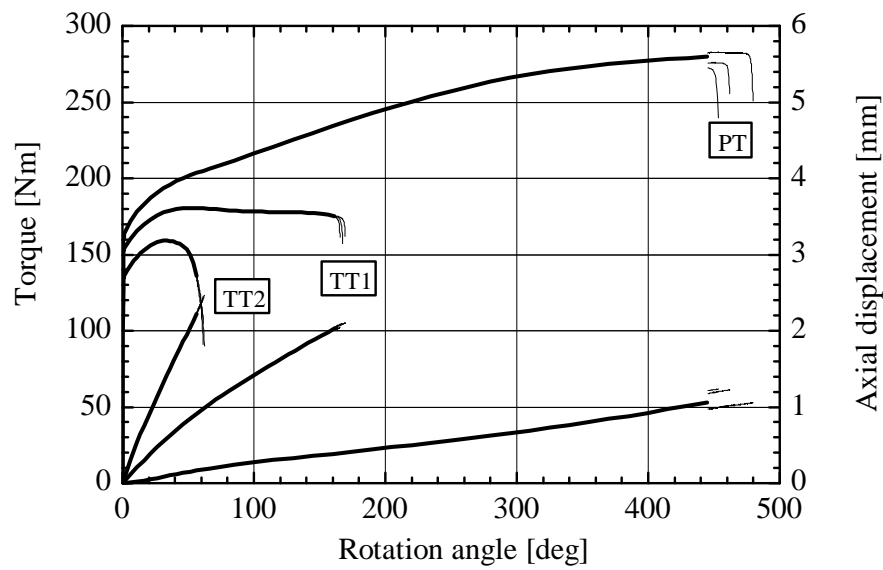


Figure 4.5: A2 pure torsional (PT) and tensile-torsional (TTx) test results.

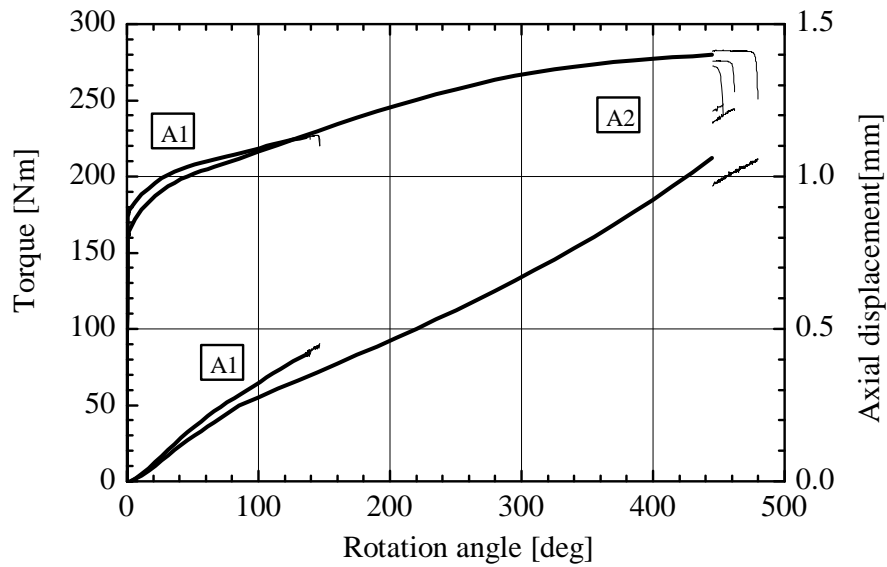


Figure 4.6: Comparison of A1 and A2 pure torsional (PT) test results.

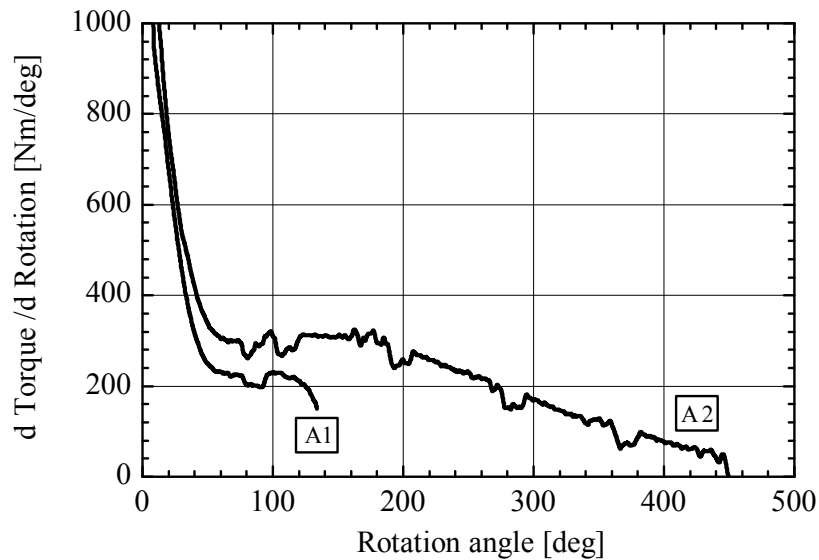


Figure 4.7: Rate of torque increase vs sample rotation angle in the PT sample. Data were filtered to remove "noise", due to short range fluctuations.



from void growth that might arise using the A1 alloy.

Figure 4.8 presents equivalent stress - equivalent plastic strain plots in a representative range for the A2 material calculated from *ST* and *PT* tests. The constitutive laws calculated directly from experiments are plotted with solid lines, while the dotted line represents the Ludwik power law extrapolation of the *ST* constitutive law. The details of the calculation and extrapolation of the constitutive laws are provided in Section 3.4.1.

Different stresses at the initial yield under different loadings may be attributed to the initial anisotropy which affects yielding differently in tension and in shear. Different strain hardening rates may be explained by the effect of texture, evolving dissimilarly under different loading modes. At an equivalent strain of approximately 0.6, the strain hardening becomes roughly linear for the *PT*.

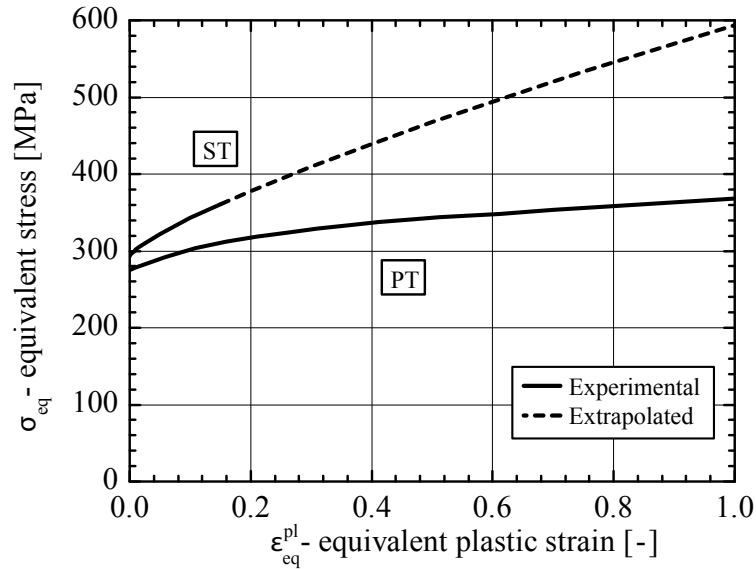


Figure 4.8: A2 constitutive law obtained from *ST* and *PT* tests.

### Texture measurements

Several samples were EBSD scanned to measure texture evolution upon deformation. Figures 4.9 and 4.10 present contour pole figures for the A2 material. These plots show the strength of the clustering of poles relative to that obtained from a random distribution, i.e. in terms of multiples of uniform density (MUD). This means that the pole figure of a random standard sample

would be '×1' at all points. Pole figure regions with intensities higher than '×1' indicate that more lattice planes are aligned in those directions than in a sample with random texture and vice versa. In the presented figures, directions  $Y0$  and  $X0$  correspond to the axial and radial direction of the sample, respectively.

Figures 4.9(b) and 4.10(b) present pole figures for the undeformed material (the figure is replotted to facilitate comparison with pole figure plots for the deformed material in different loading modes). Initial texture is present. As plastic deformation increases, the nonuniform distribution of iso-density lines intensifies and their relative distance becomes closer. This means that the material becomes more textured as plastic deformation progresses. This effect is observed in both tensile (Figure 4.9) and pure torsional loading (Figure 4.10). Approximate values of the  $\varepsilon_{eq}^{pl}$  were obtained from the  $J_2$  plasticity calculations.

We also observe that the isolines for samples tested in tension and torsion concentrate in different regions of pole figures. Based on this we consider that texture is different in tensile or shear dominated loadings. Quantitative analysis of the texture would require considerable work and is outside the scope of our research.

### Texture implications

We have shown in Figure 4.8 that the stress-strain curves derived from tensile and torsion tests differ markedly. We have also shown that a strong texture develops during deformation, particularly in the torsion test. We therefore attribute the difference in the tensile and torsion stress-strain curves to differences in the development of texture in the two tests. As a consequence the exact stress-strain state in a textured deforming sample cannot be calculated with isotropic constitutive laws. The  $J_2$  calculations are not capable of predicting different strain hardening under various loading conditions. This affects pure torsion and tensile torsion calculations; elongation of the samples is not predicted correctly and thus the stress-strain predictions are unreliable. As a consequence, a crystal plasticity model needs to be used. In Section 4.2.3 we compare whole sample simulation results using  $J_2$  plasticity and crystal plasticity.

### 4.2.3 Numerical simulations

Figures 4.11 - 4.17 present results of the  $A2$  macroscopic sample simulations using the  $J_2$  plasticity and the crystal plasticity model (UMAT). The crystal plasticity model is presented in Section 3.4.4. Simulation results are compared with experiments. In addition to the  $A2$  experimental data we also

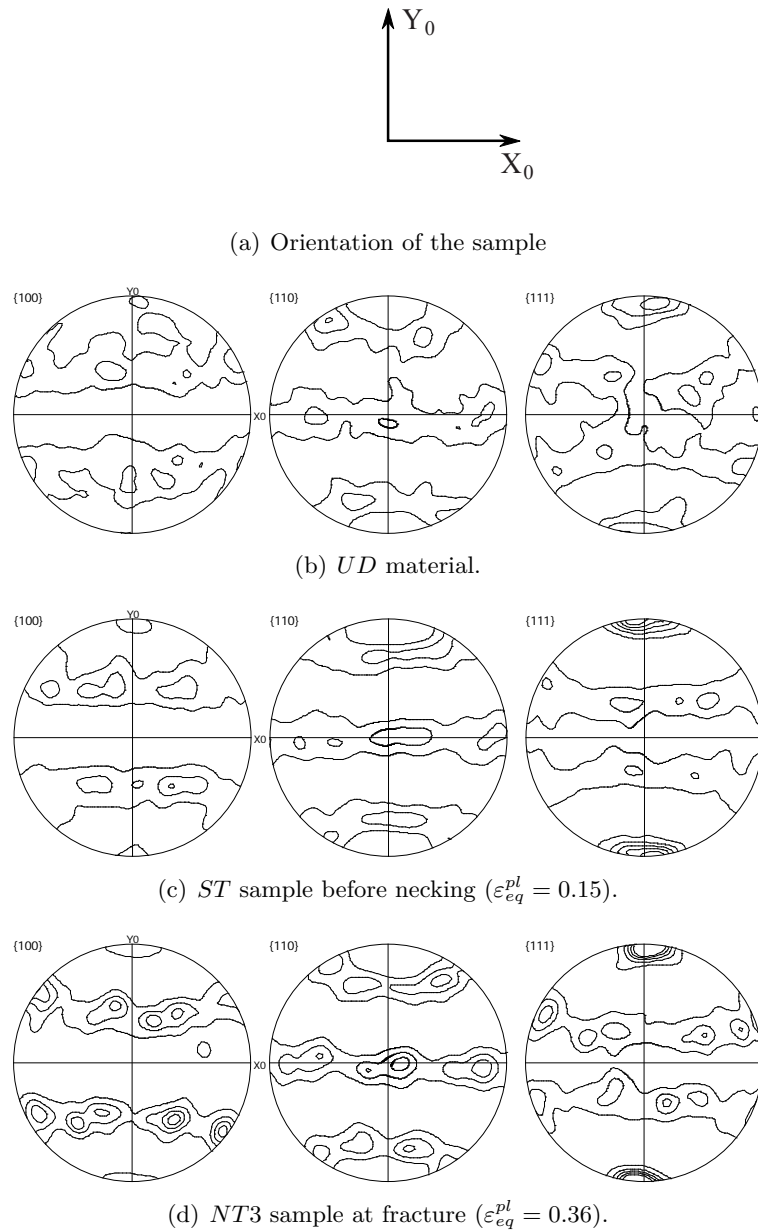


Figure 4.9: A2 pole figures for undeformed material (*UD*), smooth round tensile (*ST*) and notched round tensile (*NT3*) tests. Isovalues correspond to natural multiples ( $\times 1, 2, \dots$ ) of uniform density (*MUD*).  $Y_0$  - axial direction, and  $X_0$  - radial direction.

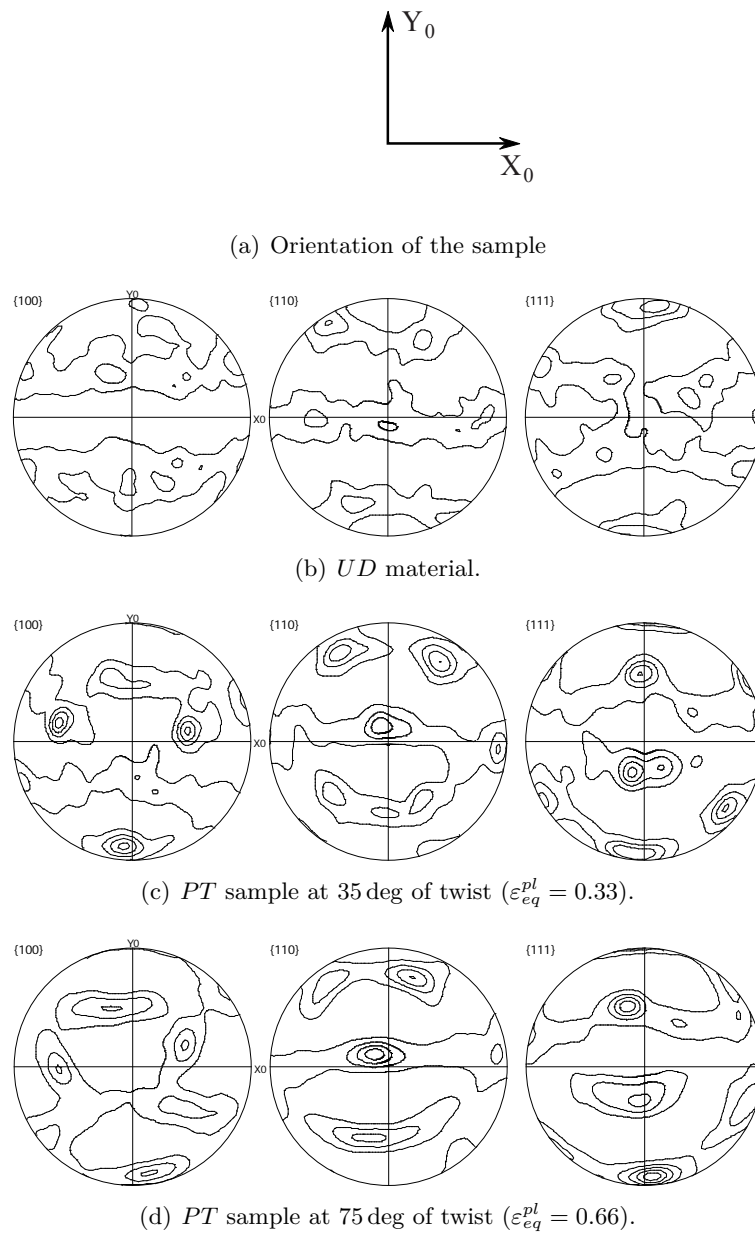


Figure 4.10: A2 pole figures for undeformed material (*UD*) and two pure torsional (*PT*) tests. Isovalues correspond to natural multiples ( $\times 1, 2, \dots$ ) of uniform density (*MUD*).  $Y_0$  - axial direction, and  $X_0$  - radial direction.

present the *A1* sample response to elucidate the effect of initial void content on material behavior.

Figure 4.11 compares the  $J_2$  and UMAT simulations with experimental results of the *ST* test. Before necking, and for limited necking, both material models reproduce the experimental results (onset of necking in experiments - peak loads - are presented in Figure 3.8(a)). While the neck grows,  $J_2$  performs better than the UMAT, but still does not reproduce experimental results ideally as no void growth causing load drop is accounted for. The UMAT does not predict the localization of deformation and suppresses extensive necking.

In notched tensile simulations, *NT1* and *NT2* (Figures 4.12- 4.13), both material models perform similarly at the beginning of the loading curve. It is only in the case of *NT3* presented in Figure 4.14 that the UMAT performs distinctly better.

Under shear dominated loading, the UMAT constitutive model gives results which are much closer to the experimental results in terms of torque - grip rotation angle. This is evident in the case of the *PT* experiment presented in Figure 4.15. The  $J_2$  simulation overpredicts, by a factor of approximately two, the torque at fracture in the *A2* alloy. The UMAT gives reliable results up to 200 degrees of rotation while for higher strains it underpredicts the torque. Note, however that the UMAT crystal plasticity model was calibrated using the *ST* data. We observe in Figure 4.17, that none of the material models can reproduce localization followed by a drop of torque in the *TT2* sample.

In the examples of *PT* and *TT1*, it was impossible to run the simulations to the end due to convergence problems resulting from the very large deformations. Figure 4.18 presents the extent of deformation in tested *A1* and *A2* samples.

In the case of predictions of the axial elongation in torsion samples, it is either  $J_2$  or UMAT which performs better, depending on the loading type. In the most interesting experiment, *PT*,  $J_2$  underestimates axial elongation over the whole range of sample twist. UMAT gives relatively good results up to 80-90 degrees of grips rotation, at which point, there is a change of elongation rate in the tested samples. UMAT is unable to predict this change and starts to overpredict sample elongation.

From the comparison of the two material models with the experimental observations, we can conclude that the UMAT model is more appropriate than  $J_2$  for simulating the behavior of the selected model materials under wide ranges of loading conditions. In particular it is able to simulate reasonably well the *PT* test. However, it cannot correctly account for the localization of the deformation. Since neither the  $J_2$  or the UMAT material model work perfectly we continue to use both.

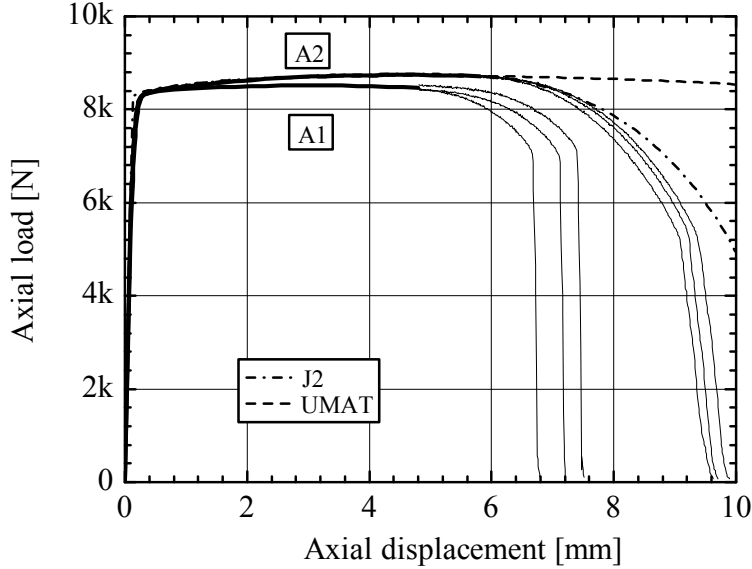


Figure 4.11: ST experimental and simulation results.

### Shape changes of the PT sample

With the aim of comparing experimental observations with numerical simulations, changes of shape of the *PT* sample were investigated. Three main parameters describing the gauge section of the tubular thin-walled sample were taken into account: external diameter  $D$ , internal diameter  $d$  and wall thickness  $t$ .

Figures 4.19, 4.20 and 4.21 present measurements and simulation results of  $D$ ,  $d$  and  $t$ , respectively. In these figures, the simulation results are denoted by dashed and dashed-dotted lines, while measurements (normalized to the nominal size of the sample, as discussed below) are denoted by continuous lines with circles. In Figure 4.21 continuous lines with circles denote  $t$  values calculated as the difference between  $D$  and  $d$  ( $t = (D - d)/2$ ).

We performed 9 tests for each model material with increments of 15 deg of sample twist. The smallest section of each sample was measured before and after the test. External diameter  $D$  was measured using a caliper with a resolution of 0.01 mm. Internal diameter  $d$  was measured using a micrometer screw gauge with a resolution of 0.005 mm. Averages of three measurements for each parameter were calculated.

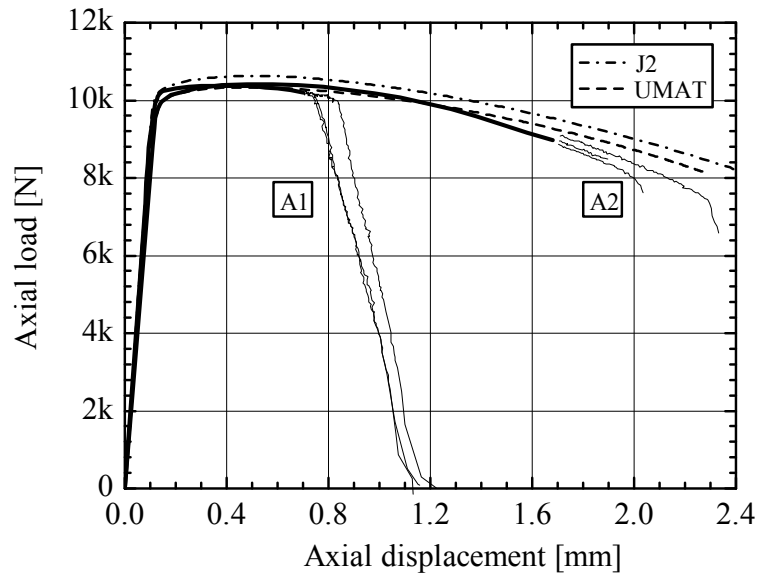


Figure 4.12: NT1 experimental and simulation results.

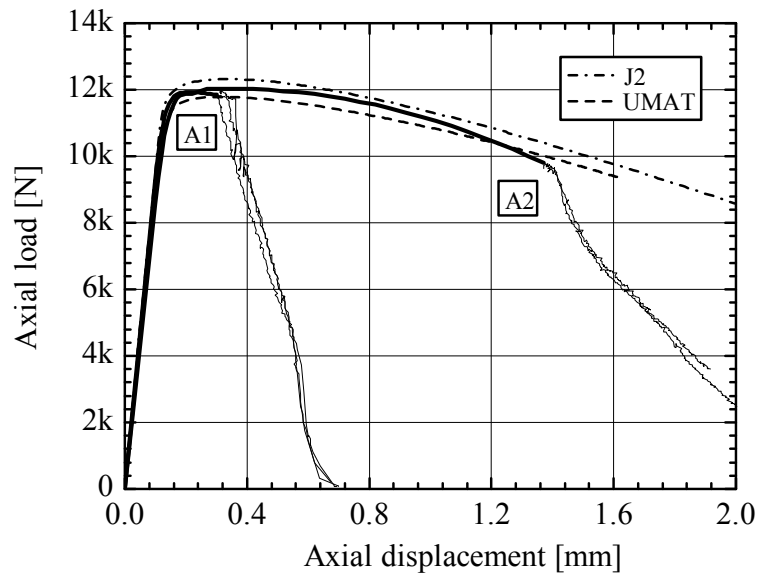


Figure 4.13: NT2 experimental and simulation results.

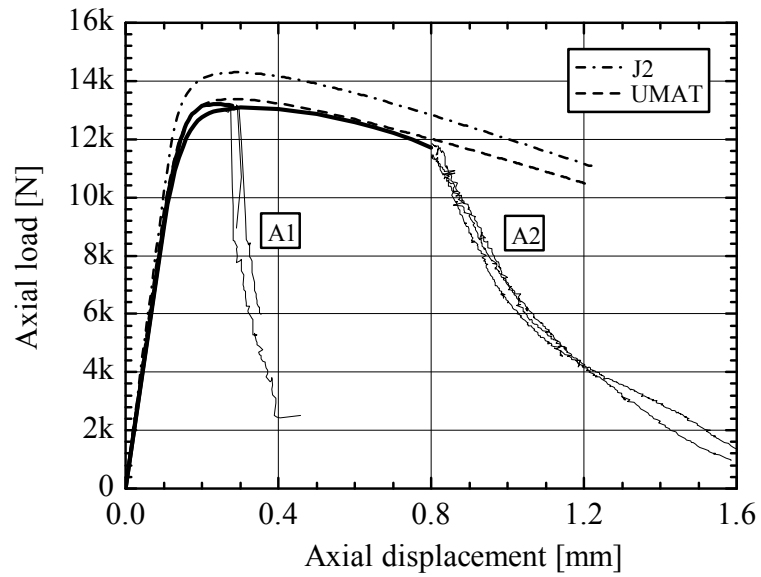


Figure 4.14: NT3 experimental and simulation results.

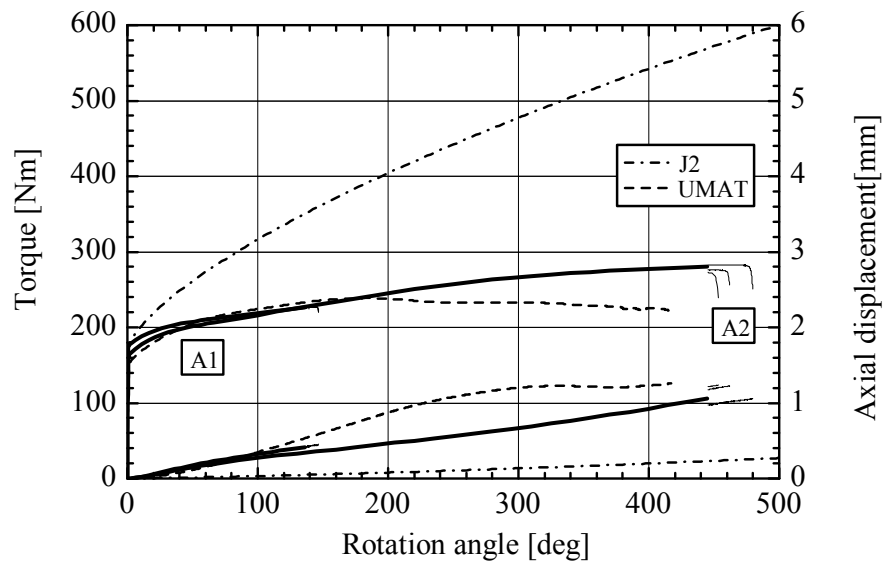


Figure 4.15: PT experimental and simulation results.



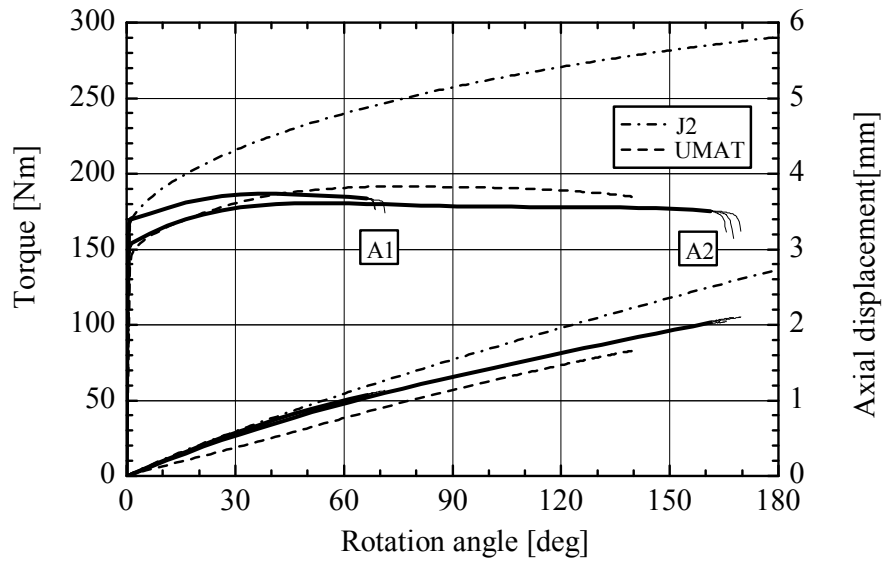


Figure 4.16: TT1 experimental and simulation results.

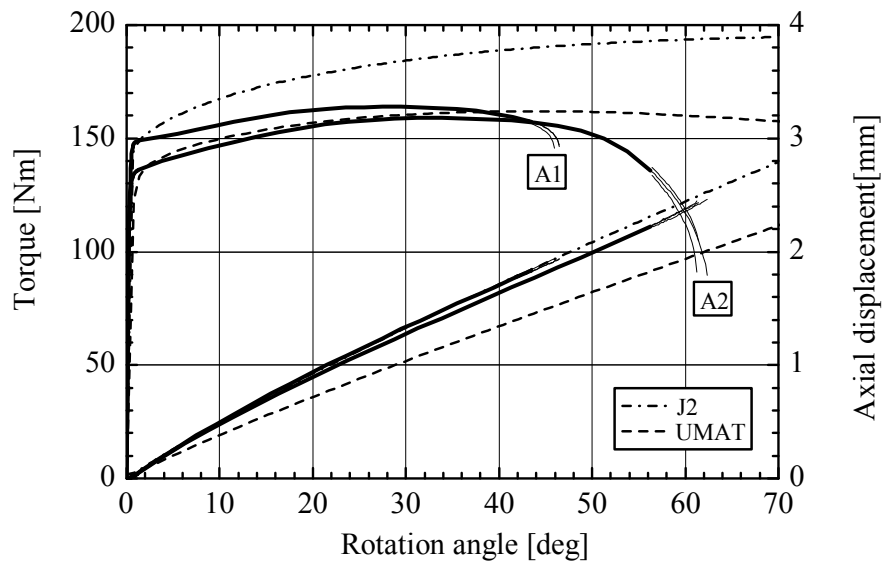


Figure 4.17: TT2 experimental and simulation results.

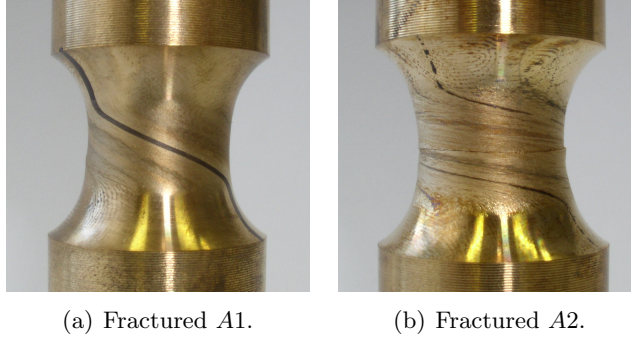


Figure 4.18: Samples deformed up to fracture under PT loading. The lines drawn on the samples were vertical before the PT tests.

We found that the original, untested samples vary in size by 0.15% in the case of  $D$  (20.00 – 20.03 mm), by 0.34% in the case of  $d$  (15.990 – 16.045 mm), and by 1.30% in the case of  $t$  (1.993 – 2.019 mm). The measured variability in thickness of undeformed samples is on the order of magnitude of the  $t$  change during deformation.

We calculate true change in dimensions  $D$  and  $d$  from the measurements of the undeformed and deformed samples. In order to be able to compare all the results we then transform these data to express change in nominal dimensions. To do so we multiply the nominal values of  $D$  and  $d$  by the measured relative change in dimensions. Finally  $t$  was calculated using normalized  $D$  and  $d$  values as  $t = (D - d)/2$ .

It can be observed that the tested sample behaves notably differently compared to simulations using both material models. In general, the  $J_2$  material model underestimates the  $D$  and  $d$  reduction, while the UMAT overestimates them. As far as the wall thickness is concerned, both material models predict no significant  $t$  change within the presented deformation range. Neither of the material models were capable of predicting variations of the  $D$  and  $d$  rates of change. These changes appear at the sample twist angle corresponding to the change in sample elongation rate (90 deg approx. in the A2 and 60 deg approx in the A1) presented previously in Figure 4.6 and 4.7 indicating their microstructural origin.

If the UMAT material model performs better in comparison with the  $J_2$  model in terms of torque-angle rotation as presented in Section 4.2.3, the situation is more contrasted for size and shape changes. Whereas for small deformations the UMAT simulations track experiments rather well, whereas  $J_2$  simulations underpredicts them, for large deformations UMAT simulations and experiments diverge completely.

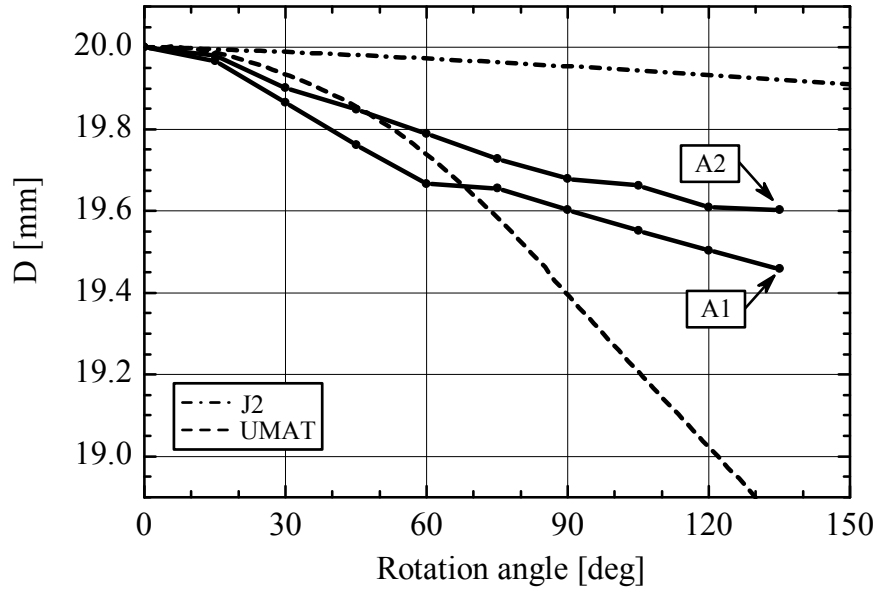


Figure 4.19: Evolution of  $D$ , external diameter in the PT sample. UMAT simulation stopped at 366 deg,  $D = 14.74$  mm.  $J_2$  simulation stopped at 500 deg,  $D = 19.53$ .

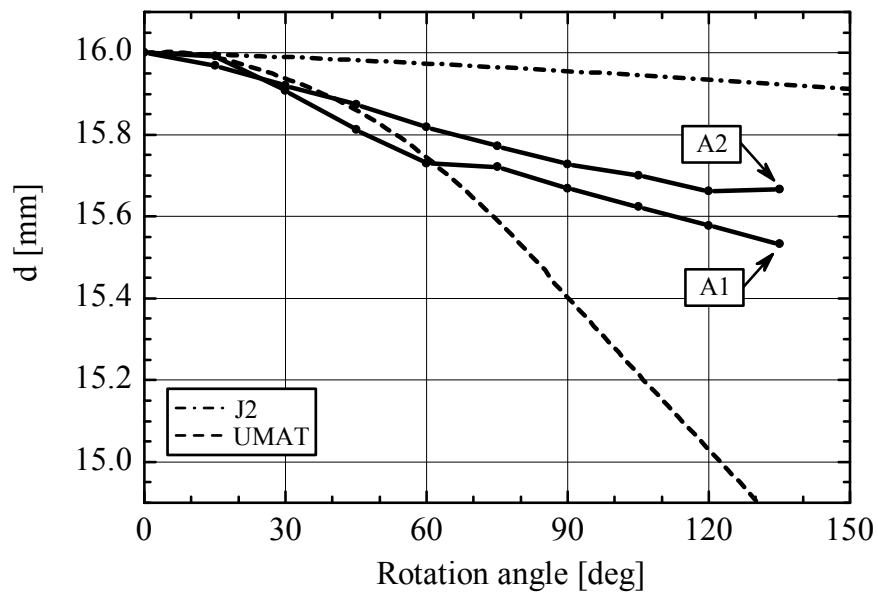


Figure 4.20: Evolution of  $d$ , internal diameter in the PT sample. UMAT simulation stopped at 366 deg,  $d = 10.67$  mm.  $J_2$  simulation stopped at 500 deg,  $d = 15.54$ .

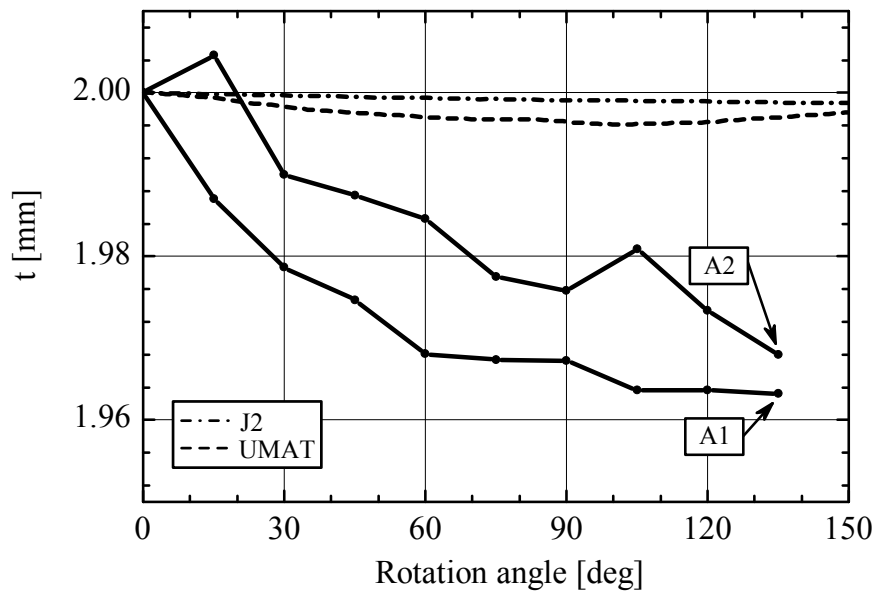


Figure 4.21: Evolution of  $t$  wall thickness in the PT sample. Continuous lines with circles denote  $t$  calculated as  $(D - d)/2$ , where  $D$  and  $d$  are presented in Figures 4.19 and 4.20, respectively.

## 4.3 Fracture behavior

This section describes and compares in detail the fracture behavior of the *A1* and *A2* alloys. In the description, we follow the sequence of stages of the ductile fracture: nucleation, growth and coalescence of voids. Section 4.3.1 shows the nucleation stage. Section 4.3.2 concerns void evolution and presents the stable void growth stage in the most interesting loading case for us, which is pure torsion loading. Evolution of voids is described in terms of shape and orientation change. Section 4.3.3 concerns fracture initiation and describes the effects of the coalescence (or unstable/localized void growth) stage of fracture. Coalescence itself is a very abrupt and difficult process to capture experimentally, thus in this section we present only its effects. Section 4.3.4 concerns fracture mechanisms and summarizes observed processes of fracture. This section also provides a set of micrographs which illustrate, at different magnifications, fracture surfaces and cross sections of samples tested under each loading condition.

### 4.3.1 Void nucleation

#### Void nucleation in the *A1* alloy

In the *A1* alloy, the nucleation phase of fracture does not exist and zero nucleation strain can be assumed as each lead inclusion contains a void, and starts growing or deforming as soon as load is applied (see Section 3.2.5). The mechanism of creation of these voids was described for lead-containing copper alloys in general, in Section 3.2.4.

In fractured samples, we also observe evidence of the presence of the pre-existing voids in lead inclusions. Figure 4.22 presents the fracture surface of a notched round tensile *NT3* sample. Inside the lead inclusions, which appear bright, we observe dark spots. The dark spots are indicated by arrows and are locations where a void was initially present at the interface of the matrix and the lead inclusion in the undeformed sample.

All the observed dimples contain lead and thus we conclude that there is no secondary void population nucleating at features other than lead inclusions. However, inclusions of another type were also observed. These inclusions are similar to the ones observed in the *A2* alloy and always appear within big lead inclusions. For this reason they do not act as nucleation sites for a second population of voids. In addition, being trapped in soft lead, they will not be able to wedge open the deforming voids under low triaxiality loadings.

The situation described in the previous paragraphs is typical of all the fracture surfaces of samples fractured under different loading conditions. Although we observe lead inclusions in the majority of dimples, we were not able to identify nucleating inclusions in some of them. Figures 4.23(b) and

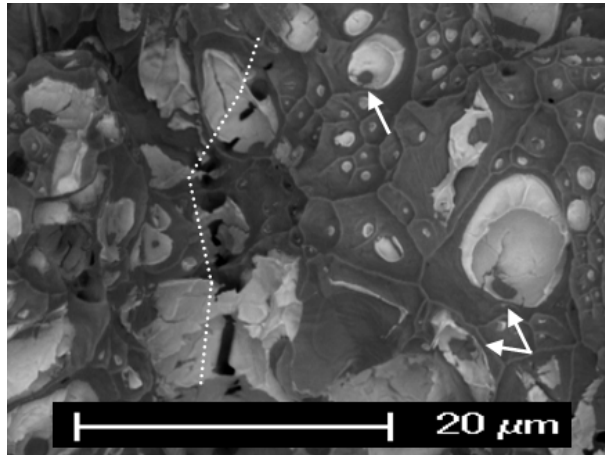


Figure 4.22: A1 round notched tensile NT3 fracture surface (BSE). Arrows indicate the location of pre-existing voids, the dotted line follows the intergranular fracture.

4.23(d) present representative dimples observed in the *PT* sample with SE and BSE respectively. However, the distances between dimples, which are similar to those observed in the *NT3* sample (Figures 4.23(a) and 4.23(c)), suggests that these voids were also nucleated at lead inclusions. Possibly, the nucleating lead inclusions are located at the bottom of dimples which are not visible due to extensive shearing of the material.

### Void nucleation in the A2 alloy

The A2 alloy also contains pre-existing voids which are associated with hard particles as shown in Figure 4.24(a). The inclusion-matrix decohesion always appears at the poles of inclusions aligned in the direction of the axis of the round bar (vertical direction in Figure 4.24). This fact suggests that the pre-existing voids associated with hard inclusions originate during the manufacturing of the round bars and are not an effect of etching. The voids grow, even for relatively small deformations (compared to strain to fracture), as presented in Figure 4.24(b). The A2 alloy was also found to nucleate voids at traces of lead or another elements such as sulfur, appearing occasionally in the alloy.

Figure 4.25 compares fracture surfaces of the A2 alloy, tested under *NT3* and *PT* loadings. In the notched tensile samples, voids are observed to grow until the intervold ligaments neck down to sharp edges. Inclusions of the A2 type do not break, thus some of them stay at the other matching fracture surface and are not visible in the depicted micrograph. In the *PT* sample, a population of small voids can be observed. These small voids did not contain any nucleating inclusions. This may indicate that in some locations the A2 alloy may nucleate a second population of small voids, e.g. at dislocation pile-

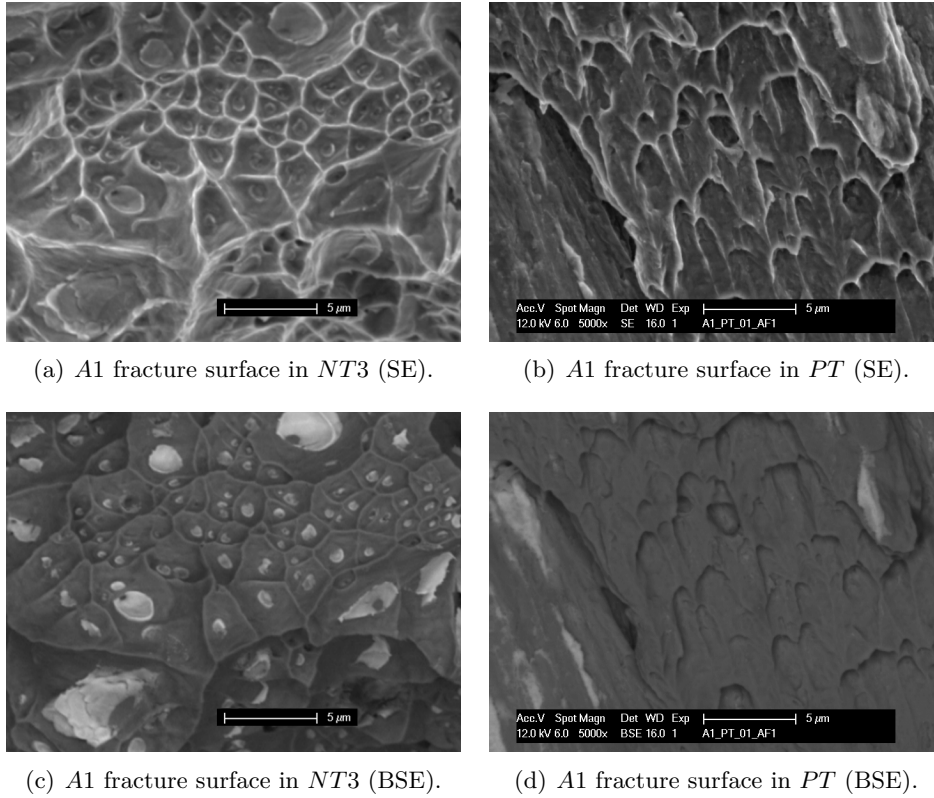


Figure 4.23: A1 fracture surfaces resulting from *NT3* and *PT* loading conditions.

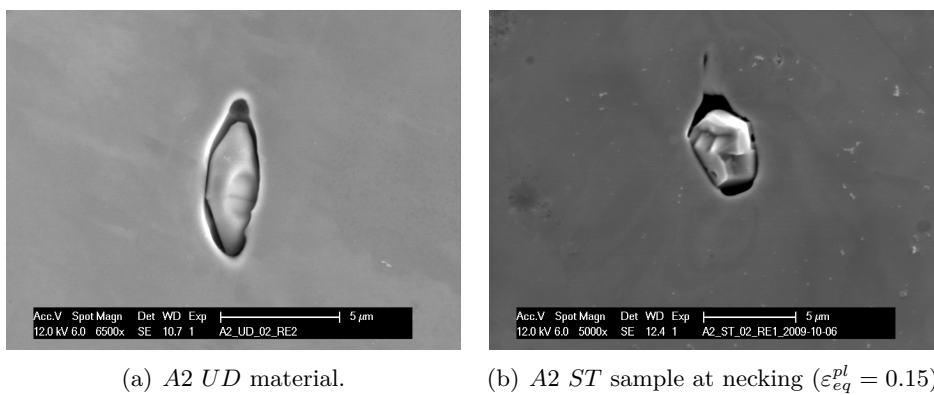


Figure 4.24: A2 hard inclusions in electro-polished samples (SE).

ups at the twin interface, intersection of twins (Smallman and Ngan, 2007) or other structural defects. Dimples are overall bigger in the *A2* alloy compared to the *A1* under *PT* loading (see Figures 4.23(d) and 4.25(b)).

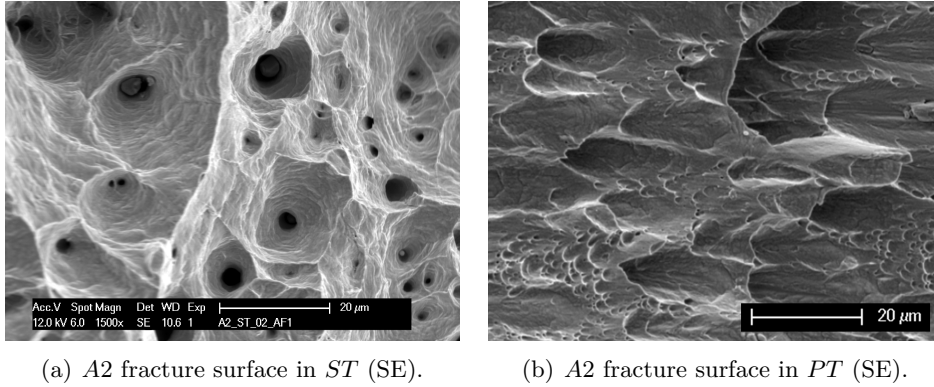


Figure 4.25: *A2* fracture surfaces resulting from *ST* and *PT* loading conditions.



### 4.3.2 Void evolution

#### Void evolution in the A1 alloy

The lead inclusions, initially elongated in the direction of the axis of the sample, were found to re-orientate under torsion dominated loading conditions. We tracked the evolution of the shape of lead inclusions under *PT* loading by performing interrupted tests at different levels of deformation as presented in Figure 4.26 as numbered points.

Figure 4.27 presents the evolution of the shape of lead inclusions observed in the *AT* plane. The vertical direction always corresponds to the direction of the axis of the undeformed sample. In Figure 4.27(a) we observe that the lead inclusions have an initial preferential orientation due to processing. Subsequent figures illustrate how the inclusion realignment becomes more pronounced as deformation increases. The inclusions rotate and elongate gradually as the twist angle of the sample (rotation of grips) increases. There is no obvious wedging effect of the inclusions on the void walls, and the observed minor axis shortens. The evolution of pre-existing voids in terms of the orientation change, the elongation of the void axes, and the volume growth in the A1 alloy will be described in detail in Section 4.4.

Figure 4.27(f) depicts void shape at the final stage of loading (P4), observed in the *AR* plane, which is perpendicular to the *AT* plane. Voids are orientated in the horizontal direction, which in the *AR* plane is the radial direction. Voids also give the impression of elongation in the radial direction.

#### Void evolution in A2 alloy

A procedure similar to the procedure described in Section 4.3.2 was performed in order to track the evolution of voids in the A2 material. Several interrupted tests were performed at different levels of deformation as indicated in Figure 4.28 as numbered points.

The resulting evolution of void shape and orientation observed in the *AT* plane is presented in Figure 4.29. The orientation of the voids changes, and becomes almost perpendicular to the initial direction at the end of torsional deformation. Voids elongate and tend to close around the hard inclusions, which becomes apparent with larger deformations.

The locking effect of hard inclusions was studied for tensile loads by Siruguet and Leblond (2004a,b). The hypothesis for the model of void growth and coalescence, that the void always remains spheroidal, becomes erroneous for large deformations. In their single cell computations, the void ultimately takes the shape of a "double pear" (spheroid with inflated equator region), and for large strain values, the void growth predicted in their model is notably overesti-

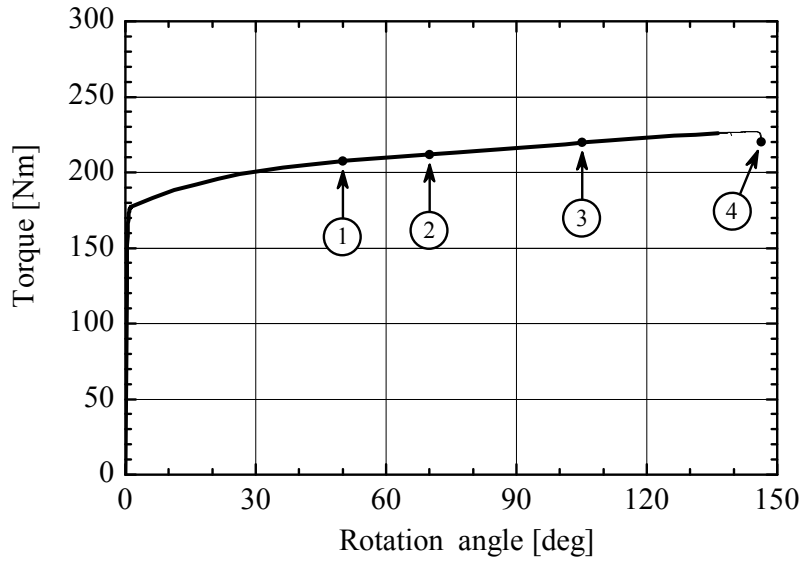


Figure 4.26: A1 PT experimental results - interrupted tests.

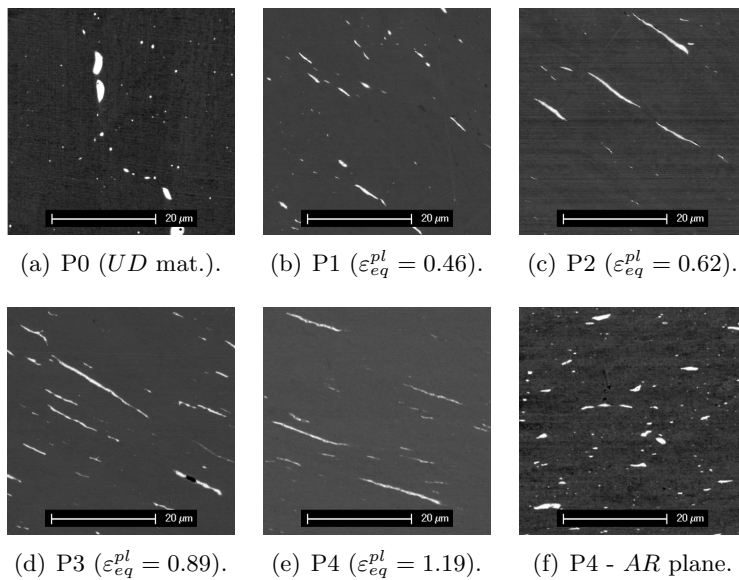


Figure 4.27: Shape and orientation of inclusions in A1 at various extents of PT loading as presented in Figure 4.26 (BSE). Approximate  $\varepsilon_{\varepsilon q}^{pl}$  values obtained from  $J_2$  simulation.

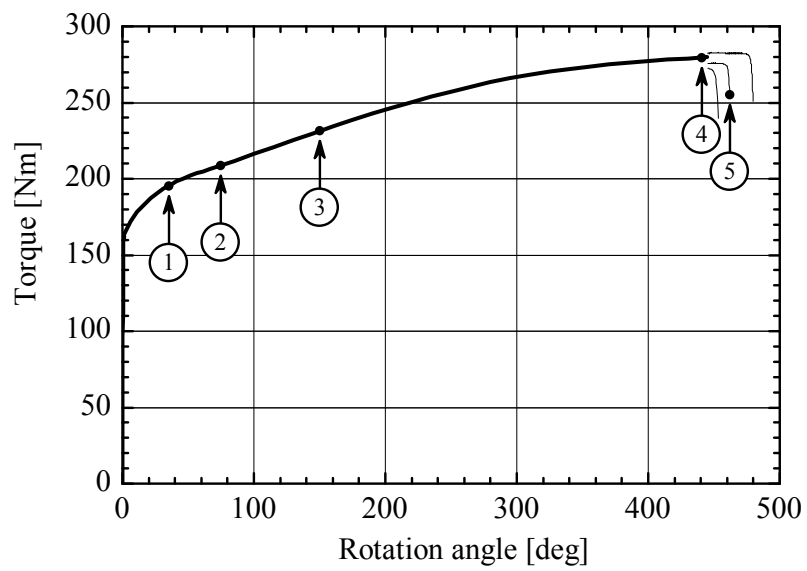


Figure 4.28: A2 PT experimental results - interrupted tests.

mated.

In the presented micrographs, it can be observed that under shear loading at relatively low deformation, the inclusion wedges the void, but later for larger deformations, plasticity overrides wedging and allows the voids to close up.

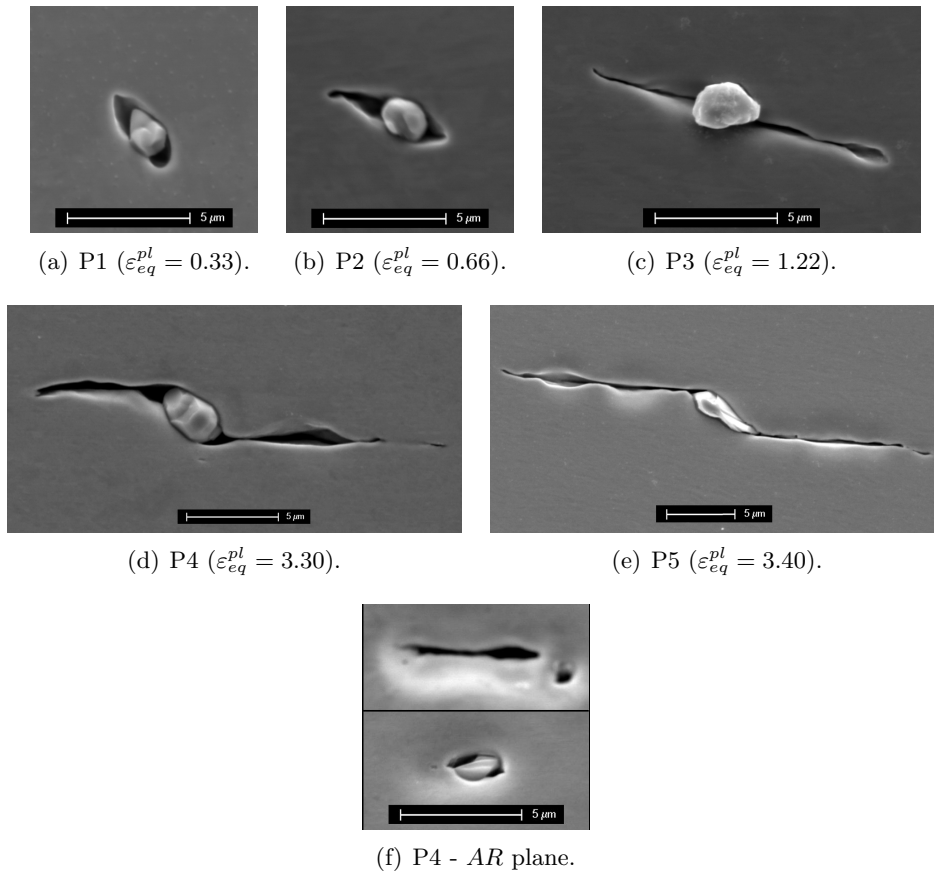


Figure 4.29: Shape and orientation of A2 inclusions at various extents of PT loading as presented in Figure 4.28 (SE). Approximate  $\varepsilon_{eq}^{pl}$  values obtained from the  $J_2$  simulation.

### 4.3.3 Fracture initiation

#### Fracture initiation in the A1 alloy

Figure 4.30 shows results of interrupted notched tensile *NT1* tests. The thick line represents averaged test results of three samples (the same as in Figure 4.2), the thin lines represent test results at the final stage for each of the tests. Dots indicate at which level of deformation the additional tests were interrupted. The microstructural differences are shown in Figure 4.31.

Figure 4.31 depicts micrographs of the cross section of *NT1* interrupted samples. The sample presented in Figure 4.31(a) and 4.31(c) was interrupted before the onset of rapid loss of load carrying capacity (point 1 in Figure 4.30), and the sample presented in Figure 4.31(b) and 4.31(d) was arrested just after the load started to drop (point 2 in Figure 4.30).

We see that the rapid loss of load carrying capacity is related to the development of multiple cracks in the center of the sample. The second sample, presented in micrographs taken at low magnification, exhibit visible damage (Figure 4.31(b)), which is not present in the first sample (Figure 4.31(a)). In the high magnification micrographs, we can deduce that the cracks seem to follow grain boundaries, and result from the coalescence of several voids.

In samples arrested before and after the rapid loss of carrying capacity, (Figure 4.31(c) and 4.31(d) outside the main crack, respectively) accelerated growth of voids allowing several voids to link up is not seen. This indicates that the rapid growth of voids in the *NT1* sample followed by linking up, happens shortly before crack formation and is a very localized process.

### Fracture initiation in the A2 alloy

Figure 4.32 presents results of interrupted round notched tensile *NT1* tests. The thick line represents averaged test results of three samples (the same as in Figure 4.3), the thin lines represent the actual results of the three tests. One test was interrupted at 1.9 mm axial displacement, that is, before the onset of the rapid loss of load carrying capacity. The other test was interrupted just after this point.

Figure 4.33 depicts micrographs of the cross sections of interrupted *NT1* samples. The sample presented in Figure 4.33(a) and 4.33(c) was arrested before the onset of rapid loss of load carrying capacity (point 1 in Figure 4.32), and the sample presented in Figure 4.33(b) and 4.33(d) was arrested just after this point (point 2 in Figure 4.32).

We observe that the rapid loss of load carrying capacity is related to the development of multiple cracks at the center of the sample. The second sample, presented in micrographs taken at low magnification, exhibit visible damage (Figure 4.33(b)). This damage is not present in the first sample presented in Figure 4.33(a). In the middle of Figure 4.33(d) we observe an empty space left by a grain that detached from adjacent grains, which demonstrates that the cracks follow grain boundaries.

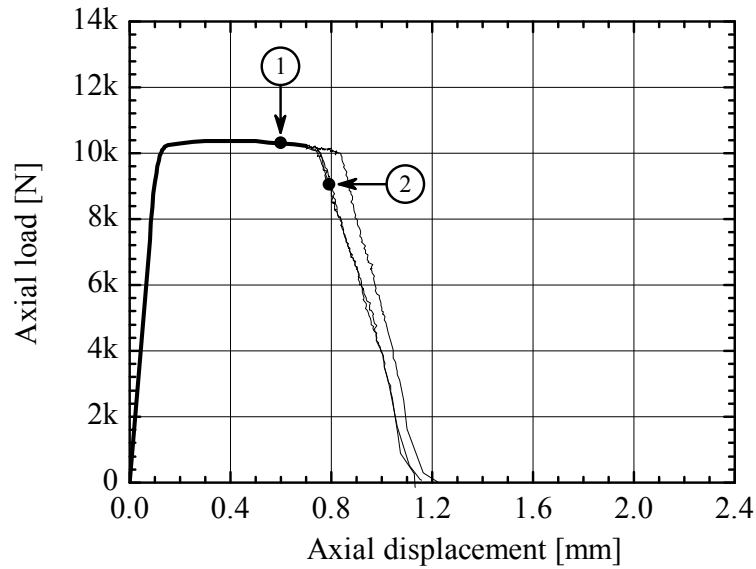
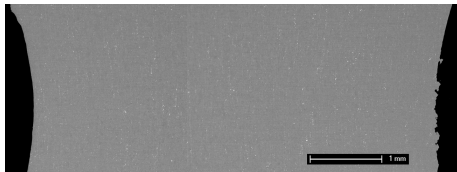
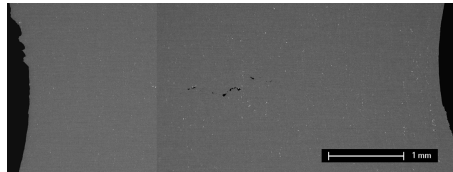


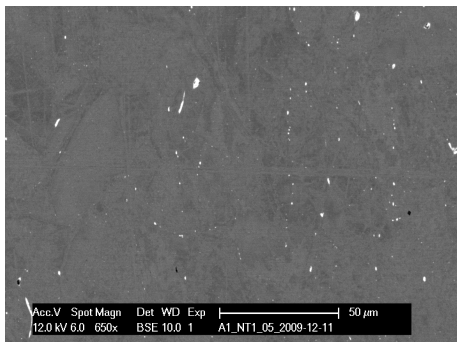
Figure 4.30: A1 round notched tensile NT1 interrupted test.



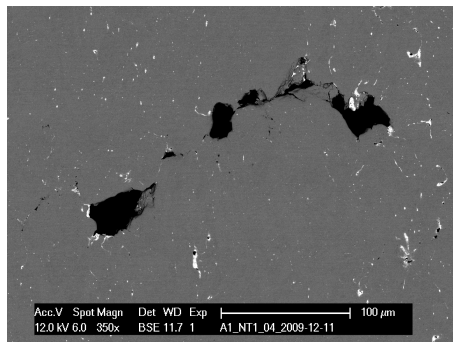
(a) A1 NT1 sample at point 1 of loading.



(b) A1 NT1 at point 2 of loading.



(c) A1 NT1 sample at point 1 of loading.



(d) A1 NT1 at point 2 of loading.

Figure 4.31: A1 NT1 interrupted test samples at points 1 and 2 in Figure 4.30 (BSE).

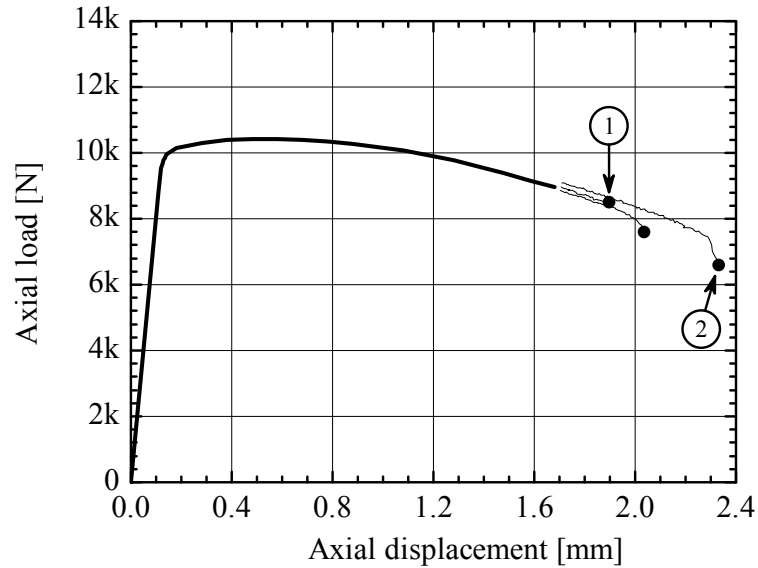
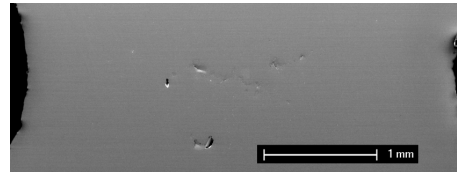
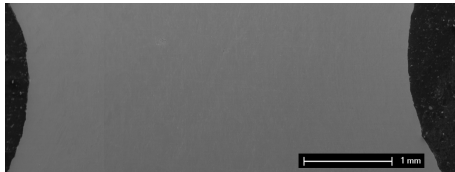
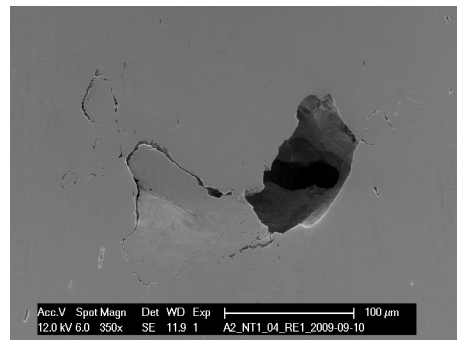
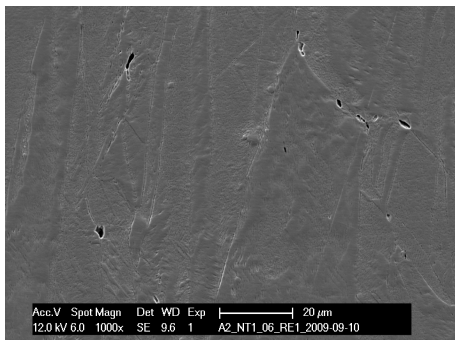


Figure 4.32: A2 round notched tensile NT1 interrupted test.



(a) A2 NT1 sample at point 1 of loading (electro-polished).

(b) A2 NT1 at point 2 of loading (mechanically polished).



(c) A2 NT1 sample at point 1 of loading (electro-polished).

(d) A2 NT1 at point 2 of loading (electro-polished).

Figure 4.33: A2 NT1 interrupted test samples at points 1 and 2 in Figure 4.32 (SE).

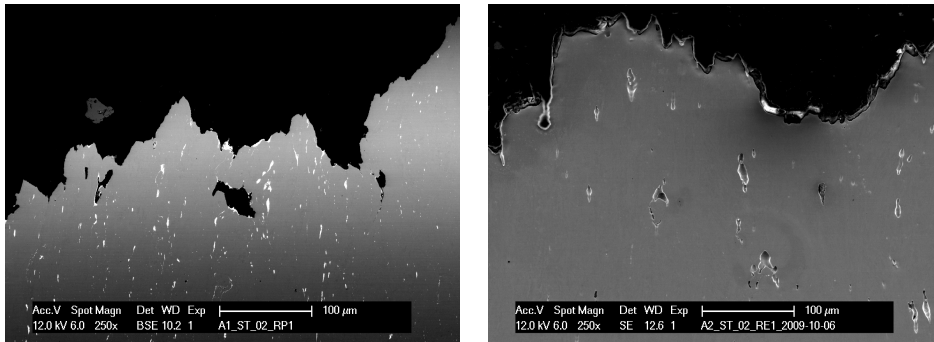
#### 4.3.4 Fracture mechanism

Under tension and notched tension loadings, both the investigated alloys, *A1* and *A2*, exhibit intergranular fracture.

In the *A1* alloy the intergranular fracture is determined by the tendency of large lead inclusions to appear at grain boundaries. Upon loading the pre-existing voids in lead, the inclusions grow to coalesce by necking the intervoid ligaments. Cracks formed in this way follow chains of lead inclusions as observed in the middle of Figure 4.22.

In the *A2* alloy under notched tensile loading, voids nucleated at hard inclusions also coalesce by necking the intervoid ligaments down to a sharp edge, as observed in Figure 4.25(a).

Figure 4.34 compares cross sections of *ST* specimens of the *A1* and *A2* alloys. Because of higher void volume fraction, the damage in the *A1* alloy is more localized. The coalescence we observe in the *A1* is concentrated for the most part on what becomes the fracture surface and below this plane at locations where there was unusually high concentration of lead particles. Measurements of this limited void growth away from the fracture surfaces and coalesced regions will be presented in Section 4.4. In the *A2* alloy, higher intervoid distances allow voids to grow more (relative to their initial size) before coalescence occurs. Due to this damage mechanism, the *A2* alloy has a more diffused character requiring higher strains to fracture.



(a) *A1* polished cross section (*BSE*). (b) *A2* electro-polished cross section (*SE*).

Figure 4.34: *A1* and *A2* alloy *ST* sample cross sections close to the fracture surface.

Under torsional and tensile torsional loadings, it is more difficult to identify the fracture mechanism because the fracture surfaces are highly distorted. In addition etching of sample cross sections does not reveal grain boundaries due to the high density of dislocations.



In the *A1* alloy, the distances between dimple centers are similar for *ST* and *PT* samples. We therefore expect that there is no nucleation of a second population of voids, although in some small dimples, lead was not observed. It is possible that very small lead inclusions nucleating the small voids remained attached to the matching fracture surface, or are hidden at the bottom of sheared dimples.

In the *A2* alloy we also observed some dimples that did not contain inclusions. It is possible that in the case of large empty voids, the missing inclusion remained attached to the matching fracture surface. On the other hand, clusters of small empty dimples were observed. This may indicate that at some locations, the *A2* alloy may nucleate a second population of voids at intersections of dislocations or at grain boundaries and triple points, as mentioned before.

To complete the data set, we present micrographs of fracture surfaces of samples tested under each loading condition. Micrographs taken at the same magnification using both SE and BSE detectors have the same location in a sample:

- Figure 4.35 - tensile dominated loadings in *A1*.
- Figure 4.36 - tensile dominated loadings in *A2*.
- Figure 4.37 - torsion dominated loadings in *A1*.
- Figure 4.38 - torsion dominated loadings in *A2*.

Additionally, we present cross sections of tension-torsion samples observed at different magnifications. *A1* samples are observed with the BSE detector, while *A2* samples are observed with the SE detector:

- Figure 4.39 - torsion dominated loadings in *A1*.
- Figure 4.40 - torsion dominated loadings in *A2*.

These figures confirm the observations made earlier on other micrographs regarding mechanisms and void kinetics.

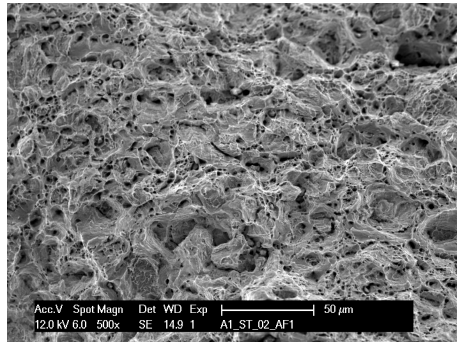
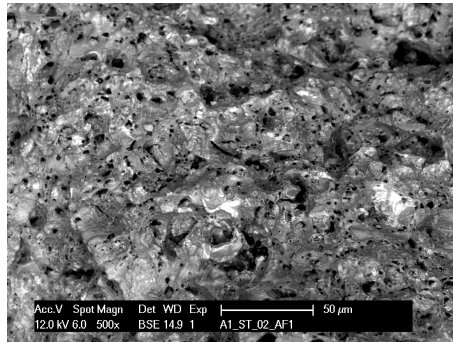
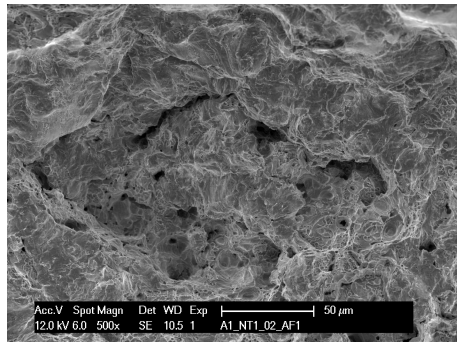
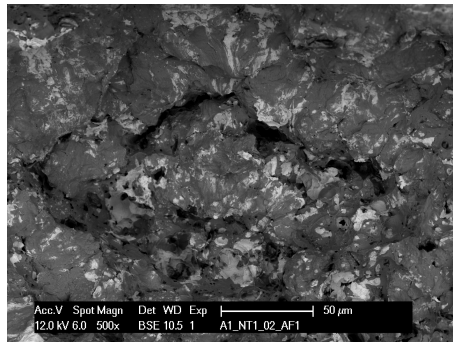
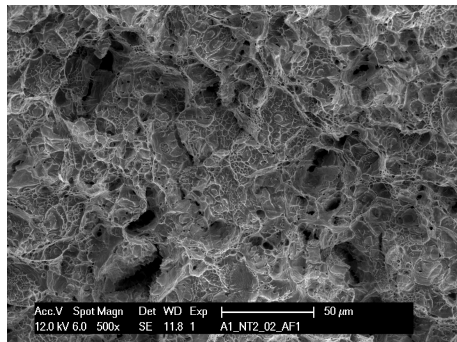
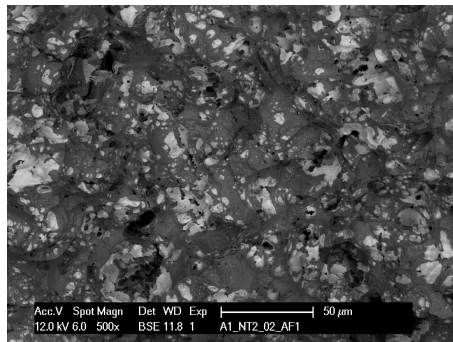
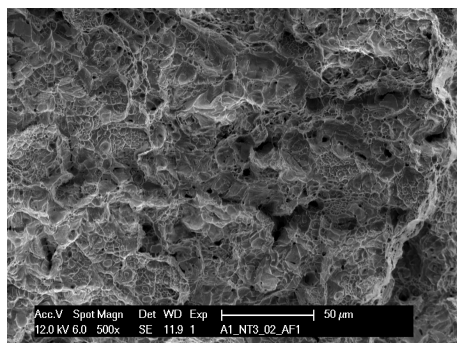
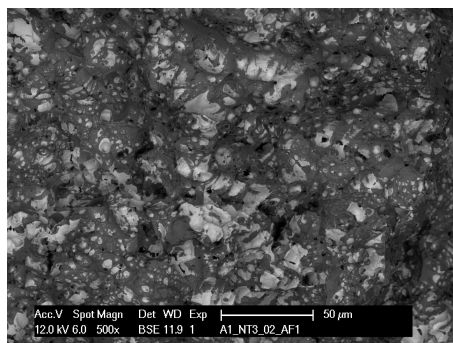
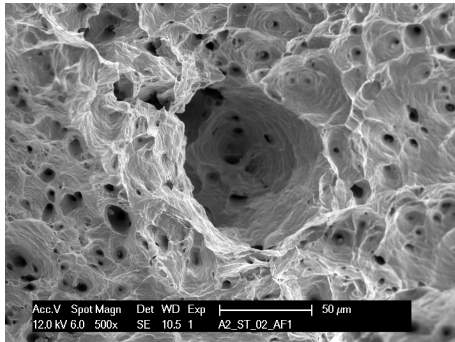
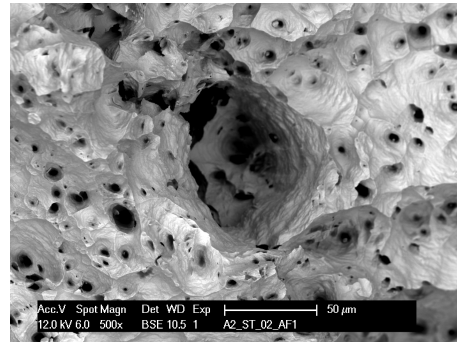
(a) *ST (SE)*.(b) *ST (BSE)*.(c) *NT1 (SE)*.(d) *NT1 (BSE)*.(e) *NT2 (SE)*.(f) *NT2 (BSE)*.(g) *NT3 (SE)*.(h) *NT3 (BSE)*.

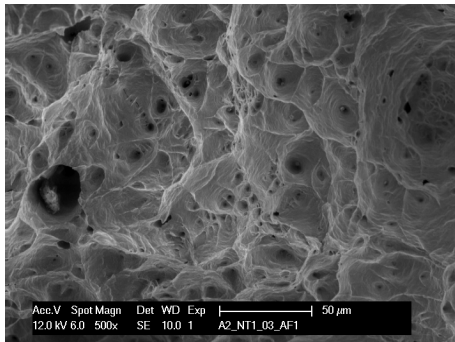
Figure 4.35: A1 tensile fracture surfaces.



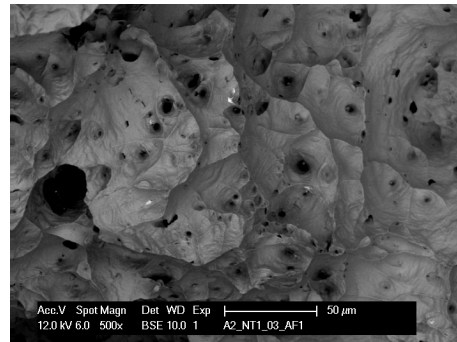
(a) *ST (SE)*.



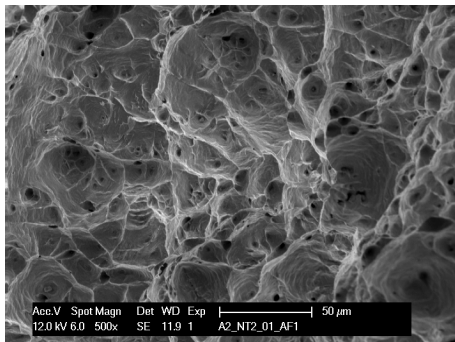
(b) *ST (BSE)*.



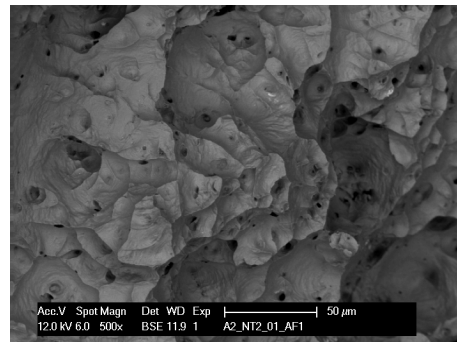
(c) *NT1 (SE)*.



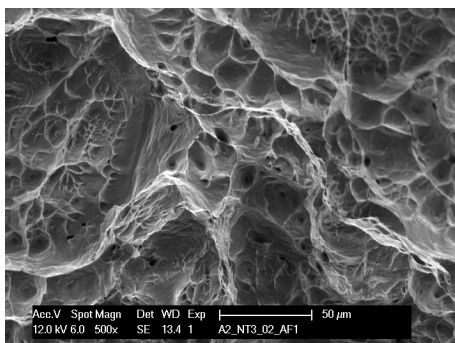
(d) *NT1 (BSE)*.



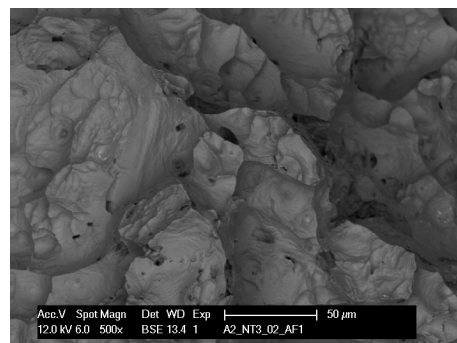
(e) *NT2 (SE)*.



(f) *NT2 (BSE)*.



(g) *NT3 (SE)*.



(h) *NT3 (BSE)*.

Figure 4.36: A2 tensile fracture surfaces.

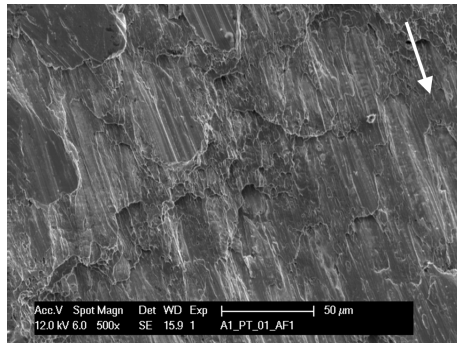
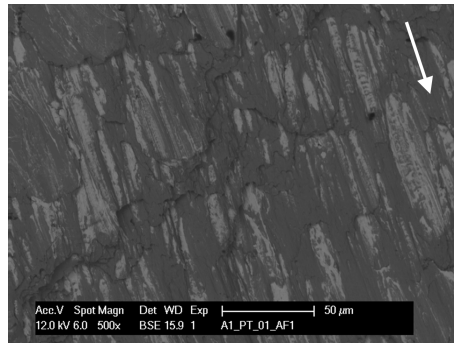
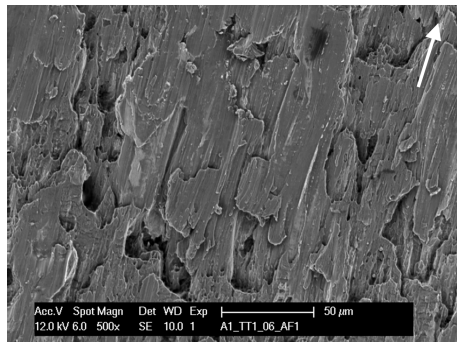
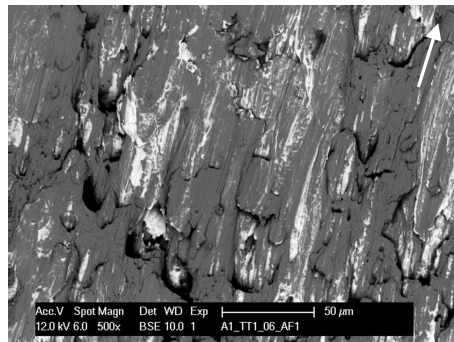
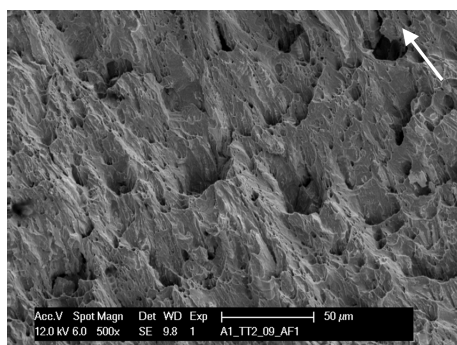
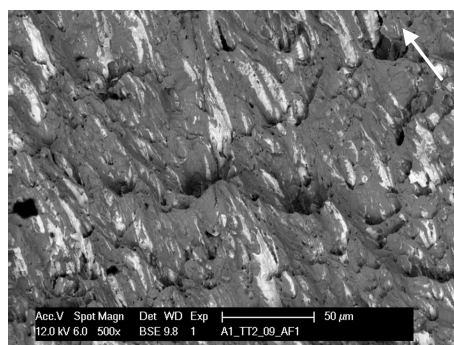
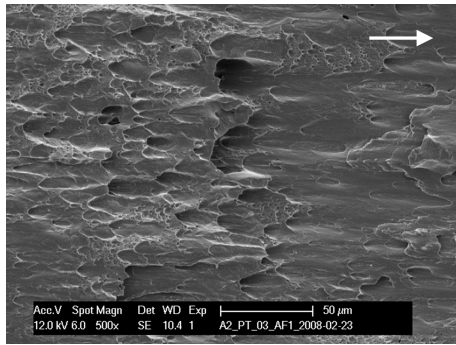
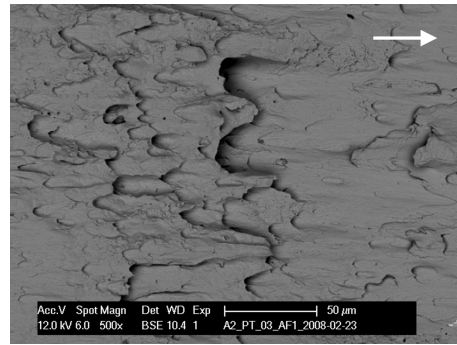
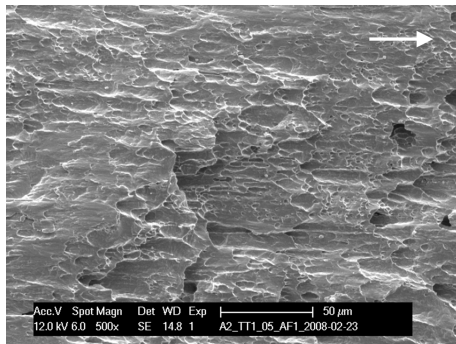
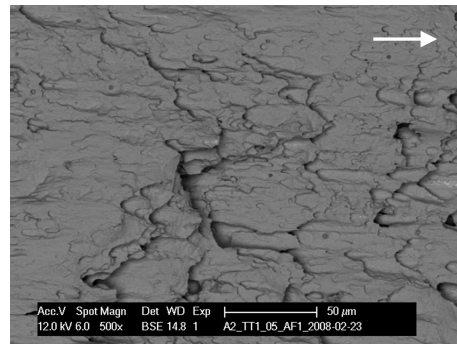
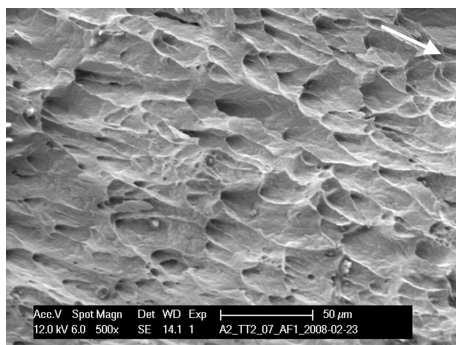
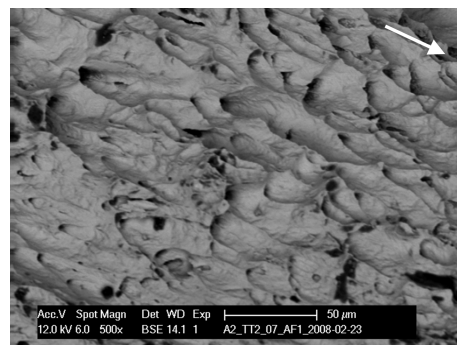
(a) *PT (SE)*.(b) *PT (BSE)*.(c) *TT1 (SE)*.(d) *TT1 (BSE)*.(e) *TT2 (SE)*.(f) *TT2 (BSE)*.

Figure 4.37: A1 torsion fracture surfaces.

(a) *PT (SE)*.(b) *PT (BSE)*.(c) *TT1 (SE)*.(d) *TT1 (BSE)*.(e) *TT2 (SE)*.(f) *TT2 (BSE)*.*Figure 4.38: A2 torsion fracture surfaces.*

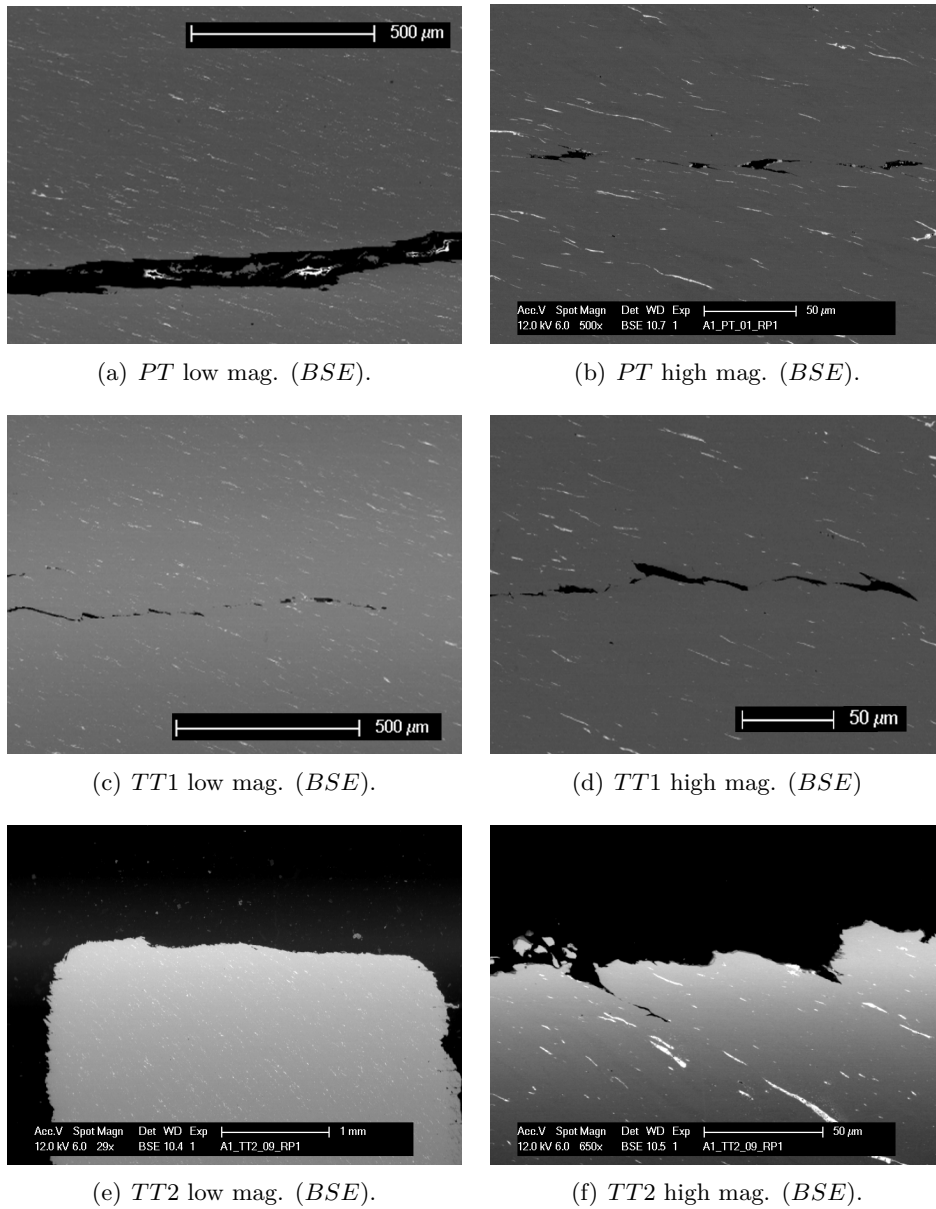


Figure 4.39: A1 torsion cross sections, AT plane.

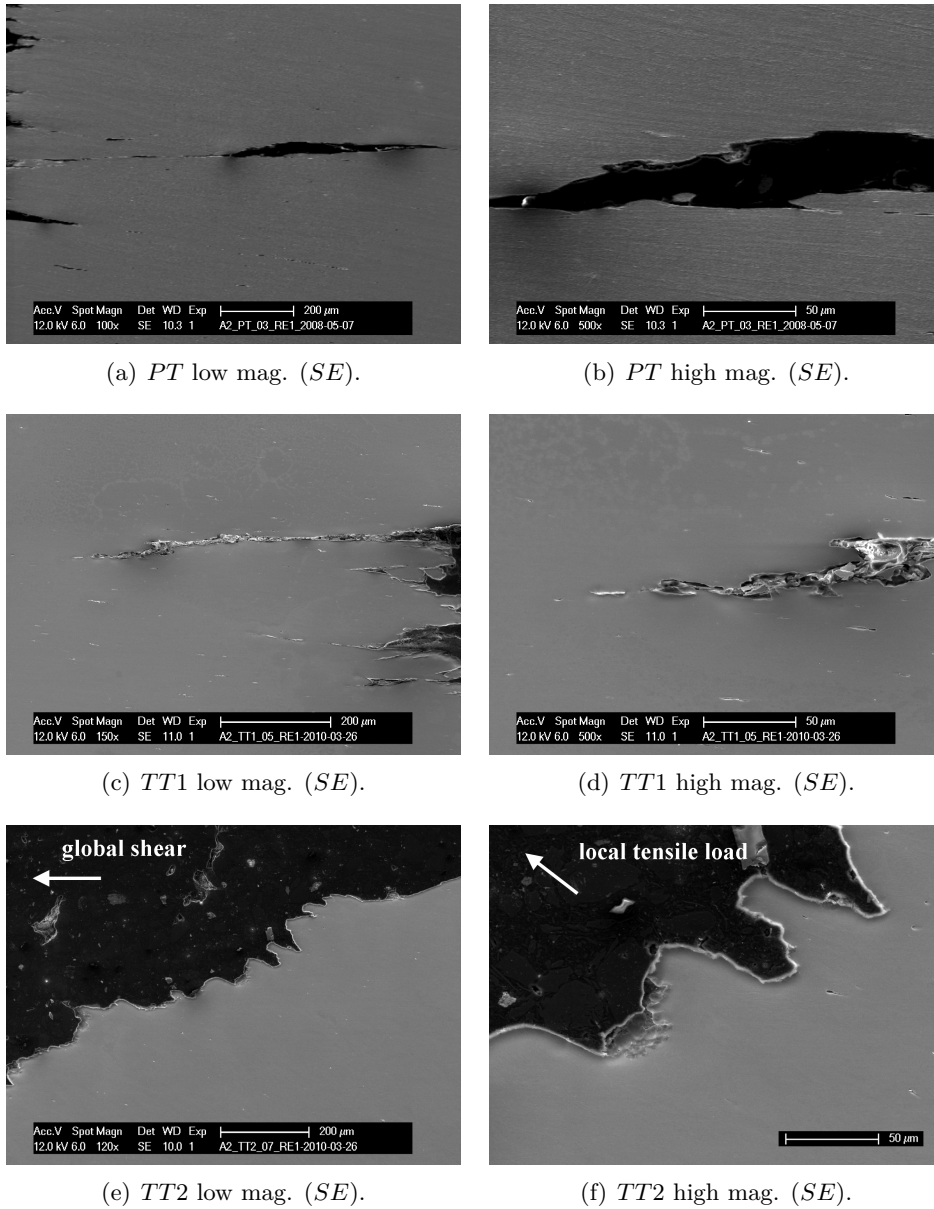


Figure 4.40: A2 torsion cross section, AT plane.

## 4.4 Void size analysis

This section provides results of the void size analysis in the *A1* lead-containing alloy. We measure evolution of voids/inclusions and characteristic shape parameters (orientation, lengths of the major and minor axes) in undeformed material and in samples fractured under various loading conditions, assuming an ellipsoid shape of the voids. We use these values to calculate the void volume fraction ( $VVF$ ). In our analysis, we consider both lead inclusions and an internal void to be one feature, thus the  $VVF$  incorporates both the lead volume fraction and internal void volume fraction. Micrographs analyzed for void orientation and void size were taken close to the fracture surfaces of tested samples. As a result, the obtained measurements refer to the situation just before the onset of coalescence and we know from Section 4.3 that coalescence in the *A1* alloy is a very localized process and does not occur distant from the created macroscopic cracks. Further details of this analysis are provided in Section 3.3.4.  $VVF$  obtained from microscopic observations of torsion samples were also compared to values calculated from densitometry measurements.

### 4.4.1 Void orientation

#### Void orientation in the undeformed material

We know from Section 3.3.4 that inclusions observed in two perpendicular planes  $AR$  and  $AT$ , have initial orientation of their major axis in the direction of the axis of the sample. This orientation occurs during the manufacturing of the bar (Figure 3.15). On the basis of this information and comparison of two inclusion size distributions obtained in the  $AR$  and  $AT$  planes (Figure 3.18), we can assume that 3D inclusions are axisymmetric in the undeformed material (around the axis of the extruded bar).

#### Void orientation in tensile samples

Figure 4.41 presents the distribution of orientation of voids in fractured tensile and notched tensile samples. The main loading and deformation are in the direction of the preferential initial void orientation, and therefore the distribution of void orientation does not differ qualitatively from the one of the undeformed material  $UD - avg$ . Quantitatively, it can be observed that in deformed samples, more voids have an orientation close to  $0 \text{ deg}$  because the grain boundaries containing inclusions tend to reorientate and elongate in the direction of loading. Further details on this mechanism will be provided below.

#### Void orientation in torsion samples

The assumption of axisymmetry of inclusions is not valid for material having undergone torsional and tensile torsional loading and an independent mea-



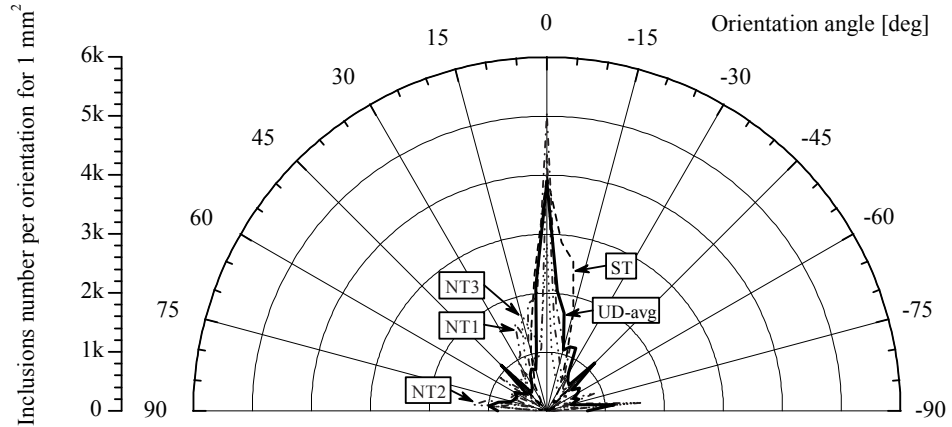


Figure 4.41: Inclusion orientation in tensile and notched tensile samples.

surement of void orientation in the *AT* and *AR* planes is necessary.

Inclusions observed in the *AT* plane reorient as shown in Figure 4.42. This orientation change originates from rotation of the matrix and elongation of inclusions. It is directly correlated to the sample twist angle to fracture presented in Figure 4.4. The higher the twist angle to fracture, the larger the void rotation.

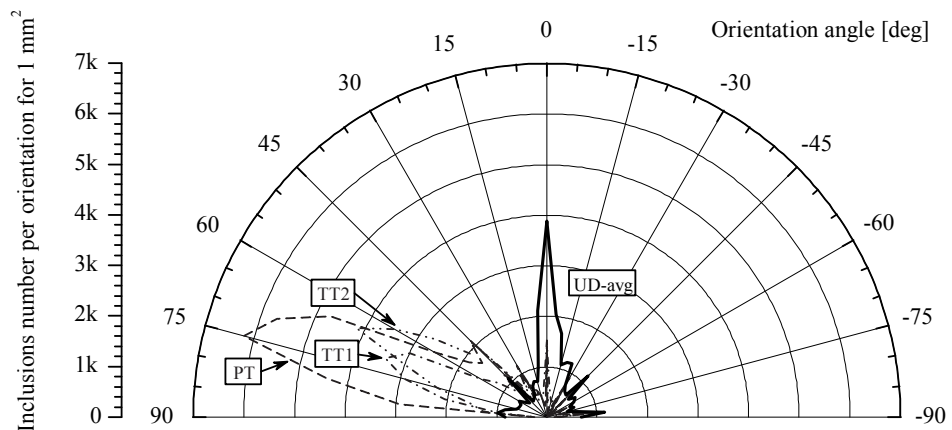


Figure 4.42: Inclusion orientation in *AT* plane for torsional loadings.

Figure 4.43 depicts the distribution of void orientation in the *AR* plane. Due to the "squeezing" resulting from rotation in the *AT* plane, inclusions observed in the *AR* plane change their aspect ratio. The resulting preferential orientation is thus perpendicular to the initial orientation. *TT2* loading is an exception as the preferential orientation is not pronounced, and the peak of the orientation distribution is in the direction of the sample's axis. High axial

load prevents a dramatic change in the inclusion aspect ratio and the resulting orientation distribution is more random.

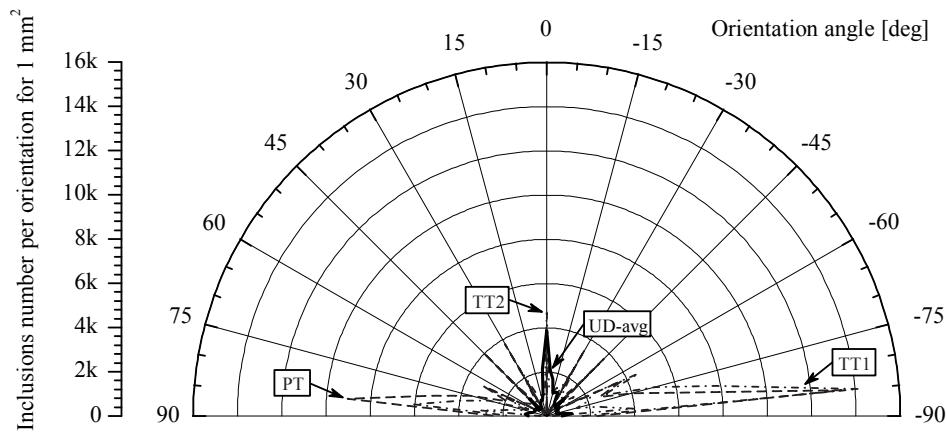


Figure 4.43: Inclusion orientation in AR plane for torsional loadings.

### Void orientation - explanation

The mechanism of reorienting inclusions to be aligned with the main loading direction is explained in Figure 4.44. Some of the inclusions appear at grain boundaries, which, in general, have random orientations (left image). After deformation, grain boundaries and the inclusions trapped between them, rotate because of elongation of the grains. In Figure 4.44 the initial configuration is drawn as dotted line for comparison.

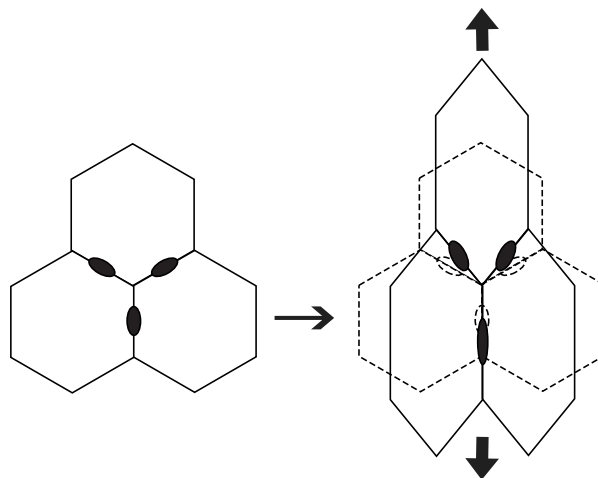


Figure 4.44: Behavior of inclusions at grain boundaries.

The change in orientation of inclusions in the  $AR$  plane to become perpendicular to the initial direction, mentioned in Section 4.4.1 as "squeezing", is explained in Figure 4.45. Let us consider an inclusion which is initially ellipsoidal and elongated in the direction of the bar. In this case, the  $AT$  and  $AR$  perpendicular planes pass through its center. The position of the two planes is associated with the initial shape of the sample as described in Section 3.3.4, and does not change. The initial shape of the inclusion is drawn as thin lines in Figure 4.45, and the shape after torsional deformation is drawn as thick lines. In the  $AT$  plane we observe how the void elongates and rotates during deformation. Seen in the  $AR$  plane, the void seems to be "squeezed" even if the void can grow in terms of volume. The change of the aspect ratio (and thus orientation) in the  $AR$  view, is caused mainly by rotation of the inclusion in the  $AT$  plane although a certain level of real squeezing (shortening of the minor axis) is also observed.

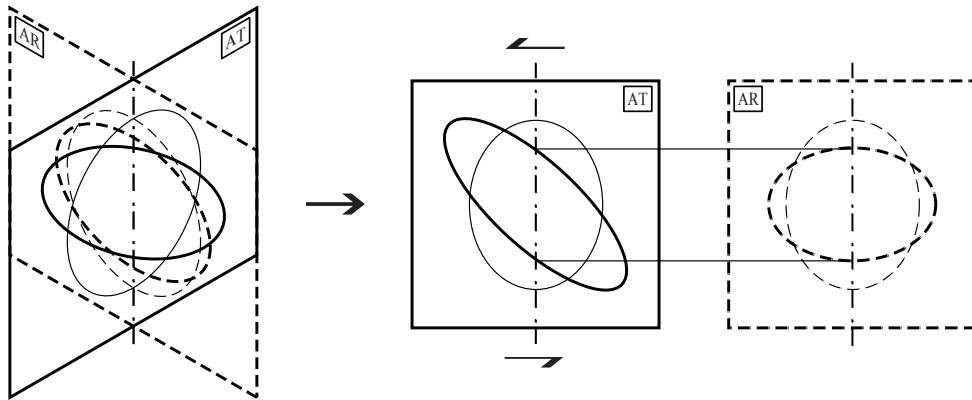


Figure 4.45: Inclusion deformation in torsional loading.

#### Void orientation: summary and implications

Orientation of the major axis of the inclusions observed in the  $AT$  and  $AR$  planes as a function of loading conditions is summarized in Figure 4.46. The dots represent the orientation angles (peaks of orientation distribution) in the  $AT$  plane, while the squares represent the orientation angles in the  $AR$  plane. Thin continuous, and dotted lines indicate the scatter of orientation in the  $AT$  and the  $AR$  planes respectively.

The peak in the distribution of orientation, means the orientation angles ( $\pm 2.5$  deg) for which the largest number of inclusions in  $1 \text{ mm}^2$  of sampled surface was observed. The scatter lines show angles of orientation for which the observed number of inclusions is still larger than the threshold value. The threshold value was established to filter the randomly oriented inclusions appearing in each sample, and is defined as twice the average number of inclusions

per angle step. The average number of inclusions per angle step was calculated by dividing the total number of observed inclusions in the whole sample by the number of angle steps (37:  $-90, -85, \dots, 85, 90$ ).

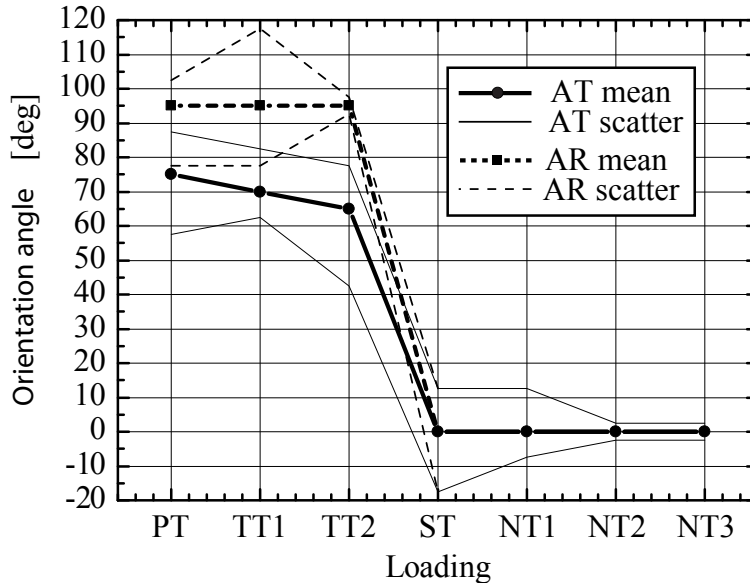


Figure 4.46: Void orientation angle as a function of loading conditions, observed in *AT* and *AR* planes in fractured samples.

In the tensile and notched tensile samples, the *AT* and *AR* planes are indifferent as the inclusions are more or less axisymmetric and oriented in the direction of the sample axis. As a consequence, the lengths of the major and minor axes of the inclusion observed in the *AT* plane are equal to the major and minor axes of the 3D axisymmetric ellipsoid.

The peak orientation angles for torsional and tensile-torsional samples observed in the *AT* plane change as the inclusions elongate and rotate when the material deforms - rotation of voids increases with material deformation. The orientation of inclusions in torsional samples observed in the *AR* plane also changes, but in this case the change results from the change in the aspect ratio. Inclusions do not rotate in the *AR* plane and as a result, the major axis of inclusions observed in the *AT* and *AR* planes stay mutually perpendicular during torsional deformation (see Figure 3.19). This allows us to measure major and minor axis of the 3D ellipsoid by measuring major and minor axes of the 2 ellipses in the *AT* and *AR* planes, as explained in detail in Section 3.3.4.

The observed scatter of inclusion orientations may be caused by the position of the lead inclusions. They are likely to appear at grain boundaries

and be squeezed in between the grain faces so that their longer axis is parallel to the orientation of the grain boundaries, which are random. Even after deformation, some of the grain boundaries are not parallel to the main loading direction. Some of the bigger inclusions appear at triple points and this also contributes to the scatter, as their shape cannot be considered as elliptical anymore. For size analysis, the very large and very small inclusions will not be considered.

#### 4.4.2 Void size distributions

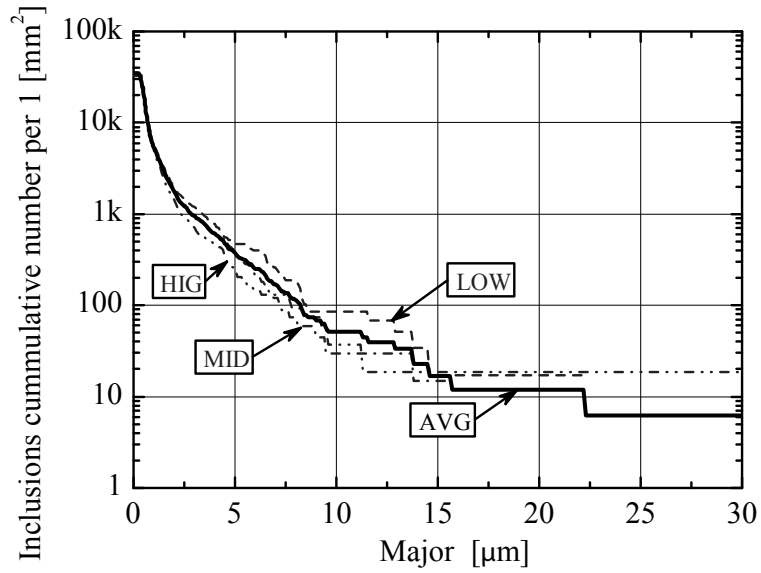
In this section we present the measured size distributions of the major ( $M$ ) and two minor ( $m_1, m_2$ ) inclusion axes. The size distributions were established following the procedure described in Section 3.3.4. For each loading case, results are presented for the whole data set and for the representative data set (see Section 3.3.3). In each figure, subfigure a) represents the whole data set, and subfigure b) represents the representative data range.

Figure 4.47 represents the size distribution of the major axis  $M$  measured 3 times in the  $AR$  plane of the undeformed sample. Measurements were taken at a distance of 4 mm ( $LOW$ ), 7 mm ( $MID$ ) and 10 mm ( $HIG$ ) from the round bar axis and so Figure 4.47 represents the scatter due to processing. Figure 4.47(a) was previously presented (see Figure 3.17) and is repeated here for convenience.

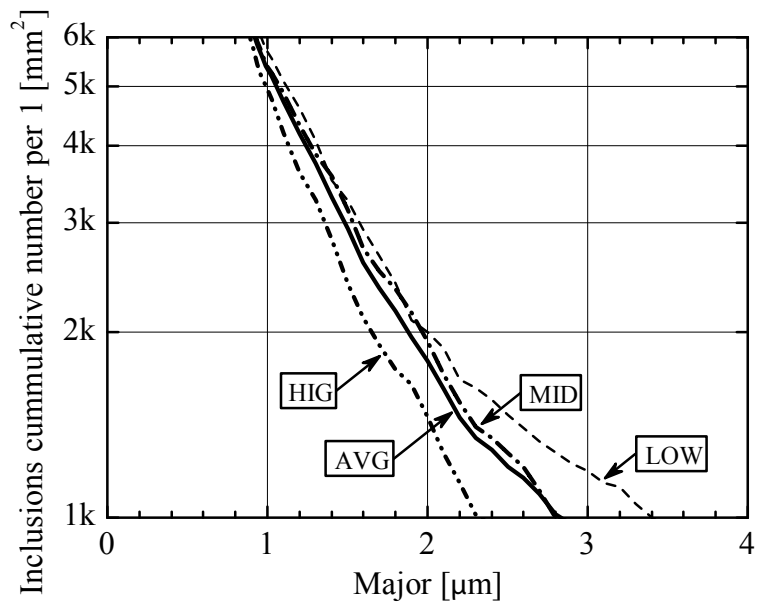
Figure 4.48 represents the size distribution of the major ( $M$ ) and minor ( $m$ ) axes in undeformed material measured in the  $AT$  and  $AR$  planes, and can be interpreted as "measurement" scatter or size distribution scatter. Figure 4.48(a) was already presented above (see Figure 3.18) and comparing it with Figure 4.48(b), we notice that results in the representative data range are more reproducible.

Figures 4.49 and 4.50 represent the  $M$  and  $m$  size distributions respectively for tensile dominated loadings. We see that the major axis  $M$ , elongates under every loading condition although the order of the distributions is not as expected. We had expected that the  $M$  axis would elongate more in samples with smaller stress triaxiality. If in the  $ST$  sample the elongation is the highest, for samples  $NT1$ ,  $NT2$  and  $NT3$ , the  $M$  axis elongates less when the stress triaxiality is higher. The minor axis  $m$  shortens in  $ST$  and  $NT1$ , stays almost unchanged in  $NT2$  and elongates in  $NT3$  samples. When analyzing these results we need to remember that the differences between results for different loadings are relatively small compared to the measurement scatter presented in Figure 4.48.

The differences between size distributions of  $M$ ,  $m_1$  and  $m_2$  under shear dominated loadings are more pronounced compared to tensile loadings because

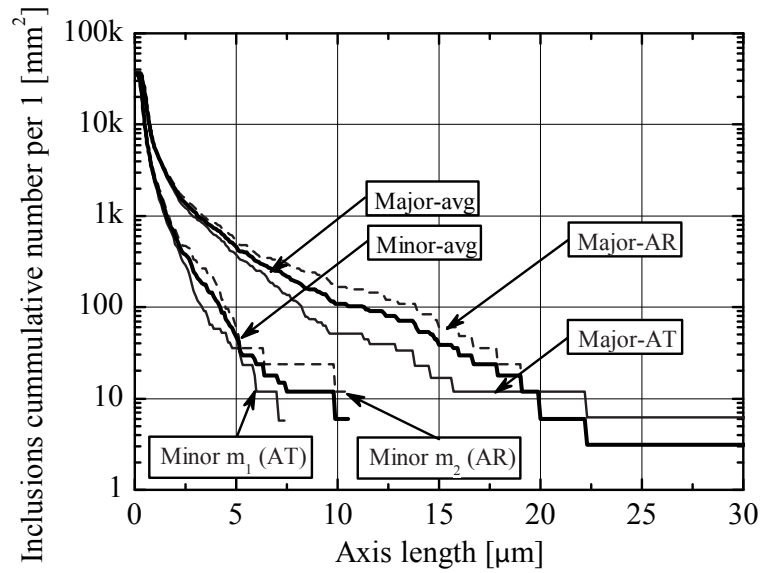


(a) Full data range.

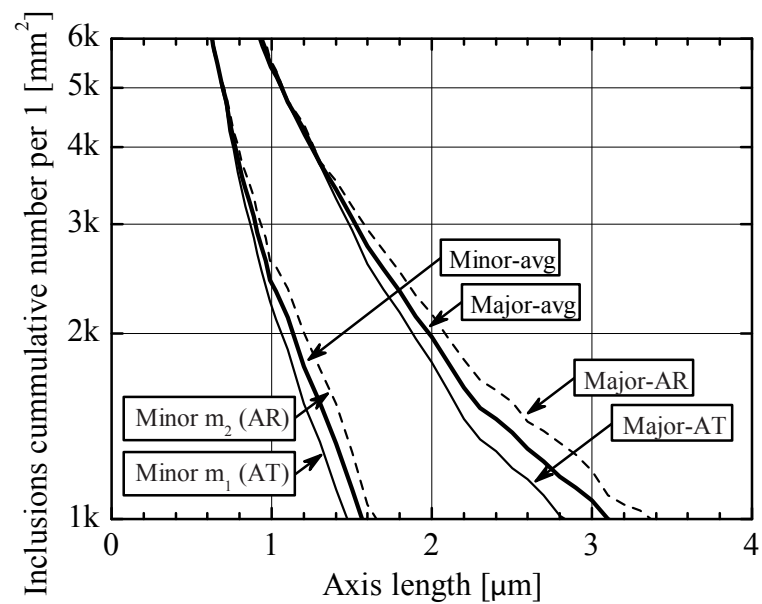


(b) Representative data range.

Figure 4.47: Cumulative size distribution of the major axis  $M$  measured in the AR plane at three locations in the same undeformed original round bar.

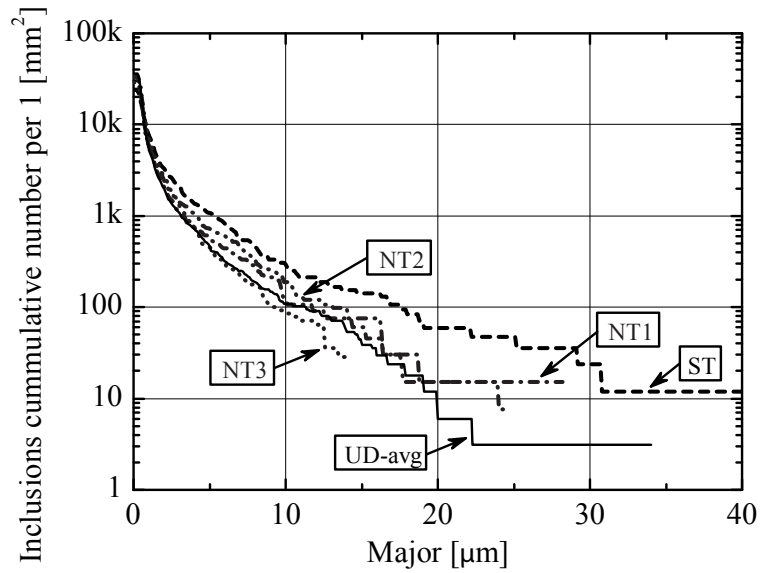


(a) Full data range.

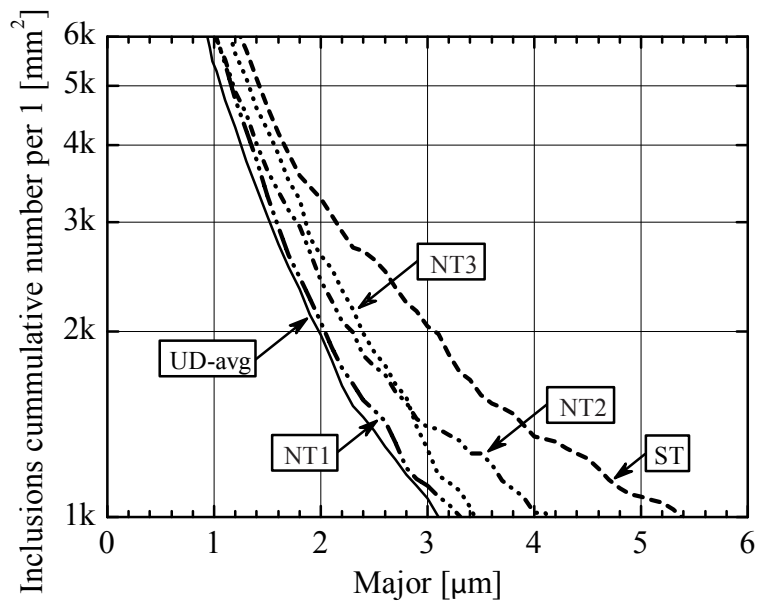


(b) Representative data range.

Figure 4.48: Cumulative size distribution of major ( $M$ ) and minor ( $m$ ) axis in undeformed material.



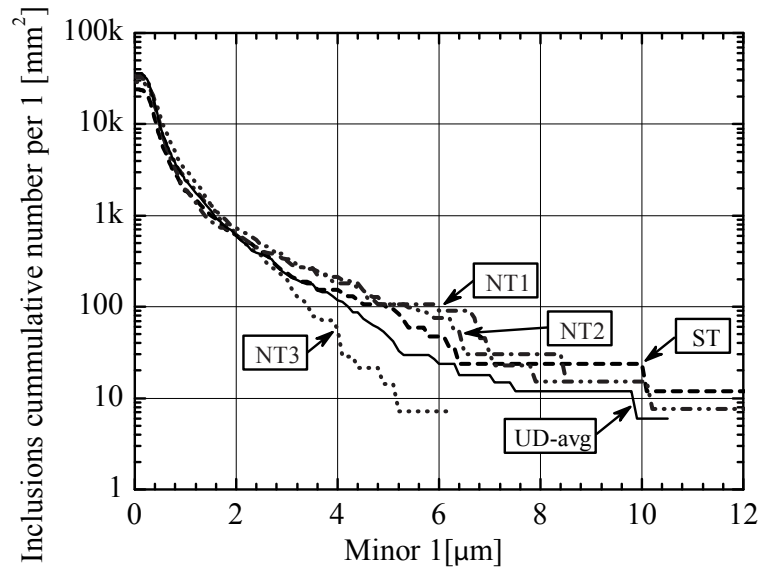
(a) Full data range.



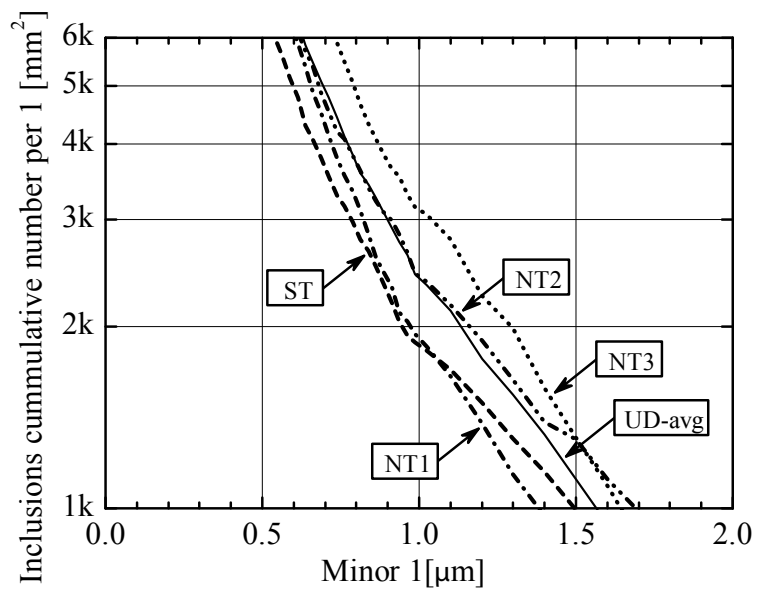
(b) Representative data range.

Figure 4.49: Cumulative size distribution of the major axis ( $M$ ) in tensile and notched tensile tests.





(a) Full data range.



(b) Representative data range.

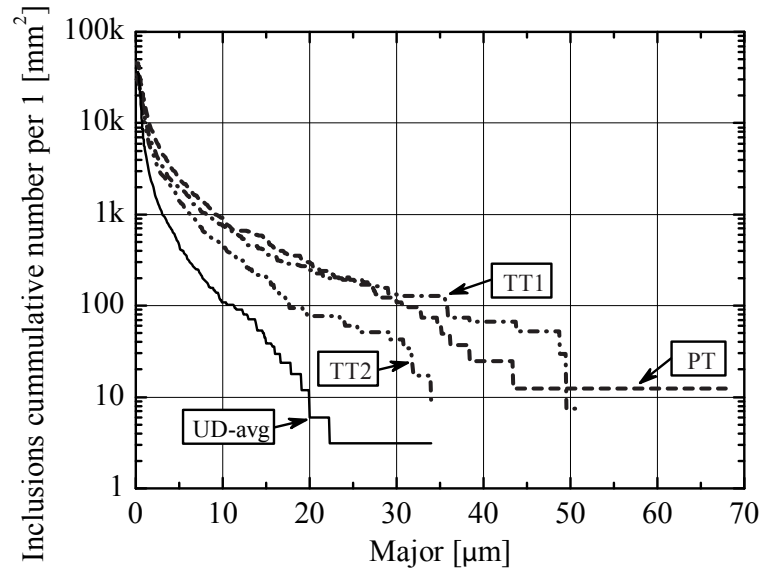
Figure 4.50: Cumulative size distribution of the minor axis ( $m$ ) in tensile and notched tensile tests.

strains to failure are significantly higher. The major axis elongates more for higher sample twist angles (Figure 4.51). The first minor axis shortens for all loading conditions (Figure 4.52). The distribution of  $m_2$  sizes is very surprising because  $m_2$  elongates under every shear dominated loading condition (Figure 4.53). The direction of  $m_2$  is the radial direction of the thin-walled tubular sample, which is a direction with no nominal load.

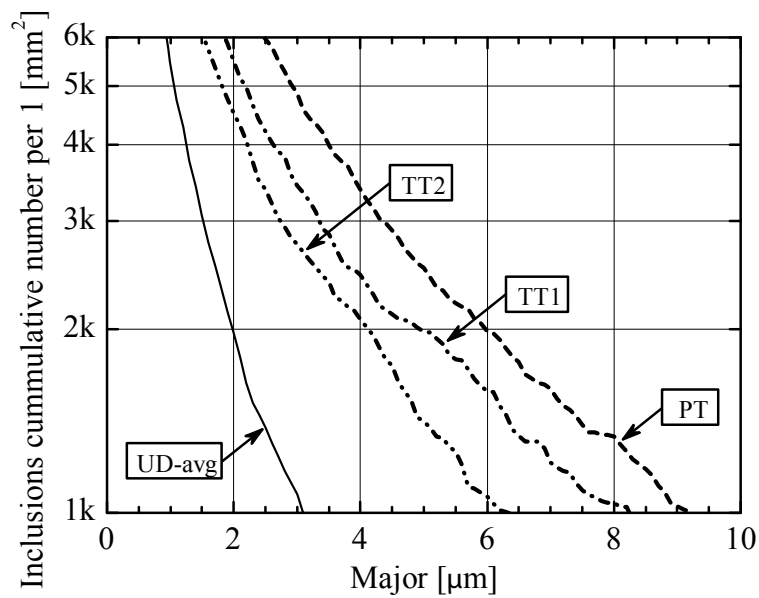
Similar void axis length analysis was performed for interrupted  $PT$  tests. Results of this analysis are presented in Figures 4.54, 4.55 and 4.56, for  $M$ ,  $m_1$  and  $m_2$  respectively. In the graphs, the  $UD - avg$  curve represents the average distribution in the undeformed material, the  $PT$  curve represents distribution in the fractured sample, while  $PT - 50$ ,  $PT - 70$  and  $PT - 105$  curves represent distributions in tests interrupted at a sample twist angle corresponding to the number in the marking. We observe that both  $M$  and  $m_2$  axes elongate also in the interrupted  $PT$  test.

In addition, computed tomography (CT) was employed to confirm the observation of void elongation in the radial direction (see Section 3.3.7 for details). We measured size distributions of inclusions in the radial direction, which roughly corresponds to the technique used to create  $m_2$  size distributions presented above. We performed this measurement on a sample tested under  $PT$  loading conditions up to fracture and on undeformed material as reference. Size distributions of  $m_2$  obtained using computed tomography, and presented in Figure 4.57 also confirm significant elongation of inclusions in the radial direction. However due to the different resolution of the CT technique, we measure mainly large inclusions outside of the representative data range.

Results concerning the elongation of the  $m_2$  axis obtained with different techniques and for different levels of deformation are consistent, and show  $m_2$  elongation in the radial direction which is a direction with no nominal load.

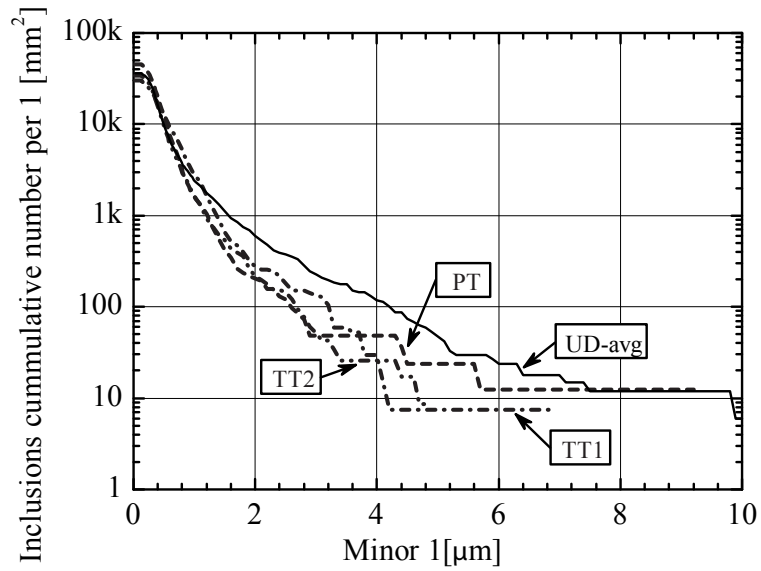


(a) Full data range.

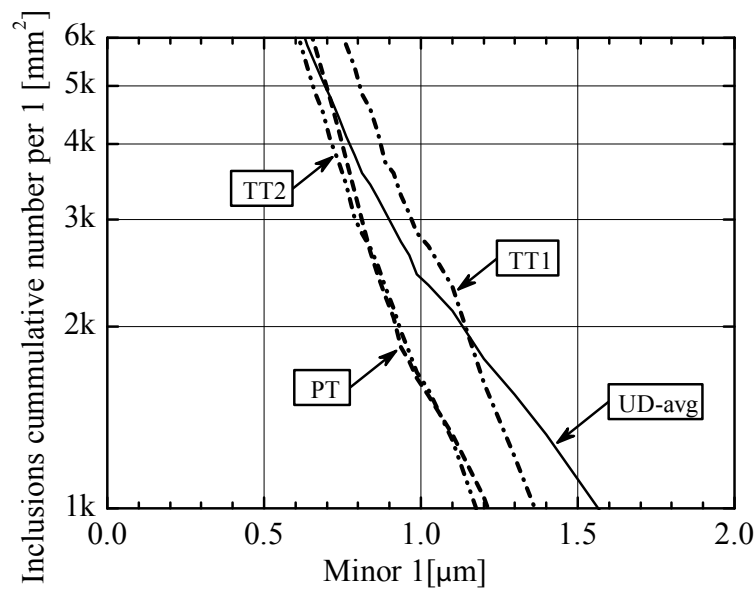


(b) Representative data range.

Figure 4.51: Cumulative size distribution of the major axis ( $M$ ) in torsion and tensile torsion tests.

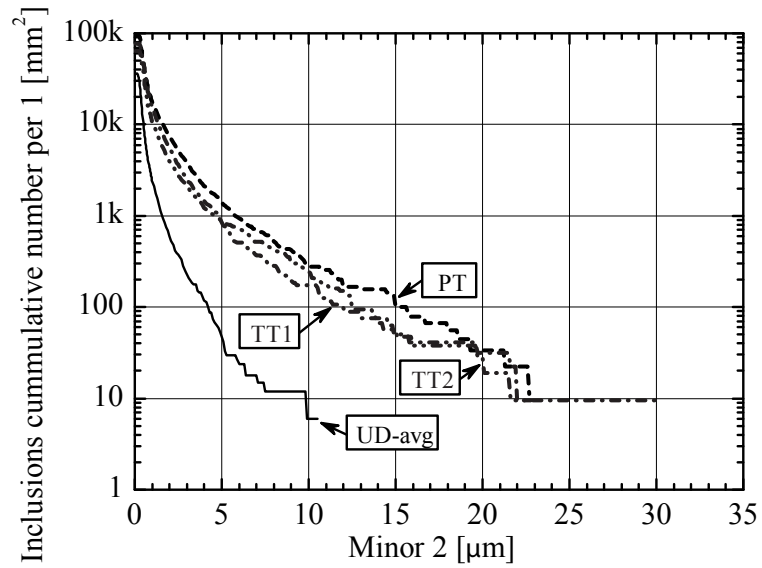


(a) Full data range.

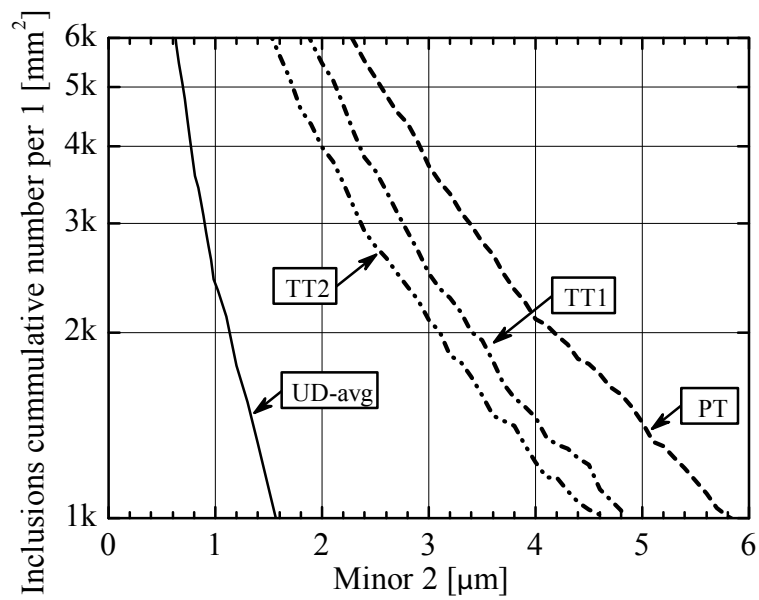


(b) Representative data range.

Figure 4.52: Cumulative size distribution of the first minor axis ( $m_1$ ) in torsion and tensile torsion tests.

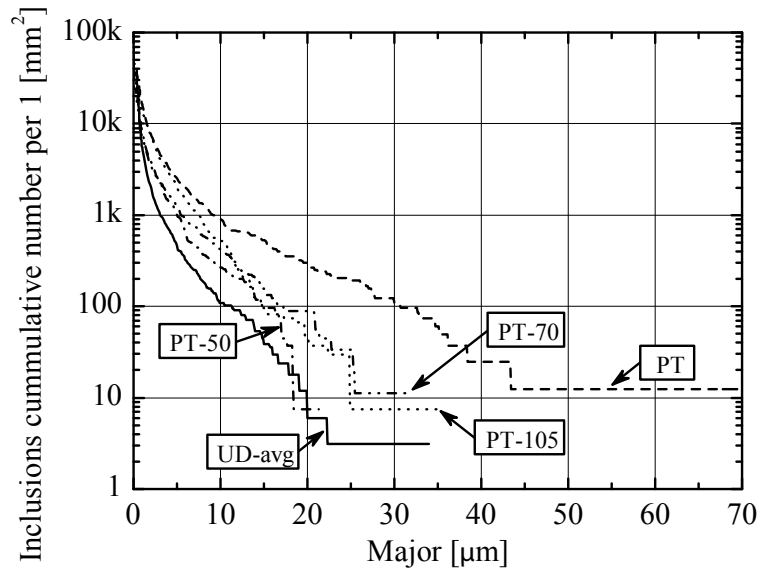


(a) Full data range.

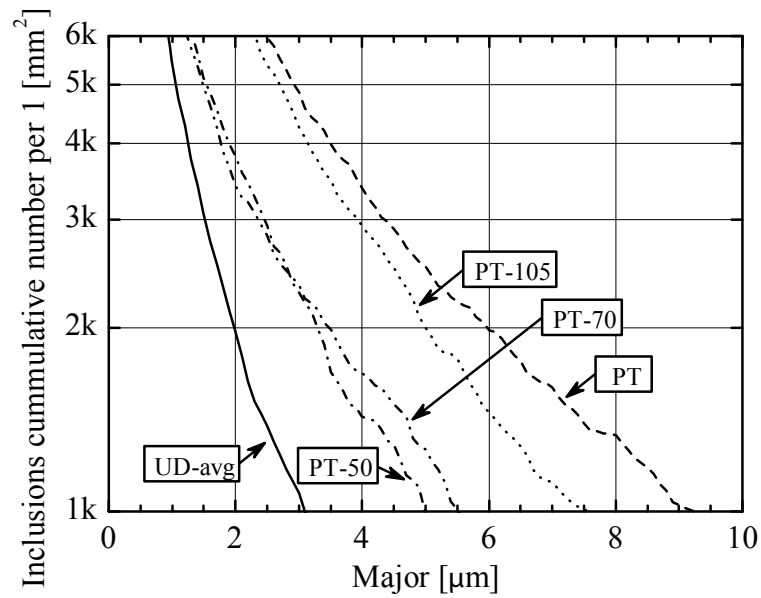


(b) Representative data range.

Figure 4.53: Cumulative size distribution of the second minor axis ( $m_2$ ) in torsion and tensile tests.

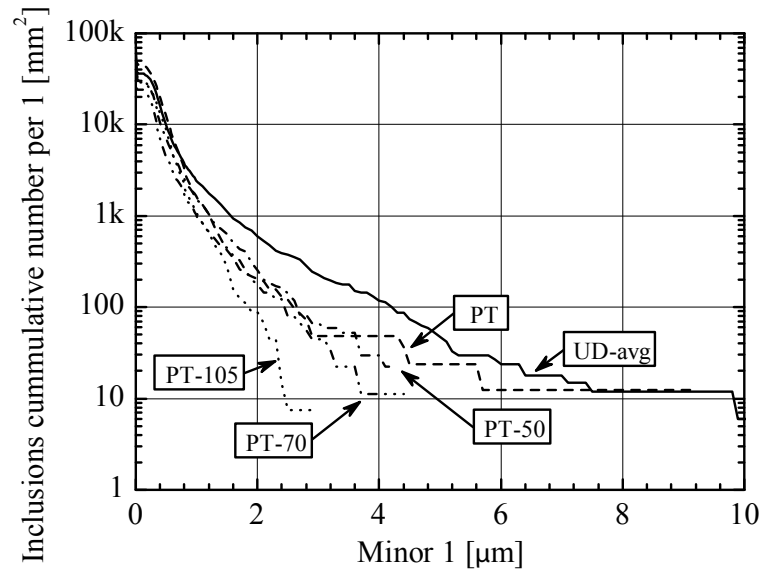


(a) Full data range.

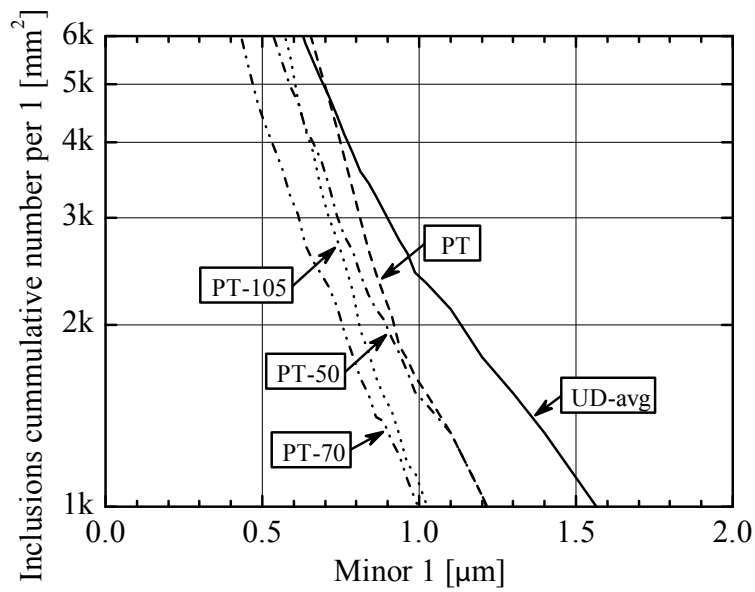


(b) Representative data range.

Figure 4.54: Cumulative size distribution of the major axis ( $M$ ) in interrupted torsion tests.

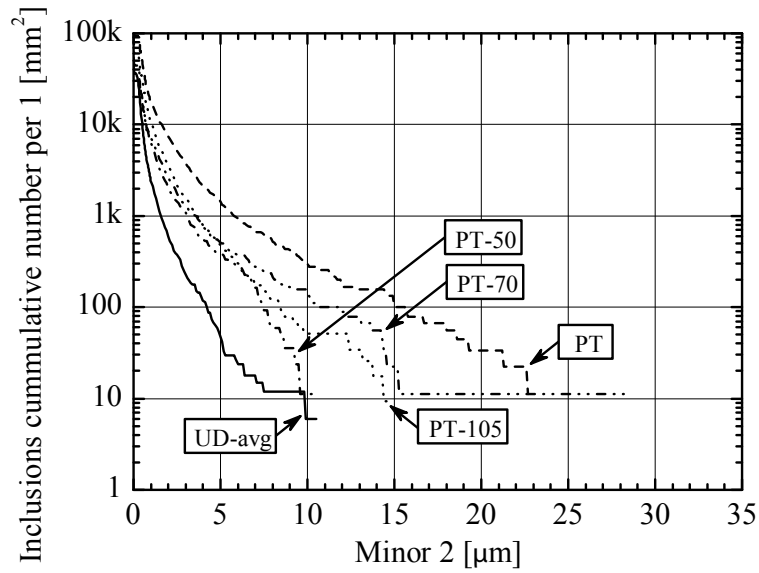


(a) Full data range.

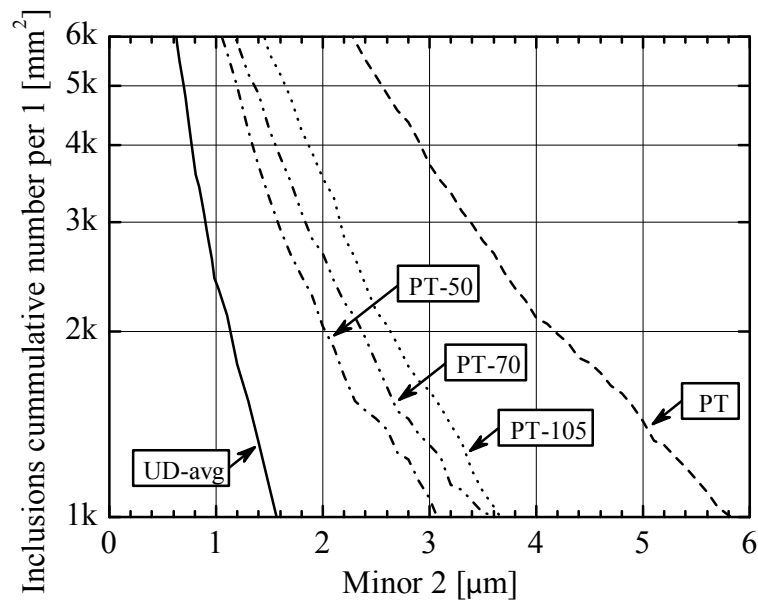


(b) Representative data range.

Figure 4.55: Cumulative size distribution of the first minor axis ( $m_1$ ) in interrupted torsion tests.



(a) Full data range.



(b) Representative data range.

Figure 4.56: Cumulative size distribution of the second minor axis ( $m_2$ ) in interrupted torsion tests.



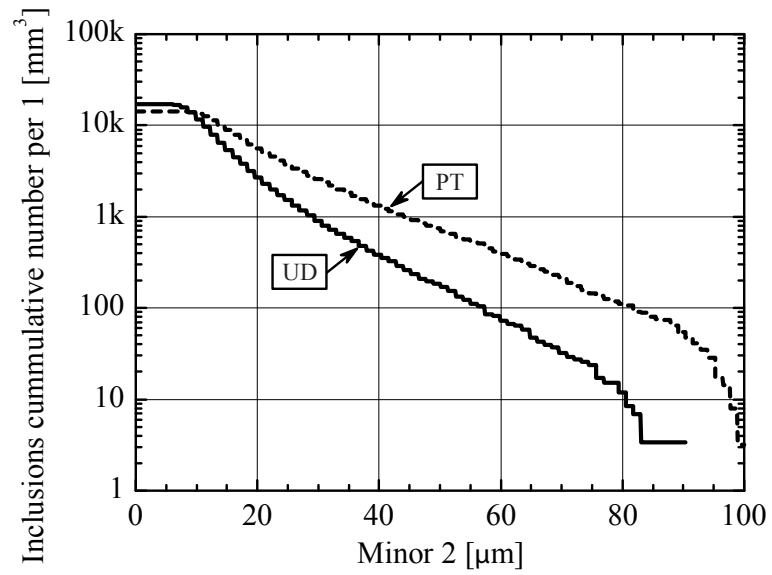


Figure 4.57: Cumulative size distribution of the second minor axis ( $m_2$ ) in pure torsion tests obtained with computed tomography.

### 4.4.3 Void elongation

Later in this section we present void axis elongation factors as a function of the initial void axis length. The plots presented reveal how the three void characteristic parameters (axis lengths), evolve under load depending on their initial size in the non-deformed material, and contain essentially the same information presented in Section 4.4.2 but presented in an way that is easier to interpret. Before presenting the void evolution data in deformed material, we use Figure 4.48 showing void size distributions in undeformed material to estimate data scatter and the initial shape of inclusions.

#### Data scatter

The scatter of the void axis elongation factor due to nonhomogeneous distribution of inclusions can be estimated using Figure 4.48, which contains the major and minor void axis size distributions in undeformed material obtained from a sample cut in the *AT* and the *AR* planes.

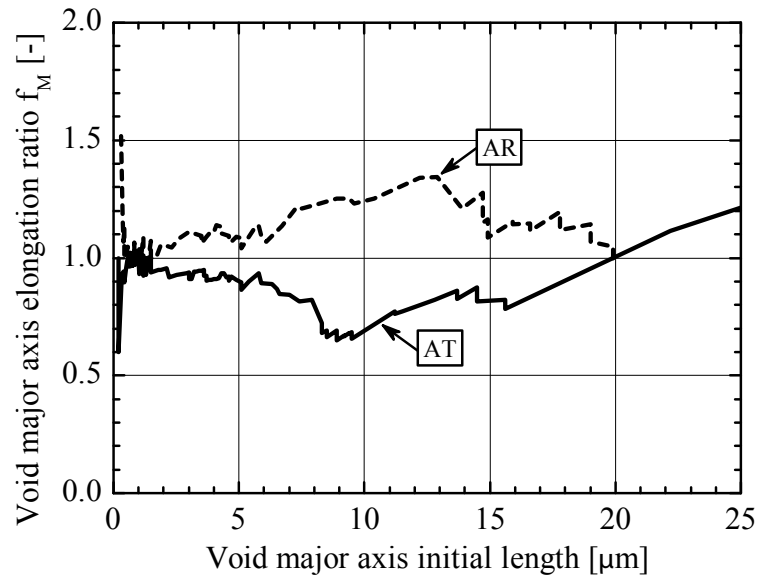
Distributions of  $M$  in the *AT* and *AR* planes are two independent measurements of the same parameter which allows the calculation of an average  $M$  distribution for use in further calculations, as discussed in Section 3.3.4. Using this average  $M$  distribution as a reference, we can use two original  $M$  distributions in the *AT* and *AR* planes to estimate void elongation factor error due to data scatter. In the calculations we follow the procedure described in Section 3.3.4, and in particular Equation 3.1, where original  $M$  distributions are the numerator and the average  $M$  distribution is the denominator.

Figure 4.58 presents the results of the described scatter analysis. If the error due to scatter was 0 ( $M$  distributions in the *AT* and *AR* planes were the same as the averaged  $M$  distribution), the obtained elongation factor  $f_M$  would be 1. Any deviations from 1 measures the error due to data scatter. Within the representative data range presented in Figure 4.58(b), the maximum observed error due to data scatter (nonhomogeneous distribution of voids) is  $\pm 10\%$ .

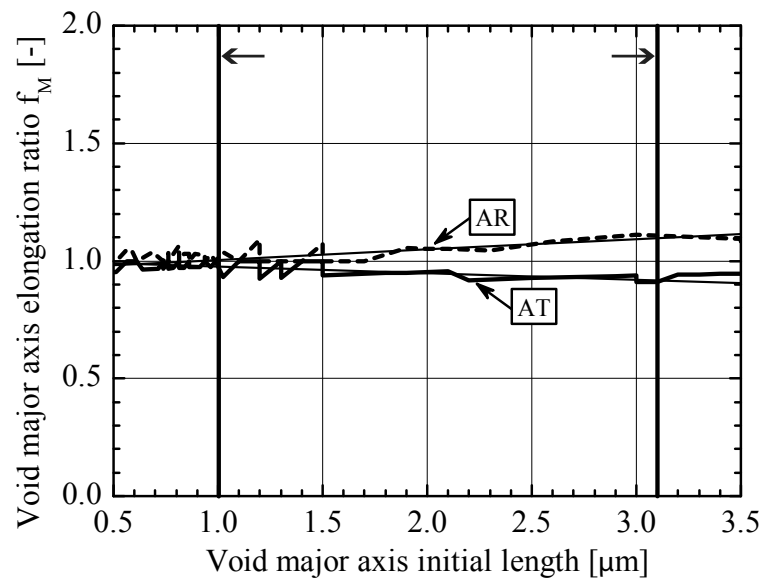
For the largest inclusions in the representative data range ( $M = 3.1 \mu\text{m}$ ), the calculated error of  $\pm 10\%$  corresponds to  $\pm 0.31 \mu\text{m}$  that is approx.  $\pm 5$  pixels. We therefore conclude that the error due to scatter is much higher than other possible errors (i.e. due to image resolution - Section 3.3.3) and assume it as total error.

#### Initial shape of voids

The initial shape of voids in terms of the void aspect ratio  $W_0$ , can be calculated using Figure 4.48, which contains major and minor void axis size



(a) Full data range.



(b) Representative data range.

Figure 4.58: Estimate of the  $f$  error.

distributions in the undeformed material obtained from a sample cut in the  $AT$  and the  $AR$  planes. The procedure we follow for this calculation is described in Section 3.3.4.

Figure 4.59 presents the initial void aspect ratio  $W_0$  as a function of the initial major axis length. We observe in Figure 4.59 that the large voids are more elongated. This may result from the tendency of large inclusions to appear at grain boundaries. This and other results will be commented on and discussed in Chapter 5.

### Void elongation factors plots

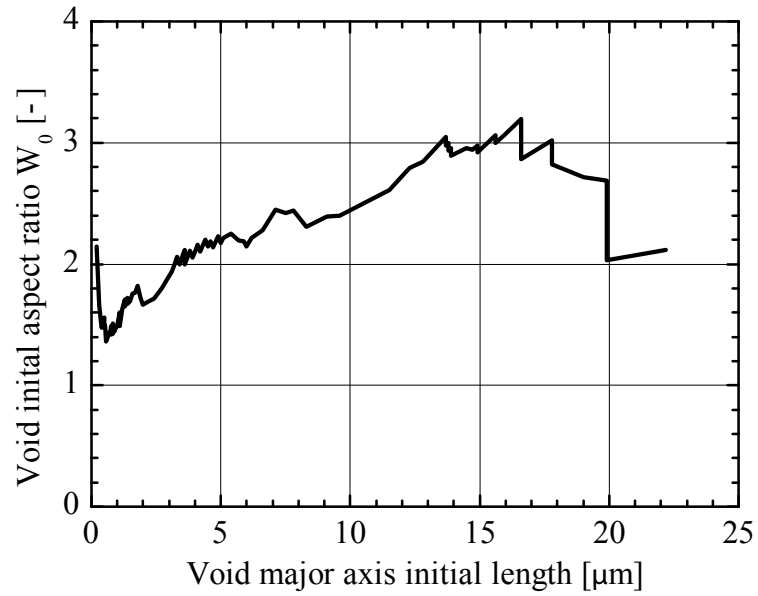
Figures 4.60-4.65 present the void axis elongation factors as a function of the initial void axis length, and contain essentially the same information as Figures 4.48-4.56 presented in Section 4.4.2. However, information presented in this section is easier to interpret. Comments referring to axis length changes presented in Section 4.4.2 also apply to plots shown in this section. The transformation of cumulative distributions to void elongation factors is discussed in Section 3.3.4.

The major void axis elongation factor  $f_M$  is defined in Equation 3.1. The first minor void axis elongation factor  $f_{m1}$  and the second void axis elongation factor  $f_{m2}$  are defined in a similar way. If the void axis elongation factor is bigger or smaller than one, it means that the axis elongated or shortened, respectively, during deformation.

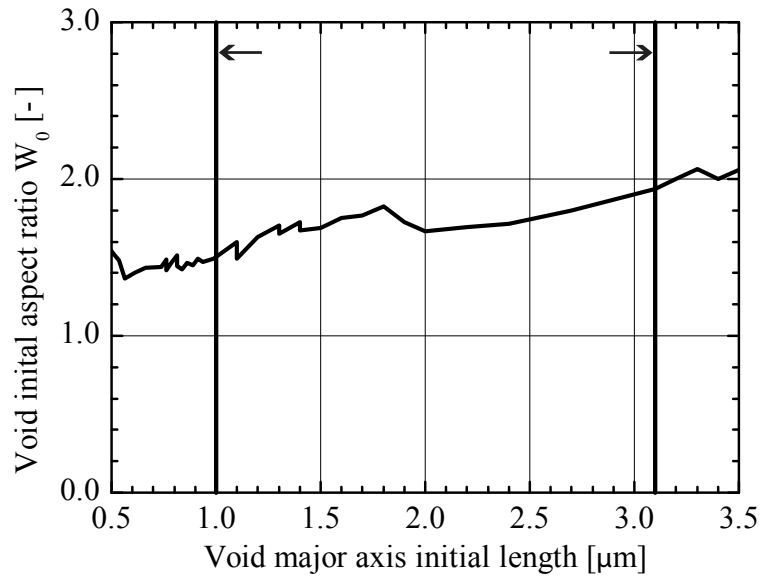
For each loading case, results are presented for the whole data set and for the representative data set (see Section 3.3.3). In each figure, subfigure a) represents the whole data set, and subfigure b) the representative data range.

Measurement of elongation of the  $m_2$  axis is repeated for verification using computer tomography. Figure 4.66 presents  $f_{m2}$  as a function of the second minor void axis initial length for the whole data set and for a specimen tested in  $PT$ . Results present significant elongation in the radial direction, which is a direction in which in  $PT$  there is no nominal load. However, the extent of elongation measured by tomography is much smaller compared to that observed in Figure 4.63 or Figure 4.65. With the CT technique we only measure large inclusions outside of the representative data range.

The evolution of void axes is summarized in Table 4.1. It presents values of the average axis elongation factors ( $f_M$ ,  $f_{m1}$  and  $f_{m2}$ ), void growth factors  $f_V$  and calculated  $VVF$  in the representative data range.

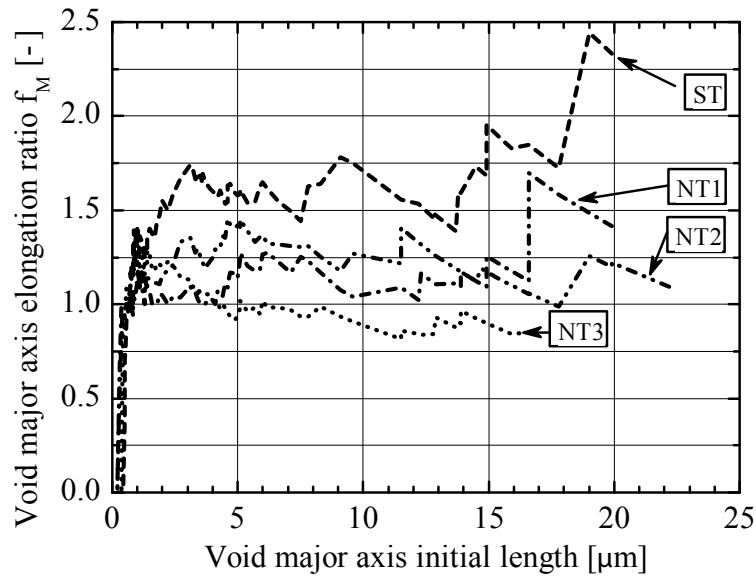


(a) Full data range.

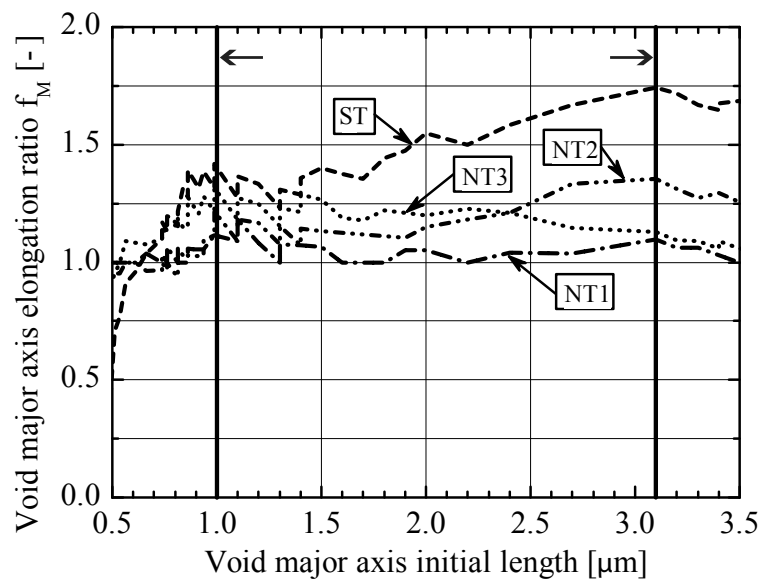


(b) Representative data range.

Figure 4.59: Initial void aspect ratio  $W_0$  as a function of major axis initial length.

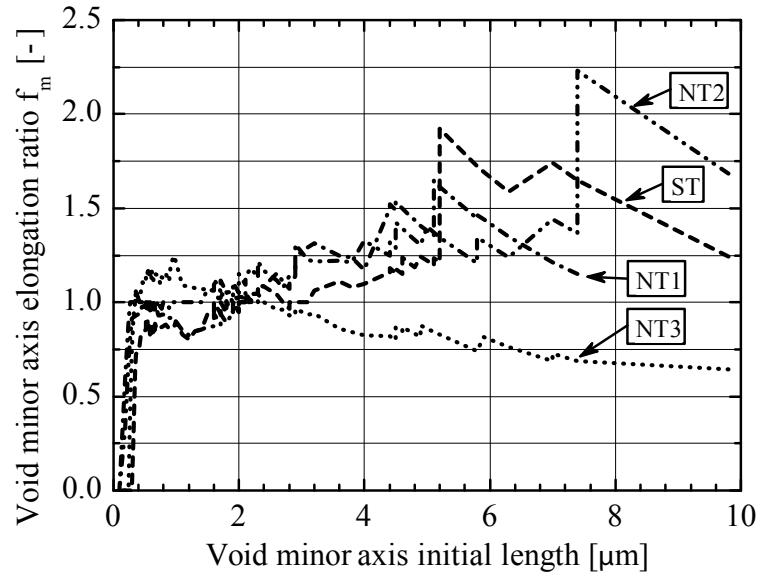


(a) Full data range.

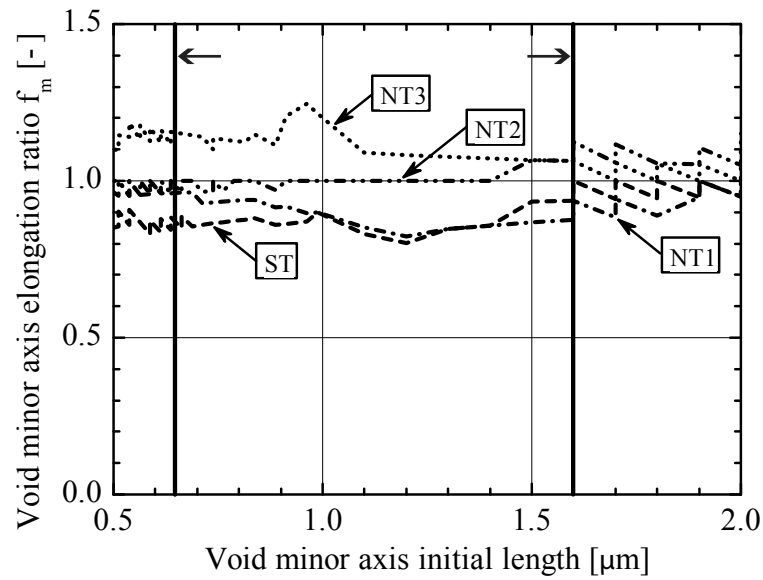


(b) Representative data range.

Figure 4.60: Major void axis elongation factor  $f_M$  at fracture under tensile loading as a function of the initial major axis length.

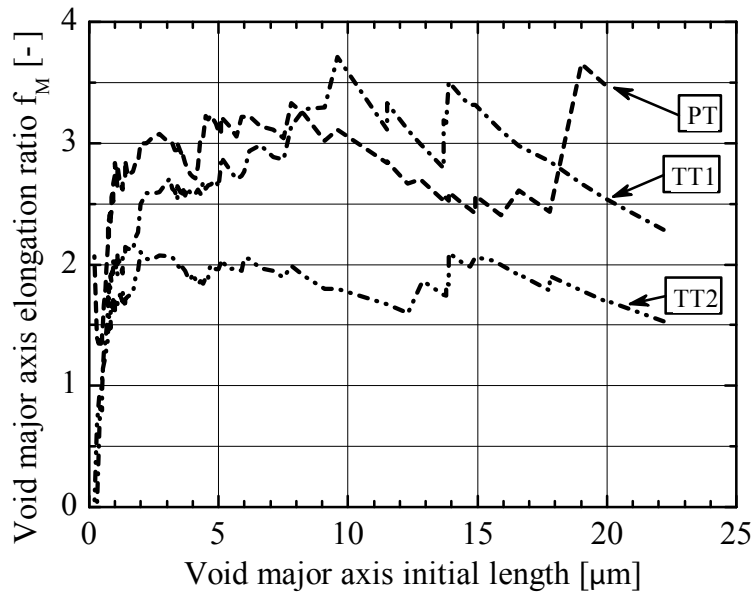


(a) Full data range.

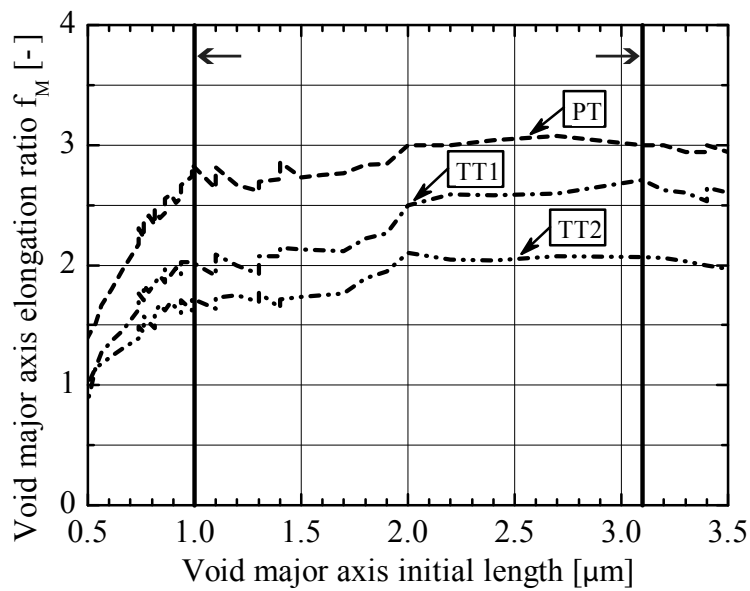


(b) Representative data range.

Figure 4.61: Minor void axis elongation factor  $f_m$  at fracture under tensile loading as a function of the initial minor axis length.



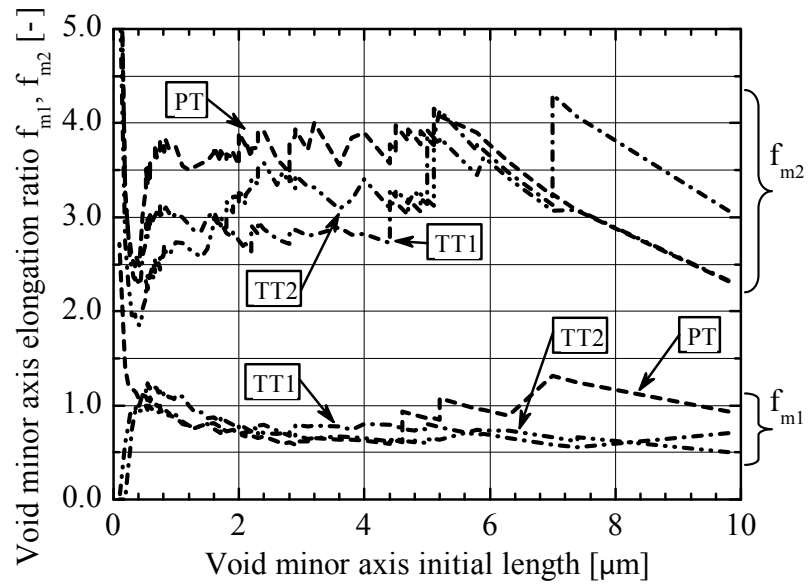
(a) Full data range.



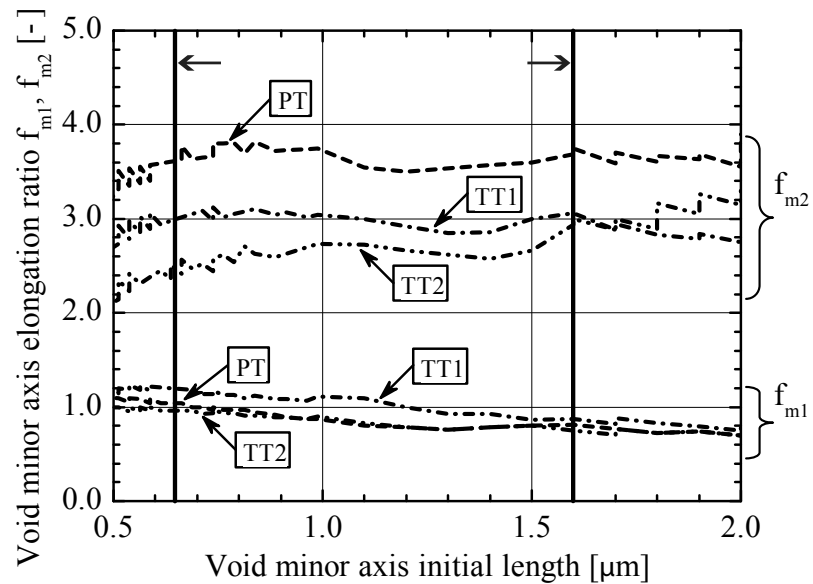
(b) Representative data range.

Figure 4.62: Major void axis elongation factor  $f_M$  at fracture under torsional loading as a function of major axis initial length.



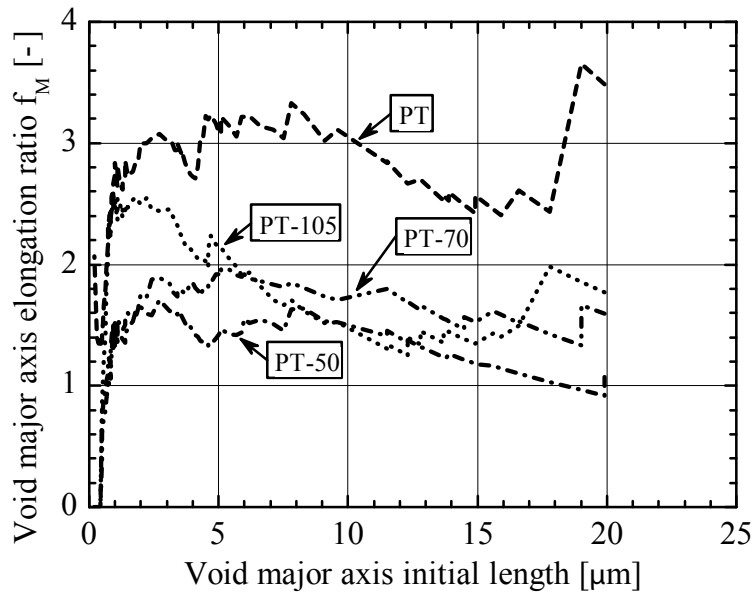


(a) Full data range.

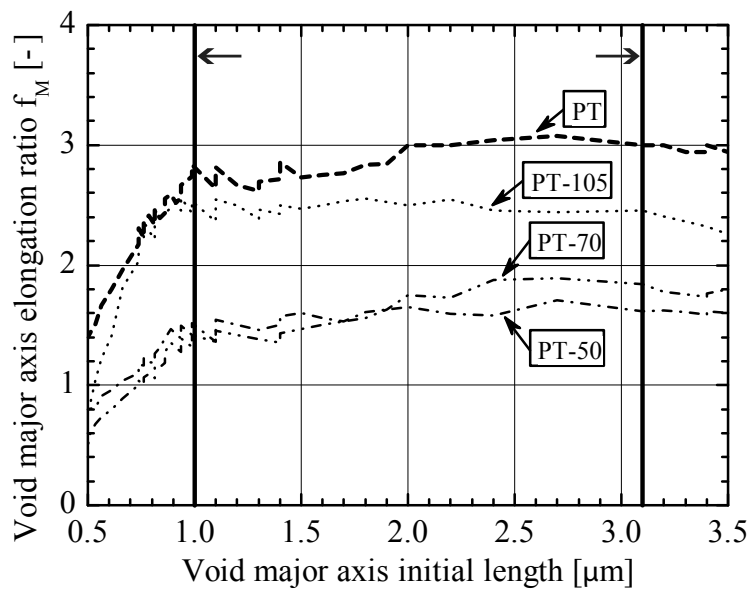


(b) Representative data range.

Figure 4.63: Minor void axis elongation factor  $f_m$  at fracture under torsional loading as a function of minor axis initial length.

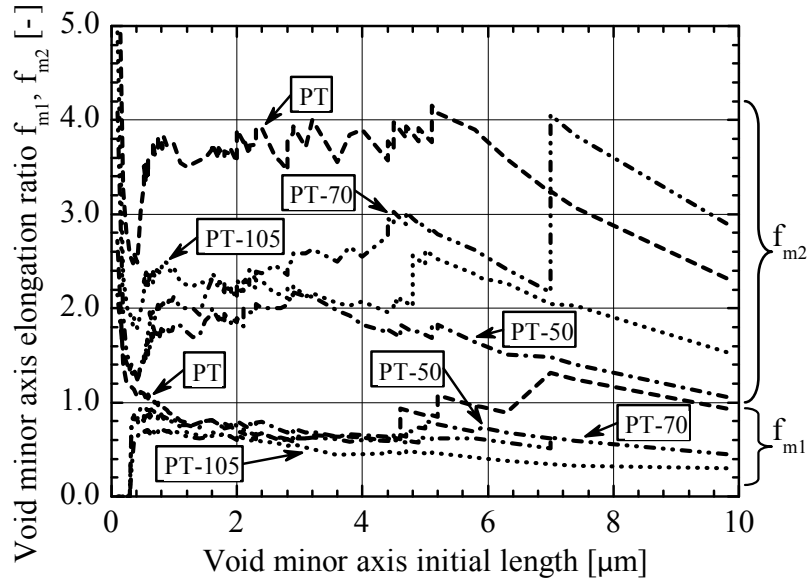


(a) Full data range.

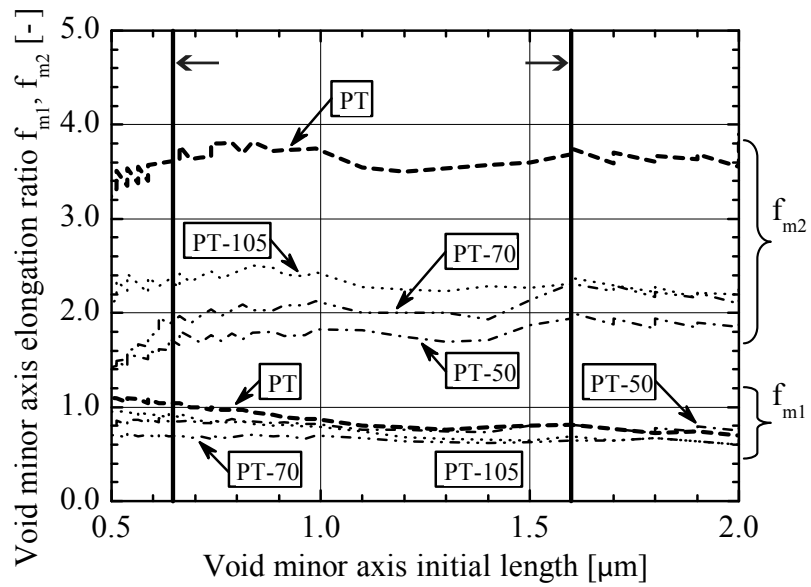


(b) Representative data range.

Figure 4.64: Major void axis elongation factor  $f_M$  at various angles of torsional deformation as a function of major axis initial length.



(a) Full data range.



(b) Representative data range.

Figure 4.65: Minor void axis elongation factor  $f_m$  at various angles or torsional deformation as a function of minor axis initial length.

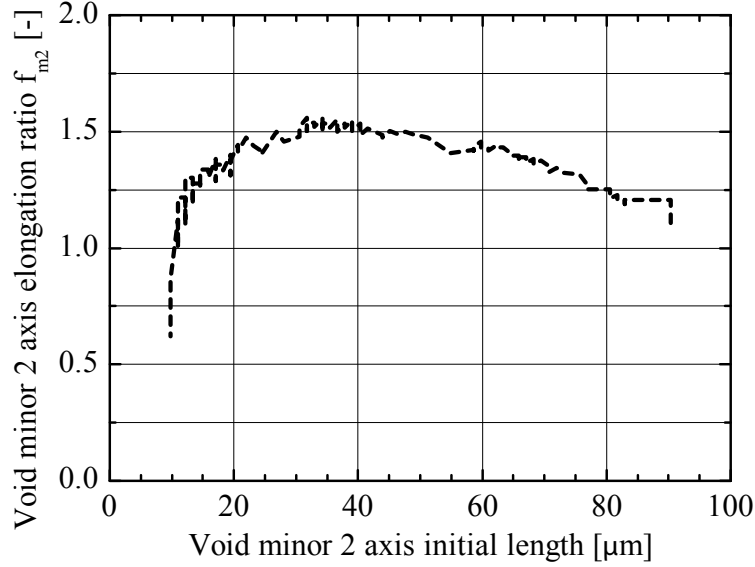


Figure 4.66: Second minor void axis elongation factor  $f_{m2}$  in pure torsion tests as a function of the initial length of the second minor axis. Results obtained using computed tomography (CT) present the whole data set.

Table 4.1: Average values of the axis elongation factors  $f_M$ ,  $f_{m1}$  and  $f_{m2}$  [-], the void growth factor  $f_V$  [-], and the resulting VVF [%] in the representative data range. In tensile and notched tensile samples  $f_{m2} = f_{m1} = f_m$ .

Load	$f_M$ $\pm 10\%$	$f_{m1}$ $\pm 10\%$	$f_{m2}$ $\pm 10\%$	$f_V$ %	VVF
<i>UD</i>	—	—	—	—	1,54
<i>PT</i> – 50	1,53	0,80	1,80	2,21	3,35
<i>PT</i> – 70	1,60	0,66	2,10	2,22	3,35
<i>PT</i> – 105	2,46	0,78	2,37	4,56	6,66
<i>PT</i>	2,84	0,90	3,66	9,36	12,77
<i>TT1</i>	2,31	1,03	2,98	7,08	9,97
<i>TT2</i>	1,86	0,86	2,68	4,27	6,26
<i>ST</i>	1,49	0,87	—	1,12	1,73
<i>NT1</i>	1,09	0,89	—	0,87	1,34
<i>NT2</i>	1,21	1,01	—	1,25	1,91
<i>NT3</i>	1,22	1,15	—	1,63	2,49

#### 4.4.4 Void growth

##### Microscopic measurement of void growth

The evolution and growth of voids can be described in terms of change of the void aspect ratio and the void volume fraction, as presented in Figures 4.67 and 4.68.

Figure 4.67 presents void aspect ratios in fractured samples as a function of the loading conditions. The loading conditions (on the horizontal axis), are arranged in order of increasing stress triaxiality and *PT* loading corresponds to zero nominal stress triaxiality. The void aspect ratios  $W_1$  and  $W_2$  were calculated from the void elongation factors following the procedure described in Section 3.3.4. Thick lines, depict the average  $W$  values, and thin lines show the extreme values observed in the representative data range. The  $W_0$  is the initial mean void aspect ratio, that is, the mean void aspect ratio in undeformed material.

In tensile samples, inclusions stay approximately axisymmetric and the two aspect ratios are indistinguishable, thus we denote them  $W$ . This symmetry is indeed prevailing, despite the processing anisotropy because the extrusion process itself is axisymmetric. The experimental data shows, and theory predicts, that under *NT3* loading,  $W$  almost does not change compared to undeformed material in sharply notched samples (i.e. under high triaxiality) and voids increase their *VVF* by expanding self-similarly.  $W$  increases (voids elongate and become more prolate) while the stress triaxiality decreases.

In tensile-torsion and pure torsion samples two aspect ratios,  $W_1$  and  $W_2$ , need to be distinguished as voids are not axisymmetric anymore.  $W_1$  increases significantly as  $M$  elongates and  $m_1$  shortens.  $W_2$  is relatively constant with respect to the loading conditions and is somehow lower than in undeformed material. The behavior of  $W_2$  is very surprising, because it means that  $m_2$  needs to elongate almost as much as the  $M$ , while in the radial direction of the sample (direction in which  $m_2$  is measured), there is no nominal load applied.

It is possible to calculate the void volume fraction at the onset of coalescence,  $VVF_f$ , if the initial void volume fraction  $VVF_0$  and the change in lengths of the axes at the onset of coalescence are known by using Equation 3.24. Figure 4.68 presents the void volume fraction in samples just before the onset of coalescence as a function of the loading conditions. Also in this figure, the loading conditions (on the horizontal axis), are arranged in order of increasing stress triaxiality and *PT* loading corresponds to zero nominal stress triaxiality. Thick lines, show average *VVF* values, and thin lines show extreme values observed in the representative data range.  $VVF_0$  is the initial void volume fraction. Figure 4.68 is based on void growth measurements and does not include effects of void coalescence.

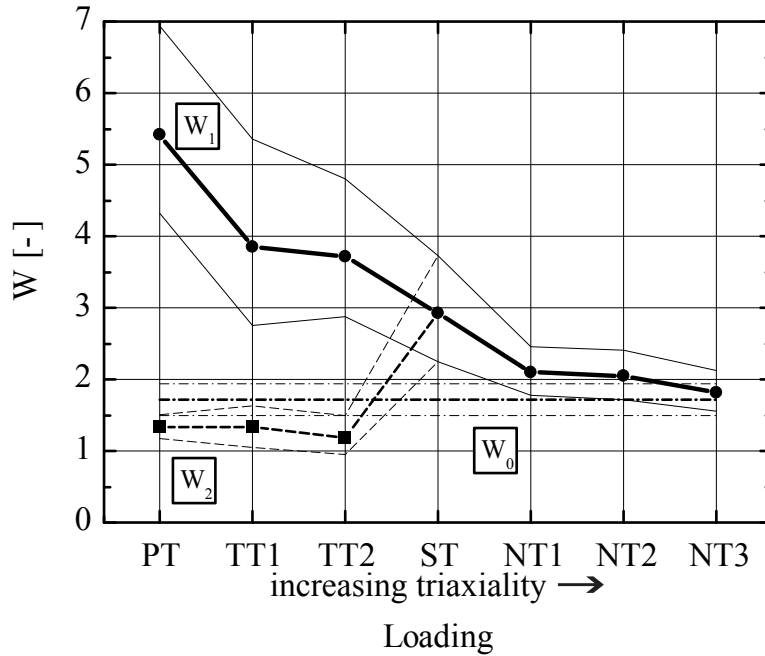


Figure 4.67: Void aspect ratios  $W_1$  and  $W_2$  at the onset of coalescence as a function of loading conditions.

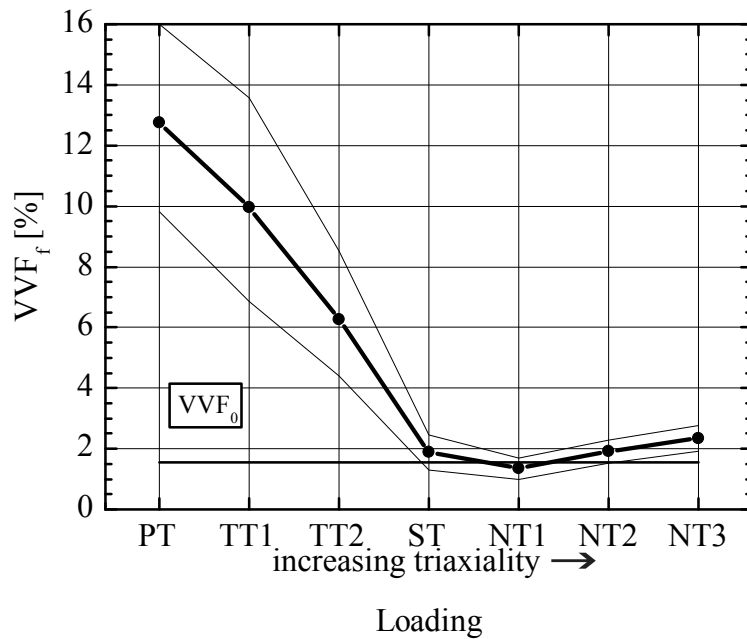


Figure 4.68: Void volume fraction at the onset of coalescence as a function of loading conditions.

In general, in the notched tensile samples, at the onset of coalescence the  $VVF$  increases as the stress triaxiality is higher. Unexpectedly, in the  $NT1$  sample, the  $VVF$  is slightly below the  $VVF_0$  value. This behavior can be attributed to a not ideally homogeneous distribution of inclusions or to the measurement error, as we do not expect voids to shrink in notched tensile samples. More surprising is the relatively high  $VVF$  value in the  $ST$  samples compared to notched samples which will be discussed in Chapter 5.

It is very interesting to observe significant void growth in torsion samples which is much larger than in notched tensile samples. The case of the  $PT$  sample is unexpected as classical fracture models do not predict void growth under zero levels of stress triaxiality.

We investigated this phenomenon in more detail by performing interrupted pure torsion tests. These interrupted samples were analyzed in the same way as fractured samples presented above ( $VVF$  calculations based on measurements of the microstructure). Figures 4.69 and 4.70 present void aspect ratio and void volume fraction as measured from micrographic data.

In Figure 4.69,  $W_1$  increases significantly with the twist angle. This is caused by the elongating major axis  $M$  and shrinking minor axis  $m_1$ . The change in  $W_2$  is not as strong, because  $m_2$  elongates at about the same proportion as  $M$ . Elongation of  $m_2$  under  $PT$  loading was also confirmed using computer tomography (see results below). Thus the observation of  $W_2$  behavior in fractured samples is confirmed.

Figure 4.70 demonstrates how the  $VVF$  changes with the sample twist angle. The zero scatter at 0 *deg* twist angle is due to the fact that a different method was used to measure this value. It was obtained by performing densitometry measurements, while  $VVF$  at non-zero levels of deformation was calculated from the elongation of void's axes.

### Densitometry measurement of void growth

Densitometry measurements using a hydrostatic weighing technique were performed to calculate the void volume fractions independently. The methodology of densitometry experiments for deformed and undeformed samples and the calculations carried out to obtain the void volume fraction in undeformed material are explained in Section 3.3.5. Figure 4.71 depicts the void volume fraction obtained from densitometry measurements and calculations.

The unexpected results of void growth under zero nominal stress triaxiality seems to be confirmed by densitometry measurements. In Figure 4.71 the calculated  $VVF$  for the  $A1$  alloy based on densitometry measurements also increases, although the obtained values do not match those presented in

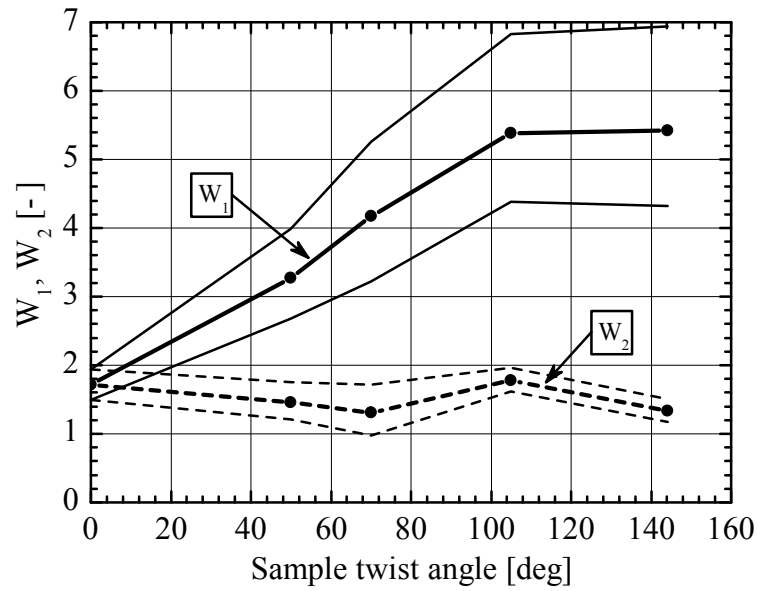


Figure 4.69: Void aspect ratios  $W_1$  and  $W_2$  in interrupted PT experiments as a function of the sample twist angle.

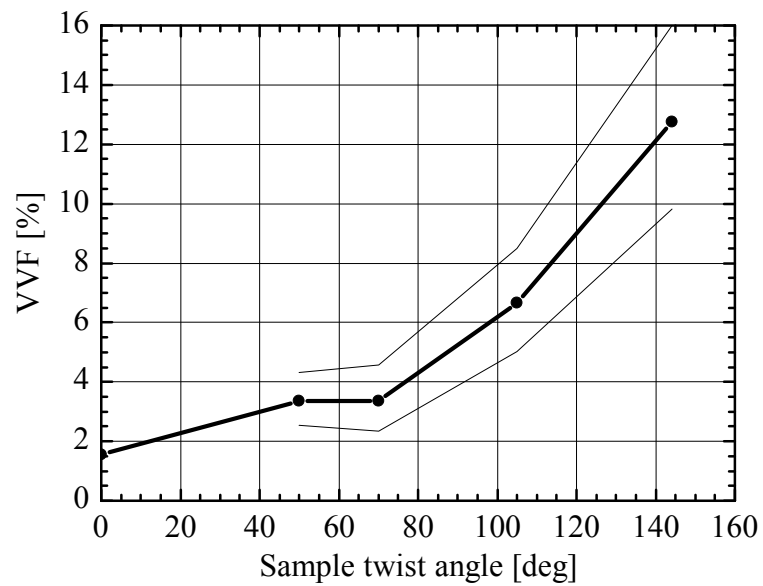


Figure 4.70: Void volume fraction in interrupted PT experiments as a function of the sample twist angle.



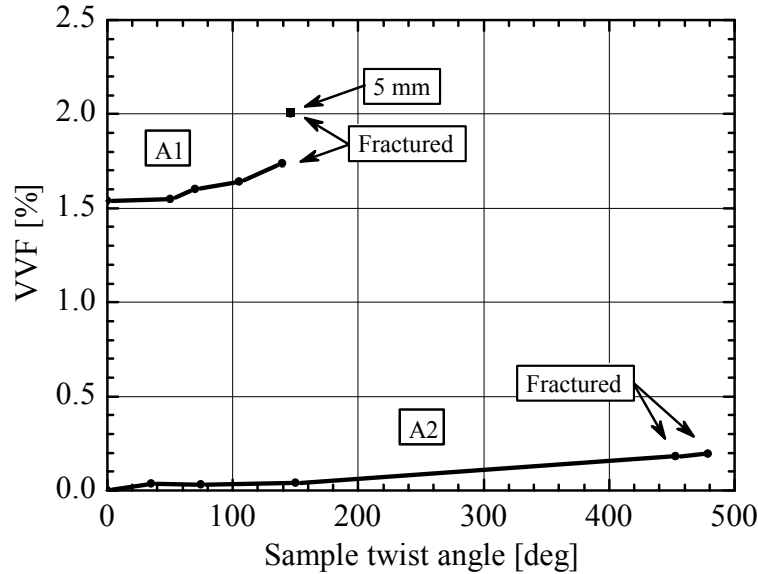


Figure 4.71: Void volume fraction under  $PT$  loading as a function of the sample twist angle - densitometry measurement.

Figure 4.70. The lower values of the  $VVF$  compared to the measurements using the elongation of the void axis could be attributed to the difference in reference volume for calculating the  $VVF$ . Because of the significant void growth gradient in the much larger volume used to perform the densitometry measurements, the average  $VVF$  could be significantly lower.

All the  $A1$  densitometry measurements were performed on 6 mm long sections of the gauge cylinder, while the  $VVF$  from micrographic observations were obtained from material close to the fracture surface, or in the middle of the gauge section for non fractured samples. The  $A1$  densitometry experiment, marked with a square, was performed on a 5 mm long section of the gauge cylinder. We observe that the  $VVF$  in the 5 mm sample is significantly higher compared to another 6 mm long fractured sample. This indicates that void growth is not equally distributed along the whole gauge section but is highest in the middle of the gauge length where the fracture eventually occurs. This results is somehow confusing because the  $J_2$  axisymmetric simulation of the  $PT$  test suggests that strain is almost constant along the gauge section.

The  $A2$  alloy was also found to increase the  $VVF$ . The absolute rate of this increase is slower than that in  $A1$ . Using densitometry measurements we also found that the  $VVF$  in the  $A2$  alloy increases with the level of deformation.

### Computer tomography measurement of void growth

X-ray Computed Tomography (XRCT or CT) was used to generate a three-dimensional image of the inside of the *A1* alloy and to measure the *VVF*. Figure 4.72 compares inclusion size, shape and distribution in the undeformed *A1* alloy and in the *PT* sample, away from the fracture surface. Scanning was performed using an approximate resolution of  $1.22 \mu\text{m}$  per pixel so all smaller inclusions are either observed as one voxel or not observable.

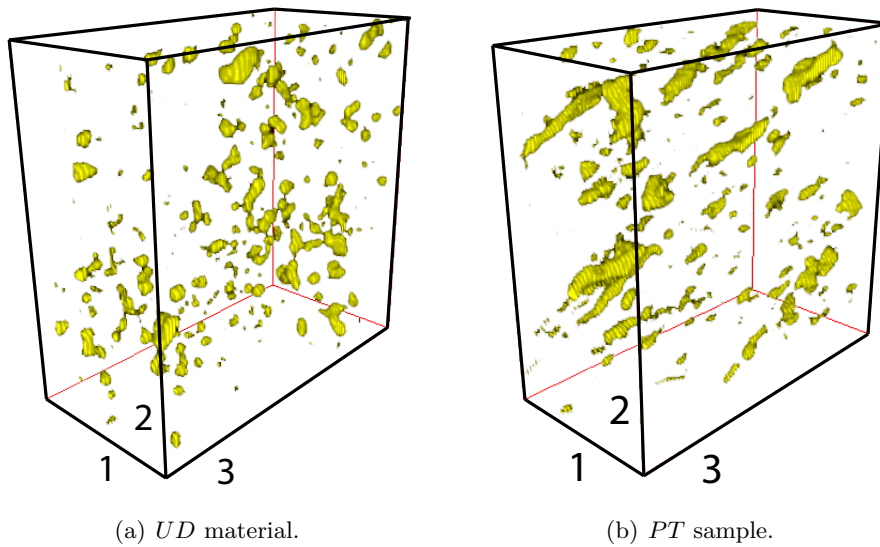


Figure 4.72: 3D images of the inside of the *A1* alloy: a) Undeformed material; b) Sample fractured under *PT* loading conditions. Images present small sections of  $50 \times 100 \times 100$  voxels ( $61 \times 122 \times 122 \mu\text{m}$ ) in size.

Due to the relatively low contrast between lead inclusions and surrounding matrix, CT was found to be very sensitive to selected threshold values (gray level threshold values used for filtering lead inclusions). Depending on the used threshold, we obtained significantly varying results, indicating either no void growth or very little void growth in the *PT* sample. The *VVF* in the undeformed sample varied between 1.22% and 1.93%, while in the tested sample it varied between 1.89% and 2.40%. Because of this uncertainty in the measurement, it is difficult to judge possible void growth in the *PT* sample. CT results will also be discussed in Chapter 5.

#### 4.4.5 Void coalescence

To complete the void growth data presented in Sections 4.4.1 - 4.4.4, we provide here some quantitative data on void coalescence in the *A1* alloy.

Lead inclusions on the fracture surface of notched tensile samples were observed not to distort significantly under loading, and maintain distinct boundaries. Also, the edges between two neighboring dimples are clearly visible (see Figures 4.22 and 4.23(c)). It is therefore possible to obtain quantitative information about the extent of unstable void growth by measuring sizes of lead inclusions and matching dimples in micrographs of the fracture surfaces.

We performed these measurements in the *NT3* sample of the *A1* alloy. We measured the diameters of several randomly selected lead inclusions and the diameters of the matching dimples. In both cases we performed several measurements in different directions, to obtain average diameter values. The acquired average diameters can then be interpreted as the average minor axis lengths because we measure in the direction perpendicular to the sample axis when observing the fracture surfaces.

We can thus define a minor void axis elongation factor after fracture  $f_m^c$  resembling the other elongation factors,  $f_m$ , defined in Section 3.3.4: The  $f_m^c$  is the ratio of the average dimple diameter (length of the minor void axis at the end of coalescence) and the average lead inclusion diameter.

For the distribution of lead inclusions, we can make either of two assumptions: a) it represents the initial distribution (lead debonds without deforming), b) it represents the void size distribution just before the onset of coalescence. We believe that lead is relatively well bonded to the matrix, and that the growth of the inclusion - void system is created by growth of the additional void in the lead inclusion. When the accelerated necking of intervoid ligaments occurs, it causes the lead lying on the wall of the void to neck and separate. Lead positions at fracture surfaces therefore indicate the size of voids at the onset of coalescence.

The process of void growth in the *A1* alloy is schematically represented in Figure 4.73. In the reference configuration (a), the lead inclusion embedded in the matrix contains an additional void. The *VVF* increase of the void-lead inclusion system is due to growth of the additional void, as lead keeps its volume (b). When accelerated necking of intervoid ligaments occurs lead inclusion also necks (c). When the coalescence is fully developed or later (d), when the material is fully separated, lead indicates the size of the void-lead inclusion system at the onset of coalescence. Figure 4.73 (d) may be compared to Figure 4.22 showing the fractured surface of the *NT3* sample.

We assume that the average lead inclusion diameter in the  $f_m^c$  definition is the length of the minor void axis at the beginning of coalescence, and the  $f_m^c$ , defined in the previous paragraphs, characterizes the elongation of the  $m$  only during the process of coalescence. Distribution of these axis elongation factors in coalescence  $f_m^c$  calculated separately for each lead inclusion - dimple couple, is presented in Figure 4.74.

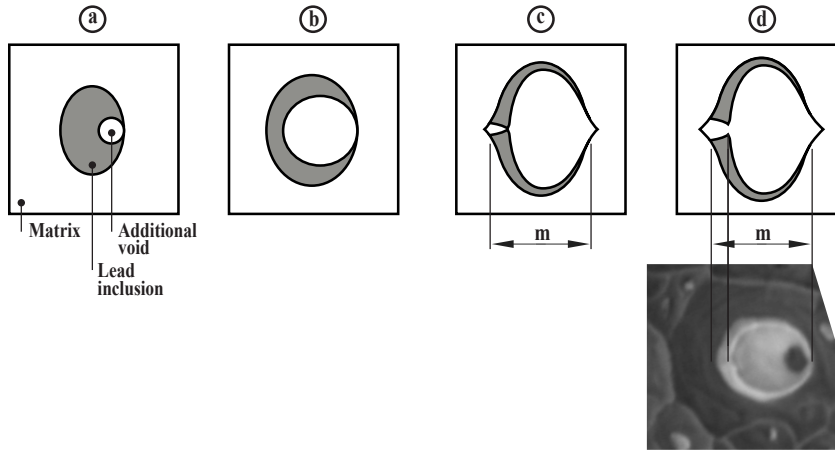


Figure 4.73: Schematic explanation of the void growth: a) initial configuration, b) growth of the additional void, c) onset of coalescence, d) necking of intervoid ligaments and the lead inclusion. The position of lead after fracture indicates the size of the minor axis  $m$  in the void-lead inclusion system at the onset of coalescence.

Figure 4.74 shows that, in general, the  $m$  elongate more in small voids than in large voids and that there is a greater scatter of the  $m$  elongation for small inclusions. Most probably small inclusions can grow the  $m$  more as the relative (to their size) distance to the closest neighbor is larger for small inclusions than for larger inclusions. Growth of some of them is stopped relatively quickly because they are located close to each other or to big inclusions. The relative distance to the closest inclusion is much smaller in big inclusions and they are unlikely to grow significantly.

This interpretation of the  $f_m^c$  distribution appears to be confirmed by a similar analysis of *NT3* fractured surfaces in the *A2* alloy, containing distributions of relatively round and equidistant hard particles. In the *A2* alloy the  $f_m^c$  is 12.64 on average (min. 4.85 - max. 25.99), while the diameter of the nucleating particles is  $1.47 \mu\text{m}$  on average (min.  $1.15 \mu\text{m}$  - max.  $1.74 \mu\text{m}$ ). The relative intervoid distance, higher in the *A2* material, causes voids to elongate the  $m$  much more than in the *A1* alloy. To interpret these results we need to remember that in the *A2* alloy the  $f_m^c$  gives total elongation of the  $m$  including both the stage of stable void growth and coalescence (hard inclusions used as reference do not change their size during deformation).

To conclude, for the amount of deformation in different stages of void growth in the *A1* alloy, we compare Figure 4.74 with Figure 4.61. In the representative data range,  $m$  elongates by only 15% in the stable void growth ( $f_{m1} = 1.15$  approx.) and it elongates by 165% during coalescence. In terms of the elongation of  $m$ , the coalescence stage of fracture dominates the stable void growth.

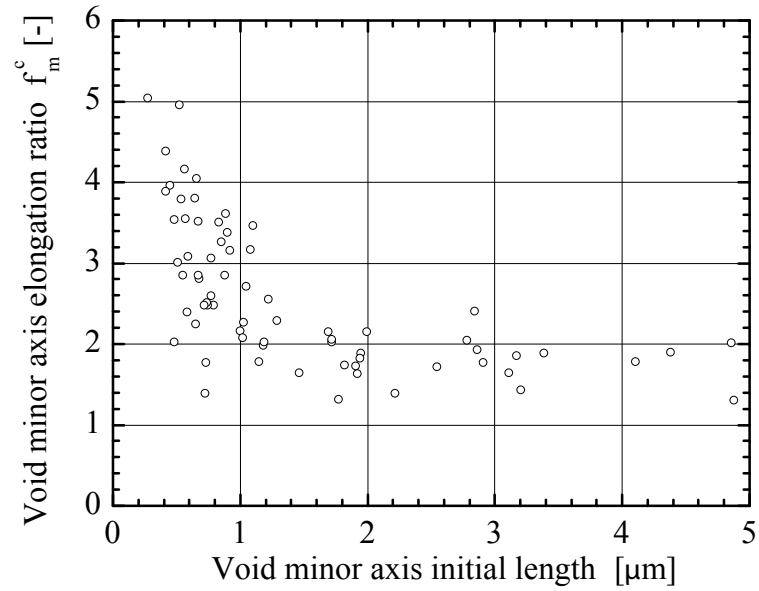


Figure 4.74: Minor void axis elongation factor at the end of coalescence ( $f_m^c$ ) in the NT3 sample of the A1 alloy as a function of minor axis length at the onset of coalescence.

Analysis of the fracture surfaces of the A1 alloy proves that the highest proportion of local deformation in the A1 alloy occurs in the unstable void growth (coalescence) stage of ductile fracture and elucidates the role of the relative intervoid spacing.

## 4.5 Void size computations

In this section we present results of the numerical simulations performed to interpret the observed evolution of voids under various loading conditions.

In Section 3.2.5 we referred to the fact that voids were observed to collapse under low stress triaxiality loadings in simplified axisymmetric single cell calculations with the  $J_2$  plastic law. This numerical result contradicts the void growth observed experimentally, even for samples with zero nominal stress triaxiality ( $PT$ ), as summarized in Section 4.4.4.

Here, we present 3D single cell simulations carried out using both the  $J_2$  and the crystal plasticity (UMAT) constitutive behavior. We also perform axisymmetric and 3D macroscopic simulations of experiments to define correct boundary conditions for the single cell simulations. Our goal is to correlate void growth observations with mechanical parameters and to provide a mechanistic explanation for the established behavior.

### 4.5.1 Macroscopic simulations

Results of macroscopic simulations of samples in terms of force - displacement or torque - sample twist graphs, were presented and commented on in Section 4.2.3. They demonstrate the influence of the evolution of texture anisotropy on the global response of the samples.

In this section, we present quantitative results of the  $J_2$  simulations which will be used as input data for single cell simulations. Average stress triaxiality will be imposed on single cells to impose loading conditions at the level of a void. Equivalent plastic strains obtained in macroscopic simulations, provide the deformation level to which we must subject the cube of the single cell.

The crystal plasticity material model (UMAT) predictions are not used for identifying stress and strain at the level of the element because they can change abruptly from one element to another (due to a random assignment of grain orientation to integration points and depending on the number of grains averaged in one integration point - see Section 3.4.4). This characteristic of the UMAT makes it inappropriate for reading stress and strain at the level of the element, but as shown previously, it describes the global behavior of samples much better than  $J_2$  plasticity.

Table 4.2 summarizes the results of the continuum numerical simulations in terms of the equivalent plastic strain  $\varepsilon_{eq}^{pl}$  at fracture and average stress triaxiality  $T_{avg}$  during the whole loading. Values were read from simulations for displacement/rotation of grips corresponding to the displacement/rotation in experiments when an accelerated drop of load carrying capacity (coalescence)

occurred. Average stress triaxialities were calculated as an arithmetic mean value of triaxialities obtained for each deformation increment.

Table 4.2: Equivalent plastic strain  $\varepsilon_{eq}^{pl}$  and average stress triaxiality  $T_{avg}$  at the onset of coalescence in tested samples for different loading conditions.

Loading	A1		A2	
	$\varepsilon_{eq}^{pl}$	$T_{avg}$	$\varepsilon_{eq}^{pl}$	$T_{avg}$
<i>PT</i>	1.168	0	3.422	0
<i>TT1</i>	0.690	0.067	1.578	0.065
<i>TT2</i>	0.573	0.166	0.814	0.169
<i>ST</i>	0.487	0.349	1.243	0.397
<i>NT1</i>	0.285	0.823	0.868	0.786
<i>NT2</i>	0.127	1.177	0.623	1.069
<i>NT3</i>	0.076	1.529	0.355	1.465

Figure 4.75 presents triaxiality histories calculated in samples during loading. In the case of the tensile and notched tensile samples, the history was calculated in the element at the center of the sample. A numerical study performed to verify triaxiality levels across the sample's wall for torsional samples, proved that the position of the element of the highest stress triaxiality differs depending on the level of the axial load but also varies with strain level. We therefore decided to record the stress triaxiality history consistently at the element of the highest equivalent strain at the outer cylindrical wall. For technical details see Section 3.4.2

In the notched tensile samples, we observe significant variations in the stress triaxiality as the sample elongates and material deforms in the neck. Under the *ST* loading, triaxiality is constant before necking and then increases linearly. The variation in the stress triaxiality under *PT* and *TTx* loadings is very small (an order of magnitude smaller than in the case of tensile and notched tensile loadings), despite the fact that the experiment was performed under constant axial force (not constant stress triaxiality).

Analyzing the results provided in Figure 4.75 and Table 4.2 we need to consider that the *TT2* simulations were not able to capture deformation localization despite a small geometric perturbation introduced in the model to facilitate necking. The calculated values of the  $\varepsilon_{eq}^{pl}$  and the  $T_{avg}$  are thus expected to underestimate the actual values.

#### 4.5.2 Void evolution under tensile dominated loadings

Figure 4.76 shows the response of the 3D single cell for tensile dominated loadings (see Section 3.4.3) under various stress triaxialities for two material

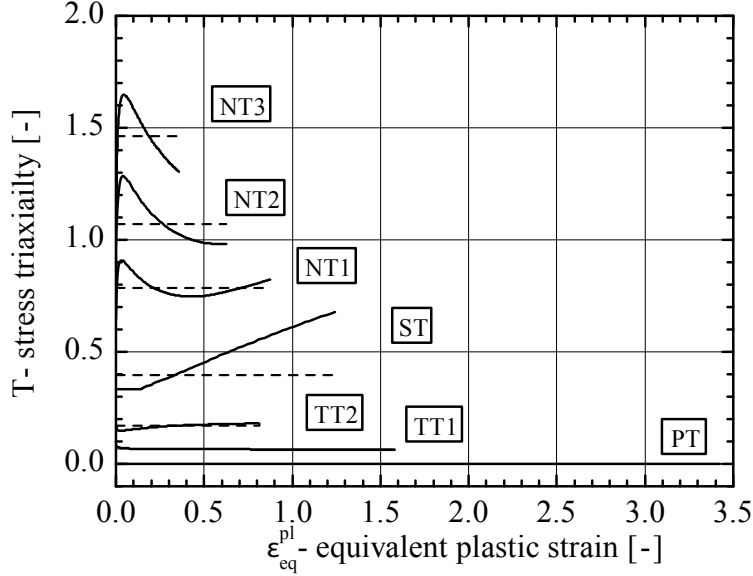


Figure 4.75: Stress triaxiality  $T$  as a function of equivalent plastic strain  $\epsilon_{eq}^{pl}$  and average stress triaxiality  $T_{avg}$  for different loading conditions, calculated with the A2 constitutive law and  $J_2$  material model.

models, the  $J_2$  and crystal plasticity UMAT models, in terms of mesoscopic equivalent stress  $\Sigma_{eq}$  and mesoscopic equivalent total strain  $E_{eq}$ .

Mesoscopic equivalent stress  $\Sigma_{eq}$  is defined as:

$$\Sigma_{eq} = \frac{1}{\sqrt{2}} \sqrt{(\Sigma_{11} - \Sigma_{22})^2 + (\Sigma_{22} - \Sigma_{33})^2 + (\Sigma_{11} - \Sigma_{33})^2} \quad (4.1)$$

where the stress components  $\Sigma_{11}$ ,  $\Sigma_{22}$  and  $\Sigma_{33}$  are sums of nodal forces in directions 1, 2 and 3, over the actual areas corresponding to surfaces perpendicular to these directions. (Directions 1, 2 and 3 are principal directions under tensile loadings).

Mesoscopic equivalent total strain  $E_{eq}$  is defined as:

$$E_{eq} = \frac{1}{\sqrt{2}} \sqrt{(E_{11} - E_{22})^2 + (E_{22} - E_{33})^2 + (E_{11} - E_{33})^2} \quad (4.2)$$

where each of the strain components  $E_{11}$ ,  $E_{22}$  and  $E_{33}$  measures the difference in actual length and initial length of the single cell divided by its initial length in an appropriate direction.



The values of the stress triaxiality in single cell simulations correspond to the average stress triaxiality in the samples during loading and were obtained in axisymmetric macroscopic simulations, presented in Table 4.2 (Mat. A2). Simulations were run until a significant drop of load carrying capacity was observed. It was impossible to observe localization and drop of load in the *ST*  $J_2$  single cell simulation, even for large deformations. The *ST* UMAT simulation stopped at large deformations due to convergence problems. For the boundary conditions and other technical details of the single cell simulations refer to Section 3.4.3.

Apart from the known effect of decreasing the strain to void coalescence with increasing stress triaxiality, we see in Figure 4.76 the effect of crystal plasticity. Single cells calculated with the crystal plasticity material model (UMAT) localize at considerably lower equivalent stress compared to the  $J_2$  calculations.

Figures 4.77 - 4.80 present void evolution in terms of the *VVF*, and the void axis elongation factors  $f_M$ ,  $f_{m1}$  and  $f_{m2}$ . The void volume fraction *VVF*, was calculated as:

$$VVF = \frac{V_{SC} - V_{EVOL}}{V_{SC}} \quad (4.3)$$

where  $V_{SC}$  is the volume of the single cell including the void calculated from nodal displacements, and  $V_{EVOL}$  is the volume of the elements composing the single cell (constant value). Void axis elongation factors were defined above in Section 3.3.4 and are ratios of the actual lengths of the void axes over their initial lengths. Lengths of the major, the first and the second minor axis were calculated as the distance from the center of the void to the most distant node defining the void in directions 1, 2 and 3 respectively,  $\times 2$ .

In the  $J_2$  simulations, initially axisymmetric voids elongate at the same rate in directions 1 and 3. As a result, voids stay axisymmetric and their void elongation factors of the minor axes  $f_{m1}$  and  $f_{m2}$  are equal. These same, initially axisymmetric voids elongate at different rates in directions 1 and 3 in simulations performed with the UMAT material model even if loads applied in these two directions are the same.

Relative growth rates for the minor axis change with the level of the  $T_{avg}$ . In Figures 4.77 - 4.80 we observe that the  $M$  axis elongates faster than the  $m_1$  and  $m_2$  for relatively low triaxialities. When  $T_{avg}$  increases, the difference in the relative rate of growth diminishes. In the *NT3* simulations  $M$ ,  $m_1$  and  $m_2$  elongate at the same rate in the  $J_2$  simulations. Use of the UMAT makes this effect more pronounced, and the elongation rates of the major and two minor axes are close to each other already in the *NT2* loading. In the *NT3*,

the minor axes elongate faster than  $M$ .

Values of the void axis elongation factors for the  $\varepsilon_{eq}^{pl}$  corresponding to the onset of coalescence (see Table 4.2, Mat. A1) presented in Figures 4.77 - 4.80, can be compared to average values of the  $f_M$ ,  $f_{m1}$  and  $f_{m2}$  obtained from metallographic observations presented in Figures 4.60-4.61. Such comparison will be presented in Chapter 5.

The  $VVF$  growth rate is also affected by crystal plasticity. This is observed in Figures 4.77(b), 4.78(b), 4.79(b) and 4.80(b): for the same deformation single cells with crystal plasticity material behavior, increase their  $VVF$  much more than with the  $J_2$  plasticity model.

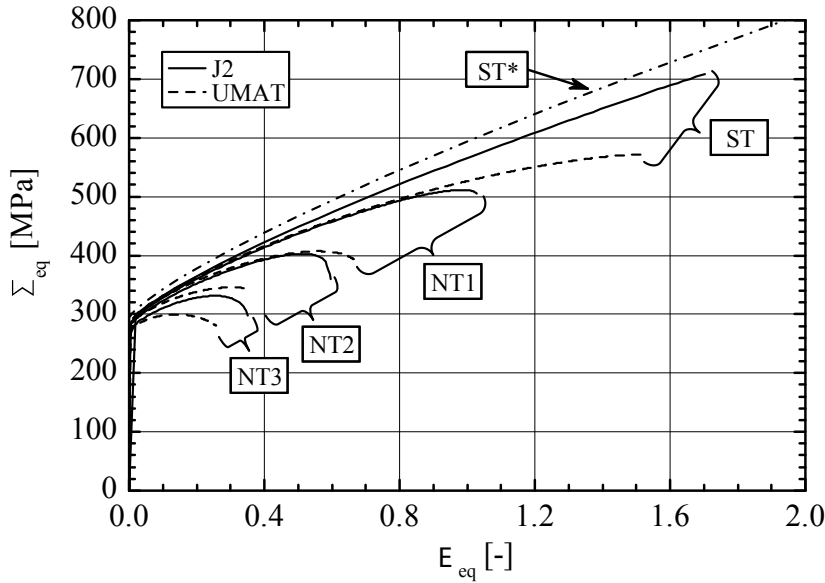
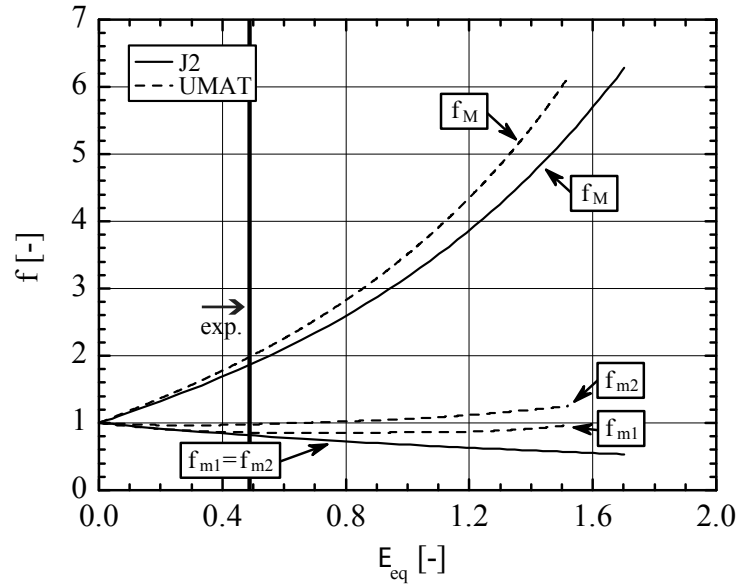


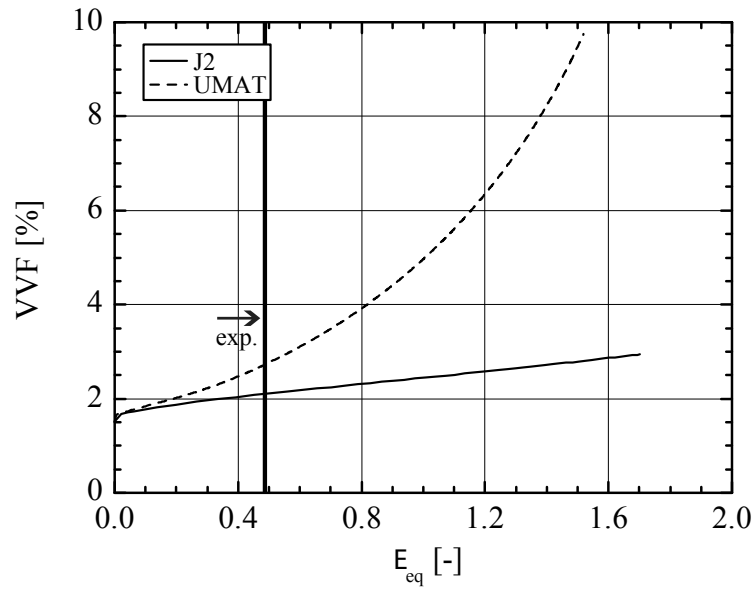
Figure 4.76: Response of the 3D single cell for tensile loadings. Line  $ST^*$  presents A2 constitutive law obtained from the  $ST$  test (Figure 4.8).

Quantitative results of the single cell simulations for tensile dominated loadings are summarized in Table 4.3 in terms of the  $f_M$ ,  $f_{m1}$ ,  $f_{m2}$ ,  $f_V$  and  $VVF$ . Results of the simulations are provided for the mesoscopic equivalent strain  $E_{eq}$  corresponding to the equivalent plastic strains  $\varepsilon_{eq}^{pl}$  in the macroscopic samples at the onset of coalescence (Section 4.5.1). Values for the UMAT and  $J_2$  material models are given with and without parentheses, respectively.

Results of the simulations presented in Table 4.3 are consistent with the relatively small void growth observed in experiments and presented in Table 4.1. The shape of the mesh of the single cell for tensile dominated loadings,

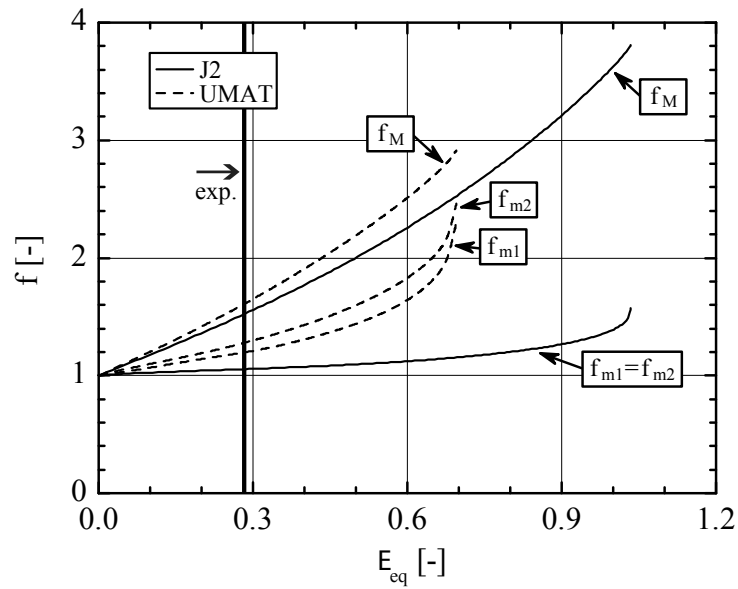


(a) Evolution of the void axis elongation factors  $f_M$ ,  $f_{m1}$  and  $f_{m2}$ .

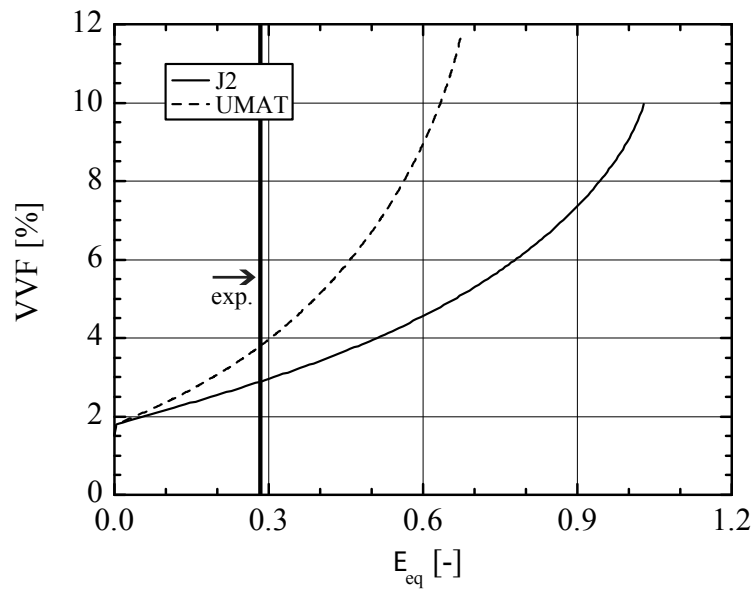


(b) Evolution of the void volume fraction  $VVF$ .

Figure 4.77: Single cell simulation results for the ST loading.

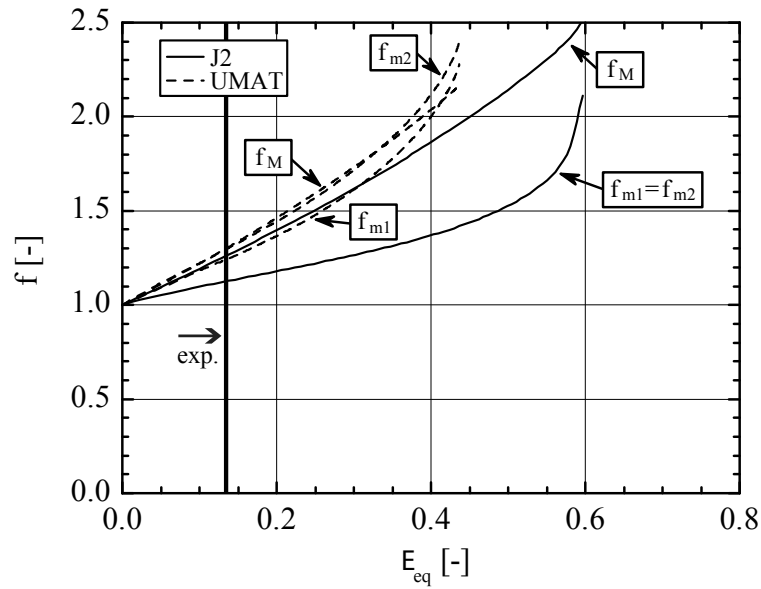


(a) Evolution of the void axis elongation factors  $f_M$ ,  $f_{m1}$  and  $f_{m2}$ .

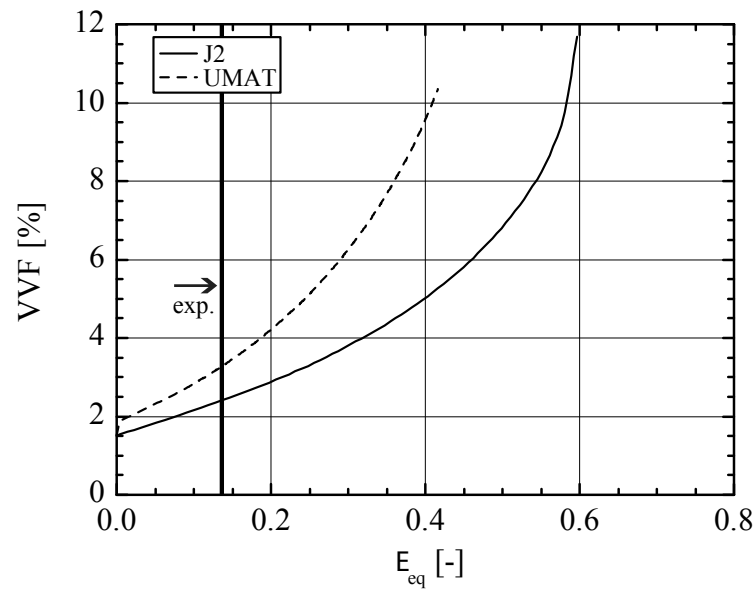


(b) Evolution of the void volume fraction  $VVF$ .

Figure 4.78: Single cell simulation results for the NT1 loading.

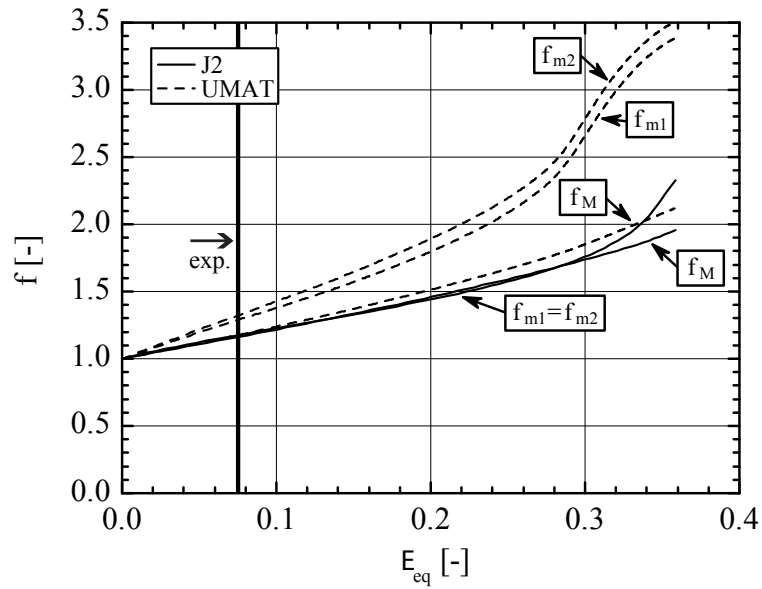


(a) Evolution of the void axis elongation factors  $f_M$ ,  $f_{m1}$  and  $f_{m2}$ .

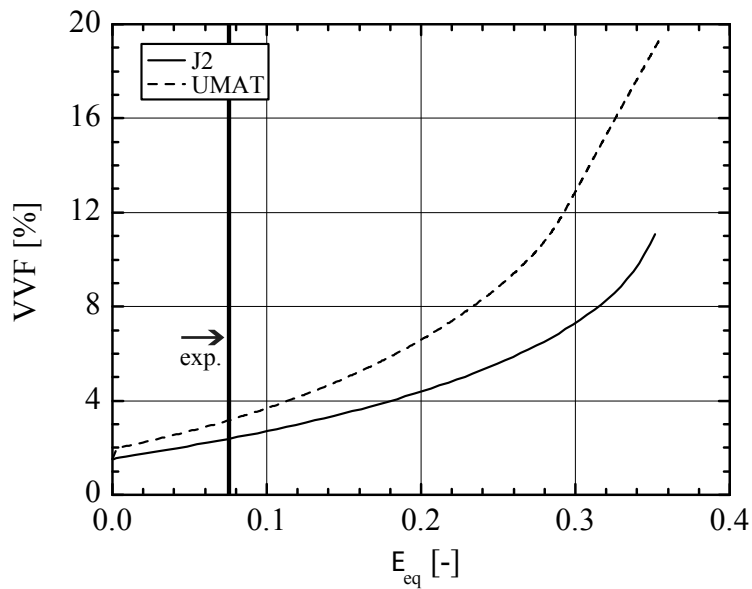


(b) Evolution of the void volume fraction  $VVF$ .

Figure 4.79: Single cell simulation results for the NT2 loading.



(a) Evolution of the void axis elongation factors  $f_M$ ,  $f_{m1}$  and  $f_{m2}$ .



(b) Evolution of the void volume fraction  $VVF$ .

Figure 4.80: Single cell simulation results for the NT3 loading.

Table 4.3: Summary of the results of single cell simulations for tensile dominated loadings in terms of  $f_M$  [-],  $f_{m1}$  [-],  $f_{m2}$  [-],  $f_V$  [-] and VVF [%]. Results for the  $E_{eq}$  corresponding to the  $\varepsilon_{eq}^{pl}$  at the onset of coalescence in macroscopic samples. Results in parentheses are for the crystal plasticity material model.

Load	$f_M$	$f_{m1}$	$f_{m2}$	$f_V$	VVF %	VVF <sub>exp</sub> *
<i>ST</i>	1.90 (1.89)	0.81 (0.86)	0.81 (0.98)	1.25 (1.66)	2.12 (2.73)	1.73
<i>NT1</i>	1.52 (1.61)	1.05 (1.20)	1.05 (1.28)	1.69 (2.47)	2.88 (3.80)	1.34
<i>NT2</i>	1.25 (1.28)	1.12 (1.23)	1.12 (1.28)	1.56 (2.03)	2.34 (3.17)	1.91
<i>NT3</i>	1.16 (1.18)	1.17 (1.29)	1.17 (1.33)	1.60 (2.03)	2.37 (3.19)	2.49

(\*Experimental values presented previously in Table 4.1)

deformed up to  $\varepsilon_{eq}^{pl}$  and corresponding to the onset of coalescence in macroscopic samples, is presented in Figure 4.81.

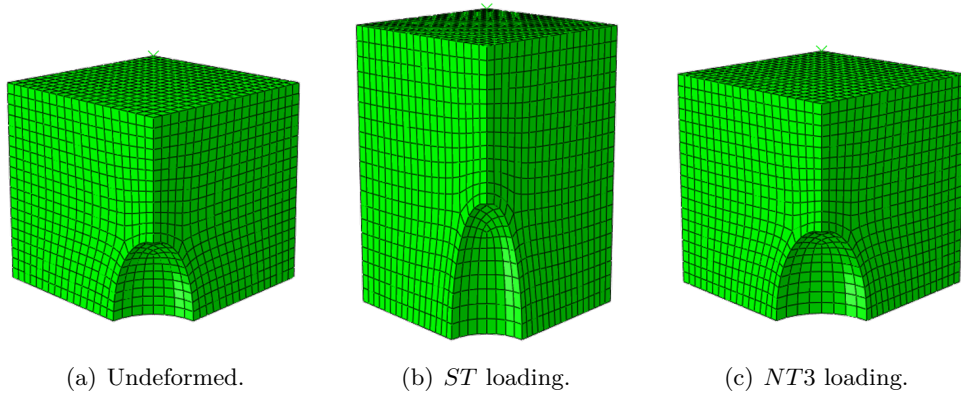


Figure 4.81: Shape of the single cell for tensile dominated loadings: (a) undeformed, (b) and (c) deformed under *ST* and *NT3* loading conditions up to  $E_{eq}$  corresponding to  $\varepsilon_{eq}^{pl}$  in macroscopic samples at the onset of coalescence using the  $J_2$  plasticity model.

### 4.5.3 Void evolution under shear dominated loadings

The mesh of the 3D single cell used in this numerical investigation for shear dominated loadings is presented in Section 3.4.3. It was designed to take into account the effects of material and void rotation under imposed loadings.

### Boundary conditions of the single cell

The single cell for shear dominated loadings has periodic boundary conditions in axial (2) and tangential (3) directions as described in Section 3.4.3. Periodic boundary conditions were obtained by imposing equations relating displacement of matching nodes lying on the opposite faces in axial and tangential directions. Displacement in 1-direction of nodes lying on the face perpendicular to the radial direction (1) follow displacement of the master node  $M$ . By controlling the displacement of the master node  $M$  in the radial direction (1), we obtain both plane strain ( $U_1^M = 0$ ) or generalized plane strain ( $U_1^M \neq 0$ ) boundary conditions.

We performed a 3D simulation of the macroscopic torsion sample under different loading conditions (Section 3.4.3) to decide which boundary conditions when imposed on the single cell, reproduce best the deformation of the torsion sample. We used two macroscopic models: with and without a finite void. During calculations the change in the length of the bottom section of the 3D models in radial ( $R$ ) and tangential ( $T$ ) directions were recorded. Results of these simulations are shown in Table 4.4 and provide change of dimensions at rotations corresponding to rotations in real samples at the onset of rapid drop of load carrying capacity (coalescence).

Table 4.4: Change in size of the 3D macroscopic sample in tangential ( $\Delta T$ ) and radial ( $\Delta R$ ) directions, calculated in the 1-3 ( $R$ - $T$ ) planes, under various loading conditions [%].

Loading	Solid model		Voided model	
	$\Delta T$	$\Delta R$	$\Delta T$	$\Delta R$
$PT$	-0.4	-0.1	-0.9	-0.7
$TT1$	-3.4	-7.2	-3.5	-8.1
$TT2$	-6.6	-16.7	-7.0	-20.4

In the  $PT$  simulation of the macroscopic sample the change in lengths is negligible, but it is significant in  $TT1$  and very significant in  $TT2$ . We therefore decided to impose the plane strain boundary condition ( $U_1^M = 0$ ) on the single cell under  $PT$  loading, and generalized plane strain boundary condition ( $U_1^M \neq 0$ ) for single cells under  $TT1$  and  $TT2$  loadings. In all cases of single cell loading, elongation in the tangential direction was not permitted ( $U_3^{REF} = 0$ )<sup>1</sup>.

Under  $TT1$  and  $TT2$  loadings, the single cell should be able to deform in all directions including direction 3. However, when the elongation of the

<sup>1</sup>The single cell simulation for the pure torsional loading with kinematic boundary conditions were also performed. In this simulation the imposed strains in directions 1, 2 and 3 correspond to changes in shape of the interrupted  $PT$  sample presented in Figures 4.19, 4.20 and 4.21, therefore  $U_3^{REF} \neq 0$ . Results of this simulations are presented in Appendix D.



single cell in the tangential direction was permitted ( $U_3^{REF} \neq 0$ ), it tended to elongate in this direction which is equal to increasing the diameter of the thin-walled sample. To avoid this non physical behavior, displacement of the REF node direction 3 was constrained.

### Void evolution

Figure 4.82 depicts the response of the 3D single cell for shear dominated loadings under various axial loads and applied for two material models, the  $J_2$  and the crystal plasticity UMAT models, in terms of mesoscopic equivalent stress  $\Sigma_{eq}$  and equivalent mesoscopic strain  $E_{eq}$ .

Mesoscopic equivalent stress  $\Sigma_{eq}$  is defined as:

$$\Sigma_{eq} = \frac{1}{\sqrt{2}} \sqrt{\Sigma_{22}^2 + (\Sigma_{22} - \Sigma_{33})^2 + \Sigma_{33}^2 + 6 \cdot \Sigma_{23}^2} \quad (4.4)$$

where the stress components  $\Sigma_{22}$ ,  $\Sigma_{33}$  and  $\Sigma_{23}$  are the forces at the master node M in directions 1, 2 and 3, over the actual areas of the appropriate surfaces.

The walls of the single cell with periodic boundary conditions ( $F21A$ ,  $F21B$ ,  $F31A$ ,  $F31B$ ,  $F13A$  and  $F13B$  shown in Figure 3.26) deform freely when the cell is loaded and in general do not stay flat. This deformation makes it difficult to define and interpret the mesoscopic equivalent strain. We decided to assume the  $E_{eq}$  of the single cell for shear loadings to be equal to the  $\varepsilon_{eq}^{pl}$  of a single element with boundary conditions and displacement of the master node corresponding to those in the single cell.

The response of the  $J_2$  single cell for all loading cases is very similar to the stress-strain curve obtained from the  $ST$  test due to the relatively small change in the void volume. Significant differences of behavior can be observed between the single cells under different loadings calculated with the crystal plasticity model. These differences result mainly from the constitutive behavior of the material as the change in the void volume is also relatively small, and this will be presented in the subsequent figures.

Figures 4.83-4.85 present the evolution of a void under shear dominated loadings in terms of the void volume fraction  $VVF$ , and the void axis elongation factors  $f_M$ ,  $f_{m1}$  and  $f_{m2}$ . The bottom axis represents the mesoscopic equivalent strain  $E_{eq}$  defined previously. The top axis plots the rotation of the 3D macroscopic thin walled sample, simulated with the  $J_2$  plasticity model and corresponding to the same displacement of the master node  $U_3^M$  as in the case of the  $E_{eq}$  calculation.

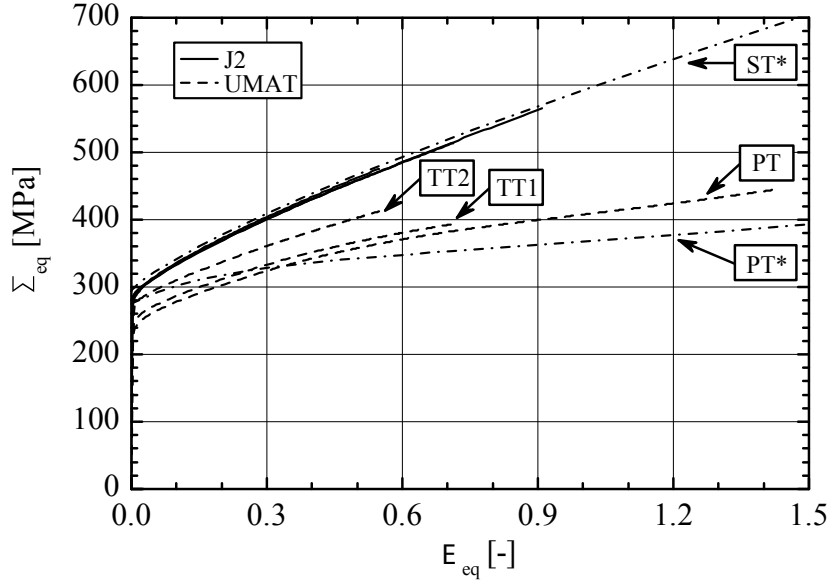


Figure 4.82: Response of the 3D single cell for shear loadings. *PT*  $J_2$  simulation was stopped when the void closed. Lines *ST\** and *PT\** present A2 constitutive laws obtained from the *ST* and *PT* tests, respectively (Figure 4.8).

Void axis elongation factors were defined previously in Section 3.3.4 and are the ratios of the actual lengths of the void axes over their initial lengths. The length of the major axis was calculated as the distance from the center of the void to the most distant node defining the void in plane 2 – 3,  $\times 2$ . The length of the first minor axis was calculated as the shortest distance from the center of the void to a line passing through the two closest nodes defining the void in the 2 – 3 plane,  $\times 2$ . The length of the second minor axis was calculated as the distance between the center of the void to the most distant node defining the void in direction 1,  $\times 2$ .

The void volume fraction  $VVF$  was calculated as:

$$VVF = \frac{V_{SC} - V_{EVOL}}{V_{SC}} \quad (4.5)$$

where  $V_{SC}$  is the volume of the single cell including the void calculated from nodal displacements, and  $V_{EVOL}$  is the volume of the elements composing the single cell (constant value, therefore we neglect the effect of elasticity on volume changes).

It is observed in Figures 4.83(a), 4.84(a) and 4.85(a) that the use of the UMAT plasticity model under shear dominated loadings has little influence

on the elongations of void axes. The largest impact of the crystal plasticity is observed for the  $f_{m1}$  under  $PT$  loadings presented in Figure 4.83(a). UMAT slows down shortening of the  $m_1$  axis and at the end of loading the void is not fully collapsed, contrary to what is observed in the  $J_2$  simulations. Under the  $PT$  loadings  $f_{m2}$  stays constant, so  $m_2$  maintains its length for the  $J_2$  and UMAT material models. We conclude from this observation that UMAT slows down the shrinkage of the  $m_1$ , but does not predict the extensive elongation of the  $m_2$  axis observed experimentally in the  $A1$  alloy.

In terms of the  $VVF$  we also observe relatively little influence of the UMAT plasticity model on void growth. UMAT either slightly slows down shrinkage of the void or slightly accelerates void growth, depending on the loading case, and has a relatively small influence on the shape of the void compared to the situation of tensile dominated loadings. The largest influence of the UMAT is under the  $PT$  loadings, where it keeps the  $VVF$  positive until the end of the simulation. Figure 4.86 compares the shape of the single cell for  $PT$  loading conditions and calculated with the  $J_2$  plasticity and UMAT models.

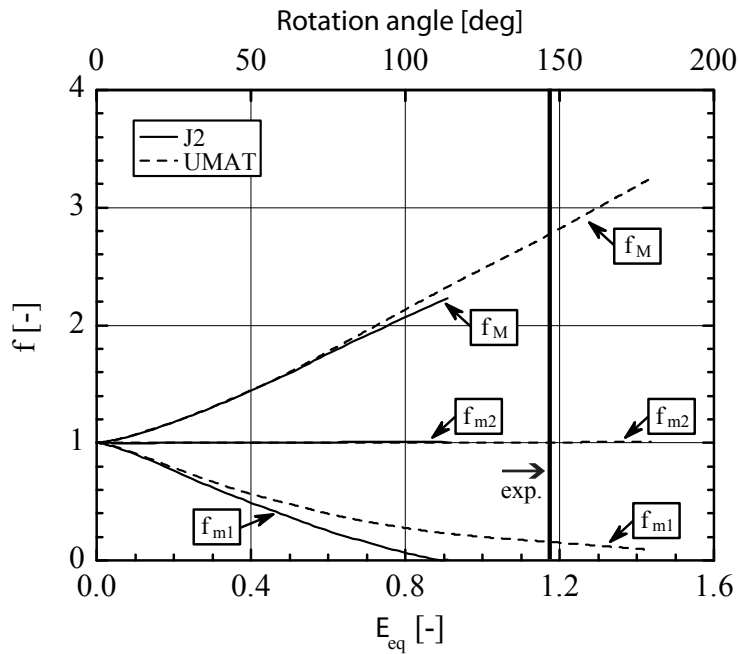
Quantitative results for the single cell simulations for shear dominated loadings are summarized in Table 4.5 in terms of the  $f_M$ ,  $f_{m1}$ ,  $f_{m2}$ ,  $f_V$  and  $VVF$ . Results of the simulations are provided for the mesoscopic equivalent strain  $E_{eq}$  corresponding to equivalent plastic strain  $\varepsilon_{eq}^{pl}$  in the macroscopic axisymmetric simulations (Section 4.5.1). In the case of the  $PT$ ,  $J_2$  simulation was stopped when the  $VVF$  became 0, that is for  $E_{eq} = 0.91$ . Values for the UMAT and  $J_2$  material models are given with and without parentheses respectively.

Results of the simulations summarized in Table 4.3 can be compared to the experimental results presented in Table 4.1. Numerical results show a relatively small influence of the UMAT on void evolution under shear dominated loadings. Single cell simulations were not able to capture the large elongation of the  $m_2$  axis observed in experiments.

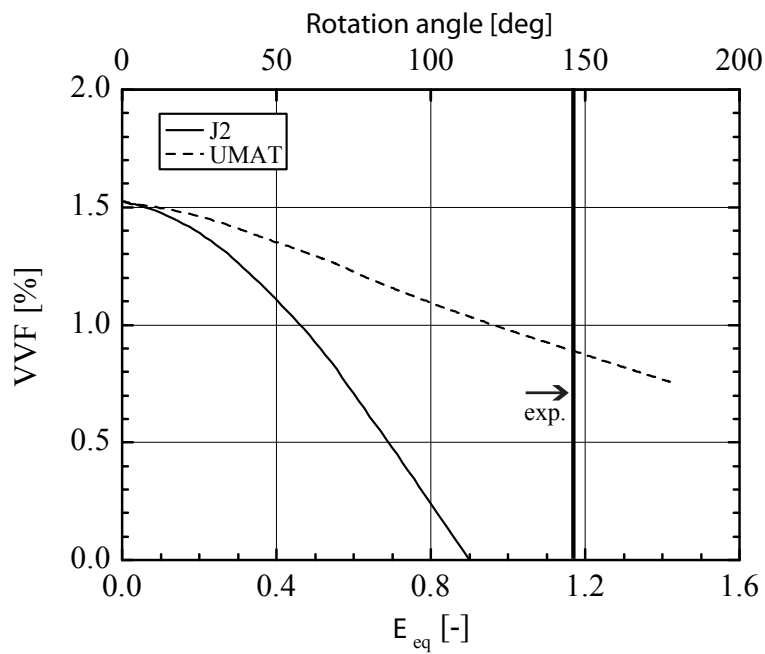
### Influence of lead inclusion

Simulations of the void-containing single cell under pure shear loadings presented in Section 4.5.3 predict collapse of the void.  $m_1$  shrinks (for the  $J_2$  plasticity it shrinks down to zero), and  $m_2$  keeps its length or elongates insignificantly. In metallographic observations of tested samples we find a considerable elongation of  $m_2$  causing the experimental  $VVF$  to grow.

We decided to run simulations of a single cell containing a lead inclusion embedded in the void to verify if this experimentally observed elongation of the  $m_2$  axis could be caused by the pressure of the soft lead being compressed. For this purpose, we use the model presented in detail in Section 3.4.3 which

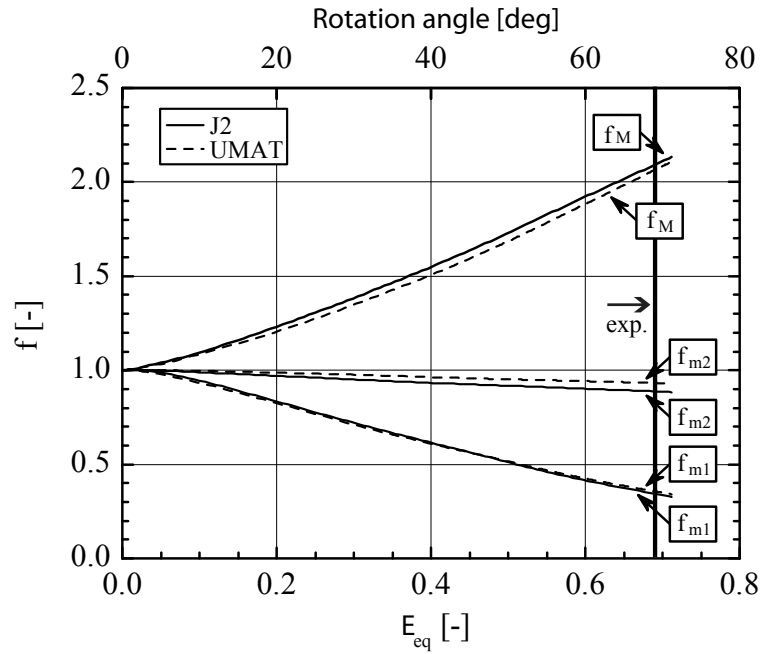


(a) Evolution of the void axis elongation factors  $f_M$ ,  $f_{m1}$  and  $f_{m2}$ .

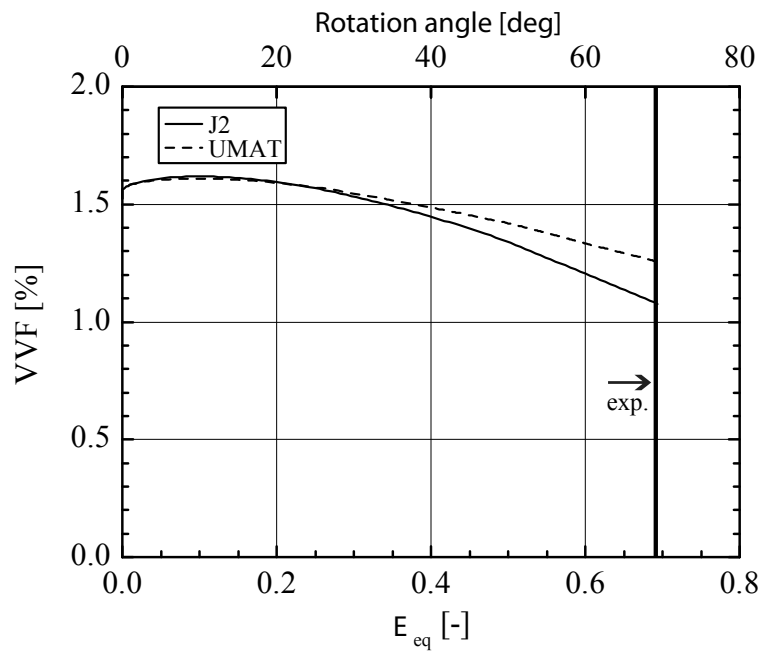


(b) Evolution of the void volume fraction  $VVF$ .

Figure 4.83: Single cell simulation results for the PT loading.

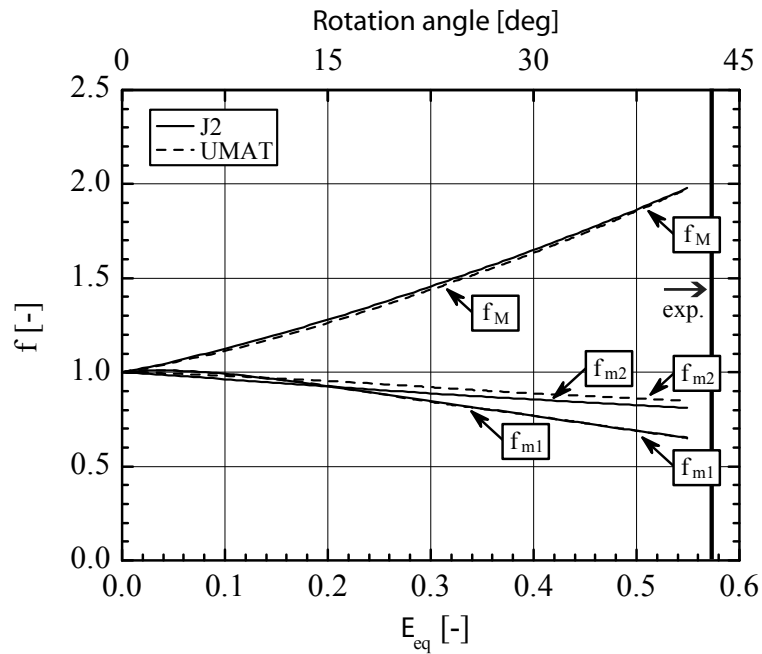


(a) Evolution of the void axis elongation factors  $f_M$ ,  $f_{m1}$  and  $f_{m2}$ .

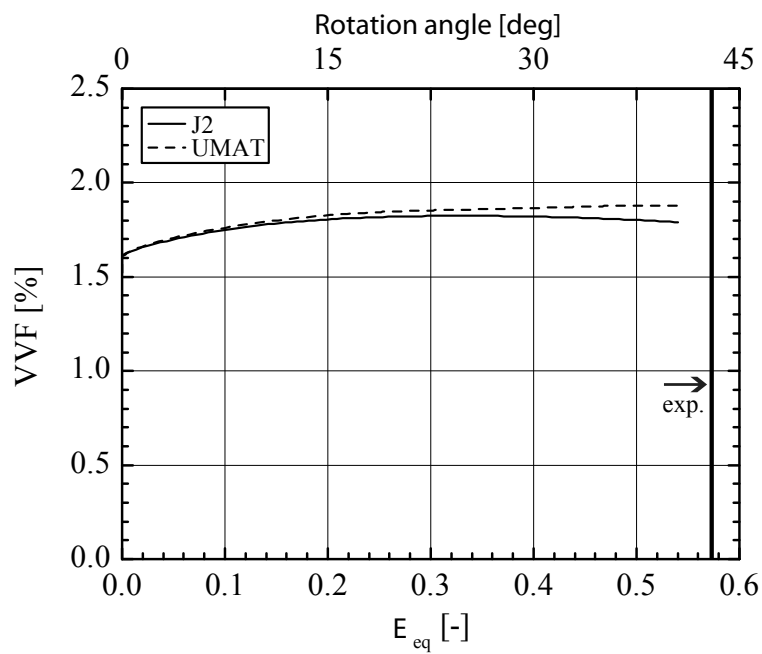


(b) Evolution of the void volume fraction  $VVF$ .

Figure 4.84: Single cell simulation results for the TT1 loading.

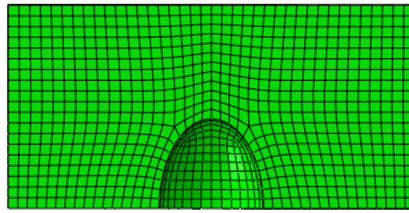


(a) Evolution of the void axis elongation factors  $f_M$ ,  $f_{m1}$  and  $f_{m2}$ .



(b) Evolution of the void volume fraction  $VVF$ .

Figure 4.85: Single cell simulation results for the TT2 loading.



(a) Undeformed.

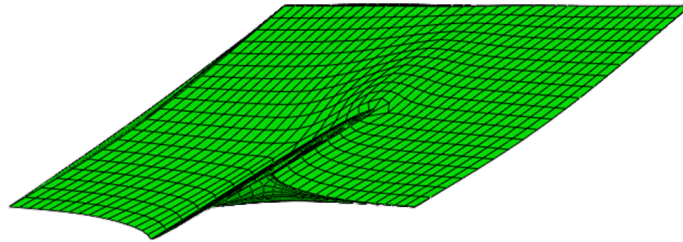
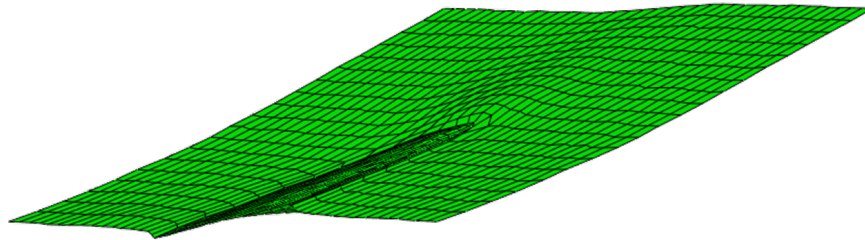
(b) *PT* loading,  $J_2$  simulation,  $E_{eq}^{pl} = 0.82$  (just before the collapse of the void).(c) *PT* loading, UMAT simulation,  $E_{eq}^{pl} = 1.17$ .

Figure 4.86: Shape of the single cell for shear dominated loadings: (a) undeformed, (b) and (c) deformed under *PT* loading conditions.

Table 4.5: Summary of results of single cell simulations for shear dominated loadings in terms of  $f_M$ ,  $f_{m1}$ ,  $f_{m2}$ ,  $f_V$  and  $VVF$  for  $E_{eq}$  corresponding to  $\varepsilon_{eq}^{pl}$  in macroscopic axisymmetric simulations. Results in parentheses are for the crystal plasticity material model. Results marked with "\*" were obtained for  $E_{eq} = 0.91$ .

Load	$f_M$	$f_{m1}$	$f_{m2}$	$f_V$	$VVF$	$VVF_{exp}$ #
<i>PT</i>	2.23*	0.00*	1.00*	0.00*	0.00*	12.77
	(2.76)	(0.16)	(1.00)	(0.44)	(0.89)	
<i>TT1</i>	2.09	0.35	0.89	0.64	1.11	9.97
	(2.06)	(0.36)	(0.93)	(0.66)	(1.27)	
<i>TT2</i>	1.97	0.65	0.81	1.05	1.79	6.26
	(1.97)	(0.65)	(0.84)	(1.09)	(1.88)	

(#Experimental values presented previously in Table 4.1)

was created to reproduce the  $VVF$  of the real *A1* alloy, integrating the lead and the volume of the additional pre-existing void in the lead inclusion (see Section 3.2.4). Lead is free to move within the void due to the frictionless contact between the void walls and the lead inclusion. Figures 4.87, 4.88 and 4.89 show results of these simulations for comparing both the single cell containing a void and a lead inclusion. The mesoscopic equivalent stress  $\Sigma_{eq}$ , mesoscopic equivalent strain  $E_{eq}$ , void volume fraction  $VVF$ , void aspect ratios  $W_1$  and  $W_2$ , and lengths of the major  $M$  and the two minor axes  $m_1$  and  $m_2$  are defined and calculated in the same way as in the previous section. For calculations we used  $J_2$  plasticity and the UMAT models to describe the brass matrix.

Figure 4.87 presents the evolution of the void or the void-lead inclusion system in terms of the  $f_M$ ,  $f_{m1}$  and  $f_{m2}$ . Comparing Figures 4.87(a) and 4.87(b) we observe a relatively small effect of the lead on elongation of the void axis. Obviously lead prevents  $m_1$  from shrinking down to zero in the  $J_2$  plasticity simulation, but it has little effect on the elongation of the  $m_2$  axis. Lengths of axes  $M$  and  $m_2$  are not really affected by lead.

Figure 4.88 depicts the evolution of the void or the void-lead inclusion system in terms of  $W_1$  and  $W_2$  under *PT* loading, which can be directly compared to the experimental observations in interrupted *PT* samples presented in Figure 4.69.  $W_1$ , obtained from numerical simulations grows much faster than in real experiments.  $W_2$  stays almost constant during loading in experiments, whereas in simulations, it grows approximately three times by the end of the loading.

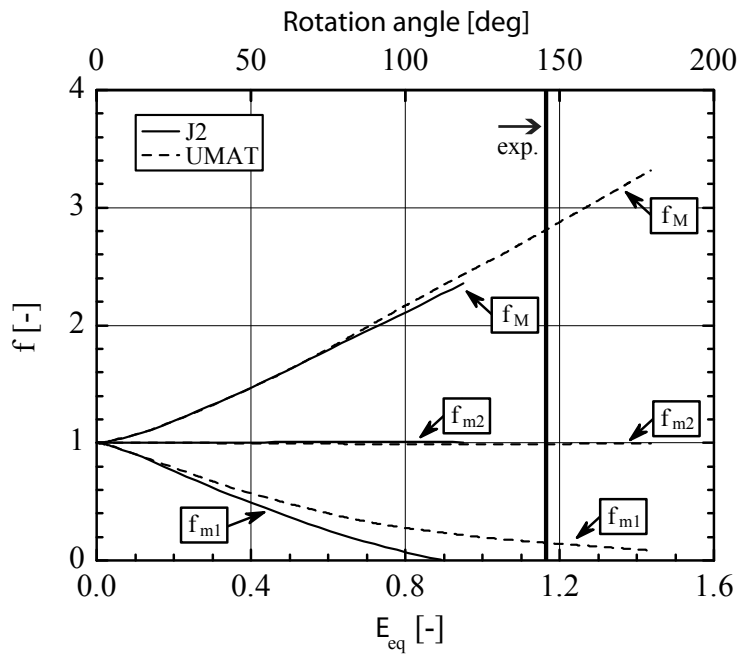
We observe in Figure 4.89 that the void closes around the lead inclusion causing the  $VVF$  of the void-lead inclusion system to stabilize. Similar behavior can be observed for simulations run with the  $J_2$  plasticity and UMAT models, although the closure happens later in the UMAT simulation. Figure 4.89 may be compared directly with Figure 4.70 which presents the corre-



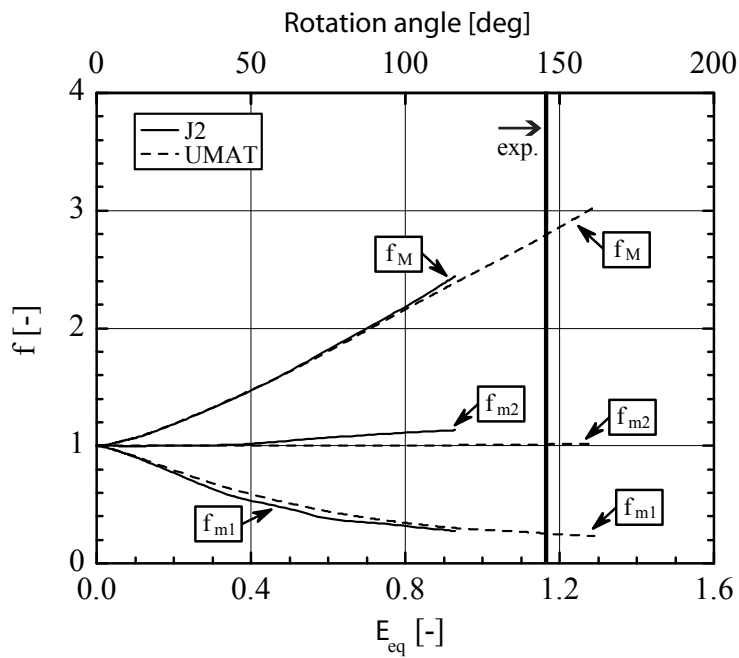
---

sponding experimental results obtained in interrupted  $PT$  tests. Numerically simulated  $VVF$  evolution does not correspond at all to the experimental results. An increase in  $VVF$  is not calculated but rather a decrease.

Comparing results of single cell simulations with experimental results we conclude that the elongation of voids in the radial direction which is observed in experiments, cannot be attributed to the influence of lead.



(a) Model containing a void.



(b) Model containing a lead inclusion.

Figure 4.87: Evolution of the void axis elongation factors  $f_M$ ,  $f_{m1}$  in single cell simulations for the PT loading, for a model containing a void and a lead inclusion.

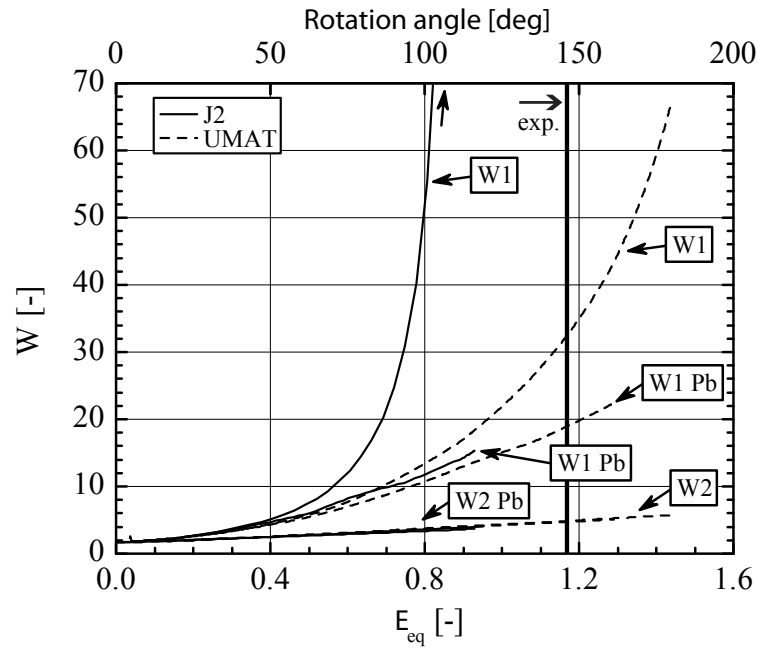


Figure 4.88:  $W_1$  and  $W_2$  single cell simulation results for the PT loading, for a model containing a void and lead inclusion. Results for the cell with the lead inclusion are marked "Pb".

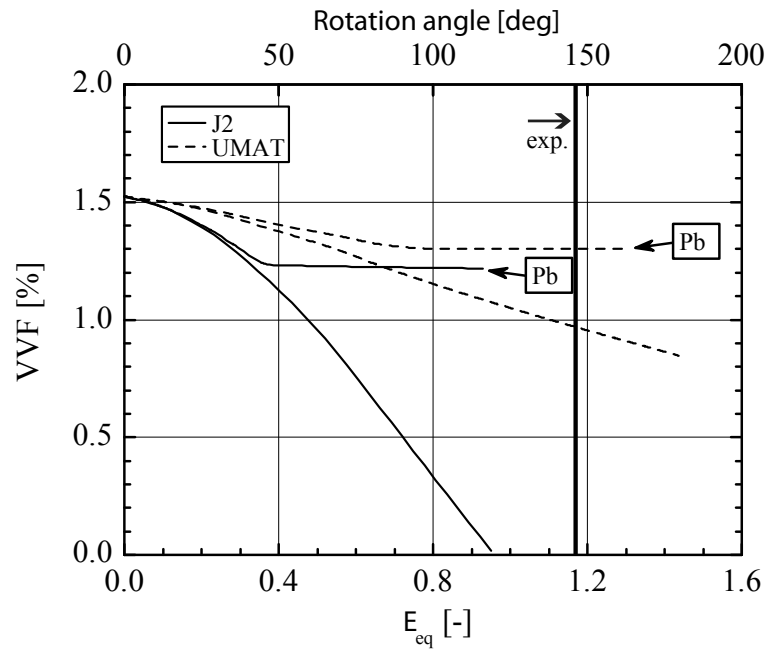


Figure 4.89: VVF single cell simulation results for the PT loading, for a model containing a void and lead inclusion. Results for the cell with the lead inclusion are marked "Pb".

## 4.6 Key experimental and numerical results

### 4.6.1 Material behavior under loading

The *A1* and *A2* alloys were found to exhibit texture anisotropy. The initial anisotropy results from the manufacturing of the bar and causes different yield stresses under different loading conditions (presented in Figure 4.8). Different strain hardening rates and elongation of the *PT* sample compared to the *ST* sample may be explained by the effect of texture evolving differently under different loading modes.

Macroscopic axisymmetric simulations prove the necessity of including anisotropy in calculations of the behavior of samples. The employed crystal plasticity material model (UMAT) is able to predict the different yield stress and strain hardening in different loading conditions, and captures elongation of thin-walled tubular samples under *PT* loading. However, it is not able to pick-up the localization of deformation in the *ST* and the *TT2* specimens, at least using the selected parameters, in particular the strain rate sensitivity as explained in Section 4.2.3. Neither the  $J_2$  nor the UMAT material model is capable of predicting the shape changes in the *PT* sample correctly.

### 4.6.2 Fracture mechanisms

Under tension and notched tension loadings, both the investigated alloys, *A1* and *A2*, exhibit intergranular fracture (Section 4.3.4). In the *A1* alloy the intergranular fracture is determined by the tendency for large lead inclusions to appear at grain boundaries. Upon loading the pre-existing voids in the lead, inclusions grow to coalesce by necking the intervoid ligaments. Cracks formed in this process follow the chains of lead inclusions. In the *A2* alloy under notched tensile loading, voids nucleated at hard inclusions also coalesce by necking the intervoid ligaments down to a sharp edge. Thus both alloys exhibit the VNGC type of fracture under tensile loading. Under torsional loading conclusions about the fracture mechanism are difficult because the microstructure is highly deformed (see Figures 4.37 and 4.38). However sheared voids, which increase in volume and coalesce by necking of the intervoid ligaments play the major role in the fracture process.

#### Void nucleation

In both alloys the nucleation phase of fracture does not exist (Section 4.3.1). In the *A1* alloy each lead inclusion contains a void which starts growing or deforming as soon as load is applied. In the *A2* alloy the pre-existing voids are associated with hard inclusions and that originate during manufacturing of the round bars.

### Void growth under tensile dominated loadings

We characterized quantitatively void growth in the *A1* alloy in Section 4.4. We found that voids can be considered as initially axisymmetric and their majority is oriented in the direction of the sample axis. They change their shape (aspect ratio) depending on the loading, and rotate to orientate in the main loading direction if it is not already the case in the undeformed sample.

We found in experiments that voids grow relatively little, less than  $\times 2$ , under tensile and notched tensile loadings and before the onset of coalescence. Single cell simulations performed with both the  $J_2$  and UMAT plasticity models confirm relatively small  $VVF$  increases. The  $VVF$  results obtained in numerical simulations are slightly higher (Table 4.3). The crystal plasticity material model causes the single cell to increase its  $VVF$  and deformation to localize faster than the  $J_2$  plasticity model.

### Void growth under shear dominated loadings

Experimental measurements suggest very significant  $VVF$  increases in torsion samples, even under pure torsion loading (Table 4.1). Measurement derived  $VVF$  values for the *PT* are several times higher than those for the *NT3* loading. These results suggest that void growth depends mainly on the strain to coalescence and less on the stress triaxiality (tensile-torsion samples with positive stress triaxiality have the  $VVF$  at coalescence smaller than the *PT* sample with 0 stress triaxiality, but with higher  $\varepsilon_{eq}^{pl}$ ). These surprising results of void growth under zero nominal triaxiality appear to be confirmed by densitometry measurements performed on interrupted *PT* samples, although the obtained  $VVF$  values are significantly smaller than determined from metallographic observations (Section 4.4.4).

Single cell simulations were not able to reproduce the behavior of the material and under *PT* loading conditions, the single cell was found to collapse the void. We observe in Figure 4.86 the shape of the single cell for shear dominated loadings. Under the *PT* loading  $m_1$  shrinks down to zero in the  $J_2$  simulation. This shortening of  $m_1$  is slower in simulations carried out using the UMAT material model and therefore the  $m$  length is positive at the end of the loading.

The second major reason for underestimated  $VVF$  predictions in single cell simulations, is the elongation of  $m_2$ . Experimentally observed elongation of  $m_2$  was reproduced neither with the  $J_2$  nor UMAT material models.

It was impossible to reproduce void growth in the *PT* loading with the single cell simulations, but the influence of the crystal plasticity on material behavior is confirmed to be large.

### Void coalescence

The coalescence stage of fracture was found to be very localized in the *A1* alloy and somewhat more diffused in the *A2* alloy. The coalescence is related to creation of the macroscopic crack in the middle of notched tensile samples, and occurs in the region of the crack tips while other regions of the sample stop growing voids.

Measurements of  $m$  elongation in the *NT3* samples provide results on the amount of deformation that the alloys undergo in the coalescence stage of fracture (Section 4.4.5). Measurements show that  $m$  elongates an order of magnitude more during coalescence compared to the stable void growth stage.

#### 4.6.3 Size dependence

The initial void aspect ratio of lead inclusions depends on their size, which results from the tendency of large inclusions to appear at grain boundaries (Figure 4.59). The void growth (elongation of the length of the axes) seems to be only slightly size dependent. This slight size dependence of the axes elongation might result from the different initial aspect ratio of the voids of different sizes.

# Chapter 5

## Discussion

### 5.1 General outline of the discussion

The aim of Chapter 5 is to comment on and discuss the experimental and numerical results presented in Chapter 4, and to correlate them with data published in the literature. Chapter 5 is composed of three main sections:

Section 5.2 - Global behavior, which discusses the influence of the texture induced anisotropy, including twinning, on the sample response in terms of the load-deformation plots and on the shape changes in the thin-walled torsion sample under pure torsion loading conditions. The influence of pre-existing voids on the strain to fracture is also analyzed by comparing the behavior of the *A1* and *A2* alloys.

Section 5.3 - Fracture behavior, which covers the entire void nucleation growth and coalescence process. We discuss, in parallel both the experimental and numerical results including changes in shape of the voids, void volume fraction and how these are affected by crystal plasticity.

Section 5.4 - Size effects, which interprets the initial scale dependent shape of voids as well as their possible size dependent evolution.

### 5.2 Global behavior

The very ductile matrix of the selected model materials can undergo large strains before fracture, which is particularly obvious with the *A2* alloy (containing a low volume of inclusions), at low stress triaxiality loadings. Addition of lead to the *A1* alloy significantly decreases strains at fracture, which remain relatively large. These large strain can cause significant changes in the microstructure of the alloy. The microstructural changes influencing the global response of the sample in terms of load-deformation, need to be taken into account for correct simulation of sample behavior. These changes such as

texture or twinning, which influence the global response of the sample, will be discussed in this section together with the effect of the inclusion volume fraction on the strain to fracture.

### 5.2.1 Texture induced anisotropy

Both model materials, *A1* and *A2*, exhibit the initial anisotropy resulting from the manufacture of the bar and also evolving anisotropy during plastic deformation. We investigated both materials, but only characterized in detail the *A2* alloy to avoid additional anisotropy and other effects resulting from void growth which might arise if using the *A1* alloy.

The influence of texture anisotropy on the constitutive behavior of different materials under tensile and shear loading is generally known, and a literature review on this effect was presented in Section 2.3. In the model materials used, the influence of texture anisotropy in the *PT* sample was found to be large.  $J_2$  isotropic material flow simulation over-predicts by a factor of two the torque, and therefore the stress, in the sample at the onset of fracture in the *A2* alloy. Significant influence of the developing texture on sample response is observed even in tensile dominated loadings. Figure 4.14 presents results of *NT3* tests with corresponding simulations using the  $J_2$  and crystal plasticity material models. Use of the isotropic von Mises plasticity model, predicts a maximal load 9.1% higher than the experimental value, while in the case of the UMAT, the error is only 2.3%.

In terms of numerical modeling of the global sample response, the crystal plasticity model performs better compared to the  $J_2$  model for all loading conditions. It convincingly predicts the force-displacement and torque-rotation angle behavior of the macroscopic samples under various loading conditions (tensile, notched tensile, torsion, tensile-torsion) but not the strain localization. We were not able to reproduce necking either in smooth round tensile samples or in tensile-torsion samples with high axial loads, *TT2*, despite the small geometrical perturbation introduced into the model. The fact that localization is poorly captured in our simulations might be due to an oversimplified hardening law, resulting from lack of twinning in the chosen model, and from a simplified treatment of viscoplasticity, or strain rate effects.

A possible way to overcome the inadequate description of the strain hardening behavior would be to calibrate the UMAT using the *PT* test results. In our approach, we calibrated the UMAT using the stress-strain data obtained in the *ST* sample for a relatively small range of strains. The stress-strain curve was then extrapolated to higher strains using the Ludwik-type power equation (Section 3.4.1). If the *PT* test was used to calibrate the UMAT, we would obtain the experimental stress-strain relationship without needing to extrapolate. However other problems might arise, for example in the *PT* and *TT1*



cases, it was impossible to run the simulations of the *A2* alloy to the end using the crystal plasticity material model, and the calculations terminated due to convergence problems (Figure 4.15 and 4.16 respectively). Observed difficulties for simulating experiments up to high strains might be due to strong mesh distortion, thus when using the model for high strains it might be necessary to introduce re-meshing to the simulation to avoid extensive mesh distortion. In the field of crystal plasticity FEM simulations adaptive mesh refinement and automatic re-meshing were used by e.g. by Resk et al (2009) to capture local strain gradients resulting from the heterogeneity in material properties.

A more advanced model of crystal plasticity which takes into consideration twinning is being developed by Professor L. Delannay and his team (Dancette et al, 2010). This "multisite" model takes into account the short- range interactions amongst adjacent grains. The model, once available, could be used to improve numerical predictions of the sample response in terms of load-displacement and in terms of shape changes discussed separately in Section 5.2.2.

In our simulations, we neglected the effects of viscoplasticity, and performed all simulations at approximately the same strain rate, arguing that strain rate dependence was not observed in our materials at room temperature. Some authors have proven the contrary in the literature (Bressan and Unfer, 2006) but the data is not consistent and provides very different values of strain rate sensitivity parameters in tensile and torsion tests). If, after implementing twinning into the model and calibrating it using the *PT* stress-strain relationship, it is still impossible to account for the strain localization, then analyzing the strain rate dependence of the model alloys would be worthwhile.

Relatively low differences in strain hardening rates between the *A1* and *A2* alloys can result from deviations from nominal chemical compositions and/or differences in composition between the two alloys or micro-structural differences such as grain size, but are most probably due to the presence of lead inclusions acting as pre-existing voids in the *A1* alloy. The Hall-Petch relationship (Hall, 1951; Petch, 1956), a linear dependence of the yield stress of metals on the inverse of the square root of the average grain size, is not generally valid in the analyzed brass alloys. We observe that with different grain sizes presented in Figure 3.1, both the *A1* and *A2* alloys exhibit the same yield stress under *ST* loading (Figure 3.8(a)). (The average grain diameter is 26 and 79  $\mu\text{m}$  for the *A1* and *A2* alloy, respectively, thus the Hall-Petch relationship would predict a factor of 1.7 difference between the yield stress of the two alloys). Under different loadings we observe small differences between *A1* and *A2* in the axial load or torque at yield.

The observed texture anisotropy also has an impact on void growth and coalescence, as well as elongation and most likely other shape changes of the thin-walled tubular torsion samples under pure torsion loading. These phe-

nomena will be discussed in separate sections.

### 5.2.2 Shape changes in PT samples

In the *PT* tests we observe an interesting behavior, notably the shape changes of the thin-walled torsion samples. The first change is the significant elongation in the axial direction. The effect of elongation of twisted samples under zero axial load is called the Poynting (Poynting, 1909, 1912) or Swift (Swift, 1947) effect for elastic and plastic deformation regimes respectively. The Swift effect is claimed to originate in anisotropy associated with developing deformation texture.

The elongation of the *PT* sample has a nonlinear character as shown in Figure 4.6. The change in the elongation rate of the *PT* sample, easily observable in the *A2* alloy at approx. 90 deg of sample twist, and evidenced in the change in pseudo torsional stiffness (or pseudo strain hardening) versus rotation angle of Figure 4.7, appears when the strain hardening of the alloy becomes linear suggesting a micro-structural origin to the two phenomena. We may attribute this change in elongation rate to twinning on the basis of microstructural observations, both our own and those reported in the literature. We refer to data presented by Asgari et al (1997) for an  $\alpha$ -brass (30% Zn). Their microscopic observations show that the plateau in the strain hardening rate can be correlated with the onset of twinning, and it is the twin-twin and twin-slip hardening interactions that arrest the decrease in the strain hardening rate in brass at these intermediate strain levels. Changes in the slope of the strain hardening rate can also result from micro-scale shear banding depending on the deformation mode; however in simple shear only deformation twins, thus no shear banding was observed (El-Danaf et al, 2000, 2001).

The microstructure of the *A1* alloy after *PT* deformation is presented in Figure 5.1. At 50 deg of sample twist the microstructure is similar to the one in the undeformed material presented in Figure 3.4(a). However, at 70 deg of sample twist, where the strain hardening rate presented in Figure 5.2 (or previously in Figure 4.7) is constant, we can observe the appearance of large numbers of twins in the microstructure.

In addition, some nonlinearities are observed in Figures 4.19, 4.20 and 4.21 indicating size changes of the external diameter  $D$ , internal diameter  $d$  and wall thickness  $t$  of the thin-walled torsion sample. The nonlinear changes in the elongation rate for  $D$ ,  $d$  and  $t$  appear again at angles corresponding to the change of axial elongation rate and strain hardening in the *PT* sample, although the number of interrupted tests for  $D$ ,  $d$  and  $t$  measurements, is not sufficient to localize the onset of nonlinearity exactly. Following the logic presented in the previous paragraph, we tend to attribute these nonlinearities in the rate of change in the *PT* sample dimensions to the twinning of brass.

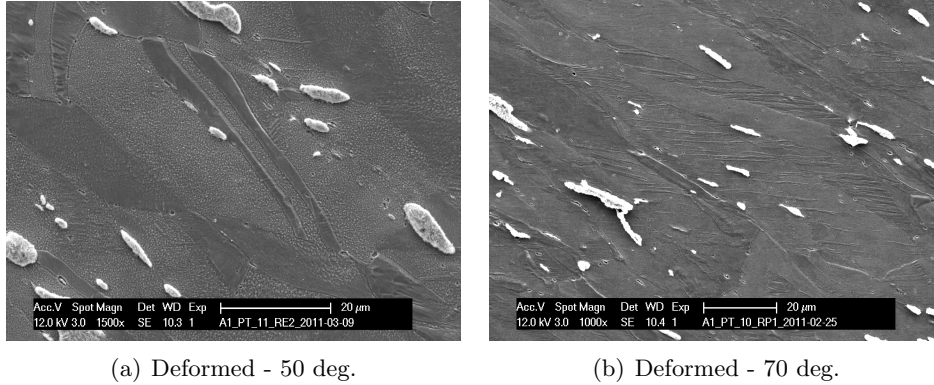


Figure 5.1: Microstructure of A1 alloy after *PT* deformation revealed by electro-etching (SE).

Neither of the two material models used, the  $J_2$  or UMAT, is capable of simulating these nonlinear rates of change or correctly predicting the shape changes of the *PT* sample. The  $J_2$  underestimates and the UMAT overestimates elongation of the *PT* sample, reduction of the  $D$  and  $d$ . Both, the  $J_2$  and the UMAT constitutive models predict no  $t$  change, while  $t$  varies significantly in real experiments. Advanced crystal plasticity models with twinning (e.g. Dancette et al, 2010) might be able to improve the results of numerical simulations and predict these nonlinear shape changes in the *PT* sample.

### 5.2.3 Effect of pre-existing voids on coalescence and ductility

By comparing force-displacement and torque-rotation angle plots, we notice a large influence of the lead inclusions on the deformation to fracture, by acting as pre-existing voids – which is demonstrated by numerical simulations using the GTN model presented in Section 3.2.5. Fracture occurs much earlier in the loading history in the lead-containing A1 alloy than in the lead-free A2, as shown in the figures of Section 4.2. For example, in the A2 smooth round tensile test, we observe a much more extensive region of stable softening before the onset of rapid drop of load carrying capacity, which can be related to the onset of coalescence. The response of samples after the onset of rapid drop of load carrying capacity is relatively stable in the A2 alloy, but has a very abrupt character in A1.

The characteristics of the softening of the sample response after the onset of coalescence are influenced by the relative spacing of voids. Relatively small distances between voids causes the A1 alloy to coalesce at an earlier stage of deformation than the A2 alloy and in a quite abrupt and uncontrolled way. Pardoen and Hutchinson (2000) also observed on the basis of simulations that

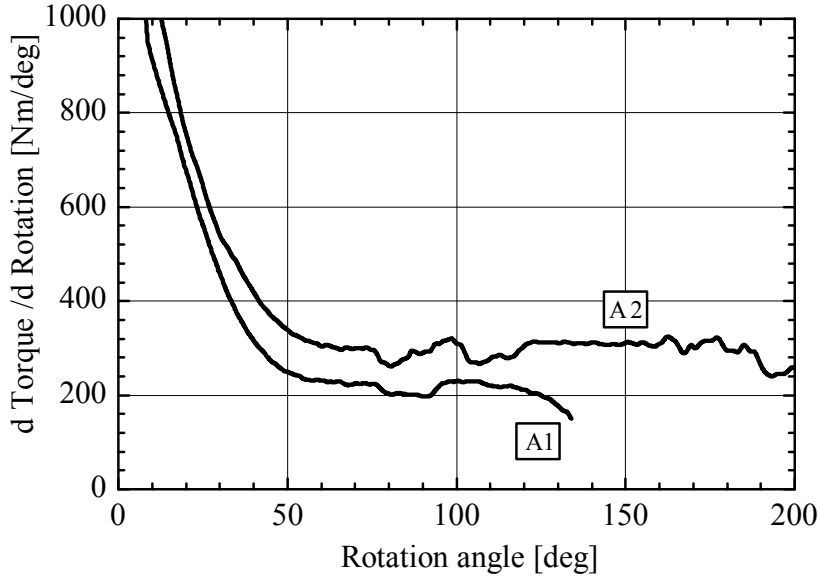


Figure 5.2: Rate of torque increase vs sample rotation angle in the PT sample. Data were filtered to remove "noise", due to short range fluctuations.

decreasing the relative inter-void spacing causes material to coalesce earlier in the loading history and that the load carrying capacity drops faster. This same mechanism causes the macroscopic crack, created in the center of tensile and notched tensile samples, to follow grain boundaries in both alloys; inclusions have a tendency to appear at grain boundaries and thus the smallest inter-void distances are in the grain boundary planes. However, we should not neglect that other micro-structural effects may also play a role.

It is generally accepted that the strain to fracture increases with decreasing stress triaxiality because of the decelerated void growth. In Table 4.2 presenting equivalent plastic strain,  $\varepsilon_{eq}^{pl}$ , at the onset of coalescence obtained in the  $J_2$  simulations, an apparent discontinuity in the theoretical trend can be observed. When changing modes from tensile dominated to shear dominated loading, the  $\varepsilon_{eq}^{pl}$  decreases even if the stress triaxiality decreases ( $\varepsilon_{eq}^{pl} = 1.243$  and  $T_{avg} = 0.397$  for the *ST* loading,  $\varepsilon_{eq}^{pl} = 0.814$  and  $T_{avg} = 0.169$  in the *TT2* sample for the deformations corresponding to the onset of coalescence in the *A2* alloy). This behavior of the strain to fracture curve obtained from the  $J_2$  simulations is graphically presented in Figure 5.3 by solid lines. A similar phenomenon was already reported in the literature by Bao and Wierzbicki (2004, 2005); Wierzbicki et al (2005); Barsoum and Faleskog (2007a,b). However, in our simulations we think that the calculated decrease in fracture strain results from poor prediction of strain localization and is not a real feature. As discussed above in Sections 5.2.1 and 5.2.2, for various reasons we were not

able to simulate correctly necking, particularly in the *ST* and *TT2* samples, and real strains in the samples are expected to be higher. This judgement is based on the equivalent plastic strain estimations from experiments which are presented in Figure 5.3 by solid lines with circles. The experimental values of strain were estimated based on the shape changes of the fractured samples, however  $T_{avg}$  values used for the experimental  $\varepsilon_{pl}^{eq}$  plot also come from the  $J_2$  simulations (see Table 4.2). The presented experimental strain values are much higher than those obtained from simulations, particularly under shear dominated loadings. In the experimental results we do not observe the discussed decrease in the strain to fracture. In the last stage of fracture there is some more pronounced shear localization in the vicinity of the fracture plane. Along 100  $\mu\text{m}$  axial line across the fracture plane of the *PT* sample of the *A1* alloy, the experimental shear strain is varying between 1.4 and 2.8 (this strain was obtained from the rotation of deformed lead inclusions in fractographs such as Figure 4.39, see also Figure 4.42).

The growth of voids in the *A1* alloy will be discussed in detail in Section 5.3.

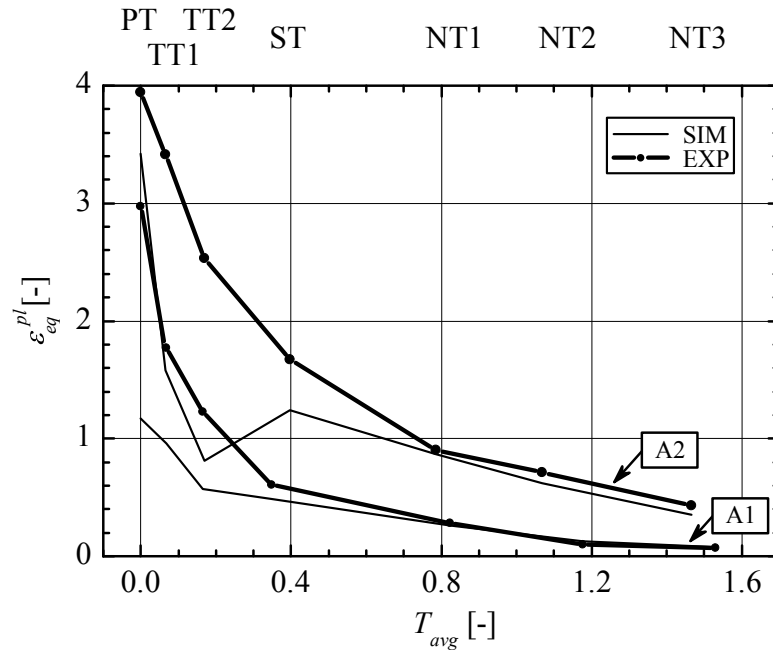


Figure 5.3: Fracture curve in the equivalent strain and stress triaxiality space.

### 5.3 Fracture behavior

*A1* and *A2* alloys exhibit void nucleation, growth and coalescence type of fracture. As a result of the very high ductility of the matrix material, using

our approach presented in Chapter 3, we can track and measure significant changes in the void shape and volume in the *A1* alloy. Voids demonstrated very interesting behavior, especially under shear dominated loadings. These results are discussed below.

Section 5.3.1 describes the fracture mechanisms and the propagation of cracks in the samples. The void nucleation, growth and coalescence stages of fracture are described in Sections 5.3.2, 5.3.3 and 5.3.4, respectively. In Section 5.3.3 we describe the evolution of void shape and volume separately for tensile and shear dominated loadings as they are of a different nature. We comment in parallel on experimental and numerical results where possible.

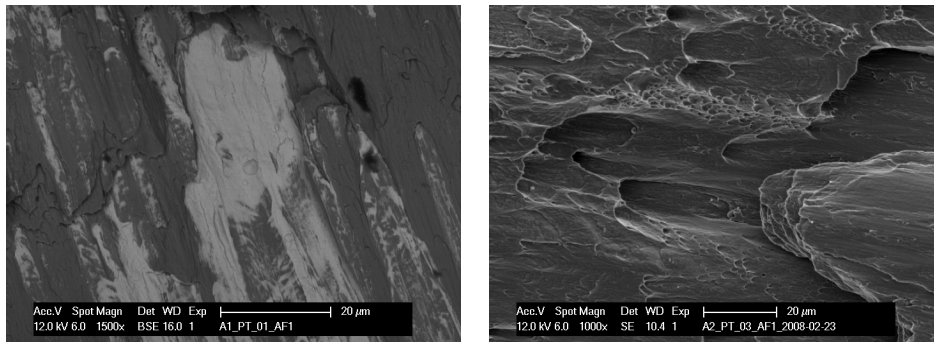
### 5.3.1 Fracture mechanism

The two tested alloys exhibit inter-granular fracture in tensile dominated loadings. In the *A1* alloy the inter-granular fracture is determined by the tendency of lead inclusions to appear at grain boundaries. Buršíková et al (2002) and Pantazopoulos and Vazdirvanidis (2008) also reported inter-granular fracture present in brasses with high Zn content. In their studies on  $\alpha - \beta$  lead-containing brass alloys, the brittle inter-granular fracture is attributed to the differences in the mechanical properties of the two phases and the authors do not consider it due to the presence of lead at grain boundaries which is not investigated in the article.

In tensile and notched tensile samples, a macroscopic crack is created in the middle of the sample which is the region of the highest stress triaxiality. A similar behavior of tensile samples was observed i.e. by Tvergaard and Needleman in their classical paper which found the onset of macroscopic fracture to be associated with a sharp "knee" on the load-deformation curve, that is with the rapid drop of load carrying capacity (Tvergaard and Needleman, 1984).

Under torsional and tensile torsional loading, it is more difficult to identify the fracture mechanisms because the microstructures and the fracture surfaces are highly deformed. Also, etching of sample cross sections does not reveal grain boundaries due to very high deformations. However, we believe that the alloys exhibit inter-granular fracture also under torsion dominated loadings. In the fracture surfaces of the *A1* alloy we observe smeared remnants of large lead inclusion, as presented in Figure 5.4(a), which usually appear at grain boundaries in the undeformed material. In the fracture surfaces of the *A2* alloy we observe shapes that can be interpreted as pulled out grains, as presented in Figure 5.4(b).

From the macroscopic cracks visible on the surfaces of the torsion samples, we conclude that in the *PT*, sample fracture initiates at the outer surface of the gauge cylinder. Macroscopic cracks visible on the outside surfaces are



(a) Large lead inclusion in the A1 alloy (BSE). (b) Grain boundary fracture in the A2 alloy (SE).

Figure 5.4: Fracture surfaces of the A1 and A2 in PT samples.

longer than cracks visible on the inside surface. After initiation, macroscopic cracks propagate simultaneously in the radial direction towards the center of the sample and in the tangential direction along the perimeter. The observation of cracks initiating at the outer surface of a thin-walled torsion sample is in agreement with crack propagation results observed in a VAR steel presented by Cannizzaro (2006). In the *TT2* sample fracture initiation happens inside the gauge cylinder, in the region of the highest stress triaxiality induced by the high axial load. The initiated macroscopic crack propagates in the radial direction towards the inner and the outer surfaces, forming shear lips. The resulting shape of the gauge cylinder cross section forms a "V".

The A1 model material produces one population of voids that originate in lead inclusions with every loading condition. The A2 alloy produces one population of voids that originate at hard inclusions in tensile loadings, however under pure torsion loading, it might nucleate a second population of voids at other microstructural defects, at intersections of dislocation pile-ups at the twin interface, intersection of twins (Smallman and Ngan, 2007) or at grain boundaries and triple points, but we have no hard evidence for that.

### 5.3.2 Void nucleation

In the A1 alloy the nucleation phase does not exist. In this alloy each lead inclusion contains a pre-existing void which starts growing or deforming as soon as load is applied (Section 3.2.5). Other researchers have come to similar conclusions: Mir et al (2005) in their studies on void growth in leaded free machining steel (FMS) in which they assume that lead inclusions behave as voids and they don't strengthen the parent metal; while Foster et al (2007) hypothesize in their research on free-cutting steel that there is no bonding strength between the MnS inclusions and matrix, because lead is often pref-

entially found at the inclusion-matrix interface.

The A2 alloy contains pre-existing voids which are associated with hard particles. The pre-existing voids always appear at the poles of inclusions aligned with the direction of the axis of the round bar. This fact suggests that the pre-existing voids originate during the manufacture of round bars, and are not an effect of etching. Similar observations of pre-existing holes induced by the extrusion process at the inclusion-matrix interface were made by Babout et al (2001). Their analysis which used high resolution X-ray tomography of commercially pure Al metal matrix reinforced by spherical ceramic particles, revealed that 50% of the particles were pre-damaged by the extrusion. It is possible that the particle/matrix decohesion was also present in the other half of particles but was not observed due to insufficient resolution of the measuring system ( $2 \mu\text{m}$ ). These observed pre-existing voids ranging in size from 40 and 60  $\mu\text{m}$ , grew during tensile loading. Our investigation shows that this phenomenon exists also on a much smaller scale (size of hard inclusions was 1.15 - 1.74  $\mu\text{m}$  in our study).

### 5.3.3 Void growth

For the analysis of void growth, our attention is focused on the A1 lead-containing alloy, which is our first model material. We measured void growth in real polycrystalline material using the approach presented in Chapter 3 and the average void evolution obtained for all grain orientations.

In the single cell simulations we reproduce this approach using the polycrystal plasticity material model presented in Section 3.4.4, and compare these predictions with those of the  $J_2$  plastic flow model.

It is worth mentioning that in single cell crystal plasticity simulations it is usual to employ single crystal plasticity models (Potirniche et al, 2006; Liu et al, 2007; Yerra et al, 2010; Ha and Kim, 2010; Yu et al, 2010). Voids are assumed to be small and embedded in single crystals, which is usually true. Following this approach the influence of crystal orientation on void growth is analyzed, which is not our goal. Our goal in the single cell simulations is to reproduce our experimental approach, in which we observe evolution of an averaged void. This evolution of an averaged or representative void was experimentally measured for all observed grain orientations, and therefore we use a polycrystalline material model to describe the average behavior of matrix material.

In this section we comment on the final results and not the technical details or intermediary results. These can be found in Chapter 3 and in Section 4.4, respectively.



### Measurement techniques

To calculate the  $VVF$  in tested samples we used measured changes of the lengths of three axes of an equivalent ellipsoidal void. The changes in length were obtained by comparing the cumulative distributions of the void axis length obtained by performing length and area measurements of the voids. Hoefnagels et al (2009) claim that methods based on area measurements are very sensitive to many experimental parameters and hence should only be used in cases where high accuracy or absolute damage parameter quantification are not necessary. Among these parameters they list the following: the manual setting of the grey value threshold, the influence of the SEM magnification used and the assumption that the surface area void fraction equals the volume void fraction (but also the influence of specimen preparation methods and the damage gradients between different cross - sections). In this section we analyze the listed sources of errors to verify their potential influence on our void growth measurements.

The micrographs used in our investigations of void size analysis were taken using the same microscope settings, i.e. microscope working distance and magnification (see Section 3.3.3), and we assume therefore, they are not a source of error in our analysis or they always cause the same error when quantifying undeformed and deformed specimens.

In the  $A1$  model material, due to the very high chemical contrast between lead inclusions and the surrounding matrix, it is easy to filter bright inclusions. Indeed, it was observed that the manual setting of the gray level threshold could influence the total number of observed inclusions (or just brighter pixels) by increasing or decreasing the number of observed small inclusions. However these small inclusions were not used for measuring void growth (see Section 3.3.3) and only the relatively large, well defined inclusions were used for the  $VVF$  calculations. Additionally, our  $VVF$  calculations are based on the relative elongation of the axes and the direct axes length measurements were not used. This reduces the influence of eventual errors in axis length measurements.

However, there may be other errors due to e.g. non ideal ellipsoidal void shape and their orientation which are difficult to estimate and therefore we ignore.

Hoefnagels et al (2009) suggest for measuring the  $VVF$  that the volume fraction methodologies, e.g. computed tomography, are more trustworthy than area measurement based methods, although the "thresholding" process of voids and material may introduce a significant systematic error. In our model material, we found that the contrast between the matrix and lead in CT micrographs is much lower compared to SEM BSE micrographs and in the end we were not able to use this method for  $VVF$  measurements. However, we found

CT very useful for visualizing the 3D morphology of the void and its evolution, or fracture process and used it to confirm some phenomena observed in our material. This will be discussed in the following sections.

### Shape of voids under tensile loading

Our research characterized voids in terms of their initial shape and the elongation of their axes. We characterize elongation by introducing the void axis length elongation factors  $f$ , which describe by how much the axis elongated with respect to their initial shapes (Section 3.3.4). We observe that in experiments, void axes elongate at different rates and extents and in different directions depending on the loading.

Figures 4.60(b) and 4.61(b) show the major and minor void axis elongation factors,  $f_M$  and  $f_m$ , as a function of the  $M$  and  $m$  initial axis length. In general, we observe that voids in samples with increasing  $T_{avg}$ , elongate less in the direction of principal loading (axis of the sample), but rather elongate in the perpendicular direction (radial direction of the sample). This is very clear in the case of the  $f_m$ :  $NT3$  elongates,  $NT2$  maintains its length and both  $NT1$  and  $ST$  shorten. Averaged values of the elongation factors presented in Table 4.1 confirm this observation. In case of the major axis this trend is not as obvious as the  $m$ , but in general we can say that samples with smaller  $T$  elongate mainly in the axial direction.

The different elongations in different directions lead to various void shapes at the onset of coalescence depending on the loading and are presented in Figure 4.67 in terms of the void aspect ratio. We observe that with increasing  $T_{avg}$ , the final shape of the void is more spherical, while the samples with smaller  $T_{avg}$ , e.g.  $ST$ , voids are more prolate.

This observation is in good agreement with data available in the literature. The influence of the stress triaxiality on the evolution of voids was widely tested both by single cell calculations and experimentally (Budiansky et al, 1982; Becker et al, 1989b,a; Sovik and Thaulow, 1997; Pardoen and Hutchinson, 2000; Benzerga, 2000; Mir et al, 2005; Lassance et al, 2007; Scheyvaerts, 2008).

As an example, Mir et al (2005) showed the effect of the void shape in terms of the void aspect ratio as a function of the distance from the center of the tensile sample. As the distance from the center of the sample increases, the stress triaxiality decreases and the mean void aspect ratio increases, meaning that voids are more elongated.

In our experimental approach we assume that voids stay axisymmetric during tensile dominated loading. This is true within the error of measure-

ment (see Figure 4.48) for voids in as received material. It is also true in the single cell simulations for tensile dominated loadings performed with the  $J_2$  material model. However in the single cell calculations performed with the crystal plasticity material model, we observe, that voids elongate at different rates in the two directions perpendicular to the principal loading directions, even if the load in these directions is the same. These shape changes in terms of  $f_M$ ,  $f_{m1}$  and  $f_{m2}$  are presented in Figures 4.77(a) - 4.80(a).

Similar changes in void shape requiring description using two aspect ratios, were observed in single cell simulations using the single crystal plasticity model e.g. by Yerra et al (2010). In our simulations, voids keep their ellipsoidal shape before the onset of coalescence. Irregular shape changes ("corners") induced by the localization of plastic flow and anisotropic behavior as reported in Liu et al (2007) were not observed.

### Void volume fraction results under tensile loadings

$VVF$  values are calculated from the experimental observation of the void axis elongation and are a direct result of the changes described in the previous section. Table 4.1 on page 144 summarizes the  $VVF$  values derived from the experimental observations in all samples at the onset of coalescence.

Experimentally observed  $VVF$  changes in the tensile dominated loadings indicate a relatively low  $VVF$  growth in the tested samples at the onset of coalescence. In general the  $VVF$  is higher in samples with higher stress triaxiality, except for the  $ST$  and  $NT1$  samples.

In the  $ST$  samples, we observe relatively high  $VVF$  growth compared to  $NTx$  samples with higher stress triaxiality. This behavior, even if non-intuitive at first glance, may not be contradictory to predictions of the fracture models taking into account shape changes or the results of single cell simulations. After the early stage of deformation, voids are more elongated than in non-deformed material and more likely to grow in the radial direction after the onset of necking. This mechanism may allow this relatively high  $VVF$  increase, however we did not investigate it in detail.

In the  $NT1$  sample, there is a small drop in the  $VVF$  observed. We do not expect the  $VVF$  to drop under notched tensile loading conditions and therefore we assume this  $VVF$  variation is due to a non-homogeneous distribution of lead inclusions in the material or, less likely, due to measurement error.

Similarly, relatively low  $VVF$  growth is observed in the single cell simulations for tensile dominated loadings. The  $VVF$  graphs as a function of the loading history are presented in Figures 4.77(b) - 4.80(b) for the different loadings. The  $VVF$  values at  $E_{eq}$  corresponding to  $\varepsilon_{eq}^{pl}$  in macroscopic samples

at the onset of coalescence are also summarized in Table 4.3.

The trend to increase  $VVF$  at the onset of coalescence with increasing stress triaxiality is not reproduced in the single cell simulations. This might be due to the use of the  $J_2$  plasticity model to calculate the  $\varepsilon_{eq}^{pl}$ . These  $\varepsilon_{eq}^{pl}$  results were then used to define the extent of deformation imposed on the single cells. As we know the  $J_2$  does not perform well due to initial and texture anisotropy present in the alloy (Section 5.2).

Nevertheless, these calculations were performed to confirm the relatively small  $VVF$  growth before the onset of coalescence and this goal was achieved. Another reason for performing these calculations was to verify the effect of crystal plasticity on void growth. We observe in the figures and table mentioned above, that crystal plasticity significantly accelerates the void growth and that the  $VVF$  calculated with UMAT are higher compared to those calculated with the  $J_2$  for the same mesoscopic equivalent plastic strains.

Other authors (Potirniche et al, 2006; Liu et al, 2007; Yerra et al, 2010; Yu et al, 2010; Ha and Kim, 2010) also report a very significant influence of the lattice orientation on void growth and therefore elongation of void axes, which becomes more significant for low stress triaxialities (Ha and Kim, 2010). Keralavarma and Benzerga (2010) observed that both prolate and oblate voids in the Hill type plastic anisotropic matrix (no crystal plasticity) can grow faster or slower in terms of porosity, than a spherical void in an isotropic matrix, depending on the chosen properties of the anisotropic matrix. In the case of the grain orientation distribution measured in our material, the crystal plasticity model accelerates the elongation of void axes in all three directions as well as void growth compared to the  $J_2$  simulations.

The observed void growth affects the response of the single cells as presented in Figure 4.76. We observe that the single cell response in terms of the mesoscopic stress - mesoscopic strain calculated with the UMAT, is much lower compared to the  $J_2$ . Benzerga and Besson (2001) made similar observations which led them to conclude that the influence of the plastic anisotropy could be detrimental in thick aluminium sheets but on the contrary, beneficial in thin zirc-alloy sheets. In our simulations, the weaker hardening response of the single cell is caused simultaneously by the different constitutive behaviors of the material model, and by the accelerated void growth which are strongly coupled. This was also noted by Yerra et al (2010). These effects, also seen at relatively low stress triaxiality, allows us to confirm that the different strain hardenings of the A1 and A2 alloys in the  $ST$  loading could be caused by the development of voids even before the onset of necking in the  $ST$  sample.

### Shape of voids under torsional loading

Although voids are usually assumed to remain axisymmetric in shear dominated loadings (Keralavarma and Benzerga, 2010), our experiments show that they do not. As a result, we need to consider an additional parameter in our study in order to describe the void shape which is the length of the second minor axis  $m_2$ , or its elongation factor  $f_{m2}$ .

Figures 4.62(b) and 4.63(b) present the void axes elongation factors  $f_M$ ,  $f_{m1}$  and  $f_{m2}$  as functions of their initial length. Due to very high strains, the differences in elongation of the void axes are very pronounced. For lower triaxialities, the major void axis  $M$  elongates more, and the first minor  $m_1$  axis shortens. This is known and expected behavior of voids, previously reported in the literature (Potirniche et al, 2006; Barsoum and Faleskog, 2007b; Tvergaard, 2008).

As far as the numerical results of  $m_1$  shortening are concerned, we obtain significantly different results, depending on the material model used. In the single cell simulation of the  $PT$  loading using the  $J_2$  plasticity model, we observe a collapse of the void -  $m_1$  shrinks down to zero before the end of loading to form a flat crack, as also observed by e.g. Tvergaard (2008). In a similar simulation using the crystal plasticity material model,  $m_1$  shrinks but stays positive even at the end of loading (corresponding to the onset of coalescence in a macroscopic  $PT$  test).

The surprise in our experimental results is the very significant elongation of  $m_2$ , that is, elongation of voids in the radial direction of the torsion sample where there is no nominal load. This result is presented in Figure 4.63(b). The ratio  $f_{m2}$  increases monotonically with increasing twist angle, as demonstrated by data obtained in interrupted  $PT$  tests and plotted in Figure 4.65(b).

We were able to confirm this elongation using computer tomography observations, comparing 3D scans of a sample of non-deformed material and a sample tested under  $PT$  loading conditions. However, observed values of the  $f_{m2}$  are not the same as those obtained in analysis of SEM micrographs. On the other hand with CT we detect only large inclusions, which are not included in our void size analysis (Section 4.4) and can be subjected to different loadings at the micro level, due to e.g. interactions of grain boundaries.

It was impossible to reproduce the elongation in the radial direction by performing single cell simulations. Neither of the material models was capable of simulating the  $f_{m2}$  increase on the same scale observed in experiments (Figures 4.83(a) - 4.85(a)). In the most interesting case of the  $PT$  loading, the  $m_2$  axis maintains its length in both the  $J_2$  and the UMAT material model (Figure 4.83(a)).

Simulations performed using a single cell containing a lead inclusion embedded in the void excluded the possibility that the void elongation in the radial direction could be a result of the pressure of lead being squeezed in the void.  $J_2$  simulation predicts little elongation, while the UMAT predicts no significant  $m_2$  elongation <sup>1</sup> (Figure 4.87(a)).

Of course, these different experimental and numerical observations imply different shapes of voids at the onset of coalescence in real material and in simulation. In experiments they elongate by a similar factor in the major direction, which rotates, and in the second minor direction, resulting in a pancake like shape. In numerical simulations, as the void does not grow much in the radial direction it looks more like a squeezed cigar.

The mechanism of void elongation in the radial direction of the torsion specimens is not clear. It is possible that it is related to the texture development and perhaps to twinning. Arguments to support this reasoning are provided in the next section.

The response of the single cell for shear dominated loadings calculated using the  $J_2$  and the UMAT material models differ significantly as shown in Figure 4.82. However, this difference results from the behavior of the matrix and not from the growth of the porosity, as the calculated void volume changes are too small to have such a remarkable impact on the equivalent mesoscopic stress and strain of the single cell. Ha and Kim (2010) report that even for the relatively low stress triaxiality tensile loadings, the deformation mode is mainly determined by the crystallographic orientation.

As far as the influence of hard inclusions on the development of voids is concerned, the wedging effect, assumed by Siruguet and Leblond (2004a,b) in their void growth model and observed by Pardoën et al (1998) for relatively low triaxialities in tensile loadings, was not observed at high strains in the A2 alloy. Under shear loadings, where the stress triaxiality is even lower compared to tensile loadings, the void wraps around the hard inclusion as presented in Figure 4.29 for different extents of plastic deformation in the *PT* sample. Despite this apparent closure of voids, using densitometry, we measure a small increase in the void volume fraction in the A2 alloy.

### Void volume fraction results under torsional loadings

Experimentally observed *VVF* changes based on micro-structural measurements in the samples with shear dominated loadings, indicate a relatively high *VVF* growth upon deformation before the onset of coalescence. The

---

<sup>1</sup>Single cell simulations of the *PT* loading using kinematic boundary conditions were also unable to reproduce the large elongation of  $m_2$ . Further details about these simulations are provided in Appendix D

$VVF$  at fracture was higher in samples with smaller stress triaxialities as presented in Figure 4.68. This is an unexpected and remarkable result, as it is widely accepted that ductile fracture in metals is strongly dependent on the state of triaxial stress (McClintock, 1968; Rice and Tracey, 1969) and it is therefore the higher triaxiality which should cause faster and more void growth. For zero and low stress triaxialities, existing fracture models predict void collapse unless a hard inclusion wedges open the void (Pardoen et al, 1998; Siruguet and Leblond, 2004a,b). This behavior was also observed by e.g. Barsoum and Faleskog (2007b) or Tvergaard (2008) in plane strain single cell simulations. Tvergaard (2008) shows that when the stress triaxiality was too low, instead of void volume growth to coalescence, there was void closure leading to micro-cracks that rotate in the shear field. At some stage of the deformation, the void surfaces would come into contact so that sliding with or without friction would start to occur.

The result of void growth under pure torsion loading conditions is confirmed by performing a similar analysis on the interrupted pure torsion tests (Figure 4.70) and by densitometry measurements and calculations of the  $VVF$  (Figure 4.71), although values obtained differ significantly. It was impossible to confirm the void growth observations in  $PT$  samples with CT scanning due to an insufficient resolution. On the other hand the observed void growth described in Section 4.4 concerns small voids, which are not measurable with the CT. We will come back to this issue later in Section 5.4.

In the experimental approach used,  $VVF$  values are calculated from experimental observations of the void axis elongations and are a direct result of void axes length changes (see Equations 3.15 and 3.24). As a consequence, the observed void growth is driven mainly by the elongation of the  $M$  and  $m_2$ , while  $m_1$  which shrinks under shear dominated loadings, diminishes the calculated  $VVF$ . In the single cell simulations of the  $PT$  loading, we were not able to predict  $m_2$  elongation, and thus we do not observe  $VVF$  growth. On the other hand, in the UMAT calculations we perceive that the rate of shrinkage of the  $m_1$  is much smaller compared to the  $J_2$  simulations and it stays positive at the end of the simulation, that is, at strains corresponding to the onset of fracture in the  $A1$  alloy. In this context the UMAT performs better compared to the  $J_2$  and has the potential of predicting  $VVF$  growth if it can simulate  $m_2$  elongation. In the  $J_2$  single cell simulations  $m_1$  shrinks down to zero and the void fully collapses before the ultimate strain is reached, a behavior seen also by Tvergaard (2008) or Barsoum and Faleskog (2007b).

The relationship of the stress triaxiality and the  $VVF$  at the onset of coalescence is very different in the measurements by micrographic observations and in the single cell simulations. In the experiments, the lower stress triaxiality results in higher  $VVF$ , while in the single cell simulations this trend is the opposite. We think that this difference indicates stronger correlation of the void growth with the plastic strain than with the stress triaxiality, at

least in the investigated range of low stress triaxialities. In Section 5.3.3 we mentioned that the  $m_2$  elongation might be related to the twinning. Similar observations can be made for the void growth results obtained from microscopic observations and densitometry measurements. These results are shown in Figures 4.70 and 4.71, respectively. In both figures we notice that the void growth is nonlinear and starts accelerating after a certain deformation which can be related to the onset of twinning by comparing it to Figure 4.7 showing the strain hardening rate as a function of strain (rate of torque increase - sample rotation angle). Void growth starts to accelerate at deformations in which there is a plateau in the strain hardening rate plot, which Asgari et al (1997) showed to be related to the onset of twinning in brass as discussed in Section 5.2.2. We therefore suggest through this two step argument that  $m_2$  and  $VVF$  increases in the  $PT$  and  $TTx$  tests could be associated to twinning. A detailed mechanism by which twinning induces these increases still eludes us.

Void growth is generally accepted to be amplified by stress triaxiality in tensile loadings. In our material, under low stress triaxialities, it is driven by strain affected by micro-structural changes in the matrix material. In tensile and notched tensile samples the voids grow faster for the same strain but the conditions of instability happen faster because of the tensile loading, while under torsion, voids grow slower but over a much larger deformation range. In this way, larger plastic deformations of the matrix material might cause higher stable  $VVF$  growth in shear than in tension. However the details of the mechanisms by which twinning might influence void growth is not known.

### 5.3.4 Void coalescence

Void coalescence is the final stage in the failure of ductile materials. It consists of the localization of plastic deformation in the inter-void ligament between neighboring voids, which drives the final separation of the material. Void coalescence has received much less attention than void growth although this situation has been changing recently.

In this section we comment on our experimental and numerical observations of void coalescence in order to elucidate the coalescence mechanism and the amount of plastic deformation involved in real materials. We concentrate on tensile loadings with high triaxiality, but we also analyze samples tested under torsional loading conditions.

#### Void coalescence under tensile loadings

We found coalescence to be a very localized process in the A1 alloy as the experimentally measured  $VVF$  growth just below the fracture plane at the onset of coalescence is relatively small. Values presented in Table 4.1 indicate



$VVF$  growth of up to  $\times 1.63$  with respect to the  $VVF_0$  in the *NT3* sample.  $VVF$  is known to grow extensively starting with the onset of coalescence until fracture. There was no such growth observed anywhere in the sample cross section, indicating that the accelerated growth of voids is localized at the fracture surface.

The onset of coalescence is easily detectable in experiments as it coincides with formation of a macroscopic crack in the middle of the notch (Section 4.3.3) which causes the slope of the load-displacement plot to change dramatically. Similar behavior of tensile samples was documented e.g. by Tvergaard and Needleman (1984).

In the single cell simulations we do not use a criterion for the onset of coalescence. The calculated values of the  $VVF$  are for  $E_{eq}$  corresponding to  $\varepsilon_{eq}^{pl}$  in tested macroscopic samples at the sudden drop of load carrying capacity. Strains in the samples  $\varepsilon_{eq}^{pl}$  were obtained in  $J_2$  simulations.  $VVF$  values obtained in single cell simulations and presented in Table 4.3 on page 163, provide results with the same order of magnitude as experiments.

The usual trend of reduction of the strain at the onset of coalescence with decreasing notch radius leading to increased stress triaxiality, can be clearly seen in Table 4.2 or in Figure 4.2. At the onset of coalescence the experimentally measured  $VVF$  vary between samples with different notch radii. This confirms observations made by some authors (Koplik and Needleman, 1988; Thomason, 1985a) that a constant critical  $VVF$  is not an appropriate coalescence criterion because the level of triaxiality significantly influences the porosity at the onset of coalescence.

The highly localized coalescence process becomes clearer if we compare the extent of deformation in the stable void growth and coalescence stages of fracture in the *NT3* sample. As a measure of the deformation we use the minor void axis elongation factor  $f_m$  for void growth and its equivalent,  $f_m^c$  for the fully coalesced voids. The elongation factor  $f_m$  describes by how much  $m$  has elongated at the onset of coalescence with respect to the original length, while  $f_m^c$  measures how much  $m$  has elongated at separation of the material (necking down to an knife-edge of the surrounding inter-void ligaments) using the  $m$  length at the onset of coalescence as a reference. Details of the definitions, measurements and possible interpretations of  $f_m^c$  are provided in Section 4.4.5. The amount of deformation at full coalescence is at least an order of magnitude higher, because  $m$  grows only by 15% at the onset of coalescence ( $f_m = 1.15$ ), and then grows additionally by 165% until the end of the fracture process.

As far as numerical methods are concerned, Schacht et al (2003); Yerra et al (2010); Liu et al (2007) investigated void growth and coalescence in single crystals by performing 3D single cell simulations. They found that the

crystallographic orientation plays a significant role in void growth and also in void coalescence. According to Yerra et al (2010) the crystal orientation dependent void growth rate can lead to significant differences in ductility defined at the onset of void coalescence. Liu et al (2007) found that "hard orientation is hard to coalesce". In their single cell containing two voids for certain orientations coalescence occurs more easily.

Our numerical results correspond well with those presented in the literature, even if, for reasons listed in Section 5.3.3 we analyzed the coalescence in the polycrystalline matrix and not in a single crystal. In our simulations we observe that the developing preferential textures due to crystal plasticity, facilitate coalescence of voids by allowing their faster growth in the direction transverses to the direction of the main loading. As a result, the minor axes  $m_1$  and  $m_2$  grow much faster in the UMAT simulations compared to the  $J_2$  simulations. The onset of coalescence occurs faster and the resulting ductility (meaning the strain to the onset of coalescence) drops in the UMAT simulations. Thus it is the same mechanism driving the accelerated void growth that causes earlier onset of coalescence. These effects are seen in Figure 4.76 which presents the response of the single cells for tensile dominated loadings in terms of the mesoscopic equivalent stress and strain, and in Figures 4.77, 4.78, 4.79 and 4.80 presenting the elongation of void axes as a function of  $E_{eq}$ .

The onset of coalescence in single cell simulations, even if they are not precisely detected, happens much later in the deformation history compared to the experimental situation. This may be caused either by imprecise strain predictions (use of the  $J_2$  material model - Section 4.5.1), or by the UMAT material model behavior not fully corresponding to the behavior of the real microstructure (twinning is not implemented in the used material model leading to poor predictions of the shape of the  $PT$  sample for example Section 5.2.2). The differences in strain at the onset of coalescence may eventually be due to inappropriate boundary conditions imposing constant stress triaxiality on the single cell, while in the macroscopic sample, it varies significantly and particularly at high strains as presented in Figure 4.75. The predictions of the onset of coalescence in the single cell simulations could be improved by imitating the grain boundary fracture by varying the aspect ratio of the single cell and therefore the intervoid distance (maintaining the same initial shape of the void), to match the experimental onset of coalescence as it was done by example by Pardoen et al (2003b).

We can draw conclusions about the influence of the relative positions of lead inclusions, from the minor axis elongation factor distribution shown in Figure 4.74. It can be observed that, in general, larger inclusions grow less relative to their initial size, compared to small inclusions and that there is a bigger scatter of the  $m$  elongation for small inclusions. Most probably small inclusions can grow the  $m$  more, as the relative (to their size) distance to the closest neighbor is larger for small inclusions than for larger inclusions. The

bigger scatter can be explained by the small inclusions, which either are close to a big inclusion or close to each other, forming a cluster that does not allow an extensive growth before meeting a neighbor. Benson (1995) argues that such small voids clusters can be considered as one large void for certain types of analyzes.

To summarize, void growth during coalescence is strongly influenced by void spatial distribution. Voids grow more if they are distributed equidistantly, and less if they are clustered. Our observations are in general agreement with other results presented in the literature by e.g. Benson (1995) or Foster et al (2007). Foster et al (2007) report that damage growth is directly related to inclusion size and that the ratio of inclusion size to spacing might be an important parameter to govern the damage growth and failure of the material. The influence of the inclusion distribution is even more clear if we compare the discussed *A1* results with *m* elongation in *A2* as seen in Section 4.4.5. In the *A2* alloy the inter-void distances are much higher, and as a result, in the *A2* alloy,  $f_m^c$  is 12.64 on average, while in the *A1* alloy it is only 2.65. Analyzing these results we need to take into account the somewhat different definitions of  $f_m^c$  in the *A1* and *A2* alloys, and the different inclusion volume fractions.

The effect of void distribution on the character of the coalescence process is also visible in Figures 4.1, 4.2 and 4.3 presenting the load-displacement results of the tensile and notched tensile tests. The slope of the curve after the onset of coalescence is much steeper in the *A1* alloy where the inter-void distances are smaller and thus the coalescence has a more abrupt character. In the *A2* alloy the slope is less steep as the bigger inter-void distances cause a more gradual character of void growth and coalescence.

The *A2* material was not investigated in single cell simulations, although its behavior should not differ significantly from that of *A1*. Under high stress triaxiality loading conditions the hard inclusions would not affect the growth of the associated void. However, some differences may result from possible scaling effects as the volume fraction of hard inclusions is much lower compared to the lead volume in the *A1* alloy (Shu, 1998; Horstemeyer and Ramaswamy, 2000; Tvergaard and Niordson, 2004). This will be discussed in Section 5.4.

### **Void coalescence under torsional loadings**

For several reasons it is more difficult to identify the coalescence mechanism under torsional loadings compared to tensile loadings; fracture surfaces are highly distorted, etching does not reveal grain boundaries in sample cross sections, behavior of single cell models does not fully correspond to experimentally observed behavior of the materials, and there are not many experimental results presented in the literature that could be compared with our data.

The coalescence in shear-dominated loadings, as in tensile samples, is also a very localized process. In Figures 4.39 and 4.40 showing cross sections of fractured samples in the *A1* and *A2* alloys respectively, we observe that the region affected by coalescence is limited to the very close neighborhood of the fracture surface.

From the macroscopic cracks visible on the surface of the torsion samples, we conclude that in torsion tests, the fracture usually initiates at the outer surface of the gauge cylinder, as discussed in more detail in Section 5.3.1. Then the crack propagates simultaneously in the radial direction towards the center of the sample and in the tangential direction along the perimeter, resulting in a different fracture mechanism compared to that in tensile samples.

Different fracture mechanisms in the *A1* and *A2* alloys under various shear dominated loadings are discussed in Section 5.3.1 and result in different shapes of the torque-rotation angle plots. Figures 4.4 and 4.5 present these plots for the *A1* and *A2* alloys, respectively. The axial load causes the *TT2* response to have a pronounced stable softening (clearly visible in the *A2* alloy), which is not present in the *PT* plot. However in the *TT2* sample, no distinct point can be identified which would indicate the onset of coalescence. Softening in those samples is a combination of geometric (through-the-thickness necking) and void softening. The usual trend of reducing the strain to fracture with increasing stress triaxiality can be clearly seen in the mentioned figures and in Table 4.2.

The directions of crack propagation discussed in Section 5.3.1 seem to support the observed void growth in the radial direction. It is possible that the  $m_2$  elongation plays a major role during the coalescence stage of fracture, by significantly reducing the thickness of the inter-void ligaments measured in the radial direction. Pardoen and Hutchinson (2000) identified the "inter-void ligament distance" in order to determine the coalescence, but in the literature (Tvergaard, 2008) it is usually the ligament in the tangent, therefore in the  $m_1$  direction which is considered responsible for coalescence under shear loadings. It may be the case that at large strains due to micro-structural changes, void coalesce in the radial direction and therefore the  $m_2$  direction. The discussed thinning of the ligament in the radial direction can either trigger the coalescence or significantly influence the crack propagation by accelerating it.

Single cell simulations of torsion do not predict the elongation of voids in the radial direction and, as a consequence, we do not predict the coalescence using either of the two material models within the reached ranges of strain. The reason is that the UMAT material model behavior does not fully correspond to reality as twinning is not implemented in this version of the code. Observed changes in the response of the single cell presented in Figure 4.82 originate therefore in the different constitutive behavior of the UMAT under different loadings and not in different coalescence mechanisms. Other possi-

ble over-simplifications of the single cell (such as not accurate enough strain predictions or too simple boundary conditions which impose a plane strain or generalized plane strain deformation on the single cell) would only have a secondary influence on the results of simulations. The key information is that with the version of the crystal plasticity model used, we are not able to simulate void growth in the radial direction.

In the *A1* alloy we assume a single population of voids nucleating at lead inclusions, because as with all the loading cases, there was lead observed in almost every dimple. In the *A2* alloy we observe some dimples that did not contain any inclusion. It is possible that in the case of the large empty voids the missing inclusion remained attached to the other matching fracture surface. On the other hand, clusters of small empty dimples were observed. This observation may indicate that at some locations, *A2* may nucleate a second population of voids at other microstructural defects (intersections of dislocations or at grain boundaries and triple points). These second void populations could additionally accelerate the coalescence process as shown by Fabrègue and Pardoën (2008) or Faleskog and Shih (1997) for example. In their study Fabrègue and Pardoën (2008) present experimental and numerical evidence that a second population of cavities nucleated on small particles can significantly affect the damage process controlled by the first population of cavities nucleated on larger particles.

The void-particle interactions have been shown to have a significant influence on coalescence, particularly at low triaxialities (Kuna and Sun, 1996; Hutchinson and Tvergaard, 1987; Staub and Boyer, 1998; Fleck et al, 1989; Siruguet and Leblond, 2004a,b). Even if current studies concern tensile loadings, it has been shown that hard particles influence the shape of the void if the stress triaxiality is low enough. In their model of void growth and coalescence, Siruguet and Leblond (2004a,b), (or previously Pardoën et al (1998)), work on the hypothesis that the void always remains spheroidal, which becomes erroneous for large deformations. In their single cell computations the void ultimately takes the shape of a "double pear" (spheroid with inflated equator region), and at large strains the values of void growth predicted by their model are notably overestimated. Such effects can be observed under zero nominal stress triaxiality in Figure 4.29 which shows the evolution of shape and orientation of a void-hard inclusion system in the *A2* alloy under *PT* loading.

## 5.4 Size effects

It is possible in the *A1* model material that we are observing two size effects. The first concerns the initial shape of the inclusion, while the second concerns the size dependent void growth.

### 5.4.1 Initial shape

The initial shape of inclusions, defined in terms of the void aspect ratio, is apparent in Figure 4.59, presenting the void aspect ratio of the inclusions as a function of their initial major axis length. Small inclusions are more spherical while large inclusions are more prolate. This trend is also observable in the representative data range (Section 3.3.3).

This can be relatively easily explained for very large inclusions by the effect of their position. In Figure 3.1(a) and 3.4(a) etched samples of the *A1* alloy in SE and BSE view are shown respectively. Notice that big inclusions exhibit the tendency to appear at the grain boundaries. In the scope of their study on temperature embrittlement of lead-containing copper alloys Felberbaum (2005) and Empl (2009) observed similar position dependent shape of lead inclusions, which being trapped between two grain walls are squeezed and thus more elongated.

In the case of smaller inclusions, which usually appear in grains, a different effect must be responsible for the size dependent shape. It could be the interfacial energy balance between the lead inclusions and the matrix for example, which depends on the manufacturing process Kamio et al (1991). An explanation of the observed size dependence of inclusion morphology would require further investigation.

### 5.4.2 Void evolution

A second possible observed size effect concerns size dependent void growth. In our void size analysis which was performed on inclusions in the representative data range, we assume the same homothetic deformation of all voids within the representative range - we calculate average elongations of void axes in this range and use it to calculate the changes in axis length and the  $VVF$  of an equivalent ellipsoid (Section 3.3.4).

However, we sometimes observe different elongations depending on the initial size. For example the  $M$  of large inclusions elongates more under tensile loadings, especially the  $ST$  case (Figure 4.60(b)) and under torsional loadings (Figure 4.62(b)), or  $m_1$  shortens more in large inclusions under torsional loadings (Figure 4.63(b)). Under  $PT$  loading, the same trends ( $M$  elongates more, and  $m_1$  shortens more for big inclusions) can be observed in samples interrupted at different degrees of deformation (see Figure 4.64(b) and Figure 4.65(b) for  $M$  and  $m_1$ , respectively).

There is no common agreement on the influence of plastic anisotropy and crystal plasticity on size dependent void growth within the community. Several authors investigated size dependent void growth, but arrived at different conclusions. Shu (1998) observed a size scale effect in plane strain single cell

simulations with a cylindrical void under uniaxial and biaxial loadings. Simulations performed led him to the conclusion that small voids have the tendency to grow slower than larger voids, also noted by Horstemeyer and Ramaswamy (2000). A similar result was obtained by Tvergaard and Niordson (2004), who applied a non-local elastic-plastic model to study the growth of voids comparable with a characteristic material length. Tvergaard and Niordson (2004) showed that the high growth rate of very small voids predicted by the conventional plasticity theory is not realistic when the effect of a characteristic length, dependent on the dislocation structure, is accounted for. On the other hand, Yu et al (2010) stated that the smaller the volume fraction is, the higher the growth rate is. Ha and Kim (2010) observed that for a small initial void volume fraction, the growth rate of a small void is rapid compared to a large one and the effect of the initial crystallographic orientation is significant. Another point of view was presented by Wen et al (2005), who extended the Gurson model to account for the void size effects. They found that for small strains and small void volume fractions, void size has practically no influence on the stress-strain curve of the porous material. The void size becomes significant only at large void volume fractions.

The above mentioned authors analyzed only initially spherical voids in uniaxial or biaxial loading and neither the effect of their shape nor the shear loading was analyzed. It is known that the growth of voids is strongly dependent on their initial shape (Budiansky et al, 1982; Becker et al, 1989a; Sovik and Thaulow, 1997; Pardoen and Hutchinson, 2000; Benzerga, 2000; Lassance et al, 2007; Scheyvaerts, 2008), yet this was not fully investigated under shear loading.

In conclusion, we observe evidence of size effects on void shape and void growth rate, but we are not able to state with enough evidence whether or not there is size dependent void growth or that the observed effects are the result of the difference in the initial inclusion shape, because the two effects are strongly coupled and the literature provides contradicting data. Drawing definitive conclusions on the possible size dependent void growth require additional parametrical study using single cell with various void shapes,  $VVF$  and crystal plasticity material model extended to account for the void size.





## Chapter 6

# Conclusions and perspectives

### 6.1 Summary of results

This work contributes to a better understanding of fracture processes by void nucleation growth and coalescence particularly under shear dominated loading conditions. The micro-damage processes controlling ductile fracture in two model materials are studied for various stress triaxiality loading conditions, including zero stress triaxiality. We focused our research on the void growth and coalescence stages of ductile fracture and we investigated them using a 9% Zn lead-containing brass as our principal model material, while the other model material, the lead-free counterpart of the first model alloy, was used to determine properties of the matrix material. The lead-containing alloy is characterized by the absence of the nucleation stage of fracture as lead inclusions act as pre-existing voids. Our research elucidates the mechanisms and kinetics of void growth and coalescence in a ductile matrix subjected to arbitrary loading and deformation by providing void shape, size and orientation distributions at the onset of coalescence. The results obtained can contribute to the improvement of existing fracture models by making available reliable experimental data for void growth and coalescence that can be used to evaluate the existing VNGC models. Our findings are pertinent, notably for low absolute values of stress triaxiality, where little information is available in the literature, although shear dominated fracture is frequently encountered in practice and is of increasing technological importance.

The significant contributions of this dissertation are briefly summarized below:

- Validated approach and use of the model materials for the fundamental study of micro-damage processes controlling ductile fracture.
- Quantified experimentally the evolution of void shape, void volume fraction and void orientation as a function of loading mode (stress triaxiality).

- Demonstrated in the model materials: the initial anisotropy, the development of texture in the microstructure and an important influence of twinning on their mechanical behavior.
- Demonstrated other microstructural effects on void growth such as the concentration of large lead inclusions at grain boundaries; this effect was, at least partially, reduced in our analysis by an appropriate treatment of the experimental data.
- Provided evidence of void growth under loading conditions of zero nominal stress triaxiality.
- Provided evidence that for large plastic strains under shear loading the influence of hard inclusions is negligible and essentially eliminated by plasticity, which closes the void around the inclusion. This observation contradicts some results of numerical simulations at lower strains.
- Quantified void growth during the coalescence stage of fracture which was found to be much higher than during the stable void growth stage.
- Documented the decrease in ductility with increasing initial void volume fraction, by comparing results of fracture tests of the lead-containing and lead-free alloy. These data can be used to validate predictions of existing models of ductile fracture.
- Illustrated, by comparing the experimental results of mechanical tests and the numerical simulations, the importance of the choice of material models on the simulated void growth mechanisms. The presented numerical simulations were not able to reproduce some of the microscopic and macroscopic experimental observations.
- Presented experimental results suggesting possible size dependent initial void shape and size dependent void growth. They indicate that sub-micron voids grow slower than larger voids.

## 6.2 Conclusions

Based on the contributions of this project listed above, we draw conclusions on the possible future developments of the models of ductile fracture:

- When developing void growth and coalescence models it is crucial to account for an appropriate description of the matrix constitutive behavior. The influence of material microstructure may dominate possible void growth effects, particularly under low stress triaxiality.

Even though, in most cases materials can be regarded as initially isotropic, when they are subjected to finite deformations, their microstructure evolves, leading to an overall anisotropic response. In our material, we observe initial and induced texturing of the matrix both of which have a large impact

on the test results compared to predictions of simulations using an isotropic constitutive law. The effect of texture induced anisotropy on the decrease of material load carrying capacity would be much higher than possible effects of material softening due to void volume changes, as in existing fracture models voids under low stress triaxiality either do not grow or collapse. To be able to simulate fracture processes correctly, it is crucial to use an appropriate constitutive model of the matrix which will account for the evolving micro-structure, including twinning.

This will have an impact on the predictions of the sample deformations at fracture and contribute to better stress-strain predictions.

- The shape of voids cannot be assumed to be axisymmetric under shear dominated loadings. The accelerated elongation of voids observed in one of the directions perpendicular to the direction of applied shear can be considered to be an effect of the developing texture, which, together with the observed void growth, can be related to twinning.

Commonly in the literature, voids are assumed to stay axisymmetric during the whole deformation process, even under shear loading conditions. In our experiments we observe significant elongation of the voids in the radial direction of the pure torsion sample, i.e. in the direction with no nominal load. This elongation of the void in the radial direction and the resulting observed void volume growth of small inclusions can be associated with developing texture anisotropy and in particular with the onset of twinning. Decreasing the size of the inter-void ligaments in the radial direction will also significantly affect the coalescence process and will affect the simulated shape of the unloading part of the load-deformation curve after the onset of coalescence. Twinning is not implemented in the polycrystalline plasticity model used to describe the behavior of the matrix material, yet we presented evidence that it plays an important role in the deformation processes and strongly interacts with slip process. Thus it was impossible to simulate accurately void growth under shear loading conditions. In order to provide more reliable tools for fracture predictions, the appropriate shape of the void inclusions should be accounted for.

- Size dependent shape and deformation of voids, as well as other scale effects should be accounted for in micro-mechanical models of nucleation, growth and coalescence.

In existing micro-mechanical models of void nucleation, growth and coalescence, damage is usually described by the evolution of a single representative void. This approach, although valid for certain applications, ignores possible size effects even if there is experimental evidence of such behavior in real materials. To be able to cope with heterogeneous microstructures fracture models

should take into account and be able to model various scale effects, such as the size dependent shape of voids, their size dependent growth (e.g. due to crystal plasticity) and possibly other scale effects such as the well known size dependent fracture loads and deformations in structures. The latter is particularly important as one of the ultimate goals of fracture mechanic theories is to be able to predict the fracture behavior of large structures using results of laboratory experiments of scaled specimens.

### 6.3 Perspectives

In this thesis we provide a void evolution database at the onset of coalescence under different loading conditions. We hope that this will have a useful impact on the development of fracture models. This project has opened up several possible new areas of investigation to extend our knowledge. It would be of high interest to:

- Investigate in detail the mechanism of void elongation in the radial direction as well as void growth under pure torsional loading. We correlated these to twinning, but the mechanism of void elongation in a direction with no nominal load must still be elucidated.
- Perform simulations of macroscopic samples using the polycrystalline plasticity material model with twinning to a) predict specimen dimensional changes, and b) correlate measured void elongation and growth to more accurate predictions of stress-strain at the onset of fracture.
- Redo single cell simulations using a polycrystalline plasticity material model with twinning to verify numerically if the twinning mechanism can improve predictions of void shape, and particularly if it can predict void elongation in the radial direction for pure shear loading.
- More precisely correlate void growth with twinning by obtaining the void volume fraction measurements for more interrupted tests with smaller intervals and comparing it with strain hardening-strain plots generated from a continuous (without regripping) pure torsion test.
- Confirm the correlation of void growth with twinning by experimentally measuring twin density in interrupted pure torsion samples.
- Analyze void growth under pure torsion loading conditions in a lead-containing copper (thus an alloy texturing differently than brass) to investigate the effect of texture on void growth.
- Crosscheck void growth measurements and contribute to the analysis of the size effect by tracking the second minor axis elongation and size dependent void growth using an alternative method to obtain void size

distributions i.e. Focused Ion Beam (FIB), offering higher resolution 3D imaging.

- Pursue the theoretical and numerical research on size dependent and initial shape dependent void growth.
- Characterize the influence of the texture induced axial deformation of the pure torsion specimen on void growth.
- Validate experimentally void rotation rates as a function of shape.
- Measure evolution of intervoid distances under different loading conditions.
- Investigate numerically void growth at grain boundaries.



# Appendix A

## Abandoned materials

Several materials were considered and examined during the selection of an appropriate model material, including cast iron, stainless steels and different copper alloys. Below we provide a brief description of these alloys and the reasons for which they were abandoned.

### A.1 GGG40

The GGG40 cast iron contained a relatively homogeneous distribution of large spheroidal, weakly bonded graphite inclusions. The relatively low ductility facilitates numerical calculations. The major concern with cast iron is the second population of small voids/inclusions detected in the alloy. There is a serious risk that the small voids would trigger a second population of voids when loading the material which would affect the void growth and coalescence. As we would like the model material to fail due to the necking of ligaments between growing voids, without nucleation of a second population of voids, the idea of using *GGG40* as a model material was abandoned.

### A.2 AISI 303, 303 SE and 304

Significant ductility and a microstructure containing weakly bonded inclusions, were the two main reasons for pre-selecting the AISI 303, the AISI 303 SE and the AISI 304 stainless steels for investigation. At the final stage of fracture, the selected alloys exhibit different extents of necking and cup-cone structure, but at the nucleation and early growth stage of fracture, they behave in very similar way. For this reason, all the steels will be described using as example AISI 303. This alloy contains MnS inclusions, pre-elongated in the rolling direction. The advantage of these particular inclusions is a low nucleation stress and strain. Inclusions break easily, forming voids between the broken parts of the inclusions at the beginning of plastic deformation. Two main disadvantages of the discussed microstructure were found. The first one

concerns the large scatter of the inclusion size and their very elongated shape, making it difficult to select an appropriate magnification for the micrographs for void size analysis. If the magnification is relatively high, a significant number of inclusions do not fit into the field of view, and if the magnification is relatively low, the small inclusions become too small to be observed and analyzed. The second serious disadvantage of the microstructure is the way broken parts of the inclusions behave. Due to large ductility, they move long distances and the spacing between parts of an inclusion grows. At a certain level of displacement it becomes impossible to identify which part belongs to which inclusion and to measure the growth of specified voids using an automated image recognition software.

### A.3 Copper alloys

Several copper alloys were examined. Their chemical composition is presented in Table A.1. 62A, E63, C97 and B98 are Swissmetal code names, and correspond to C34500, C26800, C19160 and C19000 ASTM standards respectively.  $\alpha$ - $\beta$  is CuZn39Pb3 (AISI C38500). Alloys are described in the following sections.

Table A.1: Chemical composition of abandoned materials in % by weight.

Code	Cu	Ni	Zn	Sn	Pb	Other elements
$\alpha$ - $\beta$	57.0-59.0	—	Rem.	—	2.5-3.5	Fe $\leq$ 0.35
62A	62.0-63.0	$\leq$ 0.25	Rem.	$\leq$ 0.1	1.6-2.5	Fe $\leq$ 0.1
E63	62.0-64.0	—	Rem.	—	$\leq$ 0.07	Fe $\leq$ 0.07
C97	Rem.	0.8-1.2	$\leq$ 0.25	$\leq$ 0.05	0.8-1.2	Fe $\leq$ 0.05 P 0.15-0.30
B98	Rem.	0.9-1.2	—	—	$\leq$ 0.02	Cr 0.6-1.2 P 0.15-0.25 Zr 0.05-0.20

#### A.3.1 $\alpha$ - $\beta$ - CuZn39Pb3

If the Zn content of a Cu-Zn alloy exceeds 35% it becomes a two phase  $\alpha$ - $\beta$  alloy. Figure A.1 presents the dual phase microstructure of CuZn39Pb3. This  $\alpha$ - $\beta'$  double phase microstructure might influence void growth and coalescence. First, the two phases have different strengths and may render the analysis and modeling of void growth at the mesoscopic level difficult. Second, the  $\beta'$  phase exhibits a non-homogeneous deformation behavior which may significantly affect the coalescence process by causing local strain between soft and hard grains.



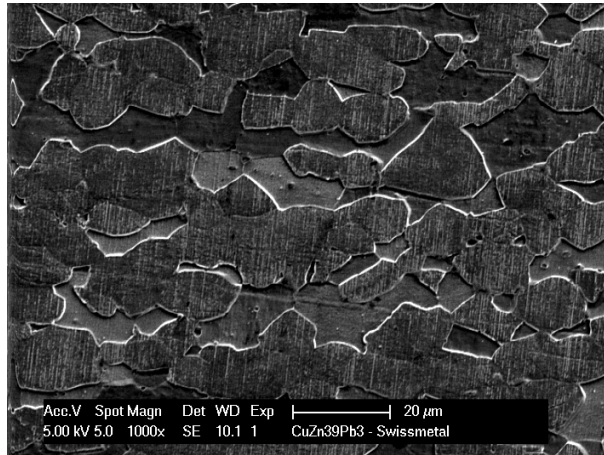


Figure A.1: *CuZn39Pb3*  $\alpha$ - $\beta$  double phase microstructure revealed by etching, SE view.

### A.3.2 62A and E63

62A is 36% Zn lead-containing brass and E63 is its lead-free counterpart. Analysis of round tensile bar experimental data revealed a serrated stress-strain curve for both of the alloys which indicates the Portevin-Le Châtelier (PLC) effect. These serrated stress-strain curves, presented in Figure A.2 have their origins at a micro-structural level (Robinson and Shaw, 1994). The appearance of a serrated stress-strain record may occur during tensile (Wijler et al, 1972), compressive (Mulford and Kocks, 1979; Huang and III, 1990), or torsional (Lopriore et al, 1982) plastic deformation. It is characteristic of deformation during a specific temperature range, strain ( $\varepsilon$ ), and strain rate ( $\dot{\varepsilon}$ ). We performed smooth round bar tests at different strain rates  $\dot{\varepsilon}=10^{-4}$ ,  $10^{-3}$  and  $10^{-2}$  in order to check the possibility of avoiding the PLC effect. We found that in this particular alloy, it is impossible to avoid serration in the tested range of strain rates. Miura and Hashimoto (1972) claim that the onset of serration depends on the solute concentration and does not depend on loading conditions. Thus we are not able to use 62A nor the E63 as our model material as serrated flow may affect the fracture mechanisms, (and this would be) unavoidable even changing loading conditions or specimen geometry. Miura and Hashimoto (1972) report also that PLC effect disappears in alloys when the Zn content is lower than 20%.

### A.3.3 C97 and B98

C97 and B98 are respectively lead-containing and lead-free Ni precipitation hardened copper alloys. In Figure A.2 we observe how addition of 0.6-1.2% of chromium to B98 influences its behavior. At the beginning of the loading curve, the lead-free alloy hardens more than the lead-containing one, but then softening, due to void interactions and coalescence, appears much earlier. As a consequence, the lead-free alloy fails at smaller strains than the

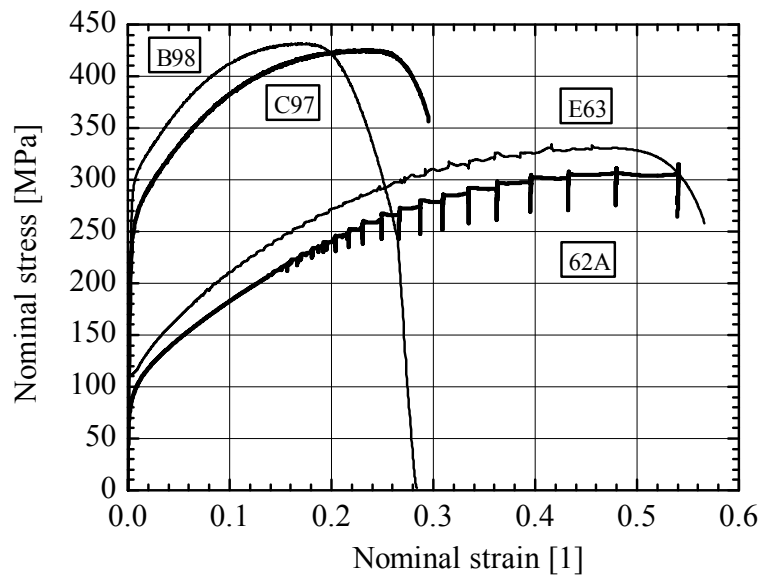
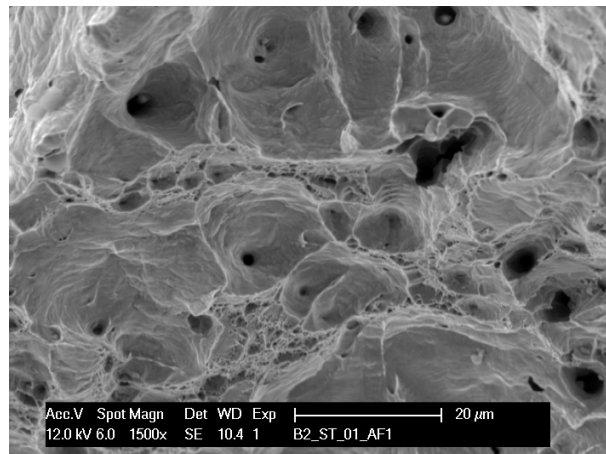


Figure A.2: 62A, E63, C97 and B98 tensile test results.

lead-containing counterpart. We believe this is caused by the second population of voids nucleating in ligaments of already grown voids as presented in Figure A.3.

The differences in chemical composition of C97 and B98 makes it impossible to conclude directly on the influence of preexisting voids because these materials exhibit different failure mechanisms. Therefore we abandoned this pair of alloys as our main model materials.



*Figure A.3: B98 fracture surface (SE).*



# Appendix B

## Sample design

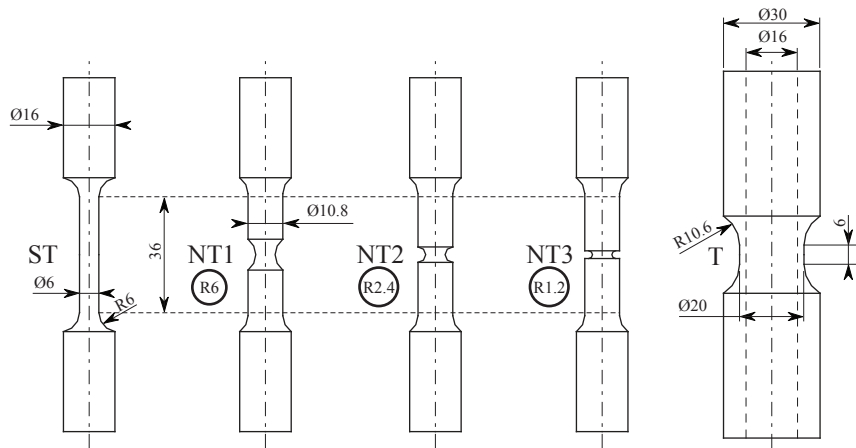


Figure B.1: Geometry of tested samples. Source Cannizzaro (2006)



## Appendix C

# Void size analysis

Figures C.1, C.2 and C.3 present distributions of orientation of inclusions in notched tensile and torsion samples, and compare them with average distribution for undeformed material (*UD – avg*). Angle 0 deg refers to the axis of the sample, positive values of orientation are in the direction of rotation of grips.

Figures bellow present in a different way the same information as Figures 4.41, 4.42 and 4.43. More explanations are provided in Section 4.4.1.

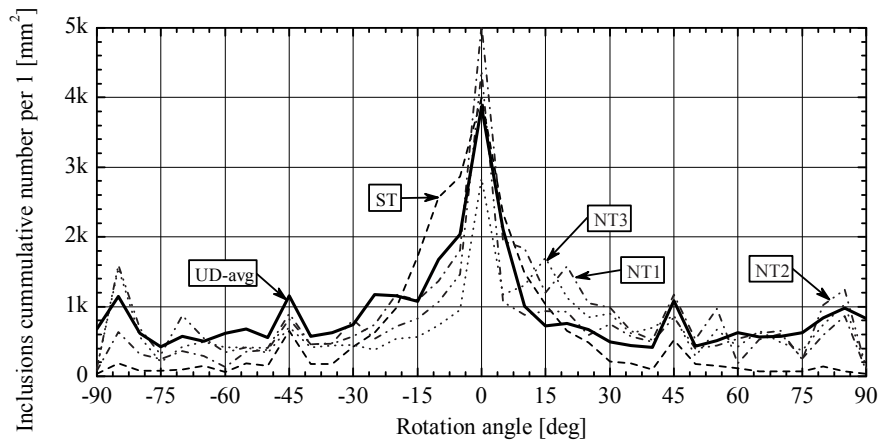


Figure C.1: Distribution of orientation of major axes in tensile and notch tensile samples.

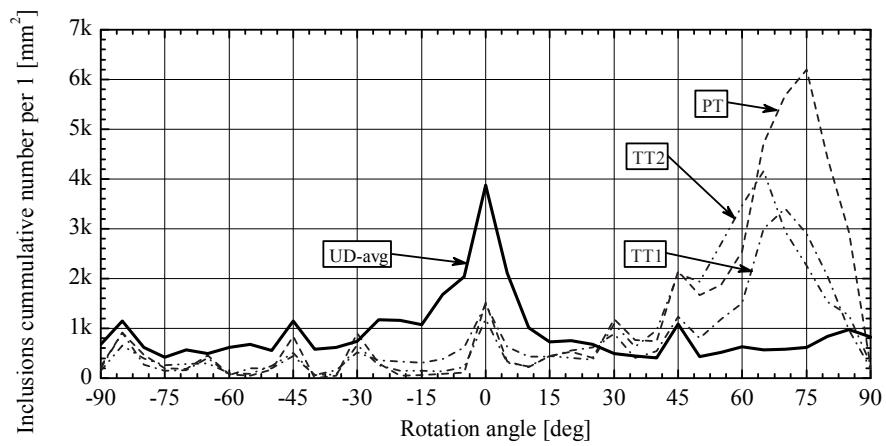


Figure C.2: Distribution of orientation of major axes in torsional and tensile torsional samples - AT plane.

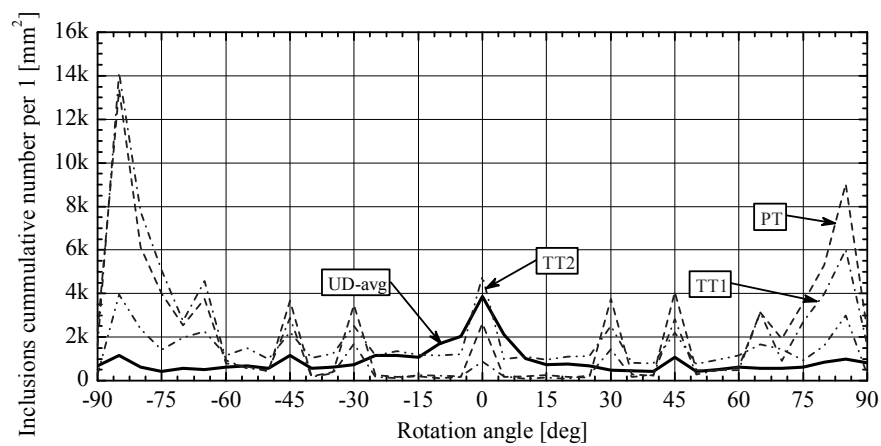


Figure C.3: Distribution of orientation of major axes in torsional and tensile torsional samples - AR plane.



## Appendix D

# Kinematic boundary conditions

In Section 4.5.3 we present results of the single cell simulations under shear dominated loadings. In these simulations we do not reproduce the elongation of the  $m_2$  axis at the extent observed in experiments nor do we observe the void growth under pure torsional loading. Since the simulations in question use simple boundary conditions, we performed another single cell simulation with the kinematic boundary conditions imposed.

The  $J_2$  simulation was performed using the 3D single cell for torsional loading as presented in Section 3.4.3. The kinematic boundary conditions resulting from the dimensional changes of the thin-walled tubular specimens as described in Section 4.2.3 (Figures 4.19, 4.20 and 4.21) were applied in directions 1 and 3. Resulting strain in the tangential direction (3) was  $-2.70\%$ , and the strain in the radial direction (1) was  $-1.84\%$  at the end of deformation corresponding to 135 deg of sample twist. Linearly increasing axial strain of up to 5.60% was imposed. This value corresponds roughly to the macroscopic axial strain resulting from the elongation of the  $PT$  sample. Results of this simulation presented in Figure D.1 can be compared with previous single cell simulations presented in Figure 4.83 or with the experimental results presented in Figure 4.70.

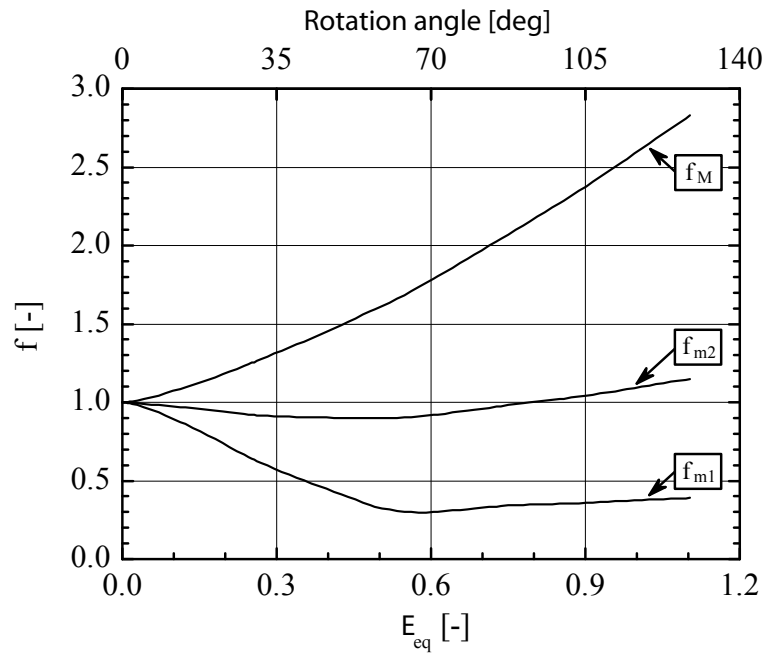
It can be observed in Figure D.1(a) that the kinematic boundary conditions affect mainly the evolution of  $f_{m1}$ . The value of  $f_{m1}$  stabilizes after deformation corresponding to approx. 60 deg of sample twist, and does not shrink down to zero. Contrary to the results presented in Figure 4.83(a),  $f_{m2}$  varies with deformation in Figure D.1(a). The change in  $f_{m2}$  however is much smaller than the experimental values presented in Figure 4.65. The imposed boundary conditions do not change the evolution of the  $f_M$  significantly.

The  $VVF$  evolution resulting from the described changes in void axis elongation factors is presented in Figure D.1(b). We observe that at the beginning

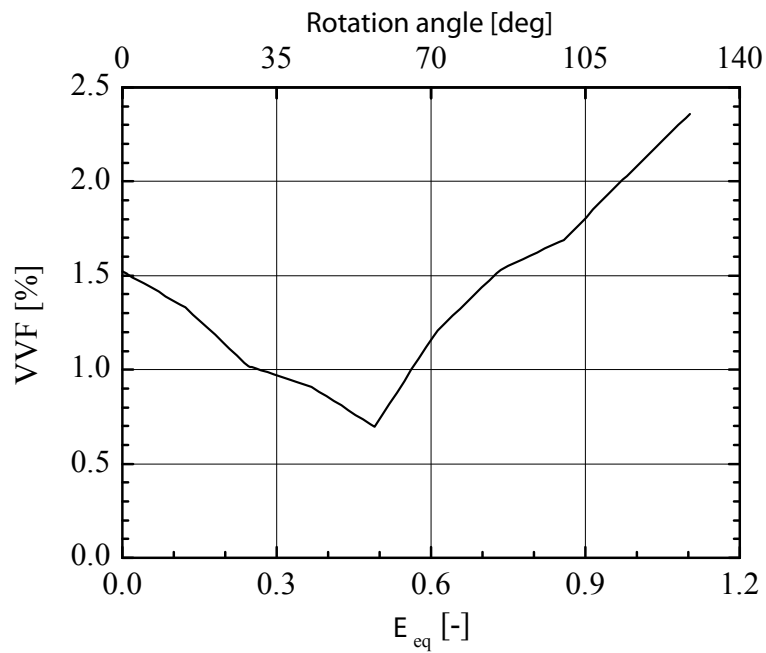
of deformation  $VVF$  decreases to start to grow after a deformation corresponding to the stabilization of the  $f_{m1}$ .

Such a change is not observed in the experiments. The difference might be due to the fact that in the single cell calculations we impose a constant axial strain rate, which might not be the case in the experiments. In this simulation we impose a linearly increasing strain in the axial direction. As the other two strains are of negative value they tend to decrease the  $VVF$ , and it is only the axial strain which acts to grow the void. We know from the experimental microscopic and densitometry measurements (Figure 4.70 and 4.71) that under pure torsional loading the  $VVF$  does not decrease and that the  $VVF$  growth rate increase with the deformation. Finally, to compensate for the  $VVF$  decrease in our simulations the axial strain rate must be higher at the beginning of the deformation.

The single cell simulations with kinematic boundary conditions however does not provide and an explanation for the experimentally observed  $m2$  elongation.



(a) Evolution of the void axis elongation factors  $f_M$ ,  $f_{m1}$  and  $f_{m2}$ .



(b) Evolution of the void volume fraction  $VVF$ .

Figure D.1: Single cell simulation results for the PT loading using kinematic boundary conditions.



# Nomenclature

90A	9% Zn lead-containing brass	$M^{AT}$	Major axis length of 2D ellipsoid inclusion observed in the <i>AT</i> plane
A1	9% Zn lead-containing brass	$M_0$	Major axis initial length of the 3D ellipsoid, $\mu m$
A2	9% Zn lead-free brass	$M_0^{AV}$	Additional void initial major axis length (Case B), = $0.175 \cdot 2$
AR	Axial-Radial plane	$M_0^{Pb}$	Lead inclusion initial major axis length (Case A and B), = $0.442 \cdot 2$
AT	Axial-Tangential plane	$M_0^{Void}$	Void initial major axis length (Case B), = $0.175 \cdot 2$
AVF	Additional volume (void) fraction	$M_A$	Mass of additional volume = 0, kg
AVF <sub>0</sub>	Initial additional volume (void) fraction	$M_L$	Mass of lead, kg
D	External diameter of the thin-walled tubular sample, mm	$M_M$	Mass of matrix, kg
DEF	Deformed (tested) material	$M_f$	Major axis final length of the 3D ellipsoid, $\mu m$
E	Young modulus	N	Inclusions cumulative number
E90	9% Zn lead-free brass	NT1	Notched round tensile test/sample 1
$E_1, E_{11}$	Mesoscopic strain in 1-direction	NT2	Notched round tensile test/sample 2
$E_2, E_{22}$	Mesoscopic strain in 2-direction	NT3	Notched round tensile test/sample 3
$E_3, E_{33}$	Mesoscopic strain in 3-direction	$N_{max}$	Higher border the representative data range
$E_{eq}$	Mesoscopic equivalent total strain	$N_{min}$	Lower border the representative data range
$F_1$	Force, applied force in 1-direction	$N_{tot}$	Inclusions total cumulative number
$F_2$	Force, applied force in 2-direction	PLC	Portevin-Le Châtelier effect
$F_3$	Force, applied force in 3-direction	PT	Pure torsion test
$J_2$	Von Misses plasticity theory	REF	Reference node
LVF	Lead volume fraction	ST	Smooth round tensile test/sample
LWF	Lead weight fraction	T	Stress triaxiality
M	Major axis length of the 3D ellipsoid, $\mu m$	T	Thin-walled tubular sample for torsion and tensile-torsion tests
M	Mass of sample, kg	TT1	Tensile torsion test 1
M	Master node	TT2	Tensile torsion test 2
MVF	Matrix volume fraction		
MWF	Matrix weight fraction		
$M^{AR}$	Major axis length of 2D ellipsoid inclusion observed in the <i>AR</i> plane		

$T_{avg}$	Average stress triaxiality	$\rho_t$	Density of theoretical fully dense A1 alloy, Mg/m <sup>3</sup>
$UD$	Undeformed (not tested) material	$\sigma_0$	Ludwik-type power law fit parameter
$UR_1$	Rotation about 1-direction	$\sigma_{eq}$	Equivalent stress, MPa
$UR_2$	Rotation about 2-direction	$\theta$	Sample twist angle in torsion and tensile-torsion experiments, deg
$UR_3$	Rotation about 3-direction	$\varepsilon_{eq}$	Equivalent strain
$U_1$	Displacement in 1-direction	$\varepsilon_{eq}^{pl}$	Equivalent plastic strain
$U_2$	Displacement in 2-direction	$d$	Internal diameter of the thin-walled tubular sample, mm
$U_3$	Displacement in 3-direction	$f_M$	Major axis elongation factor
$VVF$	Void volume fraction (includes volume of lead inclusions and additional internal void)	$f_V$	Void volume growth factor
$VVF_0$	Initial void volume fraction	$f_{m1}$	First minor axis elongation factor
$V_{A_0}$	Additional initial volume, m <sup>3</sup>	$f_{m2}$	Second minor axis elongation factor
$V_{A_f}$	Additional final volume, m <sup>3</sup>	$k$	Ludwik-type power law fit parameter
$V_A$	Additional volume, m <sup>3</sup>	$m$	First and second minor axis length of the 3D axisymmetric ellipsoid, $\mu m$
$V_{EVOL}$	Volume of elements in a single cell	$m^{AR}$	Minor axis length of 2D ellipsoid inclusion observed in the $AR$ plane
$V_L$	Volume of lead, m <sup>3</sup>	$m^{AT}$	Minor axis length of 2D ellipsoid inclusion observed in the $AT$ plane
$V_M$	Volume of matrix, m <sup>3</sup>	$m_0$	First and second minor axis initial length of the 3D axisymmetric ellipsoid, $\mu m$
$V_{SC}$	Volume of a single cell	$m_0^{AV}$	Additional void initial minor axis length (Case B), = 0.175 · 2
$V_{V_0}$	Initial volume of the representative ellipsoid void, m <sup>3</sup>	$m_{10}$	First minor axis initial length of the 3D ellipsoid $m_{10} = m_0, \mu m$
$V_{V_f}$	Volume of the representative ellipsoid void at fracture, m <sup>3</sup>	$m_{1f}$	First minor axis final length of the 3D ellipsoid, $\mu m$
$V_V$	Volume of the representative ellipsoid void, m <sup>3</sup>	$m_1$	First minor axis length of the 3D ellipsoid, $\mu m$
$W_0$	Initial void aspect ratio, $M/m_1 = M/m_2$	$m_{20}$	Second minor axis initial length of the 3D ellipsoid $m_{20} = m_0, \mu m$
$W_1$	First void aspect ratio, $M/m_1$	$m_{2f}$	Second minor axis final length of the 3D ellipsoid, $\mu m$
$W_2$	Second void aspect ratio, $M/m_2$	$m_2$	Second minor axis length of the 3D ellipsoid, $\mu m$
$\Sigma_1, \Sigma_{11}$	Mesoscopic strain in 1-direction, MPa	$n$	Ludwik-type power law fit parameter
$\Sigma_{23}$	Mesoscopic shear strain, MPa	$q_1$	GTN model parameter
$\Sigma_2, \Sigma_{22}$	Mesoscopic strain in 2-direction, MPa		
$\Sigma_3, \Sigma_{33}$	Mesoscopic strain in 3-direction, MPa		
$\Sigma_{eq}$	Mesoscopic equivalent stress, MPa		
$\nu$	Poisson ratio		
$\rho_L$	Density of technical lead, Mg/m <sup>3</sup>		
$\rho_M$	Density of A2 alloy and A1 alloy matrix, Mg/m <sup>3</sup>		
$\rho_r$	Density of A1 alloy, Mg/m <sup>3</sup>		

---

$q_2$	GTN model parameter
$q_3$	GTN model parameter
$t$	Thickness of the thin-walled tubular sample, mm
1	Radial direction
2	Axial direction
3	Hoop direction
A	Single cell loading case A - full lead inclusion
B	Single cell loading case B - lead inclusion with a void
BSE	Back scatter electron detector
C	Single cell loading case C - void
CT	Computed tomography
GTN	Gurson-Tvergaard-Needleman model
H	Hoop direction
LAF	Local approach to fracture
MUD	Multiple of uniform distribution
R	Radial direction
RT	Rice and Tracey model
SE	Secondary electron detector
SEM	Scanning electron microscopy
T	Tangent direction
UEL	User-defined element
UMAT	Crystal plasticity model
VC	Void coalescence
VG	Void growth
VN	Void nucleation
VNGC	Void nucleation, growth and coalescence
XRCT	X-ray computed tomography





# Bibliography

- Anderson T (1991) *Fracture Mechanics Fundamentals and Applications*. CRC Press
- Antoun T, Seaman L, Couran D, Kanel G, Razorenov S, Utkin A (2003) *Spall Fracture*. Springer, New York
- Aravas N, Ponte-Castaneda P (2004) Numerical Methods for Porous Metals with Deformation-Induced Anisotropy. *Computer Methods in Applied Mechanics and Engineering* (193):3767–3805
- Argon A, Im J, Safoglu R (1975) Cavity Formation from Inclusions in Ductile Fracture. *Metallurgical Transactions* (6A):825–837
- Asaro R, Needleman A (1985) Texture Development and Strain Hardening in Rate Dependent Polycrystals. *Acta Metallurgica* (33):923–953
- Asgari S, El-Danaf E, Kalidindi S, Doherty R (1997) Strain Hardening Regimes and Microstructural Evolution During Large Strain Compression of Low Stacking Fault Energy F.C.C. Alloys that Form Deformation Twins. *Metallurgical and materials transactions A, Physical metallurgy and materials science* (28(9)):1781–1795
- ASM (1979) *Metals Handbook*; 9th ed. v.2. ISBN 0-87170-008-5
- ASTM (1994) *Annual Book of ASTM Standards*, designation: e407-93. standard practice for microetching metals and alloys edn. ASTM, Philadelphia
- Babout L, Maire E, Buffiere J, Fougères R (2001) Characterization by X-ray Computed Tomography of Decohesion, Porosity Growth and Coalescence in Model Metal Matrix Composites. *Acta Materialia* (49):2055–2063
- Bao Y, Wierzbicki T (2004) A Comparative Study on Various Ductile Crack Formation Criteria. *Transactions of the ASME* (126):314–324
- Bao Y, Wierzbicki T (2005) On the Cut-Off Value of Negative Triaxiality for Fracture. *Engineering Fracture Mechanics* (72):1049–1069
- Barsoum I, Faleskog J (2007a) Rupture Mechanisms in Combined Tension and Shear - Micromechanics. *International Journal of Solids and Structures* (44):5481–5498

- Barsoum I, Faleskog J (2007b) Rupture Mechanisms in Combined Tension and Shear - Experiments. *International Journal of Solids and Structures* (44):1768–1786
- Becker R, Smelser R, Richmond O (1989a) The Effect of Void Shape on the Development of Damage and Fracture in Plane-Strain Tension. *Journal of the Mechanics and Physics of Solids* (37(1)):111–129
- Becker R, Smelser R, Richmond O, Appelby E (1989b) The Effect of Void Shape on Void Growth and Ductility in Axisymmetric Tension Tests. *Metallurgical Transactions A* (20A):853–861
- Benson D (1995) The Effect of Void Cluster Size on Ductile Fracture. *International Journal of Plasticity* (11(5)):571–582
- Benzerga A (2000) Rupture Ductile des Tôles Anisotropes: Simulation de la Propagation Longitudinale dans un Tube Pressurisé. PhD thesis, École Nationale Supérieure des Mines de Paris
- Benzerga A (2002) Micromechanics of Coalescence in Ductile Fracture. *Journal of the Mechanics and Physics of Solids* (50):1331–1362
- Benzerga A, Besson J (2001) Plastic Potentials for Anisotropic Porous Solids. *European Journal of Mechanics A/Solids* (20A):397–434
- Benzerga A, Leblond J (2010) Ductile Fracture by Void Growth to Coalescence. *Advances in Applied Mechanics* (44):169–305
- Benzerga A, Besson J, Pineau A (1999) Coalescence-Controlled Anisotropic Ductile Fracture. *Journal of Engineering Materials and Technology* (121):221–229
- Benzerga A, Besson J, Pineau A (2004a) Anisotropic Ductile Fracture - Part I: Experiments. *Acta Materialia* (52):4623–4638
- Benzerga A, Besson J, Pineau A (2004b) Anisotropic Ductile Fracture - Part II: Theory. *Acta Materialia* (52):4639–4650
- Berg C (1970) Plastic Dilatation and Void Interaction. *Inelastic Behavior of Solids* (3):171–210
- Besson J (2004) *Local Approach to Fracture*. Les Presses de l'École de Mines, Paris, ISBN 2-911760-55-X
- Besson J, Guillemer-Neel C (2003) An Extension of the Green and Gurson Models to Kinematic Hardening. *Mechanics of Materials* (35):1–18
- Besson J, Devillers-Guerville L, Pineau A (2000) Modeling of Scatter and Size Effect in Ductile Fracture: Application to Thermal Embrittlement of Duplex Stainless Steel. *Engineering Fracture Mechanics* (67):169–190

- Billington E (1976) Non-Linear Mechanical Response of Various Metals: II. Permanent Length Changes in Twisted Tubes. *Journal of Physics D: Applied Physics* (10(4)):533–552
- Bonfroh N, Lipinski P, Carmasol A, Tiem S (2004) Micromechanical Modeling of Ductile Damage of Polycrystalline Materials with Heterogeneous Particles. *International Journal of Plasticity* (20(1)):85–106
- Bordreuil C, Boyer JC, Sallé E (2003) On Modeling the Growth and the Orientation Changes of Ellipsoidal Voids in a Rigid Plastic Matrix. *Modelling and Simulation in Materials Science and Engineering* (11):365–380
- Bourcier R, Koss D, Smelser R, Richmond O (1986) The Influence of Porosity on the Deformation and Fracture of Alloys. *Acta Metallurgica* (34(12)):2443–2453
- Bressan J, Unfer R (2006) Construction and Validation Tests of a Torsion Test Machine. *Journal of Materials Processing Technology* (179):23–29
- Budiansky B, Hutchinson J, Slutsky S (1982) Void Growth and Collapse in Viscous Solids. *Mechanics of Solids (The Rodney Hill 60th Anniversary Volume)*:13
- Buršíková V, Buršík J, Navrátil V, Milička K (2002) Creep Behavior of Leaded Brass. *Materials Science and Engineering A* (324):235–238
- Cannizzaro D (2006) Mechanisms of Void Initiation at Small Hard Particles and Implications for Ductile Fracture. PhD thesis, *École Polytechnique Fédérale de Lausanne*, no. 3579
- Cannizzaro D, Giovanola J, Doglione R, Rossoll A (2005) Observations of Ductile Fracture Processes Under Very Low Triaxiality in VAR Steel and Preliminary Interpretation. *Proceeding of the 11th International Conference on Fracture - ICF 11, Torino, Italy*
- Chin G (1975) Development of Deformation Textures. In: Argon A.S. (Ed.), *Constitutive Equations in Plasticity*. 431-447
- Cox TB, Low JR (1973) An Investigation of the Plastic Fracture of AISI 4340 and 18 Nickel-200 Grade Maraging Steels. *Metallurgical and Materials Transactions B* (5(6)):1457–1470
- Curran D, Seaman L, Shockey D (1987) Dynamic failure of solids. *Physics Reports* (147):253–388
- Danas K, Ponte-Castaneda P (2009a) A Finite-Strain Model for Anisotropic Viscoplastic Porous Media: I - Theory. *European Journal of Mechanics A/Solids* (28):387–401

- Danas K, Ponte-Castaneda P (2009b) A Finite-Strain Model for Anisotropic Viscoplastic Porous Media: II - Applications. *European Journal of Mechanics A/Solids* (28):402–416
- Dancette S, Delannay L, Jodlowski T, Giovanola J (2010) Multisite Model Prediction of Texture Induced Anisotropy in Brass. *Proceedings of the 13th International Conference on Material Forming, Brescia, Italy*
- Delannay L, Béringhier M, Chaster Y, Logé R (2005) Simulation of Cup Drawing Based on Crystal Plasticity Applied to Reduced Grain Samplings. *Materials Science Forum* (495-497):1639–1644
- Devillers-Guerville L, Besson J, Pineau A (1997) Notch Fracture Toughness of a Cast Duplex Stainless Steel: Modeling of Experimental Scatter and Size Effect. *Nuclear Engineering and Design* (168):211–225
- Dillamore I, Roberts W (1964) Rolling Texture in F.C.C. and B.C.C. Metals. *Acta Metallurgica* (12):281–293
- Drouin D, Couture A, Joly D, Tastet X, Aimez V, Gauvin R (2007) CASINO V2.42 - A Fast and Easy-to-Use Modeling Tool for Scanning Electron Microscopy and Microanalysis Users. *Scanning* (23(3)):92–101
- Eberle A, Klingbeil D (1996) Durchführung von Zellmodellrechnungen mit dem FE-Programm ABAQUS und der Riks-Methode, BAM-V31 Bericht 96/1
- Edelson B, Baldwin W (1977) The Effect of Second Phases on the Mechanical Properties of Alloys. *Transactions of the American Society of Metals* (55):238–250
- El-Danaf E, Kalidindi S, Doherty R, Necker C (2000) Deformation Texture Transition in Brass: Critical Role of Micro-Scale Shear Bands. *Acta Materialia* (48):2665–2673
- El-Danaf E, Kalidindi S, Doherty R (2001) Influence of Deformation Path on the Strain Hardening Behavior and Microstructure Evolution in Low SFE FCC Metals. *International Journal of Plasticity* (17):1245–1265
- Empl D (2009) Intermediate Temperature Grain Boundary Phenomena in Copper Alloys. PhD thesis, École Polytechnique Fédérale de Lausanne
- Enakoutsa K, Leblond J, Audoly B (2005) Influence of Continuous Nucleation of Secondary Voids Upon Growth and Coalescence of Cavities in Porous Ductile Metals. *Proceeding of the 11th International Conference on Fracture - ICF 11, Torino, Italy*
- English A, Chin G (1965) On the Variation of Wire Texture with Stacking Fault Energy in FCC Metals and Alloys. *Acta Metallurgica* (13):1013

- Fabrègue D, Pardoën T (2008) A Constitutive Model for Elastoplastic Solids Containing Primary and Secondary Voids. *Journal of the Mechanics and Physics of Solids* (56):719–741
- Faleskog J, Shih C (1997) Micromechanics of Coalescence - I. Synergistic Effects of Elasticity, Plastic Yielding and Multi-Size-Scale Voids. *Journal of the Mechanics and Physics* (41(1)):21–50
- Felberbaum L (2005) Microstructure and Embrittlement of Lead-Copper Alloys. PhD thesis, École Polytechnique Fédérale de Lausanne
- Flandi L, Leblond JB (2005a) A New Model for Porous Nonlinear Viscous Solids Incorporating Void Shape Effects - I: Theory. *European Journal of Mechanics A/Solids* (24):537–551
- Flandi L, Leblond JB (2005b) A New Model for Porous Nonlinear Viscous Solids Incorporating Void Shape Effects - II: Numerical Validation. *European Journal of Mechanics A/Solids* (24):552–571
- Fleck N, Hutchinson J (1986) Void Growth in Shear. *Proceedings of the Royal Society of London (A407)*:435–458
- Fleck N, Hutchinson J, Tvergaard V (1989) Softening by Void Nucleation and Growth in Tension and Shear. *Journal of Mechanics and Physics of Solids* (37):515–540
- Foster A, Lin J, Farrugia D, Dean T (2007) Investigation Into Damage Nucleation and Growth for a Free-Cutting Steel Under Hot-Rolling Conditions. *Journal of Strain Analysis for Engineering* (42):227–235
- Gammage J, Wilkinson D, Brechet Y, Embury D (2004) A Model for Damage Coalescence in Heterogeneous Multi-Phase Materials. *Acta Materialia* (52):5255–5263
- Gan Y, Kysar J, Morse T (2006) Cylindrical Void in a Rigid-Ideally Plastic Single Crystal. Part II: Experiments and Simulations. *International Journal of Plasticity* (22):39–72
- Garrison W, Moody N (1987) Ductile Fracture. *Journal of Physics and Chemistry of Solids* (48(11)):1035–1074
- Giovanola J, Cannizzaro D, Doglione R, Rossoll A (2006) Ductile Fracture by Void Nucleation at Carbides, Fracture of Nano and Engineering Materials and Structures. *Proceedings of the 16th European Conference on Fracture, Alexandroupolis, Greece*
- Gologanu M, Leblond JB, Devaux J (1993) Approximate Models for Ductile Metals Containing Non-Spherical Voids - Case of Axisymmetric Prolate Ellipsoidal Cavities. *Journal of the Mechanics and Physics of Solids* (41(11)):1723–1754

- Gologanu M, Leblond JB, Devaux J (1994) Approximate Models for Ductile Metals Containing Non-Spherical Voids - Case of Axisymmetric Oblate Ellipsoidal Cavities. *Journal of Engineering Materials and Technology* (116):290–297
- Gologanu M, Leblond J, Perrin G, Devaux J (1997) Recent Extensions of Gurson's Model for Porous Ductile Metals, continuum mechanics, p.suquet, ed. *cism lectures series edn*. Springer, New York
- Gologanu M, Leblond J, Perrin G, Devaux J (2001a) Theoretical Models for Void Coalescence in Porous Ductile Solids. I. Coalescence in Layers. *International Journal of Solids and Structures* (38(32-33)):5581–5594
- Gologanu M, Leblond J, Devaux J (2001b) Theoretical Models for Void Coalescence in Porous Ductile Solids. II. Coalescence in Columns. *International Journal of Solids and Structures* (38(32-33)):5595–9604
- Goodman S, Hu H (1968) Texture Development in Copper and 70 – 30 Brass. *Transactions of the Metallurgical Society of AIME* (242):88–93
- Gurson A (1977) Continuum Theory of Ductile Rupture by Void Nucleation and Growth: Part I - Yield Criteria and Flow Rules for Porous Ductile Media. *Journal of Engineering Materials and Technology* (99):2–15
- Ha S, Kim K (2010) Void Growth and Coalescence in F.C.C. Single Crystals. *International Journal of Mechanical Sciences* (52):863–873
- Hall E (1951) The Deformation and Ageing of Mild Steel: II Characteristics of the Lüders Deformation. *Proceedings of the Physical Society (London)* (B64):742–749
- Hancock J, Mackenzie A (1976) On the Mechanisms of Ductile Failure in High-Strength Steels Subjected to Multi-Axial Stress-States. *Journal of Mechanics and Physics of Solids* (24):147–169
- Hashin Z, Shtrikman S (1963) A Variational Approach to the Theory of the Elastic Behavior of Multiphase Materials. *Journal of the Mechanics and Physics of Solids* (11):127–140
- Heye W, Wasserman G (1968) The Formation of the Rolling Textures in FCC Metals by Slip and Twinning. *Scripta Metallurgica et Materialia* (2):205–207
- Hoefnagels J, Tasan C, Louws L, Geers M (2009) Comparison of Quantitative Damage Characterization Methodologies. *Proceeding of the 12th International Conference on Fracture - ICF 12*, Ottawa, Canada
- Horstemeyer M, Ramaswamy S (2000) On Factors Affecting Localization and Void Growth in Ductile Metals: A Parametric Study. *International Journal of Damage Mechanics* (9):5–28

- Huang J, III GG (1990) Serrated Flow and Negative Rate Sensivity in Al-Li Base Alloys. *Scripta Metallurgica et Materialia* (24):89–90
- Huang Y (1991) Accurate Dilatation Rates for Spherical Voids in Triaxial Stress-Fields. *Journal of Applied Mechanics-Transactions of the ASME* (58(4)):1084–1086
- Huber G, Brechet Y, Pardoën T (2005) Void Growth and Void Nucleation Controlled Ductility in Quasi Eutectic Cast Aluminium Alloys. *Acta Materialia* (53):2739–2749
- Hutchinson J, Tvergaard V (1987) Effect of Particle Void Interaction on Void Growth in Tension and Shear. *Proceedings of the 34th Sagamore Conference Innovation in Ultrahigh-Strength Steel Technology* pp 835–853
- Jia S, Raiser G, Povirk G (2002) Modeling the Effects of Hole Distribution in Perforated Aluminium Sheets I: Representative Unit Cells. *International Journal of Solids and Structures* (39):2517–2532
- Kailasam M, Ponte-Castaneda P (1998) A General Constitutive Theory for Linear and Nonlinear Particulate Media with Microstructure Evolution. *Journal of the Mechanics and Physics of Solids* (46):427–465
- Kailasam M, Ponte-Castaneda P, Willis J (1997) The Effect of Particle Size, Shape, Distribution and Their Evolution on the Constitutive Response of Nonlinearly Viscous Composites - II. Examples. *Philosophical Transactions of the Royal Society A* (355):1853–1872
- Kailasam M, Aravas N, Ponte-Castaneda P (2000) Porous Metals with Developing Anisotropy: Constitutive Models, Computational Issues and Applications to Deformation Processing. *Computer Modelling in Engineering and Sciences* (1):105–118
- Kalidindi S (2001) Modeling Anisotropic Strain Hardening and Deformation Textures in Low Stacking Fault Energy FCC Metals. *International Journal of Plasticity* (17):837–860
- Kalidindi S, Bronkhorst C, Anand L (1992) Crystallographic Texture Evolution in Bulk Deformation Processing of FCC Metals. *Journal of the Mechanics and Physics of Solids* (40(3)):537–569
- Kamio A, Kumai S, Tezuka H (1991) Solidification Structure and Monotectic Alloys. *Materials Science and Engineering (A146)*:105–121
- Karaman I, Sehitoglu H, Beaudoin A, Chumlyakov Y, Maier H, Tomé C (2000) Modeling the Deformation Behavior of Hadfield Steel Single and Polycrystals due to Twinning and Slip. *Acta Materialia* (48):2031–2047
- Keralavarma S, Benzerga A (2008) An Approximate Yield Criterion for Anisotropic Porous Media. *Comptes Rendus Mecanique* (336):685–692

- Keralavarma S, Benzerga A (2010) A Constitutive Model for Plastically Anisotropic Solids with Non-Spherical Voids. *Journal of the Mechanics and Physics of Solids* (58):874–901
- Klocker H, Tvergaard V (2003) Growth and Coalescence of Non-Spherical Voids in Metals Deformed at Elevated Temperature. *International Journal of Mechanical Sciences* (25):1283–1308
- Koplik J, Needleman A (1988) Void Growth and Coalescence in Porous Plastic Solids. *International Journal of Solids and Structures* (24(8)):835–853
- Kouzeli M (2001) Tensile Behaviour of Aluminium Reinforced with Ceramic Particles. PhD thesis, École Polytechnique Fédérale de Lausanne, no. 2348
- Kuna M, Sun DZ (1996) Analyses of Void Growth and Coalescence in Cast Iron by Cell Models. *Journal de Physique IV, Supplément au Journal de Physique III* (6):113–122
- Kysar J, Gan Y, Arzuza G (2005) Cylindrical Void in a Rigid-Ideally Plastic Single Crystal. Part I: Anisotropic Slip Line Theory Solution for Face-Centered Cubic Crystals. *International Journal of Plasticity* (21(8)):1461–1657
- Lassance D, Scheyvaerts F, Pardoën T (2006) Growth and Coalescence of Penny-Shaped Voids in Metallic Alloys. *Engineering Fracture Mechanics* (73):1009–1034
- Lassance D, Febregue D, Delannay F, Pardoën T (2007) Micromechanics of Room and High Temperature Fracture in 6xxx Al Alloys. *Progress in Materials Science* (52):62–129
- Lebensohn R, Tomé C (1994) A Self-Consistent Viscoplastic Model: Prediction of Rolling Textures of Anisotropic Polycrystals. *Materials Science and Engineering (A175)*:71–82
- Leblond J, Mottet G (2008) A Theoretical Approach of Strain Localization within Thin Planar Bands in Porous Ductile Materials. *Compte Rendus Mécanique* (336):176–189
- Lee B, Mear M (1992) Axisymmetric Deformation of Power-Law Solids Containing a Dilute Concentration of Aligned Spheroidal Voids. *Journal of the Mechanics and Physics of Solids* (40(8)):1805–1836
- Lee B, Mear M (1999) Stress Concentration Induced by an Elastic Spheroidal Particle in a Plastically Deforming Solid. *Journal of the Mechanics and Physics of Solids* (47(6)):1301–1336
- Leffers T, Juul-Jensen T (1991) The Relation Between Texture and Microstructure in Rolled FCC Materials. *Textures and Microstructures* (14(18)):933–952



- Leffers T, Ray R (2009) The Brass-Type Texture and its Deviation from the Coppers-type Texture. *Progress in Materials Science* (54):531–396
- Leffers T, Van-Houtte P (1989) Calculated and Experimental Orientation Distributions of Twin Lamellae in Rolled Brass. *Acta Materialia* (37):1191–1198
- Liu W, Zhang X, Tang J, Du Y (2007) Simulation of Void Growth and Coalescence Behavior with 3D Crystal Plasticity Theory. *Computational Materials Science* (40):130–139
- Lopriore G, McComick P, Gifkins R (1982) *Strength of Metals and Alloys*. Pergamon Press
- Ludwik P (1909) *Elemente der Technologischen Mechanik*. Springer, Berlin
- Magnusen P, Dubensky E, Koss D (1988) The Effect of Void Arrays on Void Linking During Ductile Fracture. *Acta Metallurgica* (36(6)):1503–1509
- Marini B, Mudry F, Pineau A (1985) Experimental Study of Cavity Growth in Ductile Rupture. *Engineering Fracture Mechanics* (22(6)):989–996
- McClintock F (1968) A Criterion for Ductile Fracture by the Growth of Holes. *Journal of Applied Mechanics* (35):363–371
- McMeeking R (1977) Finite Deformation Analysis of Crack-Tip Opening in Elastic-Plastic Materials and Implications for Fracture. *Journal of the Mechanics and Physics of Solids* (5):357–381
- Michel JC, Suquet P (1992) The Constitutive Law for Nonlinear Viscous and Porous Materials. *Journal of the Mechanics and Physics of Solids* (40):783–812
- Miller M, McDowell D (1996a) The Effect of Stress-State on the Large Strain Inelastic Deformation Behavior of 304L Stainless Steel. *Journal of Engineering Materials and Technology* (118(1)):28–36
- Miller M, McDowell D (1996b) Modeling Large Strain Multiaxial Effects in FCC Polycrystals. *International Journal of Plasticity* (12(7)):875–902
- Mir A, Barton D, Andrews T, Church P (2005) Anisotropic Ductile Failure in Free Machining Steel at Quasi-Static and High Strain Rates. *International Journal of Fracture* (133):289–302
- Miura S, Hashimoto S (1972) Portevin - Le Châtelier Effect in  $\alpha$ -Brass During Cyclic Straining. *Scripta Metallurgica* (6):673–676
- Monchiet V, Cazacu O, Charkaluk E, Kondo D (2008) Macroscopic Yield Criteria for Plastic Anisotropic Materials Containing Spheroidal Voids. *International Journal of Plasticity* (241):158–189

- Montheillet F, Cohen M, Jonas J (1984) Axial Stress and Texture Development During the Torsion Testing of Al, Cu and  $\alpha$ -Iron. *Acta Metallurgica* (32(11)):2077–2089
- Montheillet F, Cohen M, Jonas J (1985) Relation Between Axial Stress and Texture Development During Torsion Testing: A Simplified Theory. *Acta Metallurgica* (33(4)):705–707
- Mudry F (1985) Methodology and Applications of Local Criteria for Prediction of Ductile Tearing. *Elastic-Plastic Fracture Mechanics* pp pp. 363–371
- Mulford R, Kocks U (1979) New Observations on the Mechanisms of Dynamic Strain Aging and of Jerky Flow. *Acta Metallurgica* (27):1125–1134
- Nahshon K, Hutchinson J (2008) Modification of the Gurson Model for Shear Failure. *European Journal of Mechanics A/Solids* (27):1–17
- Nielsen K, Tvergaard V (2009) Effect of a Shear Modified Gurson Model on Damage Development in a FSW Tensile Specimen. *International Journal of Solids and Structures* (46):587–601
- O'Regan T, Quinn D, Howe M, McHugh P (1997) Void Growth Simulations in Single Crystals. *Computational Mechanics* (20):115–121
- Orsini V, Zikry M (2001) Void Growth and Interaction in Crystalline Materials. *International Journal of Plasticity* (17):1393–1417
- Pantazopoulos G, Vazdirvanidis A (2008) Failure Analysis of a Fractured Lead-Brass (CuZn39Pb3) Extruded Hexagonal Rod. *Journal of Failure Analysis and Prevention* (8):218–222
- Pardoën T (2006) Numerical Simulation of Low Stress Triaxiality Ductile Fracture. *Computers and Structures* (84):1641–1650
- Pardoën T, Hutchinson J (2000) An Extended Model for Void Growth and Coalescence. *Journal of the Mechanics and Physics of Solids* (48):2467–2512
- Pardoën T, Hutchinson J (2003a) Micromechanics-Based Model for Trends in Toughness of Ductile Metals. *Acta Materialia* (51):133–148
- Pardoën T, Doghri I, Delannay F (1998) Experimental and Numerical Comparison of Void Growth Models and Void Coalescence Criteria for the Prediction of Ductile Fracture in Copper Bars. *Acta Materialia* (46):541–552
- Pardoën T, Dumont D, Deschamps A, Brechet Y (2003b) Grain Boundary versus Transgranular Ductile Failure. *Journal of the Mechanics and Physics of Solids* (51):637–665
- Pardoën T, Hachez F, Marchioni B, Blyth H, Atkins A (2004) Mode I Fracture of Sheet Metal. *Journal of Mechanics and Physics of Solids* (52):423–452

- Perrin G, Leblond J (1990) Analytical Study of a Hollow Sphere Made of Plastic Porous Material and Subjected to Hydrostatic Tension - Application to Some Problems in Ductile Fracture of Metals. *International Journal of Plasticity* (6(6)):677–699
- Perrin G, Leblond J (2000) Accelerated Void Growth in Porous Ductile Solids Containing Two Population of Cavities. *International Journal of Plasticity* (16):91–120
- Petch N (1956) XXX. The Lowering of Fracture-Stress due to Surface Adsorption. *Philosophical Magazine* (1(4)):331–337
- Pineau A, Pardoen T (2007) Failure Mechanisms of Metals. In: *Comprehensive Structural Integrity Encyclopedia*, volume 2, chapter 6 edn. Elsevier, ISBN 2-911760-55-X
- Ponte-Castaneda P (1991) The Effective Mechanical Properties of Nonlinear Composites. *Journal of the Mechanics and Physics of Solids* (39):45–71
- Ponte-Castaneda P (1992) New Variational Principles in Plasticity and Their Application to Composite Materials. *Journal of the Mechanics and Physics of Solids* (40):1757–1788
- Ponte-Castaneda P, Zaidman M (1994) Constitutive models for Porous Materials with Evolving Microstructure. *Journal of Mechanics and Physics of Solids* (42):255–268
- Potirniche G, Hearndon J, Horstemeyer M, Ling X (2006) Lattice Orientation Effects on Void Growth and Coalescence in FCC Single Crystals. *International Journal of Plasticity* (22):921–942
- Poynting J (1909) On Pressure Perpendicular to the Shear-Planes in Finite Pure Shears, and on Lengthening of Loaded Wires when Twisted. *Proceedings of the Royal Society of London* (82):546–559
- Poynting J (1912) On the Changes in the Dimensions of a Steel Wire when Twisted, and on the Pressure of Distortional Waves in Steel. *Proceedings of the Royal Society of London* (86):534–561
- Puttick K (1959) Ductile Fracture in Metals. *Philosophical Magazine* (4):964–969
- Qi W, Bertram A (1999) Anisotropic Continuum Damage Modeling for Single Crystals at High Temperature. *International Journal of Plasticity* (15):1197–1215
- Ragab A (2004) Application of an Extended Void Growth Model with Strain Hardening and Void Shape Evolution to Ductile Fracture under Axisymmetric Tension. *Engineering Fracture Mechanics* (71):1515–1534

- Rangaswamy P, Bourke M, Brown D, Kaschner G, Stout M, Tomé C, Rogge R (2002) A study of Twinning in Zirconium Using Neutron Diffraction and Polycrystalline Modeling. *Metallurgical and Materials Transactions A* (33(3)):757–763
- Rashid M, Nemat-Nasser S (1992) A Constitutive Algorithm for Rate-Dependent Crystal Plasticity. *Computer Methods in Applied Mechanics and Engineering* (94):201–228
- Resk H, Delannay L, Bernacki M, Coupez T, Logé R (2009) Adaptive Mesh Refinement and Automatic Remeshing in Crystal Plasticity Finite Element Simulations. *Modelling and Simulation in Materials Science and Engineering* (17):1–22
- Rice J, Tracey D (1969) On the Ductile Enlargement of Voids in Triaxial Stress. *Journal of the Mechanics and Physics of Solids* (17):201–217
- Robinson J, Shaw M (1994) Microstructural and Mechanical Influences on Dynamic Strain Aging Phenomena. *International Materials Reviews* (39(3)):113–122
- Rousselier G (1986) Ductile Fracture Models and their Potential in Local Approach of Fracture. *Nuclear Engineering and Design* (105):97–111
- Sachs G (1928) Zur Ableitung einer Fließbedingung. *Zeitschrift des Vereines Deutscher Ingenieure* (72):734–736
- Schacht T, Untermann N, Steck E (2003) The Influence of Crystallographic Orientation on the Deformation Behaviour of Single Crystals Containing Microvoids. *International Journal of Plasticity* (19):1605–1626
- Scheyvaerts F (2008) Multiscale Modeling of Ductile Fracture in Heterogeneous Metallic Alloys. PhD thesis, Université Catholique de Louvain
- Scheyvaerts F, Pardoën T, Onck P (2010) A New Model for Void Coalescence by Internal Necking. *International Journal of Damage Mechanics* (19):95–126
- Shu J (1998) Scale-Dependent Deformation of Porous Single Crystals. *International Journal of Plasticity* (10-11):1085–1107
- Siruguet K, Leblond J (2004a) Effect of Void Locking by Inclusions Upon the Plastic Behavior of Porous Ductile Solids - I: Theoretical Modeling and Numerical Study of Void Growth. *International Journal of Plasticity* (20(2)):225–254
- Siruguet K, Leblond J (2004b) Effect of Void Locking by Inclusions Upon the Plastic Behavior of Porous Ductile Solids - II: Theoretical Modeling and Numerical Study of Void Coalescence. *International Journal of Plasticity* (20(2)):255–268

- Smallman R, Green D (1964) The Dependence of Rolling Texture on Stacking Fault Energy. *Acta Metallurgica* (12):145–154
- Smallman R, Ngan A (2007) *Physical Metallurgy and Advanced Materials*. ISBN 978-0-7506-6906-1
- Sovik O, Thaulow C (1997) Growth of Spheroidal Voids in Elastic-Plastic Solids. *Fatigue and Fracture of Engineering Materials and Structures* (20(12)):1731–1744
- Staroselsky A, Anand L (1997) Inelastic Deformation of Polycrystalline Face Centred Cubic Materials by Slip and Twinning. *Journal of the Mechanics and Physics of Solids* (46(4)):671–696
- Staub C, Boyer J (1998) A Ductile Growth Model for Elasto-Plastic Material. *Journal of Materials Processing Technology* (77):9–16
- Steglich D, Brocks W, Heerens J, Pardoën T (2008) Anisotropic Ductile Fracture of Al 2024 Alloys. *Engineering Fracture Mechanics* (75):3692–3706
- Sun Z, Hashimoto H, Barsoum M (2007) On the Effect of Environment on Spontaneous Growth of Lead Whiskers from Commercial Brasses at Room Temperature. *Acta Materialia* (55):3387–3396
- Suquet P (1993) Overall Potentials and Extremal Surfaces of Power Law or Ideally Plastic Materials. *Journal of the Mechanics and Physics of Solids* (41):981–1002
- Swift H (1947) Length Changes in Metals Under Torsional Overstrain. *Engineering* (163):253–257
- Talbot D, Willis J (1985) Variational Principles for Inhomogeneous Nonlinear Media. *IMA Journal of Applied Mathematics* (35):39–54
- Tanaka K, Mori T (1970) The Hardening of Crystals by Non-Deforming particles and Fibres. *Acta Metallurgica* (18):931–941
- Taylor G (1938) Plastic Strain in Metals. *Journal of the Institute of Metals* (62):307–324
- Thomason P (1985a) A Three Dimensional Model for Ductile Fracture by the Growth and the Coalescence of Microvoids. *Acta Metallurgica* (33(6)):1087–1095
- Thomason P (1985b) Three-Dimensional Models for the Plastic Limit-Loads at Incipient Failure of the Intervoid Matrix in Ductile Porous Solids. *Acta Metallurgica* (33(6)):1079–1085
- Thomason P (1990) *Ductile Fracture of Metals*. Pergamon Press, Oxford
- Thomason P (1998) A View on Ductile-Fracture Modeling. *Fatigue and Fracture of Engineering Materials and Structures* (21):1105–1122

- Thompson A, Weirauch P (1976) Ductile Fracture: Nucleation at Inclusions. *Scripta Metallurgica* (10):205–210
- Tomé C, Lebensohn R, Kocks U (1991) A Model for Texture Development Dominated by Deformation Twinning: Application to Zirconium Alloys. *Acta Metallurgica et Materialia* (39):267–2680
- Tóth L, Gilormini P, Jonas J (1988) Effect of Rate Sensitivity on the Stability of Torsion Textures. *Acta Metallurgica* (36(12)):3077–3091
- Tóth L, Jonas J, Gilormini P, Bacroix B (1990) Length Changes During Free End Torsion: A Rate Sensitive Analysis. *International Journal of Plasticity* (6(1)):83–108
- Truszkowski W (2001) *The Plastic Anisotropy in Single Crystals and Polycrystalline Metals*. Kluwer Academic Publishers, ISBN 0-7923-6839-8
- Tvergaard V (1981) Influence of Voids on Shear Band Instabilities Under Plane Strain Conditions. *International Journal of Fracture* (17):389–407
- Tvergaard V (1982) On Localization in Ductile Materials Containing Voids. *International Journal of Fracture* (27):237–251
- Tvergaard V (2008) Shear Deformation of Voids With Contact Modelled by Internal Pressure. *International Journal of Mechanical Sciences* (50):1459–1465
- Tvergaard V, Needleman A (1984) Analysis of the Cup-Cone Fracture in a Round Tensile Bar. *Acta Metallurgica* (32):157–169
- Tvergaard V, Niordson C (2004) Nonlocal Plasticity Effects on Interaction in Different Size Voids. *International Journal of Plasticity* (20(1)):107–120
- Van-Houtte P (1978) Simulation of the Rolling and Shear Texture of Brass by the Taylor Theory Adapted for Mechanical Twinning. *Acta Metallurgica* (26):591–604
- Van-Houtte P, Li S, Seefeldt M, Delannay L (2005) Deformation Texture Prediction: From the Taylor Model to the Advanced Lamel Model. *International Journal of Plasticity* (21):589–624
- Wasserman G (1963) Der Einfluss Mechanischer Zwillingsbildung auf die Entstehung der Walz-Texturen Kubisch Flächenzentrierter Metalle. *Zeitschrift für Metalkunde* (54):61–65
- Weber L, Moser B, Kunzi H, Mortensen A (2000) Swift and Inverse Swift Effect in Alumina Fiber Reinforced Aluminium Wires. *Acta Materialia* (48):2451–2459
- Weck A, Wilkinson D, Toda H, Maire E (2006) 2D and 3D Visualization of Ductile Fracture. *Advanced Engineering Materials* (8(6)):469–472

- Weck A, Wilkinson D, Maire E, Toda H (2008) Visualization by X-ray Tomography of Void Growth and Coalescence Leading to Fracture in Model Materials. *Acta Materialia* (56):2919–2928
- Wen J, Huang Y, Hwang K, Liu C, Li M (2005) The Modified Gurson Model Accounting for the Void Size Effect. *International Journal of Plasticity* (21(2)):381–395
- Wierzbicki T, Bao Y, Lee YW, Bai Y (2005) Calibration and Evaluation of Seven Fracture Models. *International Journal of Mechanical Sciences* (47):719–743
- Wijler A, Schade-Van-Westrum J, Van-Den-Beukel A (1972) A New Type of Stress-Strain Curve and the Portevin-Le Châtelier Effect in Au (14 at. Cu). *Acta Metallurgica* (20):355–362
- Willis J (1977) Bounds and Self-Consistent Estimates for the Overall Moduli of Anisotropic Composites. *Journal of the Mechanics and Physics of Solids* (25):185–202
- Willis J (1978) Variational Principles and Bounds for the Overall Properties of Composites. In: Provan J. (Ed.), *Continuum Models and Discrete Systems*. University of Waterloo Press, 185-212
- Xue L (2007) Damage Accumulation and Fracture Initiation in Uncracked Ductile Solids Subject to Triaxial Loading. *International Journal of Solids and Structures* (44):5163–5181
- Yerra S, Tekoğlu C, Scheyvaerts F, Delannay L, Van-Houtte P, Pardoen T (2010) Void Growth and Coalescence in Single Crystals. *International Journal of Solids and Structures* (47):1016–1029
- Yu Q, Hou N, Yue Z (2010) Finite Element Analysis of Void Growth Behavior in Nickel-Based Single Crystal Superalloys. *Computational Materials Science* (48):597–608
- Zhang Z, Thaulow C, Odegard J (2000) A Complete Gurson Model Approach for Ductile Fracture. *Engineering Fracture Mechanics* (67):155–168





# Curriculum Vitae

## Personal Data

Name	Tomasz Jodłowski
Date of Birth	27 November 1979
Place of Birth	Nowy Sącz, Poland
Nationality	Polish

## Education

2006 - 2011	Ph.D. in Technical Science Swiss Federal Institute of Technology - EPFL Mechanical Systems Design Laboratory - LCSM Lausanne, Switzerland
1998 - 2004	M.Sc. in Mechanical Engineering Cracow University of Technology - PK Faculty of Mechanical Engineering - WM Kraków, Poland

## Professional Experiences

2006 - 2011	Research and Teaching Assistant at Swiss Federal Institute of Technology - EPFL in Lausanne, Switzerland
2005 - 2006	Research and Development Engineer at Tenneco Automotive Eastern European Engineering Center in Gliwice, Poland.
2003 (9 months)	Research and Teaching Assistant Trainee at Cracow University of Technology - PK in Kraków, Poland.
2003 (2 months)	Project Associate at CERN in Geneva, Switzerland
2002 (9 months)	Marketing Trainee at Energocontrol in Kraków, Poland.
2001 - 2002	Technical Student at CERN in Geneva, Switzerland